ABSTRACT

Title of dissertation: STATISTICAL MECHANICAL THEORY FOR AND SIMULATIONS OF CHARGED FLUIDS AND WATER

Jocelyn Michelle Rodgers, Doctor of Philosophy, 2008

Dissertation directed by: Professor John D. Weeks
Department of Chemistry
Institute for Physical Science Technology

Treatment of electrostatic interactions in simulations remains a topic of current research. These interactions are present in most biomolecular simulations, and they remain an expensive part of the simulation. Herein we explore the application of local molecular field (LMF) theory to this problem. Local molecular field theory splits the Coulomb potential $1/r$ into short-ranged and long-ranged components. The short-ranged component may be treated explicitly in simulations and the long-ranged component is contained in a mean-field-like average external electrostatic potential. In this thesis, the derivations and approximations inherent in using the previously developed LMF theory are explored, and connections to classical electrostatics are made. Further the approach is justified for molecular systems. The application of LMF theory to several systems is explored. First, a simple system of uniformly charged walls with neutralizing counterions is treated via simulations using LMF theory. We then explore systems involving molecular water at ambient conditions. A simple approximation to LMF theory using only the short-ranged component of

$1/r$ is quite powerful for bulk water. A full treatment using LMF theory extends the validity of such spherical truncations to nonuniform systems. This thesis studies the successful treatment of water confined between hydrophobic walls with and without an applied electric field – a system which is a classic example of the failings of spherical truncations in molecular simulations. Additional results exemplify the applicability of LMF simulations to more molecularly realistic simulations. Connection is also made between these simulations of confined water and a related theory of hydrophobicity due to Lum, Chandler, and Weeks (1999).

STATISTICAL MECHANICAL THEORY FOR AND SIMULATIONS OF CHARGED FLUIDS AND WATER

by

Jocelyn Michelle Rodgers

Dissertation submitted to the Faculty of the Graduate School of the
University of Maryland, College Park in partial fulfillment
of the requirements for the degree of
Doctor of Philosophy
2008

Advisory Committee:
Professor John D. Weeks, Chair/Advisor
Professor Michael E. Fisher
Professor Christopher Jarzynski
Professor Devarajan Thirumalai
Professor Sergei Sukharev, Dean's Representative

Acknowledgements

I would like to thank my advisor, Professor John Weeks, for his guidance over the last few years and for my introduction to the theoretical underpinnings of this thesis. I would also like to thank the rest of his research group. I owe his former student Dr. Yng-Gwei Chen a particular debt of gratitude. She pioneered the application of LMF theory to charged systems, and her work was absolutely crucial in developing the research in this thesis. She will be missed.

I would also like to thank the rest of my committee – Professors Michael Fisher, Chris Jarzynski, Dave Thirumalai, and Sergei Sukharev – for agreeing to serve on my committee. I appreciate their effort and time. And I owe both John Weeks and Michael Fisher for teaching classes in thermodynamics and statistical mechanics that I truly enjoyed.

The Chemical Physics graduate program has been a great place to be a student over the last few years. I thank both Professor Michael Coplan and Debbie Jenkins for their guidance and help over the last few years. Also, the support of the UMD Chemical Physics-NIST joint fellowship was appreciated.

I also thank Herman Keith for mentoring me for my first research project in high school, and Professor Don Truhlar for introducing me to computational and theoretical chemistry research.

Finally I would like to thank my family and friends for their support over the years. Most of all, I would like to thank my husband Mike O'Hara for his love, encouragement, helpful writing comments, and computer tips.

Table of Contents

List of Figures

List of Tables

List of Symbols and Abbreviations

$*$	Convolution	82
ϵ	Dielectric constant of a given medium. May either be assumed as a constant or calculated based on the response of molecules to an applied field	25
$\mathcal{L}$	System Lagrangian	214
$\mathcal{U}$	Total system potential energy	35
$\mathcal{V}$	Externally imposed electrostatic potential	81
$\mathcal{V}_0$	Short-ranged portion of $\mathcal{V}$	82
$\mathcal{V}_1$	Long-ranged portion of $\mathcal{V}$	82
$\mathcal{V}_R$	Local molecular field theory rescaled electrostatic potential	82
$\mathcal{V}_{R1}$	Slowly-varying component of $\mathcal{V}_R$	82
ϕ	Externally imposed potential energy surface	9
ϕ_0	Short-ranged portion of ϕ	21
ϕ_1	Long-ranged portion of ϕ	21
ϕ_R	Local molecular field theory rescaled potential energy function	9
Φ_{pol}	Electrostatic potential determined from equilibrated simulation charge density profile	145
ϕ_{R1}	Slowly-varying component of ϕ_R	21
$\rho^{(1)}(\mathbf{r})$	(Singlet) density at position $\mathbf{r}$	12
$\rho^{(2)}(\mathbf{r}, \mathbf{r}')$	Two-particle density representing the density associated with finding one particle at position $\mathbf{r}$ and another particle at position $\mathbf{r}'$.	13
ρ^{q_σ}	Smoothed charge density profile consisting of ρ^q convoluted with ρ_G, a Gaussian of width σ	83

ρ^q	Charge density profile	81
ρ_G	A normalized Gaussian of width σ, $\exp\left(-r^2/\sigma^2\right)/\sigma^3/\pi^{3/2}$	82
$\rho_M(\mathbf{R}_\mathrm{M})$	Density associated with a specific orientation of molecule M defined by $\mathbf{R}_\mathrm{M}$	109
$\rho\left(\mathbf{r}'\middle\|\mathbf{r}\right)$	Conditional density at position $\mathbf{r}'$ given that a particle is positioned at $\mathbf{r}$	13
$\varrho_{M\|\alpha}(\mathbf{R_M}\|\mathbf{r})$	Intramolecular conditional density of molecular orientation $\mathbf{R_M}$ given that an intramolecular site α is located at $\mathbf{r}$.	110
σ	Smoothed truncation length used to split $1/r$ into components	24
σ_LJ	Lennard-Jones core size	10
σ_min	Approximate smallest length-scale for accurately using the LMF splitting of $1/r$.	25
ε_LJ	Lennard-Jones attractive well depth	10
ξ	Coupling strength for charged wall system	34
E_0	Externally applied electric field	151
e_0	Elementary unit of charge, approximately 1.6×10^{-19} Coulombs	32
E_{pol}	Electric field due to molecular polarization determined from equilibrated simulation charge density profile	152
g_opp	Two-dimensional radial distribution function between particles on opposite sides of midplane	59
g_same	Two-dimensional radial distribution function between particles that are on the same side of midplane	59
L_B	Bjerrum length for a pair of ions of specified valence	33
L_G	Gouy-Chapman length for a charged wall and an ion of specified valence	33
L_w	Length defining the area on a wall neutralized by a counterion	34

L_{nn}	Average nearest neighbor distance in two wall simulations	60
P_{contact}	Osmotic pressure between charged walls as determined by the density of ions in contact with a wall	63
P_{midplane}	Osmotic pressure between charged walls as determined by ion density in the central region	64
P_{osm}	Osmotic pressure	235
q_w	Uniform surface charge density of each wall in Chapter 3	31
r_0	The position of Lennard-Jones energy minimum, equal to $2^{1/6}\sigma_{\text{LJ}}$	10
$u_0(r)$	Short-ranged part of a pair-potential $w(r)$	9
$u_1(r)$	Long-ranged or residual part of a pair-potential $w(r)$	10
$u_{\text{attr}}(r)$	Attractive portion of the LJ potential used as $u_1(r)$	10
$u_{\text{WCA}}(r)$	Repulsive core of the LJ potential used as $u_0(r)$	10
u_{LJ}	Lennard-Jones potential energy function	10
$v_0(r)$	Short-ranged part of the Coulomb potential $1/r$ defined as $\text{erfc}(r/\sigma)/r$ in LMF theory	25
$v_1(r)$	Long-ranged part of the Coulomb potential $1/r$ defined as $\text{erf}(r/\sigma)/r$ in LMF theory	25
$w(r)$	Full pair potential between particles; $w(r) = u_0(r) + u_1(r)$	9
Z	Valence of point counterions in Chapter 3	32
DH	Debye-Hückel	87
EPM	External potential method	95
GT	Gaussian-truncated; $1/r$ interactions between charged sites on molecules are replaced with $v_0(r)$ interactions, thereby truncating the potential smoothly	112

HA	Hydrostatic approximation	192
HLR	Hydrostatic linear response	192
IPS	Isotropic periodic sums [111]	104
LCW	Theory of hydrophobicity due to Lum, Chandler, and Weeks [62]	189
LJ	Lennard-Jones potential as defined in Eq. (2.3)	10
LMF	local molecular field	8
MC	Monte Carlo	72
MD	Molecular dynamics	114
MPB	mimic Poisson-Boltzmann	29
NVT	Canonical ensemble	114
PB	Poisson-Boltzmann	86
RC	"repulsive core" for Gaussian-truncated water, meaning that $u_{\mathrm{LJ}}(r)$ has been replaced by $u_{\mathrm{WCA}}(r)$	198
RF	Reaction field truncation of $1/r$. Actually can refer to several different truncations.	89
SCA	strong-coupling approximation	30
SF	Shifted force truncation of $1/r$	89
SPC/E	Extended simple point charge model of water [5]	113
WCA	Splitting of the LJ potential into short- and long-ranged parts attributable to Weeks, Chandler, and Andersen [104]	10
YBG	Yvon-Born-Green hierarchy of equation	12

Chapter 1

Introduction

Molecular simulations have become an increasingly important contributor to scientific study as computing power has grown and the availability of simulation packages developed by experts has increased. Appropriately designed simulations can add insight into important phenomena such as protein folding and the behavior of cell membranes. Nearly all classical molecular simulations include point charge interactions and the associated computational challenges. Biomolecular force-fields like CHARMM [64] and AMBER [25] quite generally assign effective point charges to interaction sites even in neutral molecules to represent the charge separation of the quantum mechanical electron cloud along bonds. In addition, water molecules are increasingly being included explicitly in these simulations in order to attain molecular-level detail. Effective point charges are found in most standard water models. These play a dual role, describing both the strong local forces leading to the hydrogen-bond network in liquid water and the longer-ranged dipole-dipole interactions.

In a standard simulation involving biomolecular solutes in water or salt solution, only a relatively small number of particles are considered explicitly in the simulation cell. Periodic boundary conditions are typically used to represent the isotropic nature of the solvent away from the solutes and away from the macroscopic fluid container walls [31]. For a simple fluid like argon, intermolecular interactions decay

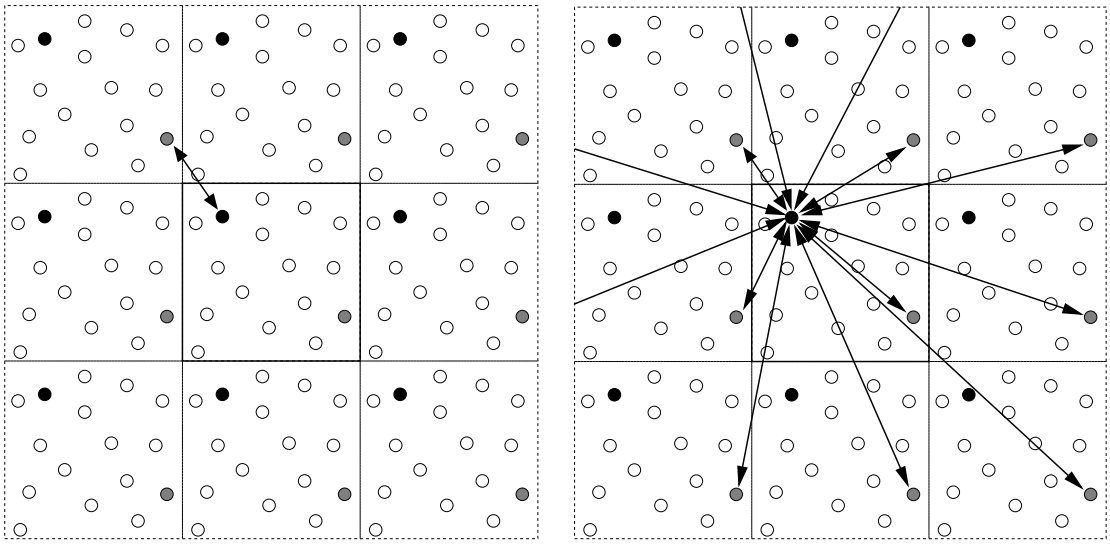

(a) Minimum Image (b) All Images

Figure 1.1: Periodic boundary conditions for simulations are traditionally treated differently depending on whether the particles are charged. The main simulation box in the center is periodically replicated to better represent the isotropic nature of the fluid. Thus there are multiple images of the black and grey particles. For typical short-ranged interactions, the minimum image convention (a) is reasonable, and the black particle in the main simulation cell interacts only with the nearest image of the grey particle. In contrast, when charges are involved, the interaction of the black particle with all periodic images (b) of the grey particle is typically included.

rapidly enough that only the minimum (closest) image of solvent particles needs to be accounted for in most cases. As shown in Fig. 1.1(a), only the pair interaction between one particle and the nearest image of another particle must be considered. In such cases, the potential is cutoff at some radius R_c, and interactions beyond R_c are neglected.

However Coulomb interactions are long-ranged and need special treatment. Neglecting $1/r$ interactions beyond a cutoff radius R_c is not reasonable as seen from the divergence of the integral of $1/r$ beyond any R_c, specifically,

$$\lim_{R\to\infty} \int_{R_c}^{R} \frac{1}{r}\, d\mathbf{r} = \lim_{R\to\infty} 2\pi r^2 \Big|_{R_c}^{R} = \infty. \tag{1.1}$$

A strict implementation of periodic boundary conditions requires summation of interactions from charges in all periodic images of the simulation cell out to some macroscopic boundary as indicated in Fig. 1.1(b). This boundary is often taken to be a sphere immersed in a conducting solution, and in general the final result depends on that macroscopic boundary condition as well. Manners of carrying out such periodic sums correctly [9, 19, 23, 24], of performing the sums in a more isotropic fashion [55, 111], and of spherically truncating the $1/r$ interaction in an optimal fashion [29, 43, 47, 50, 75, 96, 110, 115] remain topics of current research.

In this thesis, we explore a method called local molecular field (LMF) theory [14, 102, 105, 107] which also prescribes a smooth spherical cutoff of the $1/r$ interaction. A typical and valid objection to such spherical truncations was convincingly established by Feller *et al.* [28] over a decade ago. Using solely a spherical truncation leads to quite pronounced errors in properties when water is simulated in nonuniform geometries, such as in a slab between vapor layers or near a lipid bilayer. However, the LMF approach also provides a mechanism to include any net additive effects of the long-ranged forces; this is exactly what is lacking in typical spherical truncations [93]. Furthermore, LMF theory is a framework in which we may understand the net electrostatic effects of those long-ranged interactions that are often disguised by the step-by-step application of lattice summation techniques and the assignment of discrete point charges in the models. If nothing else, since spherically-truncated $1/r$ potentials are still used when lattice sum techinques are prohibitive [8, 18, 91], the LMF perspective may allow scientists to understand when spherical truncations are appropriate and when they are fraught with peril.

In Ch. 2, a derivation of LMF theory is given. The basic equation of LMF theory encompasses the net additive long-ranged forces and appears to be simply a mean-field equation; however, there are specific, physical approximations applied to exact statistical mechanical equations that lead to the LMF equation. We will explore both those approximations and also preliminary applications of LMF theory to non-charged systems. LMF theory begins by splitting the potential into short-ranged and long-ranged components, and such a split is not obvious for $1/r$. Chapter 2 explains the virtues of our chosen Gaussian-smoothed split and mentions original applications of this approach to Coulomb systems, largely due to Chen [13] and co-workers. The material discussed in this chapter has been well-established by previous researchers in the Weeks group; however, this discussion is crucial to understanding the basis for most of the work that follows.

Chapter 3 discusses the first application of LMF theory for charge interactions to Monte Carlo simulations of a nonuniform slab-like system – two uniformly charged walls with point counterions in the intermediary space. This deceptively simple system has been much studied since it exhibits like-charged attraction, a phenomenon of biophysical interest [15, 36, 52, 71, 87]. After an introduction to the rich physics of this simple system, we will discuss the application of LMF theory to simulations of this system. The two-charged-wall system provides a good base for understanding the application of LMF theory and how it ties in with the approximations made to yield the LMF equation. Also, the basis for like-charged attraction in this system is explored in the context of structural rearrangements and insight available from the LMF treatment.

In Ch. 4, the LMF equation for electrostatic interactions is shown to simply yield a static electrostatic potential due to a Gaussian-smoothed equilibrium charge density. Previous authors [13, 14] have certainly been aware of this statement; however, the implications have become clearer with our application of LMF theory to molecular systems. We rewrite the LMF equation as a rescaled electrostatic potential and introduce a Gaussian-smoothed charge density. Then the connections between the LMF approach and other approaches to electrostatics in simulations are also explored in more detail. In particular, the lattice summation techniques used as benchmarks in this thesis are discussed in Sect. 4.6.

The interpretation of the LMF equation as a rescaled electrostatic potential also proves quite useful for standard site-site molecular models. In Ch. 5, derivations of the LMF equation for such site-site models are presented. In the end, the LMF equation remains equivalent to that proposed in Chs. 2 and 4. However further physically-based approximations are required to yield the electrostatic LMF equation, Eq. (4.9). Results for LMF theory applied to the molecular dynamics of a site-site water model in bulk are also presented. These results simply follow by using only the Gaussian-smoothed spherical truncation of $1/r$ prescribed by LMF theory. The structure is quite accurate employing only this truncation, and the energy and pressure are easily corrected with the aid of simple analytical formulae based on the equivalent of the Stillinger-Lovett second moment condition for molecules. However, as mentioned previously, such truncations are well-known to lead to inaccuracies in nonuniform geometries.

In Ch. 6, the full LMF treatment is used to correctly treat molecular dynamics

simulations of water in nonuniform environments. The first system explored is water confined between two smooth hydrophobic walls. The reasons for the failure of spherical truncations are explained, and the success of a full LMF treatment of the system is demonstrated. Failings of spherical truncations are evident only when examining electrostatic properties of the system, such as the potential drop across the interfacial region, which results from ordering of the surface dipoles. These electrostatic properties result from a delicate balance between the short-ranged hydrogen-bonding of water molecules and the long-ranged opposition to severe dipolar ordering. The LMF approach provides a natural way to disentangle these two effects, which both result from the point charges on the water model.

When an electric field is applied normal to the confining walls instead, as in [112], even the density profiles of atoms are completely incorrect using solely spherical truncations. This system can also be used to calculate the dielectric constant of water, using an analogy to a classical dielectric slab. As shown in Sect. 6.4, relatively simple solutions of the LMF equation correct the structure of the water molecules in an applied field; however, accurate determination of the dielectric constant proved to be more challenging owing to the inherently greater fluctuations in the charge density profile for short-ranged systems. A heuristic ensemble-like approach proved useful in surmounting these difficulties.

The treatment of water in slab geometries is extended to enclosing surfaces with atomic-level detail [82] in the latter portion of Ch. 6. For all previous slab geometry systems, solving the LMF equation required solving a simple one-dimensional self-consistent equation since the density profile depends only on position normal to the

walls. Adding in structural detail along the surface would suggest that the density now depends on $\mathbf{r}$ rather than just z. However, analysis of simulation results shows that while the density does depend on $\mathbf{r}$, the Gaussian-smoothing of the charge density inherent in the LMF approach actually makes a one-dimensional equation quite a good approximation. This result combined with the applicability of the LMF equation for large site-site molecules shown in Ch. 5 strongly suggests that the LMF approach will be relevant for slab systems of biomolecular interest such as membranes.

In Ch. 7, some connections are also made with a standard theory for hydrophobicity developed by Lum, Chandler, and Weeks [62] (LCW). The LCW theory is related to LMF theory, using an alternate treatment developed by Weeks [102]. We then explore some observations based on the application of LMF theory to simulations of water between hydrophobic walls that may be useful in understanding results that contradict LCW conclusions and in improving on the LCW approach. In particular, the conjecture of LCW that water near a hydrophobic surface may be viewed as a shifted liquid-vapor interface has been controversial as researchers seek to identify a "vapor" layer. LMF analysis of forces exerted on water molecules near hydrophobic walls highlights how the physical framework of LCW theory could be made more quantitative using simulation data, but this research is a work in progress.

Much of the work in this thesis has very natural extensions and interesting further questions. Chapter 8 concludes this thesis and outlines some of these future directions. Also, several appendices at the end touch on subjects that were useful in finding various results in the thesis but might otherwise interrupt the logical flow of the main results presented. The reader's attention is directed to them where appropriate.

Chapter 2

Local Molecular Field Theory

Local molecular field theory will be applied primarily to charge interactions. However, the derivation is quite general. Here, we review the derivation of LMF theory for a single-component system with pair interactions $w(r)$ and an external potential energy surface $\phi(\mathbf{r})$. We will use Lennard-Jones (LJ) interactions as an initial example, following the original application of LMF theory. Then the technique as applied to simple Coulomb systems is described. These are all developments in LMF theory attributable to previous researchers in the field as reviewed by Weeks [102] and furthered for Coulomb systems as initially described by Chen, Kaur, and Weeks [14] and later extended by Chen and Weeks [15]. Thus this chapter is devoted not to new results but rather to explanation of previously known results that will be used extensively throughout the thesis. Also, since the final LMF equation appears to be merely a mean-field equation, understanding the statistical mechanical roots of LMF theory will be crucial in appreciating that the accurate results we obtain are due to reasonable approximations based on an exact statistical mechanical framework behind what might appear as a naïve mean-field ansatz. Furthermore, we will build on this derivation later in Ch. 5 to justify the application of LMF theory to molecular models, a focus of the latter half of this thesis.

The LMF formula may be derived for mixtures of particles labeled α, β, γ, and

so on, and interacting via $w^{\alpha\beta}(r)$ in various external potential energy surfaces $\phi^{(\alpha)}(\mathbf{r})$ due to fixed charged objects [15]. In Ch. 4, we will explore this formulation to reveal simpler connections of local molecular field theory to electrostatics. However the basic assumptions of LMF theory are most evident through the discussion of a single-component system, with the added benefit of substantially simpler notation. Much of the following text is adapted from [85].

2.1 Motivation

The underlying idea of LMF theory is to obtain a mapping from a full system described by pair potential $w(r)$ between particles and an external potential energy function $\phi(\mathbf{r})$ acting on each particle individually to a *mimic* system defined by shorter-ranged pair interactions $u_0(r)$ and a rescaled external potential energy function $\phi_R(\mathbf{r})$. This may be summarized as

$$\begin{matrix} \text{Full} \\ \left\{ \begin{array}{c} w(r) \\ \\ \phi(\mathbf{r}) \end{array} \right\} \end{matrix} \xrightarrow{\text{LMF}} \begin{matrix} \text{Mimic} \\ \left\{ \begin{array}{c} u_0(r) \\ \\ \phi_R(\mathbf{r}) \end{array} \right\} \end{matrix} . \tag{2.1}$$

We call the final combination a *mimic* system because we seek a system that captures much relevant behavior of the full system with an alternate pair potential and a modified external potential energy function. Further we seek this mapping to be closed, in the sense that the mapping should not require any information about the full system other than the original $w(r)$ and $\phi(\mathbf{r})$. We also define the residual pair

potential $u_1(r)$ such that

$$w(r) = u_0(r) + u_1(r). \tag{2.2}$$

We may reasonably expect that some $\phi_R(\mathbf{r})$ could account for the neglected long-ranged interactions $u_1(r)$, but we seek a more careful development of this intuition.

Certainly, the concept of mapping a pair interaction to a more short-ranged reference system is not a new idea. Thermodynamic perturbation theory begins with just such a mapping [69]. The roots of LMF theory lie in the use of the so-called WCA truncation of the Lennard-Jones (LJ) potential $u_{\mathrm{LJ}}(r)$ due to Weeks, Chandler, and Andersen [104]. The LJ potential is defined as

$$u_{\mathrm{LJ}} = 4\varepsilon_{\mathrm{LJ}} \left\{ \left(\frac{\sigma_{\mathrm{LJ}}}{r}\right)^{12} - \left(\frac{\sigma_{\mathrm{LJ}}}{r}\right)^{6} \right\}, \tag{2.3}$$

and the WCA core is defined as

$$u_0(r) \equiv u_{\mathrm{WCA}}(r) = \begin{cases} u_{\mathrm{LJ}}(r) + \varepsilon_{\mathrm{LJ}} & \text{if } r \leq r_0, \\ 0 & \text{if } r > r_0, \end{cases} \tag{2.4}$$

neglecting the purely attractive interactions

$$u_1(r) \equiv u_{\mathrm{attr}}(r) = \begin{cases} -\varepsilon_{\mathrm{LJ}} & \text{if } r \leq r_0, \\ u_{\mathrm{LJ}}(r) & \text{if } r > r_0, \end{cases} \tag{2.5}$$

as shown in Fig. 2.1. The σ_{LJ} defines the length scale of the LJ potential and is the position where the potential crosses zero, and $\varepsilon_{\mathrm{LJ}}$ defines the energy scale and the depth of the potential well. This energy minimum is located at $r_0 \equiv 2^{1/6}\sigma_{\mathrm{LJ}}$.

Chandler, Weeks, and Andersen [12] observed that the structure of the LJ fluid was reproduced much more succesfully by truncating and shifting the $u_{\mathrm{LJ}}(r)$ potential

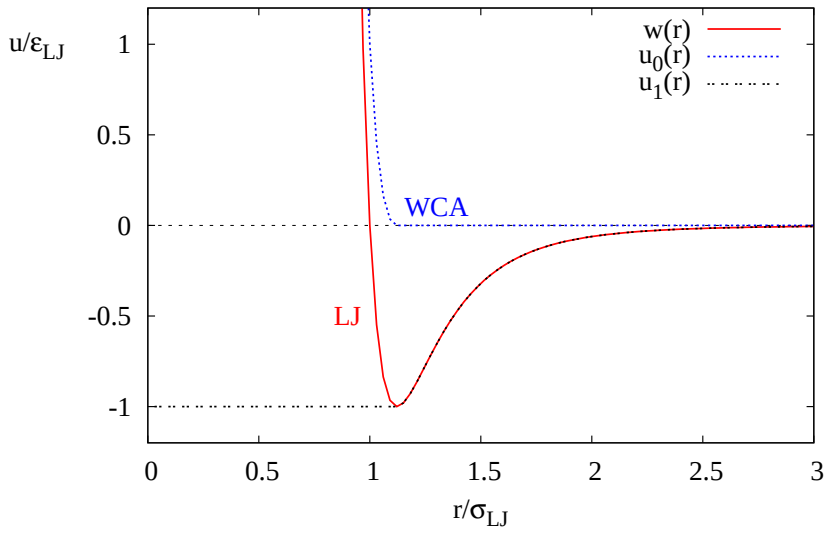

Figure 2.1: The simple Lennard-Jones (LJ) pair potential, $w(r)$, parametrized by length scale σ_{LJ} and well depth $\varepsilon_{\mathrm{LJ}}$ may be split into a repulsive core $u_0(r)$ and an attractive perturbation $u_1(r)$, following Weeks *et al.* [104].

at r_0 to yield $u_{\mathrm{WCA}}(r)$ rather than truncating $u_{\mathrm{LJ}}(r)$ at σ_{LJ} as suggested by Barker and Henderson [4]. The essence of this difference lies in that fact that the WCA truncation preserves all the repulsive forces between particles, which are impulsive in nature, and assumes that the remaining attractive forces cancel out and thus have little impact on the structure in a dense fluid. A fluid with pair potentials mapped from $u_{\mathrm{LJ}}(r)$ to $u_{\mathrm{WCA}}(r)$ is called a WCA fluid here. For a dense uniform LJ fluid, the corresponding WCA fluid is a very reasonable approximation. However, should the LJ fluid be placed in a nonuniform environment such as near a hard wall, this approximation no longer holds. The LJ fluid has net attractive forces pulling the surface particles towards the liquid phase which the WCA fluid does not have. Furthermore, in general, WCA fluids have no liquid-vapor transition because there are no attractive forces pulling them together.

This, however, does not mean that the WCA short-ranged cores are irrelevant in nonuniform situations. Rather, a method to include those net long-ranged forces, *i.e.* LMF theory, must be employed. The basic idea will be splitting $w(r)$ into $u_0(r)$ and $u_1(r)$ such that $u_0(r)$ still encompasses the short-ranged forces and $u_1(r)$ is slowly-varying over those forces. This idea is more generally applicable; therefore, for the most part, we will express the derivation in terms of general pair potentials, but we will use the LJ split to exemplify the approach after the initial derivation. This approach may be historical in nature, but it does nicely emphasize the added advantages we realize when using LMF theory to treat Coulomb interactions in lieu of LJ interactions.

2.2 Exact Starting Point for LMF Theory

Beginning with the idea that the forces are the relevant physical interaction to consider, the derivation of the LMF equation starts with an exact statistical mechanical equation involving structure and forces, the Yvon-Born-Green (YBG) hierarchy of equations [37, 69]. In one form, the first equation in the hierarchy[1] reads

$$k_B T \vec{\nabla} \ln \rho^{(1)}(\mathbf{r}) = -\vec{\nabla}\phi(\mathbf{r}) - \int d\mathbf{r}' \rho(\mathbf{r}'|\mathbf{r}) \vec{\nabla} w(|\mathbf{r} - \mathbf{r}'|). \tag{2.6}$$

This equation maps the (singlet) density profile of the system, $\rho^{(1)}(\mathbf{r})$, to the force due to an external potential energy surface, $\phi(\mathbf{r})$, and the convolution between the

[1]The determination of this equation from partition functions is relatively straightforward. Since we will be applying LMF theory to mixtures and molecules in addition to single component fluids, and those applicable YBG equations are far less available in textbooks, the derivation of Eq. (2.6) and variants is presented in Appendix A.

conditional singlet density, $\rho\left(\mathbf{r}'|\mathbf{r}\right)$, and the force between particles. The conditional singlet density $\rho\left(\mathbf{r}'|\mathbf{r}\right)$ is defined as the density at position $\mathbf{r}'$ given that a particle is at $\mathbf{r}$, and it may be defined mathematically as

$$\rho\left(\mathbf{r}'|\mathbf{r}\right) \equiv \frac{\rho^{(2)}(\mathbf{r},\mathbf{r}')}{\rho(\mathbf{r})}, \tag{2.7}$$

where $\rho^{(2)}(\mathbf{r},\mathbf{r}')$ is the two-particle density associated with finding one particle at $\mathbf{r}$ and another particle at $\mathbf{r}'$.

The YBG hierarchy in general expresses each "degree" of particle density in terms of density functions involving more particles. Thus, the single-particle density is defined via a convolution of the two-particle density. Therefore, there are two difficulties in solving the YBG equation. First of all, the density profile is defined in terms of the even more complex conditional singlet density. Secondly, there is no obvious manner to create a self-consistent loop to solve the equation.

Typical superposition closures of the YBG hierarchy resolve both difficulties simultaneously by approximating $\rho\left(\mathbf{r}'|\mathbf{r}\right) \simeq \rho^{(1)}\left(\mathbf{r}'\right)$, leading to an equation where the gradient over $\mathbf{r}$ can be interchanged with the integral in Eq. (2.6). However as shown in Fig. 2.2, even for a bulk fluid, this is a very poor approximation for any moderately dense liquid. Such an approximation neglects any excluded-volume or specific-binding interactions. Thus, the usual superposition closure is generally very inaccurate [57, 101]. The term $\vec{\nabla}\ln\rho^{(1)}\left(\mathbf{r};[\phi]\right)$ will be rapidly varying when $\phi(\mathbf{r})$ is rapidly varying, and this function is determined from the convolution of two even more rapidly-varying terms – $\rho(\mathbf{r}'|\mathbf{r};[\phi])$ and $\vec{\nabla}w\left(|\mathbf{r}-\mathbf{r}'|\right)$. Replacing the conditional singlet density with the singlet density simplifies the problem but also effectively

includes too many configurations where two particles are improbably close to each other. Over-inclusion of these improbable configurations incorrectly includes large repulsive forces in the integration and can lead to great inaccuracy.

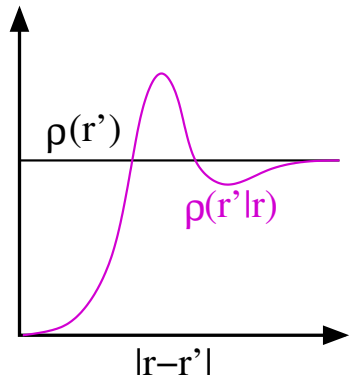

Figure 2.2: Sketch showing the distinction between the singlet density $\rho(\mathbf{r}')$ and the conditional singlet density $\rho(\mathbf{r}'|\mathbf{r})$. The conditional singlet density encompasses at least the excluded volume effects from a particle present at $\mathbf{r}$.

As we have said previously, for LJ systems at least, there exists a good choice of $u_0(r)$ that captures exactly those excluded-volume contributions. Thus, as a starting point, we write the YBG equations for both the full sytem and an LMF-mapped system as described by Eq. (2.1) as

$$\begin{aligned} k_B T \vec{\nabla} \ln \rho^{(1)}\left(\mathbf{r};[\phi]\right) &= -\vec{\nabla}\phi(\mathbf{r}) - \int d\mathbf{r}' \rho\left(\mathbf{r}'|\mathbf{r};[\phi]\right) \vec{\nabla} w\left(|\mathbf{r}-\mathbf{r}'|\right), \\ k_B T \vec{\nabla} \ln \rho_R^{(1)}\left(\mathbf{r};[\phi_R]\right) &= -\vec{\nabla}\phi_R(\mathbf{r}) - \int d\mathbf{r}' \rho_R\left(\mathbf{r}'|\mathbf{r};[\phi_R]\right) \vec{\nabla} u_0\left(|\mathbf{r}-\mathbf{r}'|\right). \end{aligned} \tag{2.8}$$

In these equations, the R subscript is meant indicate that we are now in a *reference* state defined by ϕ_R and $u_0(r)$. Further the density profiles and conditional singlet densities are described as functionals of $\phi(\mathbf{r})$ and $\phi_R(\mathbf{r})$ to again emphasize the rescaling of the external potential energy surface in the reference state.

Note that the two equations in Eq. (2.8) look quite similar. Substantial cancel-

lation becomes possible if we postulate that we choose a ϕ_R such that

$$\rho^{(1)}(\mathbf{r};[\phi]) = \rho_R^{(1)}(\mathbf{r};[\phi_R]). \tag{2.9}$$

The simplest reference system, an ideal gas with $u_0(r) = 0$, would solely require choice of ϕ_R such that $\exp\left(-\beta\phi_R(\mathbf{r})\right) = \rho^{(1)}\left(\mathbf{r}\right)$. Of course, at this point, it would require knowledge of the full system density profile in order to do so. For more general reference systems, this equation should be valid provided that the reference system does not have larger cores than the full system, a requirement we would expect any good mimic system to fulfill.

Currently, we do not have a manner to determine ϕ_R independently of the full system, but we assume that we shall be able to achieve the equality in Eq. (2.9). With this equality of singlet densities we may exactly write the difference between the two equations in Eq. (2.8) as

$$\begin{aligned} -\vec{\nabla}\phi_R(\mathbf{r}) = -\vec{\nabla}\phi(\mathbf{r}) &- \int d\mathbf{r}'\rho\left(\mathbf{r}'|\mathbf{r};[\phi]\right)\vec{\nabla}w(r)\left(|\mathbf{r}-\mathbf{r}'|\right) \\ &+ \int d\mathbf{r}'\rho_R\left(\mathbf{r}'|\mathbf{r};[\phi_R]\right)\vec{\nabla}u_0\left(|\mathbf{r}-\mathbf{r}'|\right). \end{aligned} \tag{2.10}$$

The rapidly-varying terms involving $\vec{\nabla}\ln\rho^{(1)}\left(\mathbf{r}\right)$ have been eliminated. If we could solve this equation, we would have a ϕ_R for the reference system that would exactly yield the equality of singlet densities. However, different choices of $u_0(r)$ would generate different ϕ_R, and there is no guarantee that these reference systems would *mimic* any other behavior of the full system aside from the singlet density and properties that depend solely on this singlet density. Additionally, solving this equation entails knowledge of the more complicated conditional singlet densities of *both* the reference and the full systems, so it might seem that we have made no progress.

2.3 Approximations to Yield the LMF Equation

The previous section contained exact statistical mechanical expressions, but from here on, we will be making physically-motivated approximations to the exact equations. These approximations will result in a final LMF equation below in Eq. (2.13) that has a simple mean-field form. The derivation given below will elucidate that the LMF equation is not a blind assertion of mean-field behavior but rather a valid and accurate approximation, provided that we choose our mimic system carefully.

Recalling from Eq. (2.2) that

$$w(r) = u_0(r) + u_1(r),$$

the LMF derivation focuses on making several physically-reasonable approximations based on choosing a short-ranged $u_0(r)$ that will induce the correct nearest-neighbor structure, where the conditional singlet and singlet densities differ the most, and a corresponding $u_1(r)$ that is slowly-varying on that length scale. When $u_0(r)$ and $u_1(r)$ are chosen correctly, we expect a reference system of particles interacting via $u_0(r)$ in a field $\phi_R(\mathbf{r})$ defined by LMF theory to *mimic* the behavior of the full system.

We seek a "special reference system" that we will call a "mimic system" that:

- Has a well-chosen $u_0(r)$ that *mimics* higher order correlations in the full system as well as the singlet density profile.
- Can be treated via statistical mechanics without an *a priori* knowledge of the full system other than $\phi(\mathbf{r})$ and $w(r)$.
- Has an associated $\phi_R(\mathbf{r})$ that depends only on singlet density profiles of the

mimic system and not on the more complex conditional singlet densities.

By making approximations towards these goals, the equality of densities expressed in Eq. (2.9) will no longer hold exactly, and we will find an equation based on the exact Eq. (2.10) that will also no longer be exact. But all will be accurately satisfied given optimal choices of $u_0(r)$ and $u_1(r)$.

Rewriting Eq. (2.10) in a manner evocative of the approximations we shall make, we find exactly

$$
\begin{aligned}
-\vec{\nabla}\phi_R(\mathbf{r}) &= -\vec{\nabla}\phi(\mathbf{r}) - \int d\mathbf{r}'\rho_R(\mathbf{r}';[\phi])\vec{\nabla}u_1\left(|\mathbf{r}-\mathbf{r}'|\right) && \text{(2.11a)}\\
&\quad - \int d\mathbf{r}'\left[\rho(\mathbf{r}'|\mathbf{r};[\phi]) - \rho_R(\mathbf{r}'|\mathbf{r};[\phi_R])\right]\vec{\nabla}u_0\left(|\mathbf{r}-\mathbf{r}'|\right) && \text{(2.11b)}\\
&\quad - \int d\mathbf{r}'\left[\rho(\mathbf{r}'|\mathbf{r};[\phi]) - \rho(\mathbf{r}';[\phi])\right]\vec{\nabla}u_1\left(|\mathbf{r}-\mathbf{r}'|\right). && \text{(2.11c)}
\end{aligned}
$$

Term (2.11a) of Eq. (2.11) depends only on the singlet density response of the mimic system, and no information about the density response of the full system is present. Thus if we could carefully choose $u_0(r)$ and $u_1(r)$ such that term (2.11b) and term (2.11c) will be small, then term (2.11a) alone would define an equation for the mimic system. In effect we will then have truncated the YBG hierarchy without using problematic superposition closures.

To that end, we make two physically motivated approximations to Eq. (2.11):

1. Term (2.11b) probes the difference between the conditional singlet densities for the full and mimic systems via convolution with $\vec{\nabla}u_0(r)$. The integrand will be quickly forced to zero at larger $|\mathbf{r}-\mathbf{r}'|$ by the vanishing gradient of the short-ranged $u_0(r)$. Since both the full and mimic systems have the same strong short-ranged core forces with an appropriately-chosen $u_0(r)$, which should mainly

determine the short-ranged part of the conditional densities, it seems plausible that with proper choice of $u_0(r)$, term (2.11b) can be neglected. This is significantly better than any superposition approximation for the conditional densities.

2. Term (2.11c) probes the difference between the conditional singlet density and the singlet density of the *full* system. As explained previously with relation to standard closures of the YBG equation, assuming their equality can be highly problematic. However, we are saved by the fact that this difference is paired with the term $\vec{\nabla} u_1(|\mathbf{r} - \mathbf{r}'|)$. Since $u_0(r)$ has been chosen to encompass core interactions, $u_1(r)$ will be simultaneously slowly-varying over those nearest-neighbor distances, so the associated force is essentially zero for exactly the range of correlations where the conditional singlet density and singlet density differ significantly. Thus we expect for many liquids that the integrand in term (2.11c) may also be accurately approximated as zero.

These approximations are the basis not only for finding a closed equation for ϕ_R but also for determining the appropriate $u_0(r)$ and $u_1(r)$ for which the solution of the resulting LMF equation will lead to an accurate mimic system. When these approximations are good, we expect the system prescribed by the LMF equation to *mimic* behavior that depends either on the singlet density of the full system or on the near range of the conditional singlet density of the full system.

Notably, the second approximation will fail when there are long-ranged pair correlations such as capillary waves at surfaces or the divergence of the correlation length

near the critical point. In those instances, the conditional singlet density will not be approximately the same as the singlet density beyond nearest-neighbor distances. However, we do expect this approximation to hold in charged systems away from the critical point where there exist pair correlations that decay exponentially over those nearest-neighbor interactions.

With these two approximations, we may write the LMF force equation

$$-\vec{\nabla}\phi_R(\mathbf{r}) = -\vec{\nabla}\phi(\mathbf{r}) - \int d\mathbf{r}'\rho_R(\mathbf{r}';[\phi_R])\vec{\nabla}u_1\left(|\mathbf{r}-\mathbf{r}'|\right). \tag{2.12}$$

Since the integrand contains only the singlet density as a function of $\mathbf{r}'$, we may take the gradient with respect to $\mathbf{r}$ outside of the integral and integrate this force equation over $\mathbf{r}$ to yield an equation involving energies. We find the general LMF equation

$$\phi_R(\mathbf{r}) = \phi(\mathbf{r}) + \int d\mathbf{r}'\rho_R(\mathbf{r}';[\phi_R])u_1\left(|\mathbf{r}-\mathbf{r}'|\right) + C, \tag{2.13}$$

where the constant C will be set by boundary conditions. The form of this equation highlights the connection with mean-field techniques. The rescaled potential energy ϕ_R may be viewed as an averaging of the long-ranged portions of the pair potential over the single particle density $\rho_R(\mathbf{r})$. But the LMF equation is not simply a mean-field ansatz. When we choose a $u_0(r)$ that incorporates enough of the $w(r)$ interaction to faithfully represent the core interactions, $u_1(r)$ is simultaneously slowly-varying over these core interactions. In that case, self-consistent solution of Eq. (2.13) leads to a short-ranged system that accurately mimics the nonuniform density, the pair correlations, and thermodynamic quantities of the full system.

In the end, the mean-field equation stated in Eq. (2.13) will only be reasonable when the approximations leading to its derivation are upheld. Therefore, $u_0(r)$ must

reasonably encompass nearest-neighbor correlations and $u_1(r)$ must simultaneously be slowly-varying over those correlations.

2.4 Application to a Nonuniform System

The LMF equation was derived in the context of a nonuniform fluid; in other words, the particles experience not only interparticle interactions but simultaneously an external potential energy surface that destroys the translational symmetry of the fluid. For LJ fluids, one of the motivations for deriving this equation was the failure of WCA fluids to capture the range of wetting and drying behavior of LJ fluids near walls. Depending on the state of the LJ fluid and the attractions to the walls, full LJ particles at the interface actually are pulled towards the bulk fluid and away from the wall, thus "drying" the interface. As described in previous publications from the Weeks group [53, 54, 106], this phenomenon is easily captured by the mean field in LMF theory. The LMF equation also naturally encompasses the lacking attractive forces necessary to form a liquid-vapor interface for a WCA fluid and the net attractive forces from the bulk with the insertion of a hard sphere solute.

In the context of these nonuniform LJ systems we now will present some further notation. We consider a LJ fluid next to a smoothed LJ wall, described by the external potential energy function

$$\phi_{\mathrm{LJw}}(z) = \frac{A}{z^9} - \frac{B}{z^3}, \tag{2.14}$$

where A and B are greater than zero. This function represents the integrated interaction due to the smoothing of the standard LJ pair potential for a uniform fixed

density occupying the x- and y-directions and the subspace $z \in (-\infty, 0)$. As done for the LJ pair potential, we may split this external potential energy function into two parts,

$$\phi_0(z) = \begin{cases} \phi_{\mathrm{LJw}}(z) - \phi_{\mathrm{LJw}}(z_0) & \text{if } z \leq z_0, \\ 0 & \text{if } z > z_0. \end{cases}$$

$$\phi_1(z) = \begin{cases} \phi_{\mathrm{LJw}}(z_0) & \text{if } z \leq z_0, \\ \phi_{\mathrm{LJw}}(z) & \text{if } z > z_0. \end{cases} \tag{2.15}$$

As before when r_0 was the position of the minimum for the LJ 12-6 potential, z_0 will be the position of the minimum for this LJwall potential.

Given these definitions we may rewrite the LMF mean-field equation, Eq. (2.13), as

$$\phi_R(\mathbf{r}) = \phi_0(\mathbf{r}) + \phi_{R1}(\mathbf{r}), \tag{2.16}$$

with ϕ_{R1} defined as the mean field result due to all long-ranged interactions,

$$\phi_{R1}(\mathbf{r}) = \phi_1(\mathbf{r}) + \int d\mathbf{r}' \rho_R(\mathbf{r}'; [\phi_R]) u_1 \left(|\mathbf{r} - \mathbf{r}'|\right) + C. \tag{2.17}$$

Just as we have done for the pair interactions, the rescaled external potential energy function ϕ_R may now be viewed as composed of a short-ranged part ϕ_0 and a mean-field ϕ_{R1} that encompasses all slowly-varying interactions. For nonuniform LJ systems, ϕ_{R1} is an important contributor since only for a very unique combination of ϕ_1 and $u_1(r)$ does ϕ_{R1} cancel. However, the definition of ϕ_{R1} is useful for understanding the success of the WCA reference system in bulk and its failure at sufficiently low densities.

2.5 Application to a Uniform System

While LMF theory was originally derived for nonuniform systems, the LMF equation is still applicable for uniform systems as well. The key lies in recognizing that the radial distribution function $g(r)$ often focused on in studying WCA systems may also be exactly represented by the conditional singlet density [105, 107] based on the equality

$$\rho_B \, g(|\mathbf{r} - \mathbf{r}'|) = \rho \, (\mathbf{r}|\mathbf{r}') \, . \tag{2.18}$$

Therefore by fixing one particle at the origin $\mathbf{0}$, we have

$$\rho_B \, g(r) = \rho \, (\mathbf{r}|\mathbf{0}) \, . \tag{2.19}$$

The successful WCA results may be understood as fixing one LJ particle at the origin, surrounding it with other LJ particles, and defining

$$\phi(\mathbf{r}) = u_{\mathrm{LJ}}(r), \qquad \phi_0 = u_0(r), \qquad \text{and} \qquad \phi_1 = u_1(r). \tag{2.20}$$

When the WCA reference system works, this means that the long-ranged forces effectively cancel and ϕ_{R1} is negligibly small. Therefore ϕ_R is dominated by contributions from ϕ_0. We term the approximation of ϕ_{R1} as zero the strong coupling approximation (SCA), because it works best in systems where the cores are quite strongly interacting. As demonstrated by Weeks, Vollmayr, and Katsov [107], treating a lower density WCA system simply requires the inclusion of a self-consistent ϕ_{R1} in addition to ϕ_0 about one particle. With this, substantial improvement over pure WCA systems was observed.

However, it was also noted that for LJ systems, the LMF approach is not a catch-all solution. At moderately low reduced densities such as $\rho^* = \rho\sigma_{\mathrm{LJ}}^3 = 0.1$, deviation between the self-consistent LMF solution and the true LJ system is observed. This failure may understood in two ways. Firstly, for the given $u_0(r)$, we may no longer approximate $\rho^{(2)}(\mathbf{r}, \mathbf{r}')$ as $\rho^{(1)}(\mathbf{r})$ for distances from the particle at the origin where $\vec{\nabla} u_1(r) \not\approx 0$. Thus the approximation related to the neglect of term (2.11c) in deriving the LMF equation is no longer as appropriate. As demonstrated by Fig. 2.3, this failure may be displayed by a variety of three-particle chains that do not average out in a spherical sense about the origin (due to the low density) and thus could not be reasonably captured by simply the incorporation of a mean field centered about the particle at the origin. The presence of the third particle in the chain is contingent on the presence of the intermediary particle attracted to both it and the fixed particle.

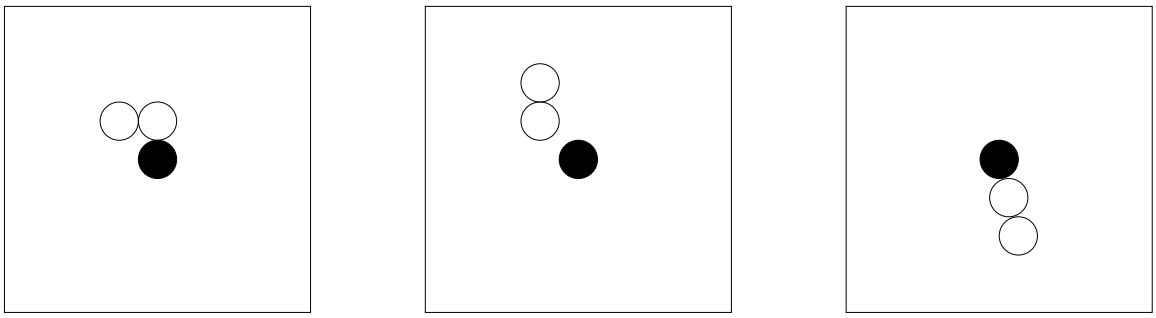

Figure 2.3: Demonstration of configurations in a low density LJ liquid that would lead to an inability to neglect the convolution of the long-ranged forces with the difference between the singlet density and the conditional singlet density. The black particle is meant to indicate the "fixed" particle necessary to apply full LMF theory to a bulk simulation.

The first explanation also suggests a second perspective. If we could somehow

increase the range of $u_0(r)$ then we might incorporate those chain interactions and simultaneously make the neglect of term (2.11c) reasonable by making $u_1(r)$ simultaneously more slowly-varying over small distances. However, for LJ interactions, such an approach is both nonintuitive and computationally nonadvantageous. Defining an alternate $u_0(r)$ for u_{LJ} is nonintuitive because the definition of *short* versus *long* is set by the functional form of the pair potential and the physical idea that it is the attractive forces that cancel in a dense, uniform LJ fluid. Further, it is computationally nonadvantageous because the LJ interaction is already perfectly reasonable to simulate. The utility of the LMF approach for LJ fluids instead lay in the possibility of developing theories around the hard-core-like WCA particles [53, 54]. These observations are not true for Coulomb interactions.

2.6 Coulomb $u_0(r)$ and $u_1(r)$

The Coulomb potential $1/r$ is a monotonically varying function, and the form of the potential does not contain an inherent length scale. This may be viewed as a difficulty of the application of LMF theory to Coulomb systems, and indeed figuring out the appropriate partition of $w(r)$ took researchers quite a while. But since there is no fixed length scale in the potential, the split between short- and long-ranged, a smoothed truncation length we will call σ, may be tailored to each situation. This is not to imply a fitting parameter, but rather a *consistency* parameter. We expect that choosing σ too small will result in poor and rapidly-varying results from full LMF theory since the mean-field average will be over rapidly-varying interactions. However

once σ reaches a $\sigma_{\min}$ that is related to characteristic nearest-neighbor interactions, the assumptions used to derive the LMF equation from the YBG hierarchy become accurate, and we expect that self-consistently applied LMF theory will yield a true mimic system. [2]

A discussion of how to ascertain that $u_0(r)$ successfully contains the core interactions in general is postponed until Ch. 3, and for the moment we shall accept that doing so is possible. A more detailed discussion of application to Coulomb systems follows here.

We define slightly new symbols. The pair interaction between two charges, q_α and q_γ, is

$$w(r) = \frac{q_\alpha q_\gamma}{\epsilon r}, \tag{2.21}$$

working in CGS units. ϵ is simply the dielectric constant of a uniform medium in which the charges are immersed. The details of charge magnitudes, signs, and occasionally choice of units (CGS versus SI) will change from system to system, but the underlying functional form $1/r$ will remain constant. Thus, following [22], we will deal with functional forms associated with the splitting of the Green's function $v(r) \equiv 1/r$ as

$$\frac{1}{r} \equiv v_0(r) + v_1(r), \tag{2.22}$$

where $v_0(r)$ and $v_1(r)$ again represent the short-ranged and long-ranged interactions respectively.

The first crucial step in application of LMF theory to Coulomb interactions in a

[2] Since we have not bounded errors for the approximations in developing LMF theory, this is an approximate lower bound on σ, *i.e.* $\sigma \gtrsim \sigma_{\min}$.

uniform dielectric constant medium lay in determining the choice of $v_0(r)$ and $v_1(r)$. Work of previous researchers [14] revealed that a beneficial choice of $v_1(r)$ is the electrostatic potential due to a Gaussian of width σ, defined as

$$\rho_G(\mathbf{r}) = \frac{1}{\sigma^3 \pi^{3/2}} \exp\left(-\frac{r^2}{\sigma^2}\right), \tag{2.23}$$

leading to a $v_1(r)$ of

$$v_1(r) = \frac{\mathrm{erf}(r/\sigma)}{r}. \tag{2.24}$$

The corresponding $v_0(r)$ will then be given as

$$v_0(r) \ = \frac{\mathrm{erfc}(r/\sigma)}{r}. \tag{2.25}$$

We term this a smooth Gaussian truncation of the $1/r$ potential because it is the electrostatic potential of a point charge surrounded by a neutralizing Gaussian charge density of width σ. This split is shown in Fig. 2.4 along with a demonstration of the impact of increasing σ on $v_0(r)$ and $v_1(r)$. The form of $v_1(r)$ is slowly varying over σ, and $v_0(r)$ approximately represents a core potential of range σ. Tuning σ to larger values increases the range of $v_0(r)$ and simultaneously increases the "slowness" of variation of $v_1(r)$ over characteristic nearest-neighbor interactions.

One possibly troubling aspect of this $v_0(r)$ is that it is not exactly zero at any r, but most short-ranged potentials including $u_{\mathrm{LJ}}(r)$ have this problem and $v_0(r)$ does decay significantly faster than the full Coulomb $1/r$ and also faster than the LJ potential. An even more advantageous reason for choosing this $v_0(r)$ was shown by Chen *et al.* [14]. Separating the k-space form of $1/r$ into a portion that quickly decays in k-space and a remainder that has only large k-components leads to this identical

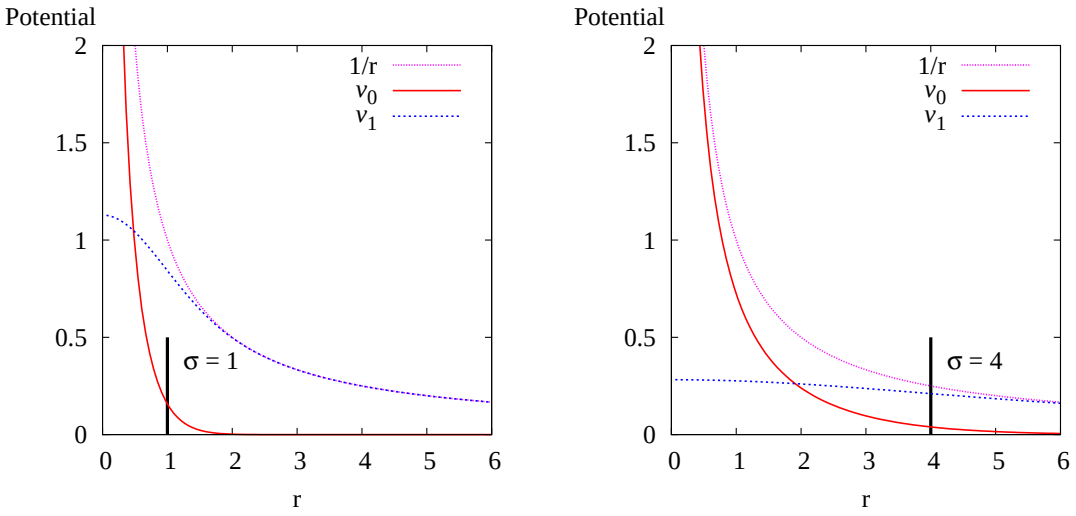

(a) $\sigma = 1$ (b) $\sigma = 4$

Figure 2.4: Demonstration of $1/r$ potential split for two different σ's. When σ is increased from 1 to 4, more of the $1/r$ core interaction is included in $v_0(r)$ and $v_1(r)$ becomes correspondingly slowly varying.

potential split:

$$\begin{aligned}\frac{1}{r} &= \frac{1}{(2\pi)^3}\int \frac{4\pi}{k^2}\cdot e^{i\mathbf{k}\cdot\mathbf{r}}\,d\mathbf{k} \\ &= \frac{1}{(2\pi)^3}\int \frac{4\pi}{k^2}\cdot e^{-k^2\sigma^2/4}\cdot e^{i\mathbf{k}\cdot\mathbf{r}}\,d\mathbf{k} + \frac{1}{(2\pi)^3}\int \frac{4\pi}{k^2}\cdot\left(1-e^{-k^2\sigma^2/4}\right)\cdot e^{i\mathbf{k}\cdot\mathbf{r}}\,d\mathbf{k} \\ &= \frac{\mathrm{erf}(r/\sigma)}{r} + \frac{\mathrm{erfc}(r/\sigma)}{r}. \end{aligned} \tag{2.26}$$

Thus defining $v_1(r)$ as $\mathrm{erf}(r/\sigma)/r$ may also be seen as choosing a $v_1(r)$ that is simultaneously slowly varying in r-space, and monotonic and localized to small k in k-space, leading to a $v_1(r)$ that is quite well-suited for LMF averaging.

Initial charged systems that this approach was applied to were:

- The one-component plasma and one-component charged hard-sphere fluid [14]. Uniform systems of point ions and point ions within a hard sphere, with neutrality maintained by a postulated uniform charge density of opposing sign

occupying all space.

- The size-asymmetric primitive model [15]. Uniform system composed of cations ($+q$) and anions ($-q$) with differing hard sphere diameters.

- Uniform charged hard walls and point counterions [15]. Uniformly charged hard walls with surface charge density $-\lambda$, infinite in the x- and y-extents. Either only one wall at the origin with counterions confined to the space $z \in [0, \infty)$ or two walls at $z = 0$ and $z = d$ with neutralizing point counterions confined to the space $z \in [0, d]$.

In this thesis, we will further examine the final model system above in Ch. 3.

2.7 Strategies for Closing the Self-Consistent LMF Loop

Recalling Eq. (2.13),

$$\phi_R(\mathbf{r}) = \phi(\mathbf{r}) + \int d\mathbf{r}' \rho_R(\mathbf{r}'; [\phi_R]) u_1 (|\mathbf{r} - \mathbf{r}'|) + C,$$

the ϕ_R determined by LMF explicitly depends on the effect of ϕ_R on the density profile $\rho_R(\mathbf{r}; [\phi_R])$. Thus the equation has been solved only when the resulting ϕ_R is consistent with the $\rho_R(\mathbf{r})$ input into the equation on the right, *i.e.* when self-consistency is attained.

In this thesis, we will address three manners of evaluating the self-consistency of Eq. (2.13) for Coulomb systems, two approximate and one "exact" in a numerical sense. Here each scheme is briefly sketched. Two approaches lie in the manner of determining the density response to ϕ_R, and one approach lies in substantially

simplifying the LMF equation itself. Further numerical details related to achieving self-consistent solution are explored in the various chapters where they are employed.

2.7.1 Explicit Simulations

This is the most accurate approach. It may be viewed as "exact" for sufficiently long simulations. Density profiles in response to a trial ϕ_R are calculated using the statistical mechanics encompassed by molecular dynamics (MD) or Monte Carlo (MC) simulations. There is no single equation associated with this density response, but rather detailed simulations are used. Such an approach is relatively simple for the two-wall system in Ch. 3, but requires more subtlety for molecular systems in Ch. 6.

2.7.2 Mimic Poisson-Boltzmann (MPB) Approximation

This approach is akin to, but more broadly applicable than, more traditional Poisson-Boltzmann (PB) approaches. For the moment we simply state that MPB treats the density response of the short-ranged system as that of an ideal gas in an external potential energy surface encompassing only the long-ranged interactions. Thus the corresponding equation is

$$\rho_R(\mathbf{r};[\phi_R]) \simeq A \exp\left(-\beta\phi_R\right). \tag{2.27}$$

During the course of Chs. 3 and 4 we will explore the appropriateness of such an approximation.

2.7.3 Strong-Coupling Approximation

We have already touched on this approximation to the LMF equation in Sect. 2.5. In a sense, the SCA approach lies along a different path than the previous two schemes and in fact can be combined with either. The strong-coupling approximation assumes that no second equation or simulation is necessary, but rather that

$$\phi_R \simeq \phi_0 \qquad \text{and thus} \qquad \phi_{R1} \simeq 0, \tag{2.28}$$

removing any need for self-consistency. This approximation may be coupled with either explicit simulations or with an MPB-type prediction of the density response.

In essence this approximation may be appropriate when the short-ranged forces dominate the long-ranged forces for the property of interest. This approach will often be used as a path of first resort throughout the thesis, but one must carefully evaluate its use.

Chapter 3

Two-Wall System

In this chapter, we explore the uniformly-charged-wall system treated by previous authors via the MPB closure of the LMF equation [15]. The first portion of the chapter will deal with the physics and phenomena of this simple system and the latter portion will detail the treatment of this system using Monte Carlo simulations. The simplicity of this system allows for a more detailed exploration of the implementation of the LMF equation and of the importance of the smoothed truncation length σ in ensuring the accurate application of the theory than we will undertake for molecular systems in later chapters. Many of the results in this chapter have been previously published by Rodgers, Kaur, Chen, and Weeks [86], and much of the text below is modified from [85].

3.1 Model System

The system examined here contains two uniformly charged walls separated by a medium occupied by point counterions, which make the overall system neutral. This model is quite simple but still exhibits the possibility of like-charged attraction of the two walls, and, as such, has been much studied [36, 52, 61, 71, 73, 99]. The system is composed of two infinite hard walls normal to the z-axis and positioned at $z = 0$ and $z = d$. Each wall has a negative surface charge density q_w. Between the walls

are positive point counterions of valence Z and charge Ze_0 at a density that exactly neutralizes the two walls. A uniform medium of dielectric constant ϵ permeates all space even though $z \leq 0$ and $z \geq d$ are inaccessible to the counterions.

We predominantly examine the two-wall system, but the corresponding one-wall system with a wall at $z = 0$ and ions confined to $z = (0, \infty)$ will give us insight into the appropriate length scales. Figure 3.1 shows examples of such systems; the length scales and potentials exhibited will be discussed in the following subsection.

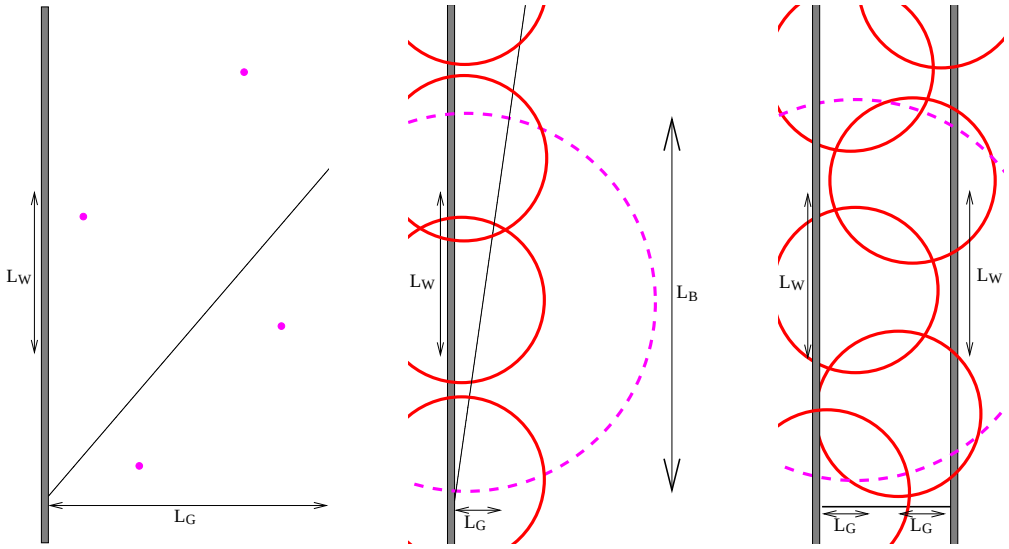

(a) Weak Coupling (b) Strong Coupling (c) Strong Coupling

Figure 3.1: The drawings illustrate the three length scales defined in the text: L_G, L_w, and L_B [indicated by small filled-in circles in (a) and by dashed circles in (b) and (c)]. Additionally the potential exerted by the wall(s) on the counterions is shown by the thin line. The one wall systems show weak coupling with $L_B \ll L_G$ in (a) and strong coupling with $L_B \gg L_G$ in (b). If counterion charge and wall charge density remain the same, L_w is constant, and the coupling (represented by the ratio L_B/L_G) is altered by shifting temperature up for weaker coupling and down for stronger coupling. The relationship of temperature to these lengths is given in the text. In the strong coupling pictures, L_B is not the length scale of nearest-neighbor interactions, and one envisions instead a "Coulomb core" of the order of L_w (represented by the solid red circles) that captures these nearest-neighbor interactions. In (c), a strongly coupled system is confined by two walls to a distance d such that the counterion layers begin to significantly overlap and a single layer begins to form.

3.1.1 Interactions and Length Scales

For this system, understanding length scales is a fruitful starting point [13, 71]. These length scales will identify the independent parameters that define different thermodynamic states and will also aid in the application of LMF theory. In particular for LMF theory, when we split the $1/r$ potential into components, we will have to ensure that the short-ranged interactions reproduce the "Coulomb core," the range of interaction needed to reproduce relevant nearest-neighbor correlations.

One important length scale is the modified Bjerrum length, namely the length at which pair interactions including ion valence equal k_BT, so that

$$L_B = \frac{Z^2\, e_0^2}{\epsilon\, k_B T}. \tag{3.1}$$

One might naïvely assume that the "Coulomb core" size is of order L_B. While this is reasonable at low densities and weak coupling when typical particle spacings are much greater than L_B, this breaks down at strong coupling, when many particles are within L_B. In such instances, we expect the core size required to accurately represent nearest-neighbor interactions to be smaller than L_B.

Additionally, the Gouy-Chapman length, L_G, may be found from the potential energy of a single counterion in the field of one wall at $z = 0$ for a counterion at z, namely

$$U_{wall} = -\frac{2\pi q_w Z e_0}{\epsilon} \cdot |z| \tag{3.2}$$

Setting this potential energy equal to the thermal energy (k_BT), one obtains the

Gouy-Chapman length, again modified to incorporate valency, as

$$L_G = \frac{\epsilon k_B T}{2\pi \left| q_w \right| Z e_0}. \tag{3.3}$$

This length will be used as the basic unit of length while $k_B T$ will be taken as the energy unit. In the two-wall system the electrostatic potential an ion experiences due to both walls is constant, regardless of position, and thus the Gouy-Chapman length scale may seem irrelevant. However it is useful to recall that this length scale will also characterize the potential energy felt by an ion near one wall arising from the layer of counterions near the distant wall, when d is large. Thus L_G still characterizes interaction lengths in the system.

A third length L_w may be defined as the length of a side of a square area of wall that one counterion neutralizes,

$$-\, q_w \, L_w^2 = Z \, e_0. \tag{3.4}$$

One may easily see that

$$L_w^2 = 2\pi L_G L_B, \tag{3.5}$$

so these three length scales are not independent.

In reduced units, which we denote by a tilde, two parameters uniquely define a thermodynamic state of the two-wall system, the coupling strength ξ and the reduced distance between the walls $\tilde{d}$ defined as

$$\xi \equiv \frac{L_B}{L_G} = \frac{2\pi Z^3 e_0^3 |q_w|}{(\epsilon k_B T)^2} \qquad \text{and} \qquad \tilde{d} \equiv d/L_G. \tag{3.6}$$

When $\xi \ll 1$, the counterions are weakly coupled; they are strongly coupled when

$\xi \gg 1$. A system's coupling may be strengthened simply by lowering the temperature since $\xi \propto 1/T^2$.

In Fig. 3.1, the small filled-in magenta circles represent L_B for the weak coupling case and the large dashed magenta circles represent the L_B of a single counterion in the strong coupling cases. The structural rearrangement of the two wall system will be discussed further later, but understanding the different drawings for the one wall situation is useful. In weak coupling, the neutrality spacing for counterions, L_w, is less than the effective width of the potential well, L_G, and so the counterions effectively organize as a three-dimensional fluid between the walls. Once T has been lowered to reach strong coupling, $L_w > L_G$, and the interparticle neutrality spacing L_w in the directions parallel to the wall is greater than their typical separation from the wall in direction normal to the wall. Thus the particles are effectively confined to a two-dimensional layer. For strong coupling, the typical particle spacing is of the order of L_w and is smaller than L_B. Thus for strong coupling, L_w better represents the "Coulomb core" size.

With L_G chosen as the length unit and the tilde indicating a value in reduced units, the relation between length scales becomes $\tilde{L}_w^2 = 2\pi\xi$.

As detailed by Moreira and Netz [71], the Hamiltonian for the two-wall system may now be converted into a simple form in the reduced energy and length units k_BT and L_G. For a system with a total of N counterions, the total potential energy is

$$\mathcal{U} = \frac{q^2 e_0^2}{\epsilon} \sum_{i<j} \frac{1}{r_{ij}} + \sum_{i=1}^{N} \phi(z_i) \tag{3.7}$$

so that we have, in reduced units,

$$\tilde{\mathcal{U}} = \sum_{i<j} \frac{\xi}{\tilde{r}_{ij}} + \sum_{i=1}^{N} \tilde{\phi}(\tilde{z}_i). \tag{3.8}$$

The volume of simulation box containing N counterions is $\tilde{V} = \tilde{A} \cdot \tilde{d}$. The surface area in the x- and y- directions may be stated in terms of ξ and N as $\tilde{A} = \frac{N}{2}\tilde{L}_w^2 = N\pi\xi$. ϕ is the potential energy due to the confining charged walls, and for the full system ϕ is a constant taken as zero (since the electric fields due to each charged wall exactly cancel).

The equilibrated nonuniform single particle density $\rho(\mathbf{r})$ will depend only on z owing to the symmetry in the x- and y-directions. Neutrality dictates that

$$\int_0^d Ze_0\, \rho(z)\, dz = -2q_w, \tag{3.9}$$

which may be rewritten as

$$\int_0^{\tilde{d}} L_w^2 L_G\, \rho(L_G\tilde{z})\, d\tilde{z} = \int_0^{\tilde{d}} n(\tilde{z})\, d\tilde{z} = 2. \tag{3.10}$$

Here we have defined a dimensionless rescaled particle density $n(\tilde{z})$ as

$$n(\tilde{z}) \equiv L_w^2 L_G\, \rho(L_G\tilde{z}) = 2\pi\xi\tilde{\rho}(\tilde{z}). \tag{3.11}$$

For a single-wall system $n(0) = 1$, but the contact value $n(0)$ is not constant in the two-wall system.

3.1.2 Effective Attraction Between Walls

Beyond studying the application of LMF theory, we also will probe the effective attraction possible between like-charged walls for strong coupling and the associated

structural rearrangements of counterions. One might infer this effective attraction for highly-charged DNA *in vivo* from its compact nuclear form as mediated by oppositely charged histones. *In vitro*, this effective attraction of highly-negatively-charged DNA is caused by the addition of multivalent cations, resulting in the formation of compact toroids [32]. Rouzina and Bloomfield presented an argument relying on a comparison of concentrations and length scales in the physical system to motivate the use of this incredibly simple model system for explaining the attraction between DNA helices [87].

The Gouy-Chapman picture for these systems has been available for a century and is described in textbooks on colloids and biological physics [27, 72]. It is a mean-field approach to electrostatics such that the equilibrium density profile is a Boltzmann factor of the electrostatic potential determined by the Poisson equation self-consistently using the same Boltzmann density profile. The failure of this approach is well known in this field as well – the Gouy-Chapman solution never predicts attraction between two walls in this system, althought that is the "biologically-relevant" phenomenon of interest here.

Other factors such as macroion geometry and discreteness of charge on the macroions have been shown to be contributors to the mechanism of attraction between real macroions; but such deficiencies in the uniformly-charged-wall model do not concern us here. For the two-wall system, the attraction is due to correlation between counterions; when correlations are important, traditional mean-field theory fails. Local molecular field theory may be simply understood as a prescription for treating longer-ranged slowly-varying interactions using a mean field while simultaneously explicitly

treating short-ranged core interactions which lead to correlations. Thus this model exhibiting like-charged attraction arising from counterion correlations will allow us to demonstrate the accuracy of the local molecular field theory separation.

The pressure in the system serves to indicate whether the system is attractive ($P < 0$) or repulsive ($P > 0$). Attraction is easily explained because any charged component of an overal neutral system will be attracted to the remainder of the system. In Fig. 3.2, this is illustrated for this simple system. The net negatively charged wall will be electrostatically attracted to the counterions and the other wall, because, in sum total, the remaining charge is positive. Repulsion results from the collisions between the counterions and the charged walls.

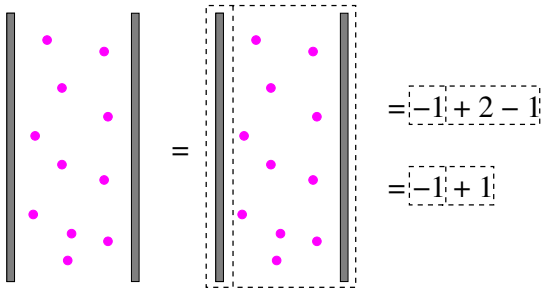

Figure 3.2: Demonstration of the origin of the effective electrostatic attraction between two like-charged walls. The two-wall model system is net neutral and therefore, one negatively charged wall is attracted to the net positive remainder of the system. The presence of attraction or repulsion depends on the balance between this electrostatic attraction and entropic repulsion due to particle collisions with the wall.

Thus, the actual force between the two walls may be understood as a balance between the electrostatic attraction between a negatively charged wall and the net positive remainder of the system and the entropic repulsions due to collisions between counterions and a wall. For this system, the exact equation for the effective pressure

follows from the "contact theorem" [108] which yields

$$\frac{\text{Force}}{\text{Area}} = P_{\text{osm}} = \rho\left(z_{wall}\right) k_B T - \frac{2\pi q_w^2}{\epsilon}. \tag{3.12}$$

The first term gives the entropic repulsions and scales as the equilibrium density of counterions contacting the wall. The second term is the electrostatic attraction between the wall and the remainder of the system. For this system the attraction is independent of wall separation due to the fact that the wall is infinite in extent and thus the forces between the wall and a counterion and between the wall and the other wall are independent of z. Thus as distance varies, only the entropic repulsions will vary due to the reorganization of counterion density between the two walls. This and other pressure formulae are explored in more detail in Appendix C.

We define a rescaled pressure as

$$\tilde{P}_{\text{osm}} = \frac{2\pi L_w^2 L_G}{k_B T} P_{\text{osm}}. \tag{3.13}$$

Thence, with the aid of Eq. (3.11), we may write a rescaled "contact theorem" as

$$\tilde{P}_{\text{osm}} = n\left(\tilde{z}_{wall}\right) - 1. \tag{3.14}$$

The switchover at $n(\tilde{z}_{wall}) = 1$ between attraction and repulsion is evident by writing the pressure in this fashion. Simulation is the only completely accurate way to determine whether a particular $(\xi, \tilde{d})$-state is attractive or repulsive.

Shown in Fig. 3.3 is a qualitative pressure versus distance curve for a moderately coupled system. Regions of both attraction and repulsion are evident. The P vs. d curve for moderately strong coupling may be understood descriptively. At infinite

d, the counterions will essentially form two uncoupled clouds concentrated predominantly in layers within a few L_G of each wall and with a few outlying ions spanning the intervening space. For the full Coulomb system, this separation into two layers may appear mysterious. A quick argument states that as $d \to \infty$, the limit of two separate one-wall systems must be recovered, and these systems have layers of charged particles next to the walls. A more careful argument observes that if the particles were uniformly spread across the distance d, this would maximize entropy, but free energy is a balance between energy and entropy, and the normal repulsions between particles in the interstitial space would be too great. Separation of the particles into two separate layers spread over a few L_G next to each wall minimizes the system's free energy. In contrast, local molecular field theory will provide a very natural explanation for this separation into two layers. The splitting of $1/r$ into short- and long-ranged components allows us to understand this layer formation in terms of a mean-field barrier formed between the two walls due to the long-ranged interactions between particles. We will discuss this in a bit more depth later once we derive the form of LMF theory for this model system.

At $d = \infty$ the net force on each wall is zero, so $P = 0$ and $n(z_{wall}) = 1$. The variation of $P(d)$ as d becomes finite depends on ξ in a complex balance between the strength of repulsions between counterions (ξ) and the space available between the walls (d). Thus we may describe qualitatively the progression of P vs. d for a strong coupling system, but the exact curve shape is not clear without actual simulations.

At large but finite separations, each counterion layer associated with one wall appears to the other layer as a charge distribution relatively smooth in the x- and

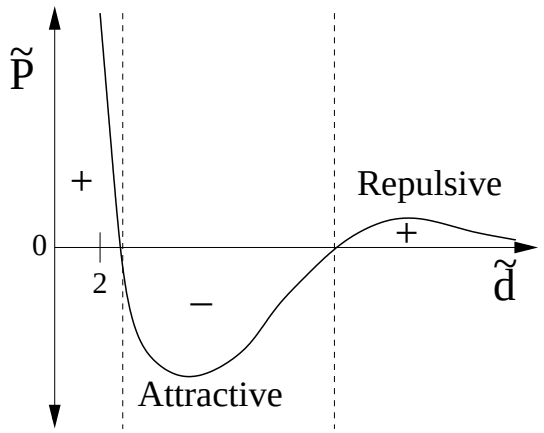

Figure 3.3: Sketch of the P vs. d curve for moderate coupling strength ξ. Regions of attraction ($P < 0$) and repulsion ($P > 0$) are evident.

y-directions. Very little microscopic structure is communicated from one side to another. The weak repulsions between the few ions in the tail of $n(z)$ in each layer resulting from confinement to a width $d/2$ raises the contact density slightly above 1, and the interaction is repulsive. This physics is well-captured by the Poisson-Boltzmann treatment even in strong coupling provided that the walls and the immediate layers of counterions are treated as a weaker rescaled wall charge density.

When the two charged walls with individual counterion layers come closer to each other, the counterions near each wall begin to "feel" the counterion structure associated with the opposite wall and structurally shift to ease the repulsions from the opposing counterions. This leads to a correlation hole opposite of each ion on the opposing charged wall, and this correlated non-uniform charge distribution leads to the onset of attraction. Figure 3.1(c) depicts this general situation.

As the walls approach even more closely, the two correlated layers progressively shift to form a single layer with the neutralizing surface area allotted per ion now $L_w^2/2$ rather than L_w^2. This phenomena was nicely demonstrated by Rouzina and Bloomfield

with simple calculations finding the lowest energy lattice structure for ∞-coupling and varying distances [87]. The concept of a "Coulomb core" encompassing relevant nearest-neighbor interactions further elucidates that this shift in layer structure would not occur until these cores (defined by neutrality spacing) significantly overlap in the z-direction. In Sect. 3.5 we will show that the formation of a true single layer uniform in the z-direction leads to the distance of maximal attraction between the walls.

The general sketch of the "phase" diagram of this system in Fig. 3.4 provides a visualization of the limits discussed. Data from careful simulations by Moreira and Netz [71] are available for this phase diagram as well as explicit $\tilde{P}$ vs. $\tilde{d}$ curves for varying ξ. We will compare our LMF results to these full simulations. Full simulations are required for evaluation of the LMF treatment of this model system since there is no exact analytical solution available for full ranges of ξ and d in the two-wall system.

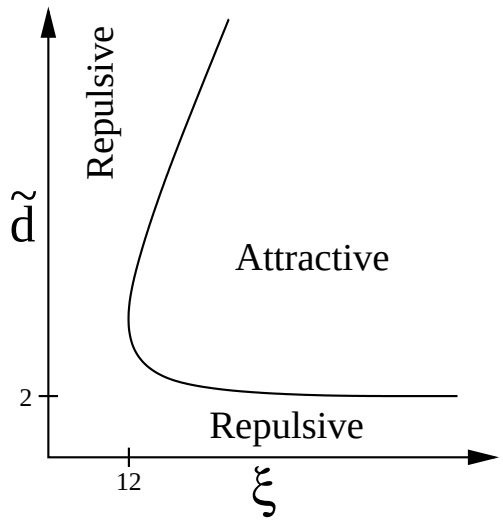

Figure 3.4: Sketch of the two-wall phase diagram separating attractive ($P < 0$) and repulsive ($P > 0$) regions on log-log scale for $\tilde{d}$ vs. ξ.

There do exist analytical expressions for two limits for the two-wall system. The weak coupling, Poisson-Boltzmann limit is $n_{\mathrm{WC}}(\tilde{z}) = A/\cos^2\left(A^{1/2}[\tilde{z} - \frac{\tilde{d}}{2}]\right)$ where A may be found by the neutrality requirement between the walls, $\int_0^d d\tilde{z}\, n(\tilde{z}) = 2$. The strong coupling limit is quite simply a constant density profile $n_{\mathrm{SC}}(\tilde{z}) = 2/d$. This may be justified by the fact that for finite d and sufficiently large coupling ξ, the counterions will be organized into a single two-dimensional layer between the walls, and thus there will be no net normal force on the particles. Therefore, in the z-direction, the particles behave as ideal gas particles in the constant external field: the density distribution in the z-direction is entirely uniform. Furthermore, this implies for very strong coupling that the lower crossover distance between repulsion and attraction will be $\tilde{d} \simeq 2$, as shown in Figs. 3.3 and 3.4.

Both of these exact limits have been derived from field theory along with correction terms [70]. However, for moderately strong coupling cases, no exact analytical solutions exist and the addition of correction terms from field theory to the two limiting laws is very inaccurate. Recently the mimic Poisson-Boltzmann approximation to LMF theory has made analytical results feasible and meaningful [15], but full simulations are the most stringent benchmark for prediction of attraction and repulsion between walls.

3.2 LMF for Wall Model System

In Ch. 2, local molecular field theory was derived for general nonuniform situations. We will simply make this formulation more specific for the wall system. As stated

before, the full system undergoes a mapping to a mimic system as

$$\underline{\text{Full}} \qquad\qquad \underline{\text{Mimic}}$$
$$\left\{ \begin{array}{c} w(r) \\ \\ \phi(z) \end{array} \right\} \xrightarrow{\text{LMF}} \left\{ \begin{array}{c} u_0(r) \\ \\ \phi_R(z) \end{array} \right\}$$

yielding $n_R(z;[\phi_R]) \simeq n(z;[\phi])$ provided that the σ used is sufficiently large for $u_0(r)$ to capture nearest-neighbor interactions and for $u_1(r)$ to be correspondingly slowly varying over those interactions. The wall system is truly nonuniform in only the z-direction as implied already in the mappings and this allows for integration over x and y.

We will introduce the LMF formula for this specific system and also develop some intuition for the previous success of the mimic Poisson-Boltzmann closure for this system [15]. Then, in later sections, we will examine simulation results in more detail.

In essence, the goal is to simulate behavior that typical short-ranged simulations would miss. Systems shown later in the thesis will be more extreme in their failure, but this system is a good initial test case. Standard minimum-image simulations neglect the net addition of long-ranged forces that occurs in the z-direction. As shown in Fig. 3.5, the $n(z)$ determined using pair interactions $u_0(r)$ and the bare external field $\phi(z) = 0$ is quite incorrect for $\xi = 10$ and $\tilde{d} = 20$, yielding a contact density indicating strong attraction, when in fact the $\xi = 10$ system is repulsive at all d. Both LMF theory using ϕ_R and the strong coupling approximation using ϕ_0 yield particle densities much more in line with expectation. The densities are so rapidly varying near the walls that we cannot see the rise above 1 on this distance scale, but

certainly it is clear that ϕ_0 and ϕ_R provide substantial wells to drive separation into two layers.

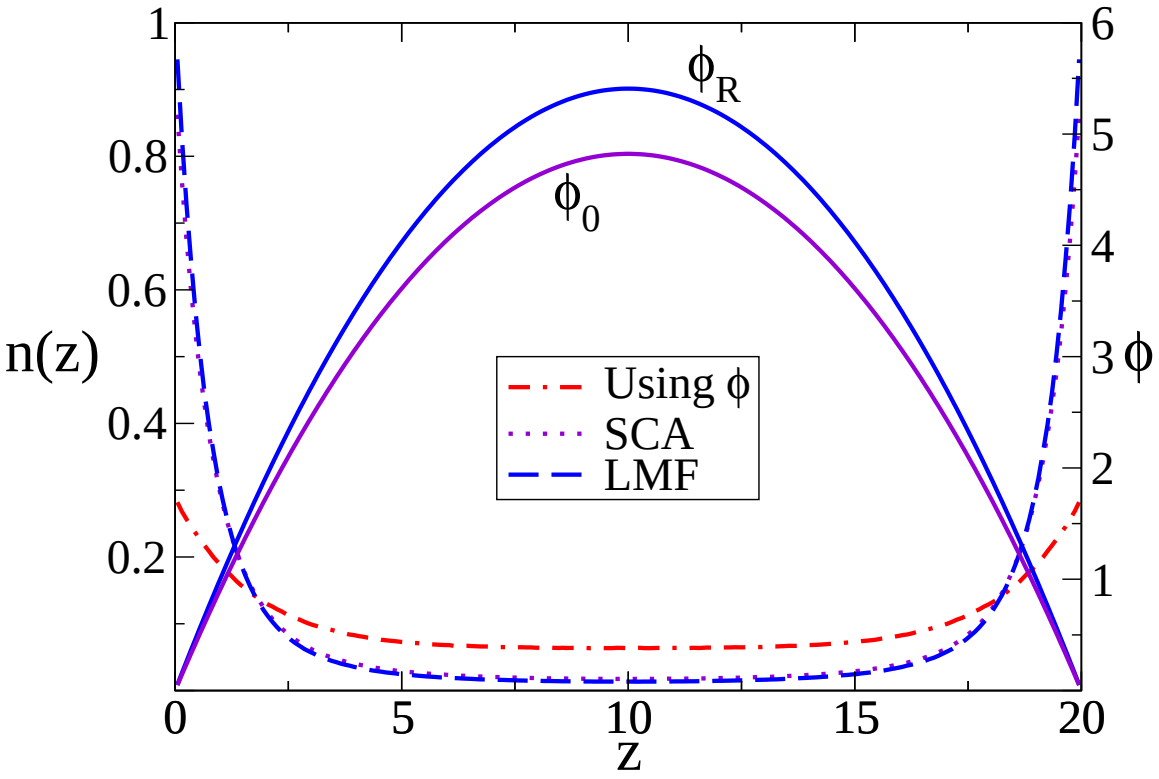

Figure 3.5: Demonstration of need for ϕ_0 or ϕ_R in determining $n(z)$ for $\xi = 10$, $d = 20$, and $\sigma = 14$. The density response to the bare field predicts strong attraction for a state that should be repulsive [71]. On this scale, the $n(z)$ due to the strong coupling approximation using ϕ_0 and full local molecular field theory using ϕ_R are barely distinguishable, but in Sect. 3.3, we will show that SCA begins to fail here.

From this point onward, all values should be assumed to be in reduced units of length in L_G and energy in k_BT since this leads to simpler forms and a simpler parameter space involving ξ and $\tilde{d}$. Values will no longer be labeled with a tilde though.

3.2.1 LMF Equation

The full LMF equation as given in Eq. (2.13) is

$$\phi_R(\mathbf{r}) = \phi(\mathbf{r}) + \int d\mathbf{r}'\, \rho_R(\mathbf{r}'; [\phi_R])\, u_1\left(|\mathbf{r} - \mathbf{r}'|\right) + C.$$

As shown in [13] and [15], for the two wall model system, immediate simplifications may be made because

$$\phi(\mathbf{r}) = \begin{cases} 0 & \text{if } z \in (0, d), \\ \\ \infty & \text{otherwise.} \end{cases}$$

Due to the fact that ϕ is solely a function of z, we also know that $\rho(\mathbf{r}) = \rho(z)$ and $\phi_R(\mathbf{r}) = \phi_R(z)$. This leads to

$$\phi_R(z) = \int_{-\infty}^{\infty} dx' \int_{-\infty}^{\infty} dy' \int_0^d dz' \rho_R(z'; [\phi_R]) u_1\left(\sqrt{x'^2 + y'^2 + (z - z')^2}\right) + C. \quad (3.15)$$

Following steps detailed in Sect. B.1, we may write the LMF equation as

$$\phi_R(z) = \int_0^d dz' n_R(z'; [\phi_R]) G(z, z'), \quad (3.16)$$

where G is defined as

$$G(z, z') = -|z - z'| \operatorname{erf}\left(\frac{|z - z'|}{\sigma}\right) - \frac{\sigma}{\sqrt{\pi}} e^{-\left(\frac{z - z'}{\sigma}\right)^2} + |z'| \operatorname{erf}\left(\frac{|z'|}{\sigma}\right) + \frac{\sigma}{\sqrt{\pi}} e^{-\left(\frac{z'}{\sigma}\right)^2}. \quad (3.17)$$

Whereas previously C was undetermined in Eq. (2.13), here the constant has been defined by the requirement that $z = 0$ is the zero of energy.

$G(z, z')$ may be understood as the electrostatic potential at z due to the convolution of rescaled positive charge density $\delta(z - z')$ with a one-dimensional Gaussian of width σ. This again emphasizes that Eq. (3.16) is simply a one-dimensional rewriting of the full three-dimensional LMF equation. Shown in Fig. 3.6 are $G(z, z')$ and also

the full Coulomb potential ϕ due to a positive planar charge density $\delta(z-z')$. Notice that G incorporates the full long-ranged forces due to this charge density at $z'=15$ but the force due to G near $z=z'$ is significantly attenuated.

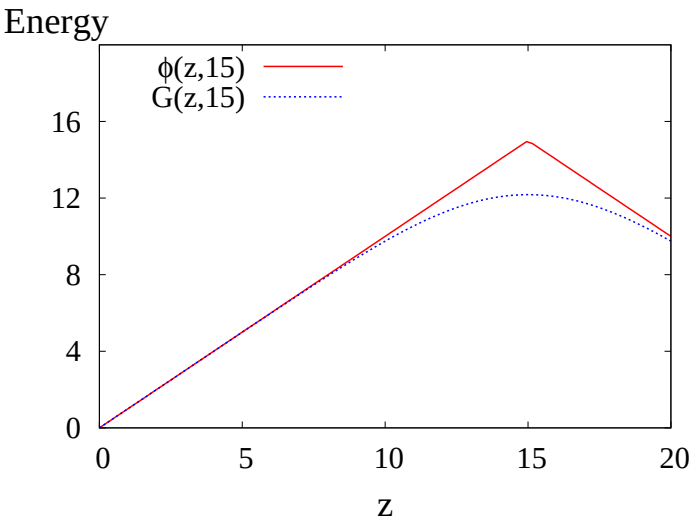

Figure 3.6: The long-ranged interactions averaged in LMF, $G(z,z')$, and the full potential due to a plane of charge at z', $\phi(z,z')$, are shown for $\sigma=5$ and $d=20$ for a plane of rescaled particle density located at $z'=15$. Near $z=z'$, G is much more slowly-varying than the full interaction ϕ.

3.2.2 Previous Work with the MPB Approximation

As shown by Chen and Weeks [15], significant quantitative agreement with the overall phase diagram sketched in Fig. 3.4 can be achieved by approximating the density profile as

$$n_{\mathrm{MPB}}(z) = Ae^{-\phi_R(z)}. \tag{3.18}$$

The normalization constant A is adjusted at each step in a self-consistent iteration so as to enforce neutrality, *i.e.*

$$\int_0^d n(z)\,dz = 2. \tag{3.19}$$

In order to achieve a semi-quantitative match, a choice of σ for each combination of ξ and d must be made. In [15], this choice is determined by a single fitting of the $n(z)$ for a *one* wall system at a moderate coupling strength ($\xi = 40$). With this single fit, a relation for all ξ along the upper and lower branches of the phase diagram was determined.

This one-to-one relation between ξ and σ seems to run counter to the initial proposal of the $1/r$ split in the derivation of LMF theory. We argued that there should in essence be some approximate $\sigma_{\min}$ such that any choice of $\sigma \gtrsim \sigma_{\min}$ will yield reasonably accurate results. However, when the approximate MPB density response is used to close the self-consistent LMF loop, this is no longer true. The reason for this is that, for the MPB approximation, a single choice of σ must represent both the long-ranged forces and the degree of cancellation of short-ranged core forces. To fully understand this statment we must examine why the MPB approach is successful for the range of ξ and d combinations.

One manner of justifying the MPB closure is noting that it captures exactly both the weak coupling (Poisson-Boltzmann) and strong coupling (thin slit) limits. Thus the MPB prediction of density response seems a natural self-consistent loop closure for spanning the range of coupling strengths. However, capturing the two extreme limits does not guarantee the remarkably accurate results possible from MPB. As noted before when Fig. 3.6 was introduced, $G(z, z')$ has attenuated forces for z within a range of approximately σ from z'. The exact Poisson-Boltzmann limit is achieved when $\sigma \to 0$ and particles within an infinitesimal distance of z' experience the full force. Physically we may understand this as representing the fact that particles are

so weakly correlated with each other that regardless of proximity they may best be represented as a sheet of charge. The strong coupling limit is reach when $\sigma \to \infty$, corresponding to no interparticle forces normal to the walls. This counterintuitive statement is true because when particles are strong correlated with each other they organize into a single two-dimensional layer and thus the only substantial interparticle forces are in the lateral direction. We may understand σ as approximating the width over which particles exist in a laterally correlated layer.

Thus MPB includes an empirical representation of the discreteness of particles by giving a width over which particles will arrange into effectively a single layer. If particles are laterally correlated then they may not reasonably interact as two sheets of charge. Therefore, the normal forces should be attenuated, as is done via $G(z, z')$. Calculating $\phi_R(z)$ with a nonzero σ can lead to physically interesting phenomena such as like-charged attraction [15]. However, since σ simultaneously represents the extent to which particles layer due to correlations and also the slowly-varying long-ranged forces, this essentially results in a one-to-one relation between a given $\xi - d$ combination and the appropriate σ within the MPB approximation.

Carrying out simulations instead removes this sensitivity in the density response to the choice of σ, and thus we can better understand the overall implementation of LMF theory. However, at least understanding the forces due to G can be useful. G incorporates the net long-ranged forces normal to the surfaces that spherical truncations neglect.

Interestingly, as a general rule, $\sigma_{\text{MPB}} < \sigma_{\text{sim}}$. This is also a result of MPB using σ to represent both the core cancellations and the long-ranged forces through the

Boltzmann approximation.

3.3 Strong Coupling Approximation for Wall System

A full solution to the LMF equation is not always necessary. We will first simulate this system using the strong coupling approximation. As described in Sect. 2.4 and [15], the external field ϕ may be split into short-ranged (ϕ_0) and long-ranged (ϕ_1) contributions.

The strong coupling approximation (SCA) consists of simulating particles interacting via $u_0(r)$ in only the short-ranged part of the external potential, $\phi_0(\mathbf{r})$. This approximation is valid when the short-ranged interactions dominate, and no self-consistency iterations are required.

3.3.1 ϕ_0 and ϕ_1 for the Wall System

The basic mechanism for splitting the external field is identical to that for splitting $1/r$. For any electrostatic potential, the long-ranged portion of the interaction may be found by convoluting the charge density with a Gaussian of the same width σ to yield ϕ_1. Then, ϕ_0 is simply the difference between ϕ and ϕ_1. Using this basic prescription for our system, we find that

$$\phi_1(z) = -G(z,0) - G(z,d), \tag{3.20}$$

and thus

$$\phi_0(z) = 0 - \phi_1(z) = G(z,0) + G(z,d). \tag{3.21}$$

We will approximate $\phi_R \simeq \phi_0$ to capture the nearest interactions between each wall and the ions, and thus, without iteration, a reasonable approximation to ϕ_R is known. Additionally, the SCA provides a very natural way to see that the counterions will begin to separate into two layers because ϕ_0 has effective potential wells near the walls. The forms of ϕ_0 and ϕ_R are shown in Fig. 3.7 for two different scenarios. When ξ is larger, the difference between the SCA potential ϕ_0 and the full LMF potential ϕ_R is smaller.

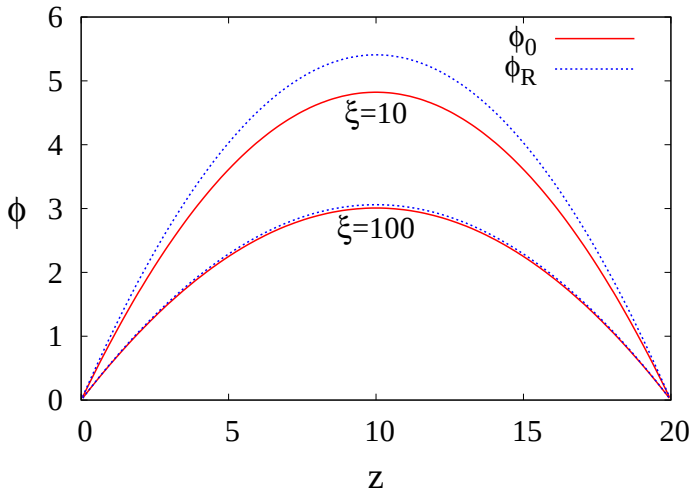

Figure 3.7: ϕ_0 and ϕ_R for $\xi = 100$ and $\xi = 10$ with $d = 20$. When the system is more weakly coupled the difference between ϕ_0 and ϕ_R (ϕ_{R1}) increases. At $\xi < 1$, we expect ϕ_{R1} to have even more significant additional contributions.

3.3.2 Finding P versus d Curves Using SCA

Since effective attraction between charged walls occurs when the system is moderately to strongly coupled, we expect the SCA to perform well for many of the (ξ, d) pairs explored. When the SCA was applied using a Boltzmann prediction for the density response, the results were incredibly sensitive to choice of σ [15]. This was due to the

fact that neutrality ($\int n(z)dz = 2$) was directly tied to the $\phi_0(z)$ functional form since $n(z) \simeq A\exp(-\phi_0)$ in the Boltzmann approximation with A determined by neutrality. However, in simulations, neutrality is determined by the number of particles in the simulation box and particle profiles are less tightly coupled to the ϕ_0 functional form. Therefore, we expect SCA to be more accurate in simulations.

As shown in Fig. 3.8, the strong coupling approximation can lead to a solid prediction of the dependence of pressure on distance between the walls for a relatively strongly-coupled situation. To emphasize this, both the results of full simulations and also of the Boltzmann density response to SCA (data from [15]) are shown. The SCA simulation results compare quite favorably to the results of the full simulations.

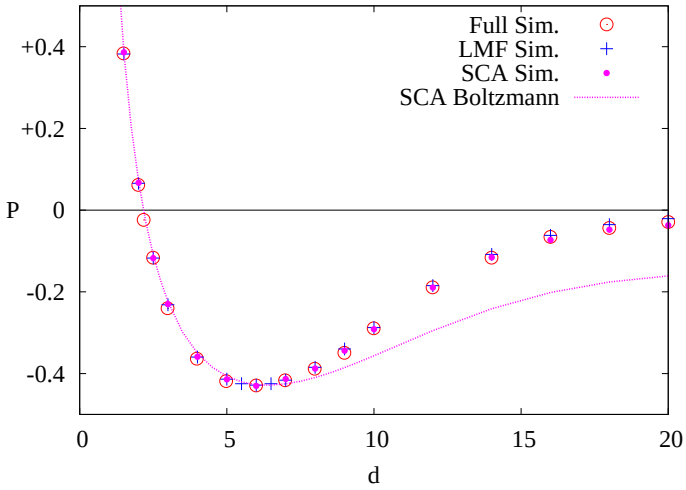

Figure 3.8: Pressure versus distance curves for the strong coupling approximation with simulations and the Boltzmann approximation from [15], compared to full simulations and LMF simulations. $\xi = 100$, and for the SCA and LMF simulations $\sigma = \sigma_{\min}$ for $d = 20$ which is 34. For the Boltzmann approximation, $\sigma = 10.7$ (determination described in [15]).

3.3.3 Breakdown of the Strong Coupling Approximation

The success displayed in Fig. 3.8 should not imply that there is no need for full LMF theory. For any given ξ, once d is large enough, ϕ_0 using a σ appropriate for full LMF theory will begin to plateau in the middle as shown for $\xi = 10$ in Fig. 3.9, and this will lead to an equilibrated situation with too much density in the center and too little near the walls. Even for distances where the plateau has not fully developed, the barrier in the center will be less high in the center. As explained previously, the effect of the plateauing will be far less than when a Boltzmann density response is postulated; however, we do expect a difference. Shown in Fig. 3.10(a) is the wall density for $\xi = 10$ at $d = 4$, $d = 10$, and $d = 20$. We can see the differences in the $n(z)$ determined by SCA and LMF theory develop as d increases, due to the difference in $\phi_R(z)$ and $\phi_0(z)$ at the center.

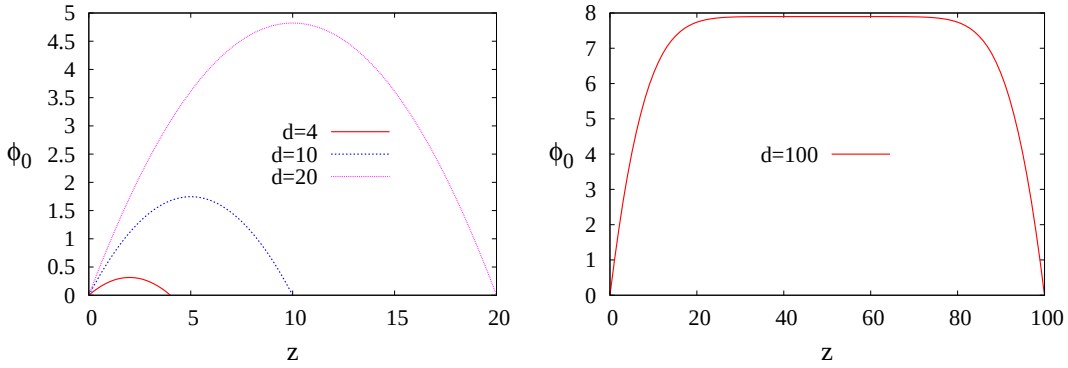

Figure 3.9: The effect of d on the form of $\phi_0(z)$ for $\xi = 10$ and $\sigma = 14$. At $d \gtrsim \sigma$, a barrier develops in ϕ_0 as shown on the left. At $d \gg \sigma$, a plateau eventually forms at intermediate z. This incorrectly predicts a finite "bulk density" as d gets larger and would wreak havoc on the equilibration of canonical simulations.

At a single distance d, the SCA breaks down as ξ decreases from strong to moderate coupling. Shown in Fig. 3.10(b) are plots for $n(z)$ determined via the strong

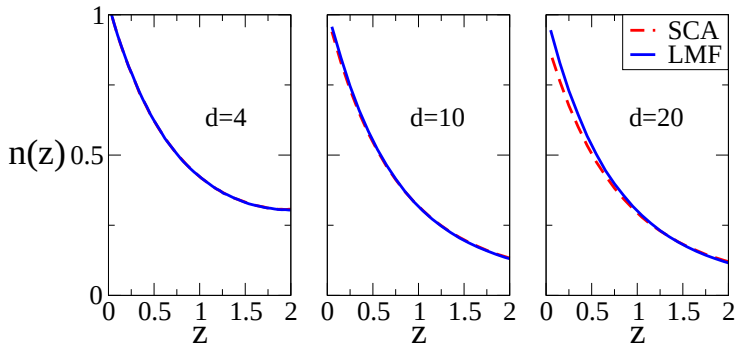

(a) Effect of d on SCA when $\xi = 10$

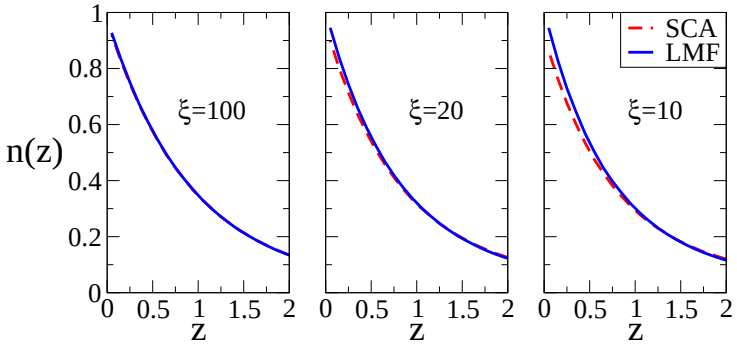

(b) Effect of ξ on SCA when $d = 20$

Figure 3.10: (a): Range of breakdown of SCA over d at $\xi = 10$. As d increases, the difference between ϕ_0 and ϕ_R increases and the resulting wall density begins to differ. (b): Range of breakdown of SCA over ξ at $d = 20$. As ξ decreases, the impact of ϕ_R over and above ϕ_0 at a given d increases. As the approximation's name implies, at even weaker coupling, SCA would be incorrect and full LMF theory is required.

coupling approximation in simulation. In each graph, $d = 20$ and $\sigma = \sigma_{\min}$ at $d = 20$. From left to right, ξ goes from 100 to 20 to 10, and the breakdown of the strong coupling approximation as the system becomes less strongly coupled is evident. As ξ approaches weak coupling, ϕ_R would have an increasingly significant impact in comparison to ϕ_0. In fact, in the limit of weak coupling, PB is completely correct so ϕ_0 would be 0, and ϕ_{R1} would completely determine the density distribution of the particles.

One could potentially resolve these issues using SCA by choosing a larger σ, but that sabotages the computational advantage of LMF theory over series summation techniques for Coulomb interactions. By increasing σ beyond the $\sigma_{\min}$ required for full LMF treatment, the number of particles necessary to make use of the minimum image convention valid for the SCA simulations becomes larger. The use of self-consistent LMF determination of ϕ_R is more appropriate to minimize computational effort.

3.4 LMF Simulation Approach

Some simulation results from a full self-consistent solution of the LMF equation have already been displayed. In this section, we will present more complete results, and the specifics of those simulations are explained in more detail.

3.4.1 Closing the LMF Equation

A full solution to the LMF equation is achieved by iteration to self-consistency since ϕ_R and n_R are interdependent functionals; in other words $\phi_R \equiv \phi_R(z; [n_R])$ and

$n_R \equiv n_R(z;[\phi_R])$. Shown in Fig. 3.11 is a scheme depicting this requisite self-consistency. The basic idea is that a Monte Carlo simulation is run with an initial guess for $\phi_R(z)$, $\phi_R^{(0)}(z)$, in order to determine $\rho(z)$. With that $\rho(z)$, a new $\phi_R(z)$ is determined via the LMF equation. And then another Monte Carlo simulation may be run with the the new $\phi_R(z)$ to determine the next $\rho(z)$. This cycle is carried on until the new ϕ_R is the same as the previous ϕ_R within some tolerance. Further details about how to implement this solution are given in Sect. 3.7. We stress that $\phi(z) = 0$ must be replaced with a reference field $\phi_R(z)$ or some reasonable approximation.

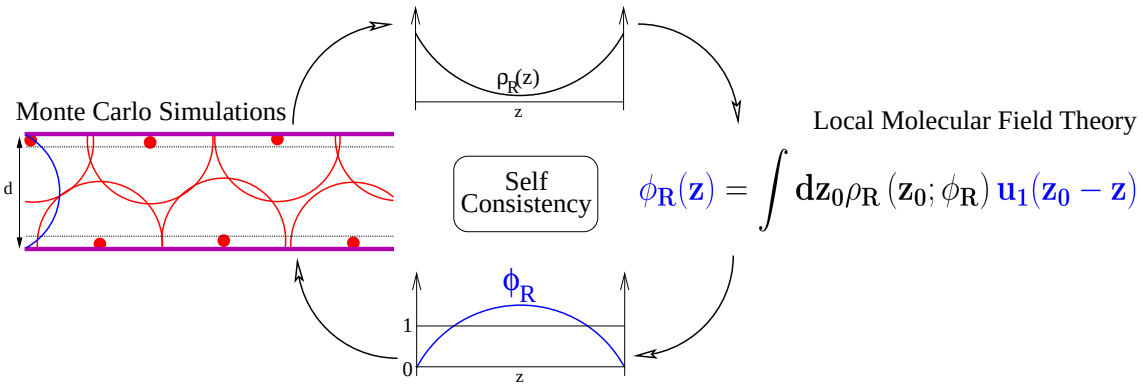

Figure 3.11: Self-consistent solution of LMF theory with no further approximations.

3.4.2 General Results

Shown in Fig. 3.12 are P vs. d curves for coupling strengths 10, 20, 100, and 10^5. Since determination of pressure is intimately linked to obtaining the correct $n_R(z)$ as suggested by the contact formula for pressure, Eq. (3.14), only P vs. d curves are shown for compactness.

Shown in Fig. 3.13 is a collapse of such curves for a wide range of ξ and d. Plotted

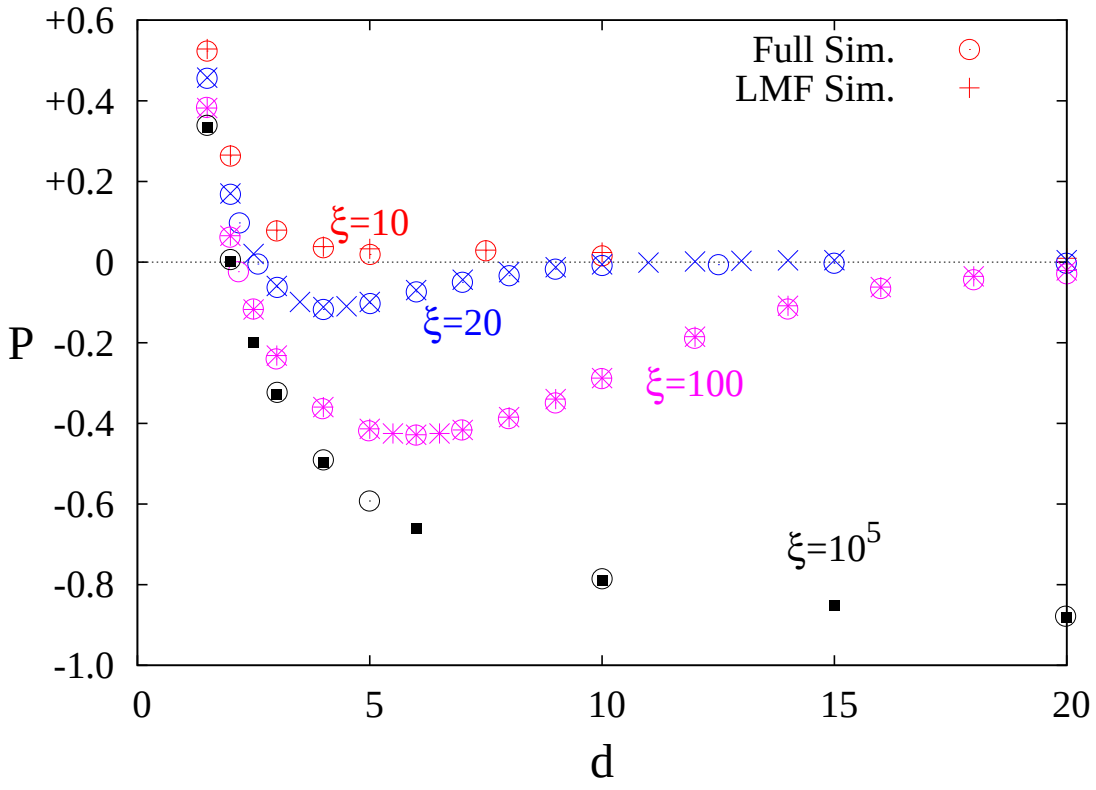

Figure 3.12: Pressure versus distance data for ξ as given by Moreira and Netz [71] and as found by simulations using full LMF theory. The values of ξ are 10, 20, 100, and 10^5, and the respective values for σ are 14, 18, 34, and 650. The manner for choosing σ is described in Sect. 3.7.

are the distances d at which $P = 0$ for a given ξ. These distances are found by fitting P vs. d curves with a spline in GNUPLOT and extrapolating to $P = 0$. The straight line on the graph fits our MC data for the position d of maximal attraction or minimal pressure; this will be addressed further in Sect. 3.5.

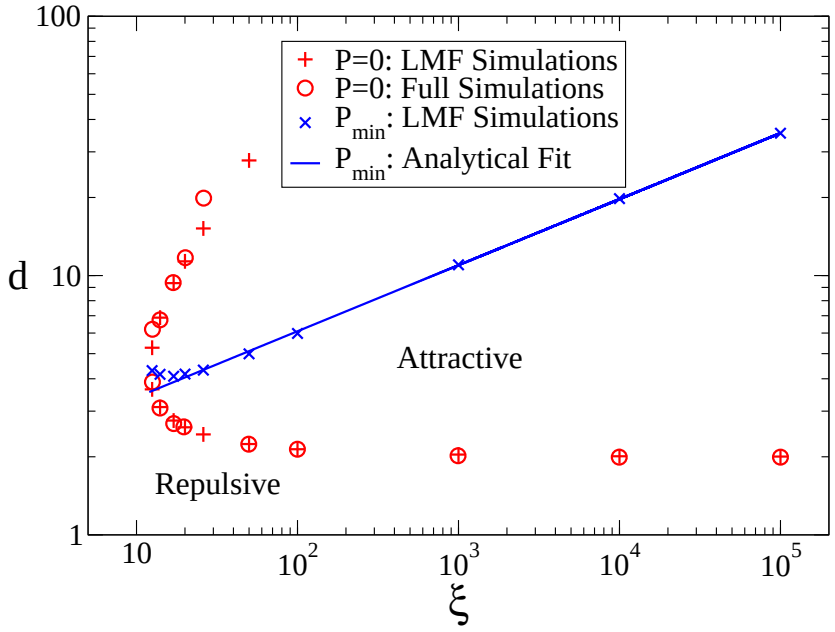

Figure 3.13: Full simulation results from [71] are compared to the results of LMF simulations for the points where $P = 0$. Additionally the points of minimum pressure and maximal attraction found in LMF simulations are shown with an analytical fit of $d_{min} = 1.18 L_w^{0.509}$ which will be explained in Sect. 3.5.

The agreement between the full simulations and short-ranged simulations using full LMF theory is quite striking. As argued in [86], this agreement is strong support for the validity of the physical approximations underlying the derivation of the LMF equation.

3.4.3 g_{2D} Correlation Functions

In [87], Rouzina and Bloomfield propose two unique two-dimensional pair correlation functions to probe the structural rearrangements between particles as d varies. A traditional g_{2D} would look at the likelihood of finding particles at a distance $r_{||}$ projected on the walls relative to a smeared uniform $n(z) = 2/d$. Instead, they suggest two different pair correlations g_{same} and g_{opp} that distinguish between pairs of particles that are on the same side of midplane and on opposite sides of midplane. This unusual definition gives us insight into structural behavior tied to the development of attraction between walls, which we will undertake in Sect. 3.5.

3.4.4 Determining the Smoothed Truncation Length σ

The crux of LMF assumptions as detailed in Ch. 2 is having a σ sufficiently large to make $u_1(r)$ slowly-varying over relevant nearest-neighbor pair correlations and to simultaneously have $u_0(r)$ capture those correlations. In [86], we introduced the first scheme to choose σ_{min} in as unbiased a fashion as possible. Since σ_{min} is the smallest σ that makes LMF theory consistent, as we increase σ in simulations with full LMF we expect properties to vary significantly until $\sigma > \sigma_{\text{min}}$. Additionally, since most systems we examine show moderate to strong coupling, we expect that σ_{min} should scale as the relevant nearest neighbor spacing $\bar{a}$, which is less than L_B. The scheme we present monitors the system's convergence of such spacing, but the scheme could easily be modified to also monitor whether a weak coupling choice of σ is more appropriate.

We examine a single, simply-calculated structural length that will level off once σ is sufficiently large if the theory is accurate. We defined L_{nn} at each Monte Carlo step as the closest distance between the particle we attempt to move and any other counterion. We average L_{nn} over the simulation, and examine the impact of increasing σ on $\langle L_{nn} \rangle$. Shown in Fig. 3.14 are $\langle L_{nn} \rangle$ vs. σ as well as the convergence parameter we examine, $\Delta \langle L_{nn} \rangle / \Delta\sigma$. A reasonable criterion for defining $\sigma_{\min}$ is the first σ at which $\left(\left\langle L_{nn}^{(j)} \right\rangle - \left\langle L_{nn}^{(j-1)} \right\rangle \right) / \left(\sigma^{(j)} - \sigma^{(j-1)} \right) < 0.005$. $\sigma_{\min}$ can be determined in this manner for each (ξ, d)-pair as shown in Fig. 3.15, and this determination reflects the structural rearrangement of the system. We expect $\sigma_{\min} = k \cdot \bar{a}$ where $\bar{a}$ is a characteristic spacing. For small d when the particles form a single two-dimensional layer such spacing is $L_w/\sqrt{2} = \sqrt{\pi\xi}$, and at larger d when the system has formed two distinct two-dimensional layers $\bar{a}$ is $L_w = \sqrt{2\pi\xi}$. With k remaining the same, we expect that $\sigma_{\min}$ should shift by a factor of $\sqrt{2}$. In the lower and upper manifolds drawn for the σ-convergence curves in Fig. 3.15(a), a factor of $\sqrt{2}$ is evident.

Both $\langle L_{nn} \rangle$ and $\sigma_{\min}$ are meaningfully related to the structure of the system. Shown also in Fig. 3.15 are those two lengths compared to g_{same}. Notice that while $\langle L_{nn} \rangle$ is smaller than the position of the peak of g_{2D}, the $\sigma_{\min}$ determined is approximately 50% larger, incorporating that nearest neighbor shell of interactions.

We may also take advantage of the rearrangement from two layers to one layer since, for a single ξ, the $\sigma_{\min}$ found at a larger d will be greater than or equal to the $\sigma_{\min}$ found for a smaller d. Thus by finding $\sigma_{\min}$ only at the maximal d studied for a certain ξ, we save computation time.

Shown in Fig. 3.16 are the values of $\sigma_{\min}$ determined for a single layer at $d = 2$

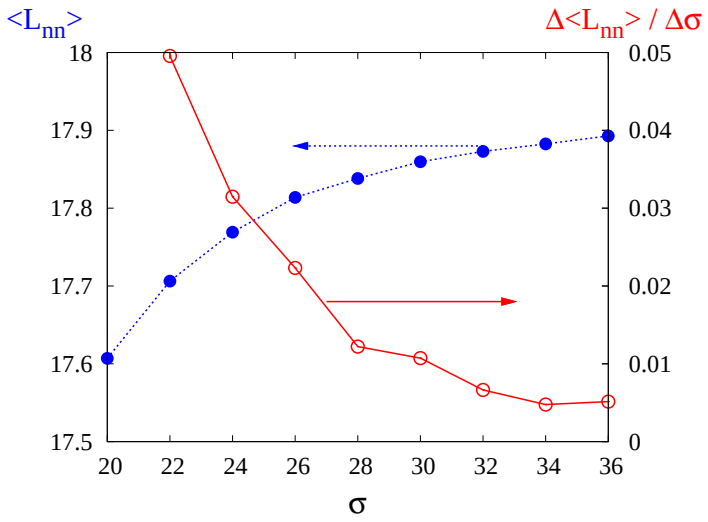

Figure 3.14: $\langle L_{nn} \rangle$ vs. σ and $\Delta \langle L_{nn} \rangle / \Delta\sigma$ vs. σ for $\xi = 100$ and $d = 20$. As σ increases, $\langle L_{nn} \rangle$ rises and eventually levels off. The convergence parameter $\Delta \langle L_{nn} \rangle / \Delta\sigma$ simultaneously falls below the convergence cutoff of 0.005.

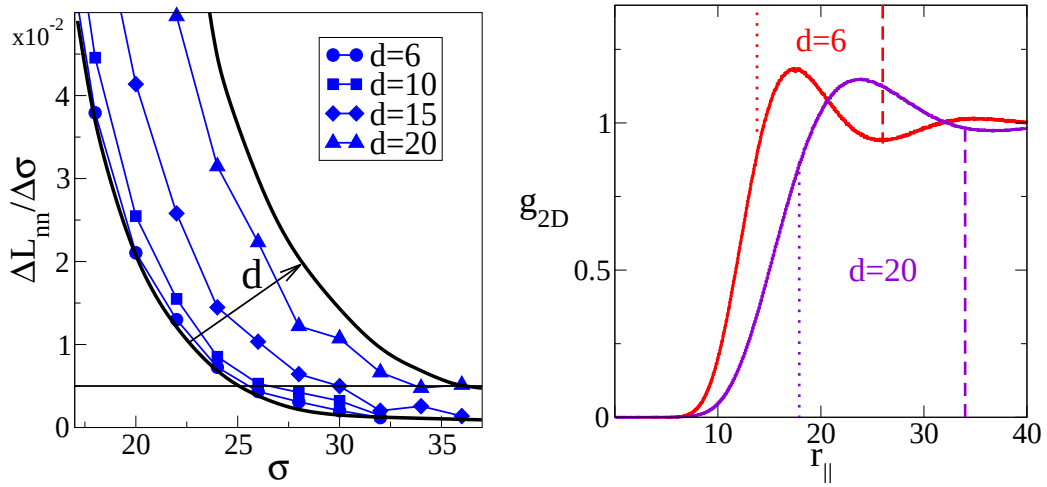

(a) σ Convergence

(b) g_{2D} with Lengths

Figure 3.15: (a) Demonstration of $\sigma_{\min}$ determination for varying d for $\xi = 100$. The smooth curves represent the upper and lower manifolds for two layers and one layer beyond which we do not expect further shifting. The $\sqrt{2}$ difference between the largest and smallest $\sigma_{\min}$ is due to the shift from two layers to a single layer. (b) g_{same} for two of the distances along with $\langle L_{nn} \rangle$ (dotted lines) and $\sigma_{\min}$ (dashed lines).

and for two layers at large d compared to the appropriate $\bar{a}$ accounting for the number of layers ($L_w/\sqrt{2}$ or L_w respectively). When $\sigma_{\min}$ is plotted relative to $\bar{a}$, all points lie along the same trend whether $\sigma_{\min}$ was determined from a one layer or two layer scenario. Since $\sigma_{\min}$ and $\bar{a}$ are in reduced units, both values increase with increasing ξ. In unreduced units, $\bar{a}$ would not vary at all with ξ; it would only depend on whether there are one or two layers. Also in unreduced units, we expect that at strong coupling $\sigma_{\min}$ will equal $k \cdot \bar{a}$ where k is on the order of 1. As coupling moderates and the particles are no longer as well represented by a two-dimensional layer, we expect $\sigma_{\min}$ be slightly larger than $k \cdot \bar{a}$ in order to include core interactions normal to the surface as well.

We therefore attempt a power law fit to all $\sigma_{\min}$ versus $\bar{a}$ data points, and find $\sigma_{\min} = 1.68 \cdot \bar{a}^{0.94}$. This is a bit under the linear scaling we expect, but recall that for moderate coupling we expect that σ will lie slightly above $k \cdot \bar{a}$ converging on linear at larger ξ. If we instead attempt a linear fit to the higher ξ data, those data points are nicely fit by the linear function $\sigma_{\min} = 1.26 \cdot \bar{a}$ with lower ξ points lying above the line.

One catch of applying the strong coupling approximation is that we should use $\sigma > \sigma_{\min}$ determined in the fashion described here, but finding $\sigma_{\min}$ requires additional computational time. For simulations in this chapter, we find $\sigma_{\min}$ only at the largest d and use that for smaller d. Alternately, we could simply choose a conservative estimate for k in $\sigma_{\min} = k\bar{a}$ such as $k \simeq 1.5 - 2.0$. In practice, we will make just such an expeditious choice in applying LMF theory to molecular systems.

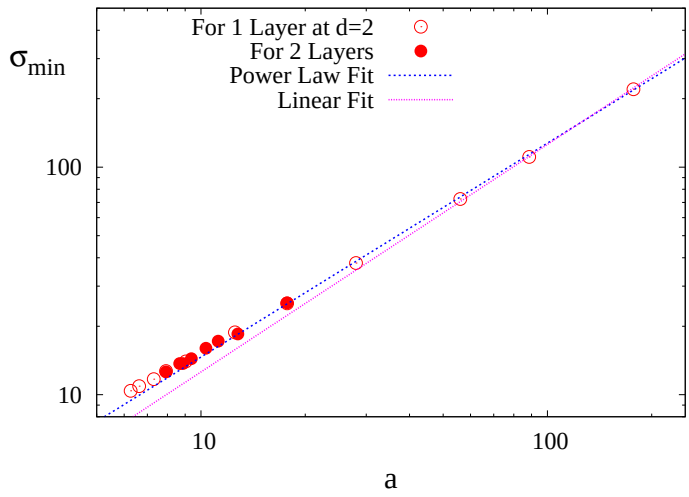

Figure 3.16: Demonstration of $\sigma_{\min}$ scaling relative to neutrality spacing parallel to the wall ($\bar{a}$ which may be either L_w for two layers or $L_w/\sqrt{2}$ for one layers). At larger $\bar{a}$, $\sigma_{\min}$ scales linearly with $\bar{a}$, and at smaller $\bar{a}$, $\sigma_{\min}$ values lie above the linear prediction.

3.4.5 Calculating Pressure: Contact versus Midplane

In Eq. (3.14) of Sect. 3.1, the contact theorem for pressure is given as

$$P_{\text{contact}} = n(0) - 1.$$

This formula is a simple connection between structure and thermodynamics, but it poses numerical difficulties in simulations, since it requires the exact contact density of particles at a hard wall. Since histograms are divided into finite-sized bins and $n(z)$ is rapidly varying near the walls, extrapolating to bins of width $\Delta z = 0$ is not easy. A formula incorporating the density at midplane would be preferable since it is quite slowly varying around $z = d/2$.

This midplane approach has been used in simulations of this system before, but it has been derived with the constraint of a hard wall at $z = d/2$ and thus only valid for large distances [36] or alternately it has been posited without reference or

proof [99]. A general formulation of such an approach is the method of planes [97]. The derivation is designed for dynamics simulations, but in the context of equilibrium simulations it says that for the geometry of this system, any dividing plane z_p may be chosen and the normal pressure of the system is simply $P = k_B T \rho(z_p) + \langle F_{LR} \rangle / A$, where F_{LR} is the force due to interactions between particles on opposing sides of z_p. Appendix C provides the justifications and derivations for this system, since they are not immediately clear from a literature search on this system. This basic statement for pressure may be used to easily obtain the contact theorem by choosing $z_p = 0^+$. Then the only "particle" to the left of the plane is the one wall, and in rescaled units the net electrostatic force per unit area is -1.

In rescaled pressure units the midplane pressure formula for full simulations is given as

$$P_{\text{midplane}} = n\left(\frac{d}{2}\right) + \frac{2\pi\xi}{A}\left\langle \sum_{i\in L}\sum_{j\in R} f^{(z)}\left(r_{ij}\right)\right\rangle - 1 \tag{3.22}$$

where the two summations pick out pairs of particles where i is to the left of midplane and j is to the right of midplane, and $f^{(z)}$ is the interparticle force in the z-direction. Appendix C gives details about the derivation of this formula. Since the forces between charged particles are also long-ranged, this midplane pressure formula requires summing out to infinity in the x- and y-directions as well.

Fortunately, LMF theory provides an approximation to the midplane pressure formula which will be accurate, provided that LMF theory is accurate. We proceed by splitting $f^{(z)}$ into short- and long-ranged parts. The average of the short-ranged forces is found via explicit summation over simulation configurations, and the average

of the long-ranged forces is found via local molecular field averaging. This approach yields

$$P_{\text{midplane}} \simeq n\left(\frac{d}{2}\right) + \frac{2\pi\xi}{A}\left\langle \sum_{i=1}^{N_L}\sum_{j=1}^{N_R} f_0^{(z)}\left(r_{ij}\right)\right\rangle + \frac{2\pi\xi}{A}\left\langle \sum_{j=1}^{N_R}\int_0^{\frac{d}{2}} dz'\, n(z')\ \text{erf}\left(\frac{z_j - z'}{\sigma}\right)\right\rangle - 1 \tag{3.23}$$

where

$$f_0^{(z)}(r_{ij}) = -\left.\frac{\partial u_0(r)}{\partial z}\right|_{\mathbf{r}=\mathbf{r}_{ij}} \tag{3.24}$$

and $\text{erf}(\Delta z/\sigma)$ is the long-ranged force on a particle at z_j on the right side of midplane due to an equilibrated particle density at z' on the left side of midplane. Since particle-particle correlation effects are now only present in the first bracketed term, the second bracketed term may be simplified with no further approximations as

$$P_{\text{midplane}} \simeq n\left(\frac{d}{2}\right) + \frac{2\pi\xi}{A}\left\langle \sum_{i=1}^{N_L}\sum_{j=1}^{N_R} f_0^{(z)}\left(r_{ij}\right)\right\rangle + \int_{\frac{d}{2}}^{d} dz \int_0^{\frac{d}{2}} dz'\, n(z)\cdot n(z')\ \text{erf}\left(\frac{z - z'}{\sigma}\right) - 1. \tag{3.25}$$

The pressures obtained from the midplane approach and the contact theorem are essentially identical at small d, and as d increases, we expect $P_{midplane}$ to be more accurate than $P_{contact}$ since the midplane densities will be better converged on the finite histogram grid. The values at large d are still close though. The density values $n(0)$ and $n(d/2)$ are made more accurate by fitting nearby data to a second order Taylor expansion about those points.

3.5 Basis of Attraction

Correlation functions and pressure have previously been discussed from the standpoint of implementation. Here, we discuss the inter-relation between the structural rearrangement encompassed in the g_{2D} correlation functions and the effective attraction between like-charged walls and show how the strong coupling approximation can add insight into this as well.

A counterion induces a so-called "correlation hole" across midplane from itself provided that the coupling is strong and the wall separation is sufficiently small. As qualitatively explained by Rouzina and Bloomfield [87], the attraction between walls is due to the cross-correlation between counterions on either side of midplane. The basic idea is that once a correlation hole forms, then a counterion on one side is exposed to a net negative wall surface area directly across from it and the net electrostatic attraction begins to dominated. This is the main reason why charge density representations smoothed in the x- and y-directions are inadequate to capture forces between the two sides of the system.

In order to better understand the cross-correlation process between particles, we discuss g_{same} and g_{opp} as proposed by Rouzina and Bloomfield. To our knowledge, an examination of these correlation functions have not been undertaken previously for the two-wall system.

These functions have expected limits for small d and large d in strongly coupled systems. As counterions move from two layers to one layer, the first peak of g_{same} should shift by a factor of $\sqrt{2}$ as the required neutrality spacing shifts from L_w to

$L_w/\sqrt{2}$. Simultaneously, in the limit of two completely uncorrelated layers, $g_{\text{opp}} = 1.0$, and as d decreases, a "correlation" hole in g_{opp} will form with a radius of about $L_w/\sqrt{2}$, and finally by $d \simeq 2$ where all particles are in a single layer we expect $g_{\text{same}} = g_{\text{opp}}$. Shown in Fig. 3.17 are these pair correlation functions for $\xi = 20$, $\xi = 100$, and $\xi = 1000$ at a range of d. These trends in g_{same} and g_{opp} are evident.

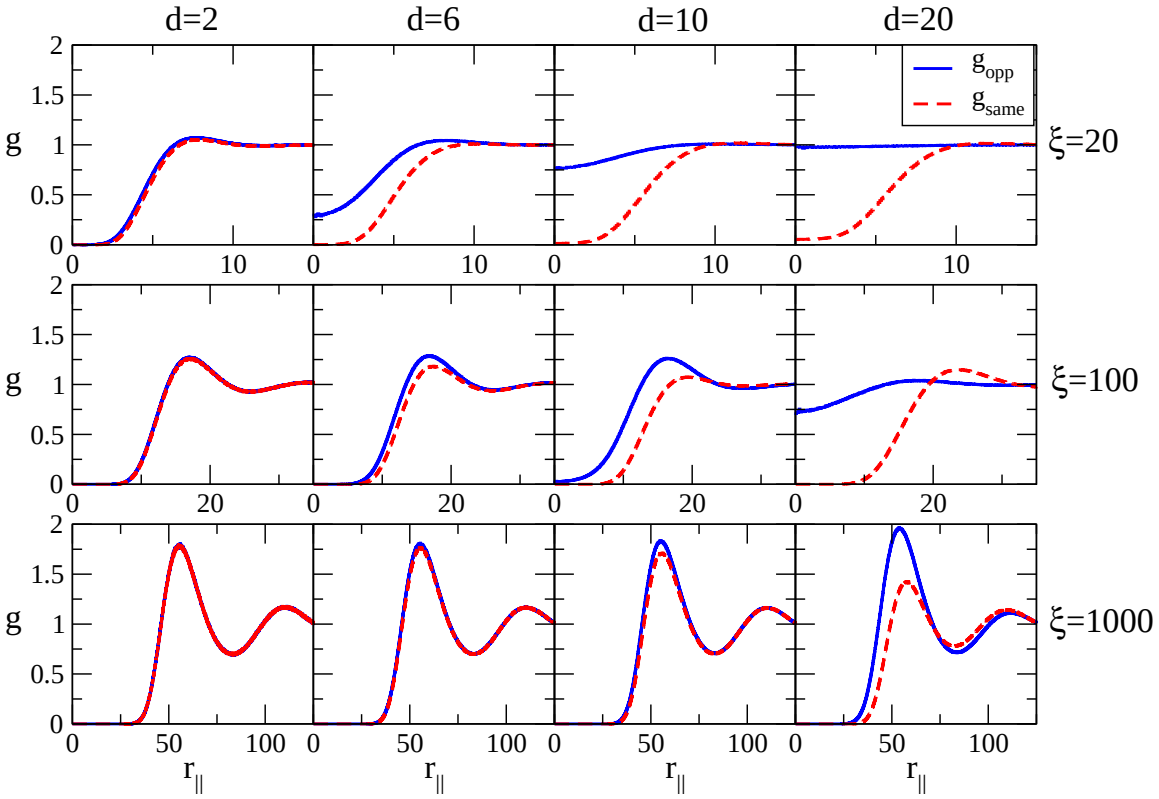

Figure 3.17: The two-wall system's g_{2D} for a range of d and ξ. For $\xi = 20$, we can observe the limits of g_{2D} functional forms. For the two larger ξ intermediate distances are on the order of d_{min} for P_{min}. For $\xi = 100$, $d_{min} = 6.0$ and we can see the start of preference for nearest neighbor ions to be on opposite sides. For $\xi = 1000$, $d_{min} = 11.2$ and at $d = 10$, we can see the peak difference developing.

Additionally we can see that as d increases beyond 2, the peak of g_{opp} is increased and the peak of g_{same} is decreased initially as particles maintain the two-dimensional spacing of a single layer but begin to have a preference to alternate sides and thus

develop some normal repulsion between each other. The development of this peak difference indicates that particles are *just* beginning to partition into two layers as d increase (or finally forming a single layer as d decreases). This first formation of a single layer should coincide with the minimum pressure between the walls (and also maximal attraction). When the single layer forms, the normal repulsion between particles is no longer present, and simultaneously, the particles have the most space available to them in the z-direction as a single layer, leading to the lowest value of $n(z)$ for a single layer and the minimum pressure.

When particles are in a single layer we expect them to transfer between sides quite easily, so one could monitor the frequency of side-switching during Monte Carlo steps; a frequency cutoff could be used to distinguish between a single layer and two layers. One could also envision quantifying this single layer formation by monitoring some difference between g_{same} and g_{opp} for varying d. However, the definition of a meaningful parameter based on these differences is not immediately obvious. Additionally analysis of either of these approaches would be rather subjective, because the transition between two layers and a single layer is a relatively fluid process, as suggested by the pair correlation functions in Fig. 3.17.

In lieu of attempting detailed analysis of simulation results, the scaling of this point of maximal attraction (d_{min}) is easily and well explained with simple analysis of the strong coupling approximation. Simply stating that maximal attraction occurs when particles first form a single layer in the z-direction, one may use the strong coupling approximation to predict a scaling between ξ and the d that yields P_{min}, called d_{min}. As first explained in [15], by Taylor expanding ϕ_0 around $z = 0$, one

finds to first order that

$$\phi_0(z) \simeq \frac{1}{\sigma_{\min}\sqrt{\pi}} \cdot 2z(d-z) \tag{3.26}$$

provided that $d < \sigma_{\min}$. With this approximation the SCA barrier at $d/2$ is $d^2/(2\sigma_{\min}\sqrt{\pi})$. If we assume that single layer formation and therefore maximal attraction occurs when this barrier is on the order of k_BT (1 in reduced units), we find $d_{min} \simeq \sqrt{2\sigma_{\min}\sqrt{\pi}}$.

We have shown in Sect. 3.7 that $\sigma_{\min}$ scales linearly with $\bar{a}$, and therefore $d_{min} \propto \sqrt{L_w} \propto \sqrt[4]{\xi}$. A power law fit between d_{min} and ξ was previously shown in Fig. 3.13 with the fitting equation being $d_{min} = 1.18L_w^{0.509}$. We may make an estimate of the ϕ_0 barrier height that leads to single layer formation based off of this fit and the linear relation $\sigma_{\min} \simeq 1.26 \cdot \bar{a} = 1.26 \cdot L_w/\sqrt{2}$ found previously in this section, by assuming that the barrier is some fraction x of k_BT, $d_{min} \simeq \sqrt{2x\sigma_{\min}\sqrt{\pi}}$. Using the simulation fits for $d_{min}(L_w)$ and $\sigma_{\min}(\bar{a})$, we find that the single layer forms when the barrier is approximately $0.44k_BT$, which is certainly on the order of k_BT.

Using a simple expansion based on the strong coupling approximation of local molecular field theory, we may make fruitful scaling predictions that would otherwise be difficult to obtain even from detailed simulation data.

3.6 Inclusion of Physical Cores

The simplicity of this model might suggest that there will be difficulty in generalizing to more typical systems where the charges are not point ions. However, LMF theory is *not* restricted to such simple model systems. Inclusion of additional pair interactions between charged particles is quite simple, since LMF in principle deals only with

the long-ranged portion of the Coulomb interaction. This is crucial because most force fields for intermolecular interactions include both charge-charge interactions and Lennard-Jones interactions meant to represent the Pauli exclusion repulsions between particles at short distances and van der Waals attractions at larger distance. These more physical cores may be added into the short-ranged simulation without further complications.

As a ready demonstration of this, simulations of $\xi = 100$ counterion-wall systems with two different WCA cores were carried out with varying d. Recall that WCA cores contain only the repulsive part of the Lennard-Jones pair interactions. The mechanisms of LMF theory and $\sigma_{\min}$ determination remain identical; we simply add $u_{\mathrm{WCA}}(r)$ to $u_0(r)$ in the pair-interaction sum in $\mathcal{U}$ for MC steps and $f^{(z)}_{\mathrm{WCA}}$ to $f^{(z)}_0$ in the discrete sum for midplane-pressure determination. In each case, $\varepsilon_{\mathrm{LJ}} = 1.0$. σ_{LJ} is either 4.0 or $L_w/\sqrt{2}$. The P vs. d curves are shown in Fig. 3.18.

As one might reasonably expect, since the WCA cores impact only the counterion interactions and not the interaction with the walls, the choice of a smaller σ_{LJ} has little impact on the pressure values in comparison to point charges because the counterions rarely if ever come within the range of the WCA core. In contrast, choosing σ_{LJ} to be larger has a significant impact on pressure when particles form two separate layers and $d \lesssim L_w/\sqrt{2}$. However, when the particles are finally forced into a single two-dimensional layer at sufficiently small d, the WCA cores have much less impact on the pressure because the forces are directed predominantly laterally along the walls rather than normal to the walls. Figure 3.18 shows this to be the case for $\sigma_{\mathrm{LJ}} = L_w/\sqrt{2}$. We expect that for even larger σ_{LJ}, forcing the particles into a single layer would require

much more force, but once the particles were in a single layer, the P vs. d profile would be identical to that of the point counterions.

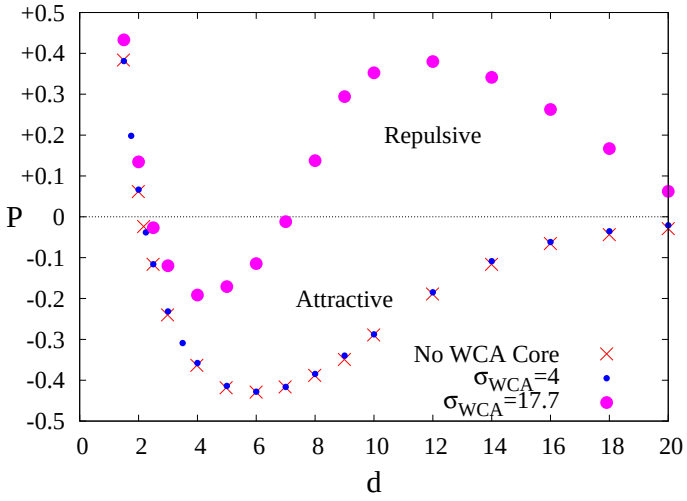

Figure 3.18: Impact of including more realistic core potentials on pressure for $\xi = 100$. The WCA potential is used with $\varepsilon_{\mathrm{LJ}} = 1.0$ and σ_{LJ} equal to 4 and $L_w/\sqrt{2} = 17.7$. The small cores have virtually no impact on pressure, while cores with a size matching the spacing in a single layer have a significant repulsive impact on the pressure until d is small enough that the particles have been forced into a single layer.

Subsequent work in this thesis extends the application of LMF theory to simulations of a water model. However, the simple extension here suggests that the LJ core of the water model used should not affect the applicability of the LMF equation to simulations. Rather, the point we will examine carefully in Ch. 5 will be the extension of LMF theory to molecular models.

3.7 Implementing Monte Carlo Simulations with LMF

This model system has provided a nearly ideal situation for testing LMF theory and SCA with simulations due to the high symmetry of the situation. Determining a converged single particle density that depends only on z-position and subsequently

solving an equation for ϕ_R that depends only on z is a numerically much simpler task than that for a general three-dimensional external field, both with respect to obtaining converged Monte Carlo particle densities and solving the LMF equation numerically.

We have been able to quite simply implement standard canonical Monte Carlo techniques with a minimum image convention. In this section we describe the details of this implementation.

3.7.1 Basics of Monte Carlo Simulations

The system is simulated using a standard canonical Metropolis Monte Carlo (MC) algorithm [31]. Thus N particles are simulated with N equal to an even integer squared so that the particles may be initially placed on a square lattice. The simulation cell has volume $L \times L \times d$ with L chosen based on the requirement of neutrality in reduced units,

$$\frac{N}{2} \cdot L_w^2 = N\pi\xi = L^2 \tag{3.27}$$

In general N is chosen with the intent that the minimum image convention is justified. As such, a mimic particle should not interact with more than a single image of any other particle. Since $u_0(r)$ is never exactly zero, we choose an R_c beyond which $u_0(r) \simeq 0$:

$$u_0(R_c) = \xi \frac{\mathrm{erfc}(R_c/\sigma)}{R_c} \leq \epsilon \tag{3.28}$$

where ϵ is a sufficiently small energy of interaction. Then, given this definition of R_c,

any N that satisfies

$$\frac{L}{2} = \frac{1}{2}\sqrt{N\pi\xi} > R_c \tag{3.29}$$

will justify the minimum image convention. ϵ is typically 10^{-3} and the smallest N possible is used. For ξ around 10^4 or 10^5, ϵ is chosen as 10^{-2}, and for smaller ξ, ϵ could be chosen correspondingly smaller. In order to ensure continuity of energy at R_c, $u_0(r)$ is shifted by the value $u_0(R_c)$.

Choosing an R_c beyond which $1/r$ could be set to zero would be completely wrong since $1/r$ decays slowly. The beauty of the mimic $u_0(r)$ is that at large r, the leading order asymptotic expansion, $\exp\left[-(r/\sigma)^2\right]/r^2$, decays significantly faster than $1/r$. A numerical truncation of $u_0(r)$ is therefore only as problematic as standard approaches for short-ranged pair interactions.

Random attempted MC steps are achieved by choosing a vector $\mathbf{s}$ of 3 random numbers between -1 and 1, and setting the $\Delta\mathbf{r}$ that is attempted equal to $l_{step}\mathbf{s}$. The attempted MC move is then accepted if the change in potential energy, ΔU, is such that a random number between 0 and 1, $\mathcal{R}$, satisfies $\mathcal{R} \leq \exp\left(-\beta\Delta U\right)$. An attempted step that maintains or lowers the potential energy ($\Delta U \leq 0$) will be accepted, and any attempted step that increases the potential energy will be accepted with a frequency of the Boltzmann factor of the energy change. The step length l_{step} in the simulations is adjusted such that between 1/3 and 1/2 of attempted MC steps are actually accepted. Particle moves are done as they would be in a three-dimensionally periodic system, except that there is no image replication in the z-direction normal to the walls. Moves are accepted or rejected based on the energy change ΔE with the typical Metropolis

scheme. Any move that places a particle at $z < 0$ or $z > d$ is immediately rejected since the wall-counterion potential is defined to be $+\infty$ in those regions.

Since the simulations were carried out in reduced units, defining ξ and d sets the thermodynamic state of the simulation. The total potential energy $\mathcal{U}$ is

$$\mathcal{U} = \sum_{i=1}^{N} \phi_R(z_i) + \xi \sum_{i<j} \frac{\mathrm{erfc}(r_{ij}/\sigma)}{r_{ij}}. \tag{3.30}$$

The distance r_{ij} is determined using the image of particle j closest to particle i in the simulation box. In the SCA we approximation ϕ_R as ϕ_0.

The initial particle distribution was obtained by placing the $N = (2m)^2$ particles on a square lattice in the x- and y-directions and choosing their z-positions based from an $n(z)$ determined from MPB theory as found described in [15], to enable faster convergence of LMF solutions. $n(z)$ was collected on a grid in the z-direction with spacing $\Delta z = \min\left(0.1, \frac{d}{100}\right)$, and $\phi_R(z)$ was calculated on the same grid.

Values of the above described parameters are given in Table 3.1. All values in the table are given in reduced units. Thus, even though in unreduced units σ and the related "Coulomb core" maintain a constant value determined by neutrality as coupling increases, in reduced units, σ increases.

3.7.2 Solving for ϕ_R

Previously shown in Fig. 3.11 in Sect. 3.2 is a diagram depicting the self-consistency required for a solution to the LMF equation. The most straightforward scheme achieving this self-consistency involves the explicit iteration of equilibrated MC simulations and $\phi_R(z)$ solutions. Schemes for mixing the impact of evolving $\phi_R(z)$ into the accu-

ξ	σ	d_{max}	R_c (ϵ)	N
10	14	20	30 (10^{-3})	144
12	14	10	36 (10^{-4})	196
12.5	16	10	41 (10^{-4})	196
14	16	10	35 (10^{-3})	144
17	18	15	39 (10^{-3})	144
20	18	20	40 (10^{-3})	196
26	20	22	45 (10^{-3})	144
50	26	40	71 (10^{-4})*	144
100	34	20	81 (10^{-3})	100
10^3	80	20	210 (10^{-3})	100
10^4	230	25	570 (10^{-2})	100
10^5	650	40	1750 (10^{-2})	100

Table 3.1: Monte Carlo simulation parameters. Since σ is given in reduced units, σ increases with increasing ξ; in unreduced units, we expect σ to converge to a constant value scaling as $\bar{a}$ (L_w or $L_w/\sqrt{2}$) as the coupling becomes stronger. *Note that $\xi = 50$ has a larger range as defined by the energy cutoff requirement ϵ. This was the largest ξ that the upper $P = 0$ value was found for, and greater numerical accuracy was needed for that calculation since the pressures were so small due to the flatness of P vs. d near the $P = 0$ point.

mulation of $n_R(z)$ were explored. However in these simulations, the only step in this direction was to assume that the changes in $\phi_R(z)$ were sufficiently small that the final configuration of counterions in $\phi_R^{(i-1)}(z)$ was taken as essentially equilibrated in $\phi_R^{(i)}(z)$. Solution of the LMF equation was iterated with simulation until self-consistency was achieved as defined by

$$\frac{1}{d}\int_0^d \left|\phi_R^{(i)}(z) - \phi_R^{(i-1)}(z)\right| dz < 0.001. \tag{3.31}$$

In these simulations, the general solution scheme is shown in Fig. 3.19. The initial particle density distribution is analytically found via MPB calculation, and the LMF equation is used to make an initial guess at ϕ_R for simulation with a σ appropriate for simulation since $\sigma_{\text{sim}} > \sigma_{\text{MPB}}$. An initial equilibration for N_{eq} Monte Carlo sweeps is carried out, and then a continual looping over $n_R^{(i)}\left(z;\left[\phi_R^{(i-1)}\right]\right)$ collection in N_{eq} sweeps and subsequent $\phi_R^{(i)}\left(z;\left[n_R^{(i)}\right]\right)$ determination is done. Once the convergence criteria in Eq. (3.31) are met after n_{iter} loops, then $n_R(z;[\phi_R])$, P, and g_{2D} are collected over N_{ave} sweeps.

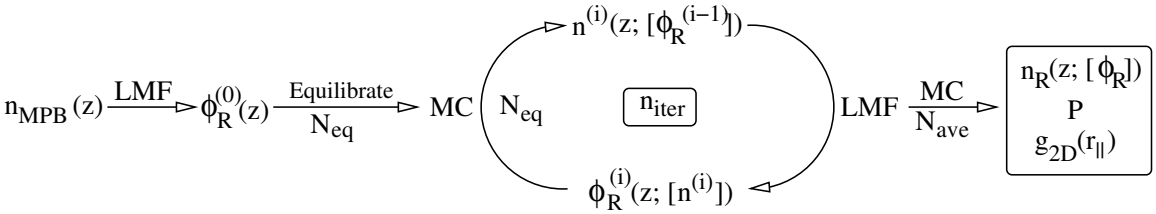

Figure 3.19: Demonstration of the full solution of LMF equation and the subsequent data collection in two wall Monte Carlo simulations. Equilibration and $n(z)$ collection for LMF iterations are done over N_{eq} Monte Carlo sweeps. The convergence criterion, Eq. (3.31), is met after n_{iter} iterations, and then averaged properties are found over N_{ave} Monte Carlo sweeps.

Shown in Table 3.2 are n_{iter} for $\xi = 50$ and various d, when $n_R^{(0)}(z) = n_{\text{MPB}}(z)$.

The scheme converges to a solution quite quickly even for larger distances.

d	5	10	15	20	25	30
n_{iter}	1	1	1	2	2	3

Table 3.2: For $\xi = 50$, n_{iter} required to reach convergence of the LMF equation when $n_R^{(0)}(z) = n_{\mathrm{MPB}}(z)$ as d increases. $N_{eq} = 10^5$ and $N_{ave} = 5 \times 10^5$.

3.7.3 Utility of ϕ_0

As shown in Sect. 3.3, the strong coupling approximation can yield accurate results in simulations. For strong coupling systems at small d, both ϕ_0 and ϕ_R have very shallow wells near the walls and thus choosing $\phi_R \simeq \phi = 0$ would even yield reasonable results. However at larger d, the net normal forces due to particles extending to ∞ in the x- and y-directions become substantial. There, inclusion of effective wells near the walls is required for simulations of short-ranged particles to correctly reproduce their separation into two separate layers, as previously shown at the start of Sect. 3.2. The strong coupling approximation and its corresponding $\phi_0(z)$ has wells of depth over $4\,k_BT$ for $\xi = 10$ and $d = 20$. To capture the separation of particles into two separate layers, the inclusion of at least ϕ_0 is absolutely crucial. As d grows larger or ξ grows weaker, choosing a self-consistent ϕ_R will instead be necessary to obtain accurate results. Already at $\xi = 10$ and $d = 20$, the SCA is beginning to break down as shown in Fig. 3.10.

Even when ϕ_R is needed, we will not always be applying LMF to a system where the mimic Poisson-Boltzmann approximation is reasonable. In the cases where coupling is strong, $\phi_0(z)$ could be a strong choice for $\phi_R^{(0)}(z)$ in LMF iterations.

3.8 Summary and Conclusions

In this chapter, we reviewed the initial application of LMF theory to *simulations* of a nonuniform charged system. The slab geometry explored will be examined again for molecular systems in Ch. 6, but most of the basic LMF equation framework will remain identical.

The model system we studied – two uniformly charged walls with interstitial neutralizing point counterions – is of physical interest because it can exhibit like-charged attraction between the two walls. In Sect. 3.1, we discussed the relevant length scales of the system's interactions to gain physical intuition about the appropriate length-scale for the split of $1/r$ into short- and long-ranged parts. Work by Chen and Weeks [15] using these lengthscale arguments in tandem with the mimic Poisson-Boltzmann approximation successfully captured the like-charged attraction. While such an approach led to very good qualitative and near quantitative agreement with a single fit to simulation data, simulations using full LMF theory lead to very accurate results for the like-charged attraction with absolutely no fitting parameters. Not only do the individual pressure versus distance curves for a range of coupling strengths agree quite well with full simulation results due to Moreira and Netz [71] as shown in Fig. 3.12, but so does the overall phase diagram in Fig. 3.13 documenting the wall separation distances at which various coupling strengths cross between attraction and repulsion.

Carrying out these simulations also allowed us to study the technical aspects of the application of LMF theory in greater detail than we shall undertake for molecular systems. We studied the accuracy of the strong coupling approximation relative to

the full self-consistent solution of the LMF equation – this relative accuracy depends both on the coupling strength of the system and the separation between the walls. Even for the nonuniform systems studied here, the applicibility of the strong coupling approximation to a given phase point is not a black-and-white question. The success of SCA and the eventual signs of the breakdown of SCA were presented in Sect. 3.3. We also presented an "unbiased" method for determining $\sigma_{\min}$ for a given coupling strength based on monitoring the average distance of closest approach between counterions as σ is increased. We found that $\sigma_{\min}$ scaled with the neutrality spacing along the walls, as physically expected. Data for ionic correlations lateral to the walls for varying coupling strengths and wall separations were collected for this two-wall system. To the best of our knowledge, this was the first simulation data for pair correlations lateral to the walls, which distinguish between particles on the same side of midplane and on the opposite side. These correlation functions exhibited the expected behavior during the transition from a single layer at small distances between walls to two layers at large wall separation.

Overall, the LMF approach to electrostatics proved accurate and useful for this simple slab system. Later in the thesis we will show that this accuracy holds for far more complex systems than that presented here.

Chapter 4

LMF Theory in Context

The treatment of Coulomb interactions both analytically and in simulations is a much-studied problem. As such it is important to understand the LMF approach in the context of other approaches. Below we will first place LMF theory more firmly in the arena of classical electrostatics. Then we will detail different techniques ranging from traditional mean-field analytical techniques to explicit series summation of Coulomb interactions in quickly-convergent manners. Connections may be drawn between each of these techniques and the LMF approach, and we will try to understand these.

4.1 Electrostatics via LMF Theory

Here we will examine the LMF equation for a mixture of species since fluids containing charges must at least be a mixture of positive and negative charges. We need only consider the mixture equation here because, with appropriate approximations, the LMF equation for standard molecular models collapses onto the mixture LMF equation, as explained in Ch. 5. The YBG equation for mixtures is given in Appendix A, and exactly the same approximations as used in Ch. 2 lead to the following LMF equation for a species α in a mixture of different species indexed by γ and including α:

$$\phi_R^{(\alpha)} = \phi^{(\alpha)}(\mathbf{r}) + \sum_\gamma \int d\mathbf{r}'\, \rho_{R,\gamma}(\mathbf{r}') \cdot u_{1,\alpha\gamma}(|\mathbf{r} - \mathbf{r}'|). \tag{4.1}$$

This general form was described by Chen and Weeks [15] in the context of charge-charge interactions. And if the interactions being treated were of general LJ form this would be the furthest simplification possible, with an LMF equation to be solved for each different species with a complicated sum of pair interactions characterized by distinct $\varepsilon_{\mathrm{LJ}}^{\alpha\gamma}$ and $\sigma_{\mathrm{LJ}}^{\alpha\gamma}$ weighted by density profiles.

However, if we apply LMF theory only to charge-charge interactions, a substantial simplification that appeals to electrostatics may be achieved by leveraging the observation by Chen and Weeks [15] that a single σ for all charged interactions proves most useful and successful. With this observation, each $u_{1,\alpha\gamma}(r)$ may be written as

$$u_{1,\alpha\gamma}(r) = \frac{q_\alpha q_\gamma}{\epsilon}\frac{\operatorname{erf}(r/\sigma)}{r} = \frac{q_\alpha q_\gamma}{\epsilon} v_1(r). \tag{4.2}$$

Thus Eq. (4.1) may be written exactly as

$$\phi_R^{(\alpha)} = \phi^{(\alpha)}(\mathbf{r}) + \frac{q_\alpha}{\epsilon}\int d\mathbf{r}' \left(\sum_\gamma q_\gamma \rho_{R,\gamma}(\mathbf{r}')\right) \cdot v_1(|\mathbf{r}-\mathbf{r}'|) \tag{4.3}$$

$$= \phi^{(\alpha)}(\mathbf{r}) + \frac{q_\alpha}{\epsilon}\int d\mathbf{r}'\, \rho_R^q(\mathbf{r}') \cdot v_1(|\mathbf{r}-\mathbf{r}'|), \tag{4.4}$$

using the natural definition of charge density as

$$\rho^q(\mathbf{r}) = \sum_\gamma q_\gamma \rho_\gamma(\mathbf{r}). \tag{4.5}$$

Noting as did Chen and Weeks [15] that $\phi^{(\alpha)}$ may be due to both electrostatic and nonelectrostatic components, we separate $\phi^{(\alpha)}$ as

$$\phi^{(\alpha)}(\mathbf{r}) = \phi_{\mathrm{ne}}^{(\alpha)}(\mathbf{r}) + q_\alpha \mathcal{V}(\mathbf{r}), \tag{4.6}$$

where $\phi_{\mathrm{ne}}^{(\alpha)}$ encompases nonelectrostatic confinements such as the smooth LJ walls used in Ch. 6 and $\mathcal{V}$ represents the general external electrostatic potential.

This observation naturally leads to the following rewriting of each LMF equation for a species α as

$$\phi_R^{(\alpha)}(\mathbf{r}) = \phi_{\text{ne}}^{(\alpha)}(\mathbf{r}) + q_\alpha \left(\mathcal{V}(\mathbf{r}) + \frac{1}{\epsilon} \int d\mathbf{r}' \, \rho_R^q(\mathbf{r}') \cdot v_1(|\mathbf{r} - \mathbf{r}'|) \right) \tag{4.7}$$

$$= \phi_{\text{ne}}^{(\alpha)}(\mathbf{r}) + q_\alpha \mathcal{V}_R(\mathbf{r}). \tag{4.8}$$

Thus we now have a single rescaled electrostatic potential $\mathcal{V}_R$ defined by one LMF equation in terms of the charge density ρ^q,

$$\mathcal{V}_R(\mathbf{r}) \equiv \mathcal{V}(\mathbf{r}) + \frac{1}{\epsilon} \int d\mathbf{r}' \, \rho_R^q(\mathbf{r}') \cdot v_1(|\mathbf{r} - \mathbf{r}'|). \tag{4.9}$$

As with an external potential energy $\phi(\mathbf{r})$, if $\mathcal{V}$ is due to fixed charge distributions, we may divide $\mathcal{V}$ into $\mathcal{V}_0$ and $\mathcal{V}_1$ as well as define a $\mathcal{V}_{R1}$ as in Sect. 2.4. In Ch. 5 we will harness such a division to explain the success of LMF in treating bulk molecular fluids. Further, we will explore an extension to systems we simulate in Ch. 6 where such a separation is useful. For the moment though, we note that Eq. (4.9) is simply a smoothed electrostatic potential due not to the convolution of the mobile charge density with the Coulomb Green's function $1/r$, but rather to the convolution of the charge density with a smoothed Green's function $\text{erf}(r/\sigma)/r$.

Since $\text{erf}(r/\sigma)/r$ is the potential due to a charge density with a Gaussian profile of width σ, the integral portion of $\mathcal{V}_R$ may be sketched as $\rho^q * \rho_G * 1/r$ where $*$ represents a convolution and

$$\rho_G(\mathbf{r}) \equiv \frac{\exp\left(-r^2/\sigma^2\right)}{\sigma^3 \pi^{3/2}}. \tag{4.10}$$

Thus we exactly rewrite the LMF electrostatic potential from Eq. (4.9) as follows:

$$\mathcal{V}_R(\mathbf{r}) = \mathcal{V}(\mathbf{r}) + \frac{1}{\epsilon}\int d\mathbf{r}'\,\rho_R^q(\mathbf{r}')\cdot v_1(|\mathbf{r}-\mathbf{r}'|) \tag{4.11}$$

$$= \mathcal{V}(\mathbf{r}) + \frac{1}{\epsilon}\int d\mathbf{r}'\int d\mathbf{r}''\,\rho_R^q(\mathbf{r}')\cdot\frac{\exp\left(-|\mathbf{r}'-\mathbf{r}''|^2/\sigma^2\right)}{\pi^{3/2}\sigma^3}\cdot\frac{1}{|\mathbf{r}-\mathbf{r}''|} \tag{4.12}$$

$$\mathcal{V}_R(\mathbf{r}) = \mathcal{V}(\mathbf{r}) + \frac{1}{\epsilon}\int d\mathbf{r}''\,\rho_R^{q_\sigma}(\mathbf{r}'')\cdot\frac{1}{|\mathbf{r}-\mathbf{r}''|}. \tag{4.13}$$

The final equation has the form of a standard definition of the electrostatic potential due to charge density as given in first-year textbooks like Purcell [80]. However, the mobile charge density appearing in the integral of Eq. (4.13) is no longer the charge density due to a simple linear combination of species' density profiles weighted by their valence, but rather a *smoothed* charge density defined as the convolution of the charge density and ρ_G via

$$\rho^{q_\sigma}(\mathbf{r}) = \int d\mathbf{r}'\,\rho^q(\mathbf{r}')\cdot\frac{\exp\left(-|\mathbf{r}-\mathbf{r}'|^2/\sigma^2\right)}{\pi^{3/2}\sigma^3}. \tag{4.14}$$

Thus the LMF equation for long-ranged interactions may be viewed as simply doing classical electrostatics on an *equilibrium*, *smoothed* charge density and defining a single external rescaled electrostatic potential. In fact we may in general represent the LMF equation as a modified Poisson's equation,

$$\vec{\nabla}^2\left[\mathcal{V}_R(\mathbf{r}) - \mathcal{V}(\mathbf{r})\right] = -\frac{4\pi}{\epsilon}\rho^{q_\sigma}(\mathbf{r}), \tag{4.15}$$

based on the smoothed charge density. This point was first made for the uniformly-charged-wall model system by Chen [13], and it is immediately generalizable to the mixture LMF equation dealt with here. Given that the LMF equation for site-site molecules is identical to that for the mixtures as will be shown in Ch. 5, this view

will also apply to most standard molecular simulations. In typical atomistic molecular models, point charges are assigned to sites on molecules as a practical representation of the quantum mechanical electron cloud and nuclear charges. The exact placement of these point charges are quite crucial for the typical local behavior including hydrogen-bonding and polar interactions. However to the extent that long-ranged forces lead to electro*static* effects, it seems counterintuitive to assign too great a weight to the exact placement of these point charges. Gaussian-smoothing of the charge density will wash out a substantial amount of detail associated with the exact location of point charges but leave the relevant accumulations of charge density. Further discussion of this point will be delayed until Ch. 6 in Sects. 6.2, 6.4, and 6.6.

4.2 Other Approaches to Electrostatics

LMF theory and the choice of $1/r$ splitting have connections to various other approaches to electrostatics. In Sect. 4.3, we will briefly discuss connections to Poisson-Boltzmann techniques which include ions implicitly through a charge density profile, but predominantly we will focus on other approaches to electrostatics in simulations. The treatment of electrostatics in simulations is a topic of continued research interest and is also covered in simulation textbooks such as Frenkel and Smit [31]. Given the substantial body of work, it is useful to understand how the LMF approach is similar to and distinct from other electrostatics approaches.

First, we recall some material from Ch. 1. Traditional simulation techniques for short-ranged interactions used the minimum image convention in order to sim-

ulate particles within an infinite system [1, 31]. As depicted for two-dimensions in Fig. 4.1(a), this approach projects periodic images of the main simulation cell out in the x- and y-directions but assumes that particle i interacts only with the nearest image of particle j. The validity of minimum image conventions hinges on the pair interaction potential $w(r)$ becoming numerically small if not exactly zero beyond some cutoff radius R_c that is less than $L/2$.

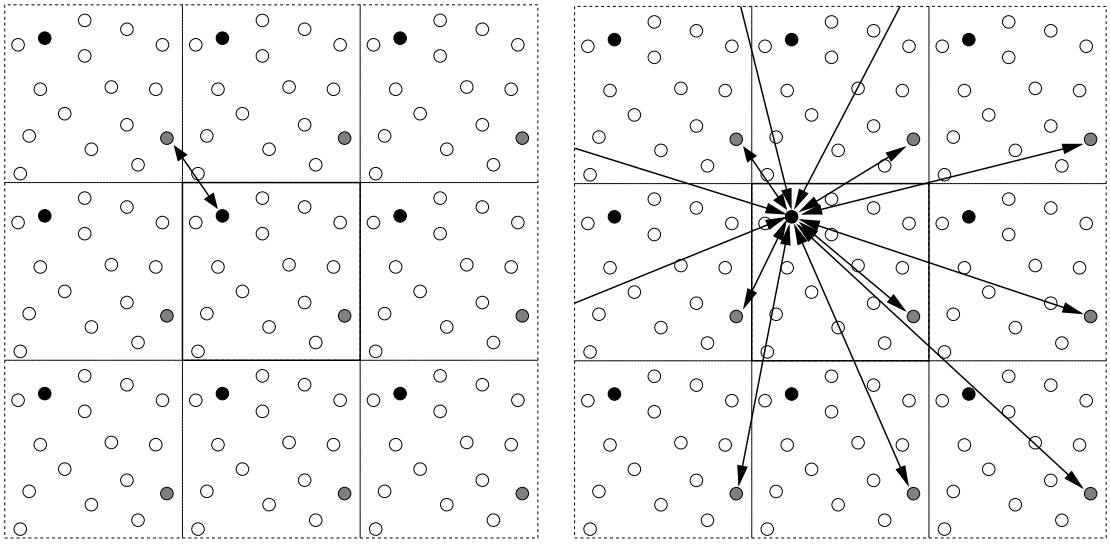

(a) Minimum Image (b) All Images

Figure 4.1: Periodic boundary conditions for simulations are traditionally treated differently depending on whether the particles are charged. The main simulation box in the center is periodically replicated to better represent the isotropic nature of the fluid. Thus there are multiple images of the black and grey particles. For typical short-ranged interactions, the minimum image convention (a) is reasonable, and the black particle in the main simulation cell interacts only with the nearest image of the grey particle. In contrast, when charges are involved, the interaction of the black particle with all periodic images (b) of the grey particle must somehow be included. (This is an exact copy of Fig. 1.1.

Naïve application of the minimum image convention to Coulomb simulations is highly problematic. Any purely minimum-image technique will neglect important long-ranged interactions. But even more problematically, the $1/r$ interaction decays

so slowly that it will never be sufficiently numerically small. In Sect. 4.4, several intelligent manners to spherically truncate $1/r$, not dissimilar to $v_0(r)$, will be discussed. However, such truncations are problematic in nonuniform geometries without a $\mathcal{V}_R$. Often simulators rely on a picture similar to that in Fig. 4.1(b) where each particle must interact with all periodic images of other particles. As such, lattice-sum approaches described in Sect. 4.6 rely on taking the periodic replication of simulations cells quite seriously and devising manners of exactly summing these interactions across the periodic lattice so that it is quickly convergent. As the figure suggests, this periodic lattice picture is less than fluid-like. Some research involves finding ways to make such series summations more "isotropic" in nature to better represent fluids, as discussed Sect. 4.6.3 [55, 111]. In the context of these simulation approaches, LMF theory could be viewed as conceptually combining spherical truncation approaches with a long-ranged electrostatic potential that very naturally encompasses the liquid-like nature of the surroundings through a convolution of interactions with the equilibrium density profile.

4.3 Poisson-Boltzmann Techniques

Poisson-Boltzmann (PB) techniques treat electrostatics by assuming that charged particles are essentially ideal gas particles responding to an electrostatic potential generated by the equilibrium charge density of the particles.

In general for a solution of n charged species, this may be expressed as [69]

$$\vec{\nabla}^2 \mathcal{V}_{\mathrm{PB}}(\mathbf{r}) = -\frac{4\pi\rho^q(\mathbf{r})}{\epsilon} = -\frac{4\pi}{\epsilon}\sum_{i=1}^{n}\rho_i q_i e^{-\beta q_i \mathcal{V}_{\mathrm{PB}}(\mathbf{r})}. \tag{4.16}$$

Often, the Poisson-Boltzmann equation is linearized leading to the Debye-Hückel equation instead [37]. Linearizing the exponentials results in

$$\begin{aligned}\vec{\nabla}^2\mathcal{V}_{\mathrm{DH}}(\mathbf{r}) &= -\frac{4\pi}{\epsilon}\sum_{i=1}^{n}\left(\rho_i q_i - \beta\rho_i q_i^2\mathcal{V}_{\mathrm{DH}}(\mathbf{r})\right) \\ &= \mathcal{V}_{\mathrm{DH}}(\mathbf{r})\sum_{i=1}^{n}\frac{4\pi\rho_i q_i^2}{\epsilon k_B T} = \kappa_D^2\mathcal{V}_{\mathrm{DH}}(\mathbf{r}),\end{aligned} \tag{4.17}$$

where the Debye length L_D is $1/\kappa_D$. For the two-wall model system previously examined in Ch. 3, linearization is not necessary for easy solution. The analytical expression for the density profile in the Poisson-Boltzmann approximation was given in Sect. 3.1.

Poisson-Boltzmann techniques with varying ϵ have often been used to map out electrostatic potentials on biomolecular surfaces based on the success of programs such as DelPhi, developed by Honig and coworkers [39, 84]. However, Poisson-Boltzmann approaches have a serious flaw in that the core interactions between particles are treated in a mean-field sense just like the long-range interactions. For dilute systems where the Coulomb interactions are weak and particles rarely come into contact with one another, the PB approach is consistent and gives the exact Debye-Hückel limiting law, but for many systems this neglect of pair correlations causes severe problems. For the wall model systems this neglect is catastrophic since the attraction between two walls is due to counterion correlations. Essentially, by including the full core repulsions, configurations where particles are strongly repulsive get included in the mean field average of the potential even though in the real system, the conditional singlet density indicates that such configurations do not occur very often.

Various corrections to the Poisson-Boltzmann approach have been proposed. A

recent example is correlation-corrected Poisson-Boltzmann (cPB) theory as devised by Forsman [30]. In the cPB approach, the core Coulomb interactions are diminished for all $r < R_c$ in the Poisson-Boltzmann equation, essentially creating a correlation "hole" and to avoid the overcounting of strong core repulsions. The approach was quite successful, and there are many similarities between cPB and the MPB approach for walls which was described in Chen and Weeks [15]. One of the reasons that the MPB approximation was so successful is because it also has this effective correlation hole included in its Boltzmann average. However, cPB has rather *ad hoc* choices of correlation core sizes and of the functional form of the remaining long-ranged interactions. Additionally, in scenarios where cPB is not as successful, ways to improve the approach are not clear. In contrast, LMF theory provides a solid framework on which to justify functional forms and to show avenues of improvement beyond the mean field Poisson-Boltzmann level.

4.4 Spherical Truncation Techniques

Current work is still devoted to ways to spherically truncated $1/r$. Each approach yields pair potentials without discontinuities in energy and force. For *uniform* Coulomb systems, these truncations are quite similar to the strong coupling approximation of LMF theory where all particles interact via $v_0(r)$ without any further modification of a $\mathcal{V}_{R1}$. While this discussion of spherical truncation techniques is certainly not meant to be comprehensive, it will hopefully give a flavor of the wide variety of truncations used and available in the literature.

Other researchers may prefer an alternate choice of $v_0(r)$ than the one proposed herein. In a certain sense, provided that $v_0(r)$ is sufficiently large to encompass the core interactions and the remaining $v_1(r)$ is slowly varying over those interactions, then another choice of $v_0(r)$ is reasonable. However, given that the choice of $v_1(r) = \mathrm{erf}(r/\sigma)/r$ optimally leads to a perturbation which is slowly-varying in r-space and localized to small k-values simultaneously in reciprocal space, likely the choice of $v_0(r)$ used here is well-posed for LMF. Also, any choice of spherical truncation will still yield difficulties in a slab geometry without an appropriate $\mathcal{V}_R$.

4.4.1 Shifted Force Truncations

Shifted force truncations are algebraically the simplest manner of obtaining zero energy and force at the cutoff radius. For all $r < R_c$, a linear function is subtracted from the potential as follows,

$$v_{\mathrm{SF}} = \left\{ \frac{1}{r} + \frac{r}{R_c^2} - \frac{2}{R_c} \right\} \Theta(R_c - r). \tag{4.18}$$

$\Theta(x)$ is the Heaviside step function. As shown in Fig. 4.2, this potential goes to zero at R_c quite smoothly. However, the neglected portion of the potential does not have a force that approaches zero for small r. Rather a constant force is subtracted from all points in the potential.

4.4.2 Site-Site Reaction Field

The reaction field approach for charged systems is an extension of Onsager's original reaction field derived for a dipolar point particle with radius R_{RF} in a dipolar fluid

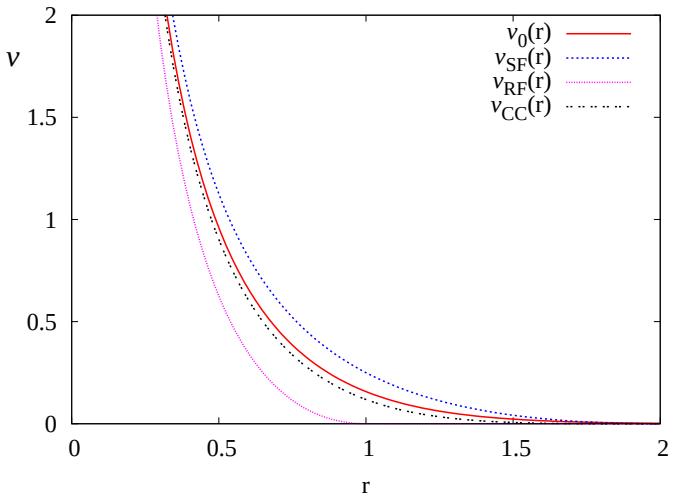

Figure 4.2: Plot of $v_0(r)$, $v_{\rm SF}(r)$, $v_{\rm RF}(r)$ and $v_{\rm CC}(r)$. $\sigma = 1.0$, and R_c for $v_{\rm SF}(r)$ is 2.0, a point where $v_0(r)$ is small. $R_{\rm RF} = 1.0$ for both $v_{\rm RF}$ and $v_{\rm CC}(r)$.

approximated as a dielectric continuum [76].

The ion-ion interaction under reaction field may be mapped from $1/r$ to

$$v_{\rm RF} = \left\{ \frac{1}{r} + \frac{r^2}{2R_{\rm RF}^3} - \frac{3}{2R_{\rm RF}} \right\} \Theta(R_{\rm RF} - r) \tag{4.19}$$

with $\epsilon = \infty$ to represent a conducting solution. This potential is also plotted in Fig. 4.2.

While alternate derivations by writing Onsager's reaction field in tensorial form are possible [45, 74], this expression may also be derived in a manner more evocative of LMF theory's $v_0(r)$. Solving for the interaction between one point charge and another point charge completely neutralized by a uniform distribution of charge within a sphere of radius $R_{\rm RF}$, as depicted in Fig. 4.3(a), also yields $v_{\rm RF}(r)$ [46].

A goal of further smoothing the interaction at $R_{\rm RF}$ motivated an extension of reaction field based on charge distributions to lead to an even more smoothly truncating potential. As described in [46, 47], such a potential may be derived by looking at the

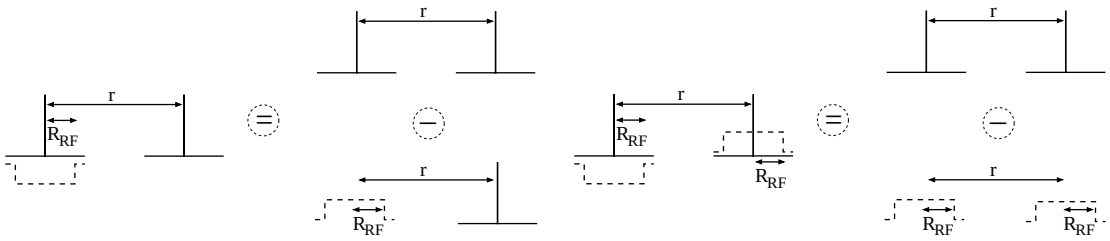

(a) Reaction Field (b) Charged Cloud

Figure 4.3: Depiction of charge distributions leading to (a) the reaction field potential and to (b) the charged cloud potential. The left portion depicts the single charge density set leading to the interaction energy. The right portion translates this to two delta functions interacting (leading to $1/r$) minus two other charge densities interacting, in a fashion similar to the LMF definition of $v_0(r)$.

interactions between one point charge with a uniform compensating spherical charge cloud and another point charge with a uniform *matching* spherical charge cloud as shown in Fig. 4.3(b). The charge distribution described may seem mysterious since one charge was neutralized and the other was augmented. However, as qualitatively shown these interactions are equivalent in r-space to taking the interaction between two point charges and subtracting out the interaction between two smoothed spheres of charge.

This description may be connected to the derivation of $v_0(r)$ for LMF applied to Coulomb systems. $v_0(r)$ may be viewed as $1/r$ with the interaction between a point charge and Gaussian charge distribution of width σ subtracted out, or alternately as $1/r$ with the interaction between two Gaussian charge distributions of width $\sigma/\sqrt{2}$ subtracted out. In some sense $v_0(r)$ is the ultimate symmetrization of charge distribution interactions because two different manners of "smoothing" the charge interactions lead to an identical functional form.

Despite similarities in the charge distribution derivation, reaction field approaches are motivated predominantly by finding a reasonable approximation to nearest-neighbor pair interactions in a *uniform* system, and there does not exist a manner to include long-ranged effects when needed. Similar issues exist with the less physically motivated shifted force truncations [28, 93, 114]. Any simple spherical truncation will fail in situations where net addition of forces in the normal z-direction due to particle density spanning x and y to infinity can lead to nontrivial effects due to the longer-ranged forces.

4.4.3 Generalized Reaction Field

Tironi *et al.* [96] developed a generalization of the reaction field approach to include both contributions from a dielectric continuum and also a salt solution. At times in the literature, generalized reaction field is used to refer to the "charged cloud" approach of Hummer *et al.* [46] described previously, so careful checking of references is required when interpreting the "reaction field" approach used in a paper.

The basis of this approach lies in defining a cutoff radius R_{RF} such that $\epsilon = \epsilon_1$ within the radius and $\epsilon = \epsilon_2$ outside the cutoff radius. Then Poisson's equation within R_{RF} is matched to a linearized Debye-Hückel solution for the given ionic strength outside R_{RF}. The resulting force equation simplifies to the reaction field expression given previously in the limit of either high ionic strength or infinite ϵ_2.

This approach to spherically-truncated pair interactions has been used in simulations of large biomolecules where the time scales of folding and unfolding are so

large that more detailed series summation techniques are prohibitively expensive [91]. Recent detailed comparisons have found that such an approach is not unreasonable for determining free energy surfaces when compared to Ewald summation [83].

4.4.4 Wolf Method

Another spherical truncation approach has been colloquially termed "Wolf sums." The original idea results from calculating energies in ionic crystals [109]. Wolf [109] observed that standard sums of Coulomb energies may rapidly converge with the observation that a given lattice region of one type of particle is neutralized by a slightly shifted "mirror" lattice of opposite charges. This has been generalized to fluids [110] by placing a neutralizing shell of charge at a cutoff radius R_c for each interacting charge within R_c. For example if a $+1$ charge is surrounded by a total charge of -1, then no neutralizing shell of charge is required. If, instead, the total charge within a distance of R_c away from the $+1$ charge is -2, then a shell of charge $+1$ would be placed at R_c in order for the sphere centered about the $+1$ charge to be net neutral. However, the authors found that this sum in fluids did not quickly converge as R_c was increased unless $1/r$ is also multiplied by a so-called "damping" function. Not coincidentally the damping function is $\mathrm{erfc}(r/\sigma)$, leading to our choice of $v_0(r)$ as the attenuated interaction between point charges.

Given the historical path of the development of the Wolf method, focus is often applied to the quasi-summation technique used within the cutoff radius. This approach has led to success for a variety of systems [20, 29, 63, 66, 115]. However we

suggest that the key to the success is *not* the summation approach applied to model neutral spheres of charge, but rather the damping function employed almost as an afterthought. In fact our accurate structural results for bulk water shown in Sect. 5.3 suggest that the damping $\mathrm{erfc}(r/\sigma)$ is actually the reason for much of the success of the Wolf method in liquids.

4.4.5 Force Matching

A final spherical truncation technique used in a recent paper on Coulomb interactions involves matching the forces due to a short-ranged potential with those due to Ewald sums in a least-squares sense [50]. The authors focus substantial attention on the ability of this force-matching technique to determine a $v_{\mathrm{FM}}(r)$ which yields quite accurate structure and thermodynamics. However examination of their analysis shows that some spherical truncation approaches used as comparison in this paper do not neglect a sufficiently slowly-varying potential. Thus we would not expect the corresponding short-ranged potentials to yield accurate structures. In one case, the authors do chose a $v_s(r)$ which is quite similar to our $v_0(r)$ chosen in Sect. 5.3; however they observe that the thermodynamic results are not as accurate. We show in Sect. 5.3.4 that accurate thermodynamic properties may be obtained by applying a simple perturbation approach to the calculation of energies and pressures.

In our view, the essence of the success of this force matching lies in the idea that the long-ranged forces cancel in a spherical sense for these essentially uniform systems. While this point in not emphasized, the authors do note that "corrections will likely

be necessary for inhomogeneous environments such as interfaces [50]." In the LMF view, this means that some sort of $\mathcal{V}_R$ must be included. In fact, as observed in the previous chapter, slab geometries require substantial $\mathcal{V}_R(z)$ due to net addition (rather than cancellation) of long-ranged forces. Every single spherical truncation approach described thus far would fail in a slab geometry without a correction similar to $\mathcal{V}_R$.

4.5 External Potential Method

The external potential method (EPM) was developed two decades ago as a heuristic algorithm to account for this net additive force due to the long-ranged images. The first signs of this approach may be found in Guldbrand *et al.* [36], and the general approach typically used is detailed in Valleau *et al.* [99]. Referring back to Fig. 4.1(a), in EPM, each particle i in the main simulation cell interacts with the nearest image of each remaining particle j via full $1/r$ interactions. Additionally, each particle i exists in a self-consistent external field $\mathcal{V}_{\mathrm{EPM}}(z)$ defined as

$$\mathcal{V}_{\mathrm{EPM}}(z) = \int_0^d \rho(z';[\phi_{\mathrm{EPM}}])v_{plate}(z'-z)\,dz' \tag{4.20}$$

where v_{plate} is the electrostatic potential generated by a plate of charge infinite in x- and y-extent with a square with area equal to the cross-section of the simulation box centered about particle i subtracted out. ϕ_{EPM} is self-consistently linked to $\rho(z)$ much as ϕ_R and ρ_R are linked in local molecular field theory. However EPM includes the long-ranged effects of force addition solely as an algorithm without any physical underpinning, so the extension to more general geometries is not clear. Also, perhaps more problematically, the separation between short- and long-ranged interactions is

sharply at the boundary of the minimum image cell – particles interact via full $1/r$ Coulomb interactions within the simulation box square prism of volume $L \times L \times d$ but just beyond that boundary the equilibrated charge density due to image particles exerts a mean external field on each particle. In some senses EPM represents the opposite extreme of spherical truncations – no concern is shown for reasonably cutting off short-ranged interactions and smoothly transitioning to a mean-field average of long-ranged interactions.

4.6 Series Summation Techniques

Series summations approaches such as Ewald summation and Lekner-Sperb summation have become the Coulomb calculation techniques of choice for high numerical accuracy. The conditionally and slowly convergent sum over images $\mathbf{n}$ is

$$U = \sum_{i<j} \frac{q_i q_j}{\epsilon} \sum_{\mathbf{n}} \frac{1}{|\mathbf{r}_i - \mathbf{r}_j - \mathbf{n}|}. \tag{4.21}$$

The basic idea of summation techniques is to rewrite the slowly convergent sum of $1/r$ pair interactions in a way that the sum is rapidly convergent. Such a sum's convergence is still conditional on the order of the summation and depends on assumptions about the sample's macroscopic shape and boundary conditions. This point will be crucial when we consider attempts to use a three-dimensional sum to treat slab geometries shortly.

Below we will discuss a few manners of rewriting this conditionally convergent summation. Since these summation techniques are the "gold standard" of approaches for Coulomb interactions, they serve as our "experimental" data throughout this the-

sis. The following is not meant to be a comprehensive discussion of these summation techniques but rather a manner of highlighting some of the approaches used as benchmarks for the performance of LMF in this thesis.

4.6.1 Three-Dimensional Lattice Sums

For three-dimensional periodicity, Ewald summation involves rewriting the sum with real-space terms $\mathrm{erfc}(\alpha r)/r$ and Fourier-space terms $\exp(-k^2/4\alpha)/k^2$, the transform of $\mathrm{erf}(\alpha r)/r$. In these functions, α is simply a parameter that alters the extent to which the $1/r$ interaction is computed in the real space sum or in the reciprocal space summation. As α is increased, the k-space summation includes a greater extent of the interactions and the r-space sum includes less. The Ewald rewriting of the lattice sum is as follows [31]:

$$\begin{aligned} U_{\mathrm{EW}} = & \sum_{i<j} \frac{q_i q_j}{\epsilon} \frac{\mathrm{erfc}(\alpha r_{ij,\mathrm{MI}})}{r_{ij,\mathrm{MI}}} \\ & + \frac{1}{2\pi V} \sum_{i=1}^{N} \sum_{i=j}^{N} \sum_{\mathbf{k}\neq 0} q_i q_j \frac{4\pi}{k^2} \exp\left(\frac{k^2}{4\alpha}\right) \cos(\mathbf{k}\cdot\mathbf{r_{ij}}) \\ & - \frac{\alpha}{\sqrt{\pi}} \sum_{i=1}^{N} q_i^2 + J(\mathbf{M}, P). \end{aligned} \tag{4.22}$$

The first term is simply a sum over the real-space interactions between pairs of particles for the minimum image (MI). Writing the first term in this fashion requires a choice of α that is sufficiently large that the neglect of $\mathrm{erfc}(\alpha r)/r$ beyond some cutoff radius that is less than half the width of the simulation box is reasonable. The second term is the sum over the long-ranged lattice interactions calculated in Fourier space. The number of k-vectors included in the sum depends on the degree of precision de-

sired and the choice of α. For a desired precision, more k-vectors must be included the larger that α is. The third term is a self-interaction term corresponding to the interaction of a particle with the images of itself being subtracted out. The fourth term represents an energy term that depends on both the polarization $\mathbf{M}$ of the simulation cell and the assumptions about the macroscopic shape P of the sample as nicely discussed in [114]. For three-dimensional Ewald sums programmed into most molecular dynamics programs, including DLPOLY as used later on [90], the assumption is that the macroscopic sample is a sphere, composed of a three dimensional lattice of cells, embedded in conducting medium. In these instances, $J(\mathbf{M}, P) = 0$. The rewritten sum given in Eq. (4.22) along with an appropriate choice of α allows one to track real-space interactions only over the minimum image and to treat the Fourier-space sums to reasonable accuracy with only a finite number of k-space lattice vectors.

Given the similarity of the three-dimensional Ewald summation's k-space term to $v_1(r)$ in LMF theory, comparisons between LMF theory and Ewald summation are inevitable. In fact the long-ranged contribution $\mathcal{V}_{R1}$ in LMF theory may be viewed as a Boltzmann-weighted average of the k-space sum in Ewald summation [21]. However there is a significant mathematical and philosophical difference between LMF theory and any series summation technique. In LMF theory, our focus is on separating the Coulomb interaction itself, and these long-ranged interactions only contribute to an overall mean field in which the short-ranged mimic particles interact. In Ewald summation, as in all series summation techniques, all interactions, both the longer-ranged and shorter-ranged parts are meant to be accounted for at every step in a simulation, and the details of the periodic boundary conditions play an

important role. While the α in Eq. (4.22) is equivalent to $1/\sigma$ in the LMF functional forms, no emphasis is placed on core interactions versus slowly-varying interactions in the implementation of Ewald sums. The choice of α is made either to minimize computational time or to allow the same choice of cutoff radius for the real-space part of the Ewald sum and for other interparticle interactions. This means that the physical meaning of $v_0(r)$ and $v_1(r)$ is often lost when using Ewald sums.

A wide variety of other lattice-like sums exist such as the fast multipole method and particle mesh techniques as summarized in [31]. While series summation techniques are more exact in accounting for explicit periodic long-ranged contributions than the LMF approach, one could also argue that the series summation technique is overly-dependent on the existence of periodic boundary conditions, which real ionic systems never have. For example the potential of mean force between two interacting ions in an explicit solvent exhibits artifacts of periodicity using Ewald summation [48]. The reliance of series summation techniques on periodic boundary conditions make them hard to implement for more general geometries, and even simple planar geometries such as the two-wall system still cause computational problems, with even more problems arising from more general geometries.

4.6.2 Lattice Sums in Slab Geometries

The nonuniform systems considered in this thesis have a slab-like geometry which is represented by nonuniformity in the z-direction and periodic replication in the x- and y-directions. Various versions of Ewald summation exist for this geometry, some gen-

eral and quite complex and expensive (two-dimensional Ewald) and others cheaper but more limited in applicability (Hautmann-Klein Ewald) [93, 114]. Here we discuss the two lattice sum approaches used for our benchmarks in slab-like geometries, Lekner-Sperb summation and corrected three-dimensional Ewald sums. There is certainly other recent research on lattice sums for such geometries [19, 23], but each of these approaches is still inherently a lattice summation, with all the difficulties and complexities that entails.

Lekner-Sperb summations [60, 92] were employed in the simulations used as a benchmark [71] for the previous chapter on the two wall problem. We will summarize the treatment as described by Moreira and Netz [71] for the charged-wall system.

For the single charged-wall system with neutralizing point counterions confined to $z \in (0, \infty)$ and with coupling strength ξ defined as in Eq. (3.6), the periodic sum in Eq. (4.21) may be rewritten using Lekner summation as

$$\tilde{U} = \frac{\xi}{\tilde{L}} \sum_{i<j} v_L(\hat{x}_{ij}, \hat{y}_{ij}, \hat{z}_{ij}) + \sum_{i=1}^{N} \tilde{z}_i - \frac{\ln(2)}{2\sqrt{2\pi}} \sqrt{\xi} N^{3/2} \tag{4.23}$$

where the tilde indicates reduced units (L_G for length and $k_B T$ for energy) and a hat indicates lengths scaled by the lateral simulation box size L in lieu of L_G. For the two-wall system, the second term representing the potential due to wall-particle interactions becomes a constant. The definition of v_L contains the now rapidly convergent summation rewritten with cosines and Bessel functions as

$$\begin{aligned} v_L(\hat{x}, \hat{y}, \hat{z}) = C &- \ln\left[\cosh(2\pi\hat{z}) - \cos(2\pi\hat{y})\right] \\ &+ 4 \sum_{l=1}^{\infty} \cos(2\pi l \hat{x}) \sum_{m=-\infty}^{+\infty} K_0\left(2\pi l \sqrt{(\hat{y}+m)^2 + \hat{z}^2}\right). \end{aligned} \tag{4.24}$$

The constant C containing terms related to an arbitrary reference state chosen in the derivation of Lekner sums and a further constant representing the self-energy of particles (scaling as N) have been neglected. The neglect of these configuration-independent constants will have no impact on acceptance ratios in the Monte Carlo scheme nor on $\langle U \rangle / N$ which was used to gauge convergence of simulations with respect to N in Moreira and Netz [71]. The sum in Eq. (4.24) is quickly convergent at large distances between particles due to the rapid decay of K_0 for large arguments; due to the divergence of K_0 for small arguments, the sum is rewritten for small $\sqrt{(\hat{y}+m)^2+\hat{z}^2}$ as recommended by Sperb [92]. This further rewriting of the sum depending on the magnitude of the argument of K_0 makes the expression of energy using Lekner-Sperb summation even more complicated.

Lekner-Sperb summations as summarized in Moreira and Netz [71] are as complicated function-wise as two-dimensional Ewald sums. One advantage posed by Lekner-Sperb summation is that the general manner in which the equations are derived is the same regardless of degree of periodicity.

Given the complexity of writing two-dimensional sums and the corresponding computational cost, a popular alternative for slab geometries is to carry out three-dimensional sums with sufficient vacuum space between slabs in the z-direction, as shown in Fig. 4.4. The justification for this idea is that the vacuum space decouples the images in the z-direction. However, Spohr [93] shows that such three-dimensional sums incorrectly treat long-ranged forces in the z-direction.

Spohr [93] correctly recognized that particles separated in the z-direction by a distance greater than $\max(L_x, L_y)$ should essentially exert the force due to a uniform

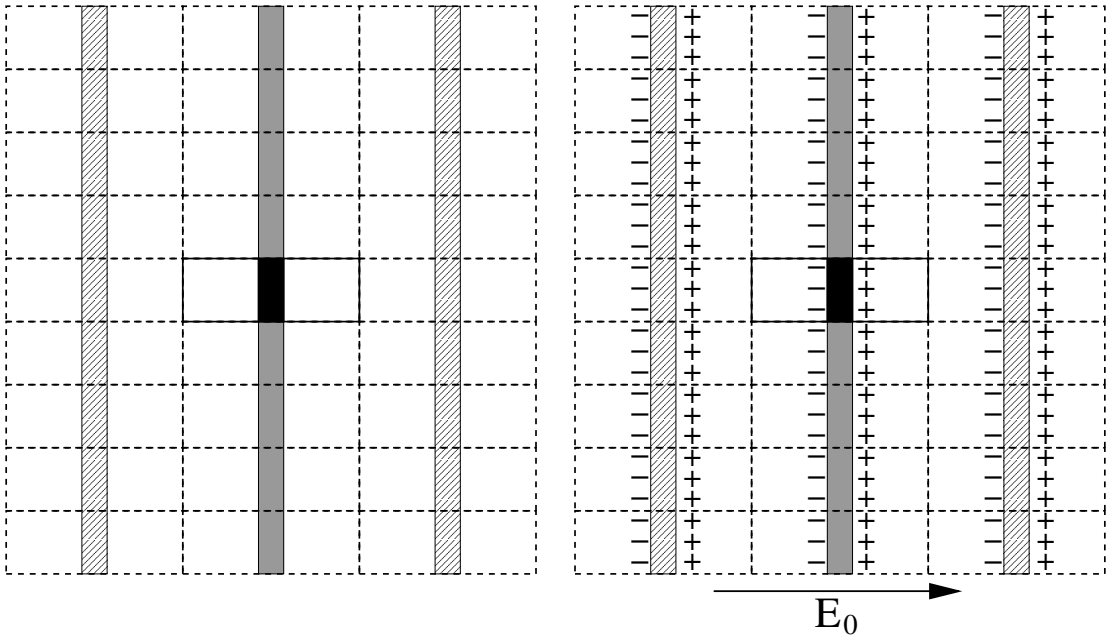

(a) General slab geometry (b) Applied Field

Figure 4.4: Demonstration of implementation of a two-dimensional slab geometry using three-dimensional replication. In each, the desired slab system including periodic repeats in the y direction (x is normal to the page) is the dark grey vertical line. The black portion in the center represents the molecules in the actual simulation cell. The white space corresponds to vacuum between images in the z-direction. (a) depicts a typically used simulation setup. Despite the long-ranged forces being wrong in detail [93], the symmetry of the system about $z = 0$ means that the equilibrium properties of this system are reasonable. In contrast, if an electric field is applied as in (b), typical three-dimensional Ewald sums fail spectactularly and one must at a minimum apply the slab correction developed by Yeh and Berkowitz [114].

plate of charge on each other. The reason for this is that at such large distances, the particles and their images in the x- and y-directions should essentially exert solely z-directional forces on each other. When analyzing the force between particles for spherical truncations and also for simple three-dimensional Ewald sums with what might be considered sufficient vacuum space, Spohr [93] found that neither approach converged to this force at large z-separations while two-dimensional Ewald sums did. Traditional three-dimensional Ewald sums are very slowly convergent as the vacuum space is increased. Often, such concerns do not have structural implications since the average polarization of the cell is zero and these long-ranged interactions average out. The $G(z, z')$ for LMF theory does have exactly this limit of constant force for large $|z - z'|$ as discussed in Sect. 3.2.

Yeh and Berkowitz [114] developed a correction to this three-dimensional approach to the slab geometry which correctly leads to this "parallel-plate" limit at large normal distances. They used this approach to treat a slab of water with an applied electric field, a situation where standard three-dimensional sums fail. The essence of their approach was realizing that a macroscopic spherical shape immersed in a medium of infinite dielectric constant was a very poor assumption for a slab-like geometry. By instead assuming a geometry that is infinitely thin in the z-direction immersed in a vacuum, the shape term J is determined to be

$$J(\mathbf{M}, P) = \frac{2\pi}{V} M_z^2 = \frac{2\pi}{V} \left(\sum_{i=1}^{N} q_i \, z_i \right)^2 , \tag{4.25}$$

and the force term is

$$- \frac{\partial J}{\partial z_i} = - \frac{4\pi}{V} q_i M_z , \tag{4.26}$$

scaling as N. With this simple term included in the standard equation for the three-dimensional Ewald sum, the long-ranged "parallel-plate" forces converge much more quickly with the increase of vacuum separation. This approach does still make an assumption of an infinitely thin slab, and newer slab approaches attempt to minimize the error in this assumption [19]. However, the simplicity of this approach makes it appealing as a slab benchmark for our later systems.

4.6.3 Isotropic periodic sums

The final electrostatic approach we will discuss is a newer approach to series summation techniques which attempts to address the lack of "fluidity" in assuming an exactly replicating periodic lattice of simulation cells [111]. We will not discuss the details of the derivation or the resulting formulae; however, it is interesting to see how this rather complex technique with unusual spherical and cylindrical images makes the LMF approach seem relatively simplistic and more general in contrast.

For an isotropic, bulk-like fluid, the assumption is that there exists some spherical local region delineated by R_c as for spherical truncations. The isotropic periodic sum (IPS) essentially carries out the summation over spherical-shell images (rather than traditional periodic images). While this approach is motivated as a summation technique, for bulk-like systems, it effectively results in a spherically truncated approach much as for the Wolf method discussed previously. In order to treat a slab-like image, using the IPS formalism, a cylindrical local region is used rather than a spherical region [111].

The IPS approach is possible for both Coulomb interactions and also LJ interactions. For LJ interactions, this allows an accurate treatment of the hexadecane liquid-vapor surface tensions with small cutoff radii. However, the authors do acknowledge that the IPS approach is expensive for broad slabs, for then interactions for all pairs in a cylinder must be calculated. Further their approach is not applicable to liquid-liquid interfaces. Therefore, in such instances, they use particle mesh Ewald for charge interactions [55]. In contrast, the LMF approach allows us to treat slabs using spherical truncations and still include long-ranged forces. There is no need to consider various shapes for "local regions." Regardless of the system geometry, the "local region" considered by LMF is spherical, but the long-ranged forces are included by solving the modified Poisson's equation described in Sect. 4.1.

Chapter 5

Generalization of LMF Theory to Molecules

While the application of LMF theory to the model charged systems dealt with previously in this thesis and in other works [14, 15, 22, 86] has been useful, the reality is that if LMF theory is going to be helpful in typical simulations, we must expand the approach to molecular systems. In particular, we must first show that the LMF theory proposed thus far is still reasonable for typical molecular simulation models. We will also explore an initial application to a model of bulk water called the extended simple point charge (SPC/E) model for both structure and thermodynamics.

5.1 LMF Equation for Molecules via Moments

As proposed by Chen in her thesis [13] and later in [15], one route to treat molecular interactions lies in splitting intermolecular electrostatic interactions based on their lowest nonzero moment. Thus, for water-water interactions, the appropriate pair interaction to split into short- and long-ranged would be the dipole-dipole interaction. As such, for two different dipoles $\mathbf{p}_i$ and $\mathbf{p}_j$ separated by position vector $\mathbf{r}_{ij}$ and angle difference $\mathbf{\Omega}_{ij}$, the $u_1(\mathbf{r}, \mathbf{\Omega})$ would be

$$u_1^{dd}(\mathbf{r}_{ij}, \mathbf{\Omega}_{ij}) = (\mathbf{p}_i \cdot \vec{\nabla})(\mathbf{p}_j \cdot \vec{\nabla}) \left(\frac{\mathrm{erf}(r/\sigma)}{\epsilon r} \right). \tag{5.1}$$

And then the short-ranged $u_0^{dd}(\mathbf{r})$ would be defined as

$$u_0^{dd}(\mathbf{r}_{ij}, \mathbf{\Omega}_{ij}) = w(\mathbf{r}_{ij}, \mathbf{\Omega}_{ij}) - u_1(\mathbf{r}_{ij}, \mathbf{\Omega}_{ij}) \tag{5.2}$$

where $w(\mathbf{r}, \mathbf{\Omega})$ contains all intermolecular interactions including the dipolar interactions. For many molecular models the intermolecular interactions may depend not just on the relative angle of dipoles, but also on atom-atom separations.

Given this approach, one may easily derive from the molecular YBG equation given in Appendix A an LMF equation quite similar to the ones we have encountered previously. The LMF equation for a single-component liquid composed of molecular dipoles would be

$$\phi_R(\mathbf{r}\Omega) = \phi(\mathbf{r}\Omega) + \int d\mathbf{r}' d\Omega' \, \rho(\mathbf{r}'\Omega') \cdot u_1^{dd}(\mathbf{r}\Omega, \mathbf{r}'\Omega'). \tag{5.3}$$

The strongest advantage of such a rewriting is that the LMF equation averages over the longest-ranged nonzero multipole moment of the molecule. Thus even if the molecular model for a neutral dipolar molecule consists of point charges situated throughout the molecule, the averaging will solely be over the dipole-dipole interactions, not over the point charge interactions which are present to give accurate short-ranged interactions in addition to the correct net dipole moment. The approach described above for treating molecules may well prove useful for analytical approaches to solving the LMF equation for molecular systems.

However, for simulations, the stark reality is that most force fields, like CHARMM [64] and AMBER [25], rely on assigning point charges to various atomic sites within the molecules. Furthermore, intermolecular interactions are determined in standard simulation packages not by calculating the relative body frames of two different molecules but rather by doing sums of various pairs of those atomic sites. The models are termed site-site molecular models. Thus by defining u_1 in an orientationally depen-

dent fashion, the resulting u_0 must be defined in a similar fashion, drastically altering the character of the intermolecular potential. In addition, the singlet densities used in the molecular LMF equation depend on molecular position and orientation. The simpler site singlet densities depend only on position and also are data more commonly collected in simulation packages.

Therefore, LMF theory will be much more straightforward to integrate into standard simulation packages if instead we divide the long-ranged electrostatics just as we have done before for point charges as

$$\frac{1}{r} = \frac{\mathrm{erfc}(r/\sigma)}{r} + \frac{\mathrm{erf}(r/\sigma)}{r} = v_0(r) + v_1(r), \tag{5.4}$$

and solve the electrostatic equation for $\mathcal{V}_R$ given in Sect. 4.1. Further the rewriting in terms of ρ^q enables one to envision the extension of the LMF equation for use in *more complex* systems where there may be many different single particle densities that could be collected, but only the singlet charge density is required. However, such an approach requires us to reexamine the derivation of the LMF equation, for now the various sites have specific bonds between them.

5.2 Deriving an LMF Equation for Small Site-Site Molecules

We start the derivation with a statement of the YBG equation for a mixture of various site-site molecules. This equation is derived in Appendix A, but we will try to make the general notation clear here. We owe much of the notation to Chandler and Pratt as used in [10, 11], however in some instances we deviate for simplicity of notation. Molecules are indexed by M and variants, and sites on molecules are indexed by

Greek letters like α and γ, as for species in mixtures.

We assume that the potential energy component of the Hamiltonian of the system, $\mathcal{U}$, may be represented by

$$\mathcal{U} = \sum_{M}\sum_{i=1}^{N_M} w_M^*(\mathbf{R_{iM}}) + \sum_{M}\sum_{i=1}^{N_M}\sum_{\alpha=1}^{n_M} \phi^{(\alpha M)}(\mathbf{r_{iM}^{(\alpha)}}) + \frac{1}{2}\sum_{M}\sum_{M'}\sum_{i=1}^{N_M}\sum_{j=1}^{N_{M'}}(1-\delta_{MM'}\delta_{ij})\sum_{\alpha=1}^{n_M}\sum_{\gamma=1}^{n_{M'}} u_{\alpha M\gamma M'}(|\mathbf{r_{iM}^{(\alpha)}} - \mathbf{r_{jM'}^{(\gamma)}}|). \tag{5.5}$$

There are N_M total molecules of each type M, and there are n_M sites on each molecular type M. [1] In the sum above $w_M^*(\mathbf{R_{iM}})$ is meant to represent the intramolecular bonding potential energy for the i^{th} molecule M in position and orientation $\mathbf{R_{iM}}$. Here $\mathbf{R_{iM}} = \{\mathbf{r_{iM}^1}, \ldots, \mathbf{r_{iM}^{n_M}}\}$. While we will mainly treat systems with rigid geometries, which would essentially result in delta-functions for constraints in the partition function, we leave the bonding potential energy function in the current formulation for generality and also greater simplicity. The second term in Eq. (5.5) represents the standard external potential energy function ϕ here applied to each molecular site with a possibly distinct form. The third term represents the summation over all pair interactions between sites on distinct molecules. $u_{\alpha M\gamma M'}(r)$ again allows for distinct pair interactions for each possible site.

For a molecule M, the singlet density profile of a given molecular orientation is described by $\rho_M^{(1)}(\mathbf{R}_M)$, where $\mathbf{R}_M$ represents the positions of all sites on the molecule, and the (singlet) density profile of a site α on the given molecule M is denoted by

[1] Each molecular site is considered unique even if there are multiple sites of the same type. This overcounting of indistinguishable sites is accounted for by a symmetry number in the partition function. Thus SPC/E water would have $n_M = 3$.

$\rho^{(1)}_{\alpha M}(\mathbf{r})$. We may write the YBG equation for a given *site* as

$$-k_BT\vec{\nabla}\left(\ln\rho^{(1)}_{\alpha M}(\mathbf{r})\right) = \int\left(\frac{d\mathbf{R}_M}{d\mathbf{r}^{(\alpha)}_{\mathbf{M}}}\right)\left[\vec{\nabla}w^*_M(\mathbf{R_M})\right]\varrho_{M|\alpha}(\mathbf{R_M}|\mathbf{r}) + \vec{\nabla}\phi^{(\alpha M)}(\mathbf{r}) + \sum_{M'}\sum_{\gamma=1}^{n_{M'}}\int d\mathbf{r}'\rho_{\gamma M'|\alpha M}(\mathbf{r}'|\mathbf{r})\vec{\nabla}u_{\alpha M\gamma M'}(|\mathbf{r}-\mathbf{r}'|) \tag{5.6}$$

Here we also have two conditional densities. $\rho_{\gamma M'|\alpha M}(\mathbf{r}'|\mathbf{r})$ is the equivalent of the conditional singlet density we considered for a singlet component fluid in Ch. 2; here it is the density of site γ on molecule M' at position $\mathbf{r}'$ given that intramolecular site α on molecule M is at $\mathbf{r}$. $\varrho_{M|\alpha}(\mathbf{R_M}|\mathbf{r})$ is the conditional density of a molecular orientation $\mathbf{R_M}$ given that site α on molecule M is at position $\mathbf{r}$. This is inherently an *intra*molecular conditional density. While not stated explicitly in the first integral, the conditional density $\varrho_{M|\alpha}(\mathbf{R_M}|\mathbf{r})$ implies that $\mathbf{r_M}^{(\alpha)}$ is set equal to $\mathbf{r}$ within $w^*_M(\mathbf{R_M})$.

For simplicity in taking differences we note that we may write the long-ranged part of the specific intermolecular pair interactions as

$$u_{1,\alpha M\gamma M'}(r) = \frac{q_{\alpha M}q_{\gamma M}}{\epsilon}v_1(r) \tag{5.7}$$

and as before the short-ranged core interactions will be defined as $u_{0,\alpha M\gamma M'}(r) = u_{\alpha M\gamma M'}(r) - u_{1,\alpha M\gamma M'}(r)$ and will encompass all LJ-like core interactions as well as the usual $v_0(r)$ terms. Furthermore, all bonding potentials will be assumed the same in the mimic and full systems.

Following the standard path to LMF derivation, we take the exact difference between the YBG equation for the full system and the YBG equation for a mimic system, assuming the equality of the singlet density profiles $\rho^{(1)}_{\alpha M}(\mathbf{r};[\phi]) = \rho^{(1)}_{R,\alpha M}(\mathbf{r};[\phi_R])$.

Thus, we find

$$\begin{aligned}\vec{\nabla}\phi_R^{(\alpha M)}(\mathbf{r}) = \vec{\nabla}\phi^{(\alpha M)}(\mathbf{r}) + \frac{q_{\alpha M}}{\epsilon}\int d\mathbf{r}'\rho_R^q(\mathbf{r}')\,\vec{\nabla}v_1\left(|\mathbf{r}-\mathbf{r}'|\right) \\ + \int\cdots\int\left[\vec{\nabla}w_M^*(\mathbf{R_M})\right]\left\{\varrho_{M|\alpha}(\mathbf{R_M}|\mathbf{r};[\phi]) - \varrho_{R,M|\alpha}(\mathbf{R_M}|\mathbf{r};[\phi_R])\right\}\left(\frac{d\mathbf{R}_M}{d\mathbf{r}_{\mathbf{M}}^{(\alpha)}}\right) \\ + \sum_{M'}\sum_{\gamma=1}^{n_{M'}}\int d\mathbf{r}'\left\{\rho_{\gamma M'|\alpha M}(\mathbf{r}'|\mathbf{r};[\phi]) - \rho_{R,\gamma M'|\alpha M}(\mathbf{r}'|\mathbf{r};[\phi_R])\right\}\vec{\nabla}u_{0,\alpha M\gamma M'}(|\mathbf{r}-\mathbf{r}'|) \\ + \frac{q_{\alpha M}}{\epsilon}\int d\mathbf{r}'\left\{\rho_{q|\alpha M}(\mathbf{r}'|\mathbf{r};[\phi]) - \rho^q(\mathbf{r}';[\phi])\right\}\vec{\nabla}v_1\left(|\mathbf{r}-\mathbf{r}'|\right). \qquad (5.8)\end{aligned}$$

Besides taking the differences as before, the sole other shift we have made is writing terms using $v_1(r)$ where possible, and thus having charge densities ρ^q and conditional charge densities $\rho_{q|\alpha M}$ in some terms. The final two terms in the above equation may be neglected for exactly the same reasons as for a simple uniform fluid.

The new integrand unique to molecules is

$$\left[\vec{\nabla}w_M^*(\mathbf{R_M})\right]\left\{\varrho_{M|\alpha}(\mathbf{R_M}|\mathbf{r};[\phi]) - \varrho_{R,M|\alpha}(\mathbf{R_M}|\mathbf{r};[\phi_R])\right\}. \qquad (5.9)$$

This integrand will to a good approximation be zero provided that

$$\rho_M\left(\mathbf{R_M};[\phi]\right) \simeq \rho_{R,M}\left(\mathbf{R_M};[\phi_R]\right). \qquad (5.10)$$

In other words, the densities of specific molecular orientations must be well approximated by the mimic system. For small molecules, this seems like an eminently reasonable approximation, since the prevalence of various relative intramolecular orientations will be dominated by short-ranged interactions and the overall molecular orientation should be quite well approximated given local short-ranged interactions and the long-ranged orientational corrections due to $\mathcal{V}_R$. For large, flexible molecules

similar to those in CHARMM [64] or AMBER [25], a less strict but sufficient approximation will be given in the final section of this chapter.

Assuming that the approximation in Eq. (5.10) is reasonable, we may write the LMF equation for site-site molecular models as

$$\begin{aligned} \phi_R^{(\alpha M)}(\mathbf{r}) &= \phi_{ne}^{(\alpha M)}(\mathbf{r}) + q_{\alpha M}\mathcal{V}_R(\mathbf{r}) \\ \mathcal{V}_R(\mathbf{r}) &= \mathcal{V}(\mathbf{r}) + \frac{1}{\epsilon}\int d\mathbf{r}'\,\rho_R^q(\mathbf{r}')v_1(|\mathbf{r}-\mathbf{r}'|)\,. \end{aligned} \tag{5.11}$$

Each molecular site now moves in a renormalized external potential due to an average charge density that is partially contributed to by it and its bound molecular sites. This might be cause for concern, since implementations of Ewald summation do remove the effect of both the charge itself and these bound charges [89]. However, we argue that this is reasonable since LMF convolutes the *average* charge density, not the instantaneous charge density, with the slowly-varying long-ranged $v_1(r)$.

The equation above is *identical* to the mixture LMF equation as related in Ch. 4. However, the preceding derivation for small site-site molecules helps us to understand that the use of the mixture LMF equation for site-site molecules still is grounded in the YBG equation with solid statistical mechanical approximations.

5.3 Results for a Bulk Fluid

We will apply the site-site LMF equation stated in Eq. (5.11) in the upcoming Ch. 6. However, here we examine the application of the strong coupling approximation (SCA) to bulk water. When we replace the point charge interactions on a water model with $v_0(r)$, we will call this Gaussian-truncated (GT) water, since $v_0(r)$ is the potential

due to a point charge neutralized by a Gaussian charge distribution. As we shall see, GT water is quite accurate in the bulk. Though, given the range of continuing research on spherical truncations for bulk fluids, this should not be surprising. We study the SPC/E model of water [5], an extension of the SPC model [7].

5.3.1 SPC/E Water Model

A diagram of the model is shown in Fig. 5.1. SPC/E stands for simple point charge model/extended, and, as can be seen in the diagram, one dominant feature of the SPC/E model is point charges assigned to the hydrogen and oxygen atomic sites. Furthermore, there is a Lennard-Jones core centered about the oxygen site. The LJ core has a σ_{LJ} of 3.166 Å. If a LJ fluid characterized by that core size were at the bulk density of water, the reduced density $\rho\sigma^3_{\mathrm{LJ}}$ would be 1.06, an incredibly high density. Also, the first peak in the oxygen-oxygen radial distribution function is located at approximately 2.7 Å - 2.8 Å, well within σ_{LJ}. The SPC/E model may be understood as frustrated ion pairing between O and H sites; the combination of the push of the LJ core with the pull of the oppositely-charged attractions results in

- hydrogen-bonding,
- a liquid structured as essentially a random tetrahedral network,
- the correct packing,
- long-ranged electrostatics such as dipoles, and
- many relevant thermodynamic properties.

As suggested by the striking list of behavior captured by the geometry, three point charges, and a LJ core, the balance of forces is quite delicate.

There are many competing models of water [35], but in essence most are similar. There are slightly different geometries, charges, and choices of σ_{LJ}, but the appropriate parametrization has a relatively tight "sweet-spot" that relies on a delicate balance between like-charged attraction and the LJ core repulsion to yield an array of properties. Thus, while SPC/E may not be the most advanced water model available, it is a reasonable representative of the general class and is used by many researchers who are expert in molecular simulation.

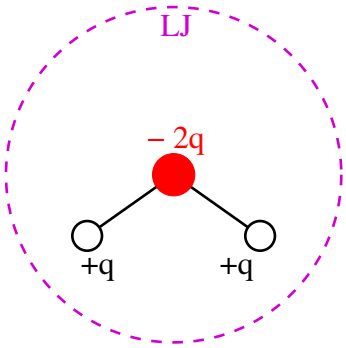

Figure 5.1: Diagram of SPC/E model of water. The OH bond length is set to 1.0 Å, and the bond angle is an idealized 109.5°. Oxygen sites have a charge of -0.8476 e_0 and hydrogen sites have a charge of $+0.4238$ e_0. Additionally a LJ core is centered on the oxygen with $\sigma_{\mathrm{LJ}} = 3.166$ Å and $\varepsilon_{\mathrm{LJ}} = 0.650$ kJ/mol.

5.3.2 Simulation Details

NVT molecular dynamics (MD) simulations of a cubic box of 1728 water molecules were carried out in a cubic box with side length 37.27 Å using the DLPOLY2.16 package [89]. The timestep was 1.0 fs and the temperature of 300 K was maintained by a Berendsen thermostat [6] with a time constant of 0.5 ps. The simulations were equi-

librated for 500 ps and then data was collected for 1.5 ns. Any error bars reported in the data were determined by splitting the 1.5 ns simulation data into 100 ps blocks and determining the standard deviation of the data set.

The smoothed truncation length σ used for $v_0(r)$ ranges from 3.0 Å to 6.0 Å – from the nearest-neighbor distance to twice that. For $\sigma \leq 4.5$ Å, R_c was set to 9.5 Å, since the LJ interactions required a cutoff at that distance already. For $\sigma = 5.0$ Å, $R_c = 11.5$ Å, and for $\sigma = 6.0$ Å, $R_c = 13.5$ Å. The benchmark for electrostatics is three-dimensional Ewald sums with $\alpha = 0.3$ Å^{-1} and $\mathbf{k}_{max} = (10, 10, 10)$.

5.3.3 Structural Results

The SCA approximation gives good results for pair correlation functions for the full range of σ examined. Shown in Fig. 5.2 are all three site-site pair correlation functions as well as the dipole-dipole correlation function. All correlation functions show remarkably good agreement.

Since the lines lie directly on top of each other, the different $g_{\mathrm{HH}}(r)$ have been staggered by 0.2 vertically in Fig. 5.2(c). This was not done for g_{OO} and g_{OH} because the initial peaks are so sharp that such a stagger does not clearly display the features of the function as a whole. The agreement is quite strong, though there are slight discrepancies in $g(r)$ near the cutoff radius R_c. Overall, these results are not that surprising or new since a large number of spherical truncations have been developed to treat $1/r$ interactions in molecules as discussed in Sect. 4.4. From the viewpoint of LMF theory, this success is due to spherical cancellation of long-ranged forces in

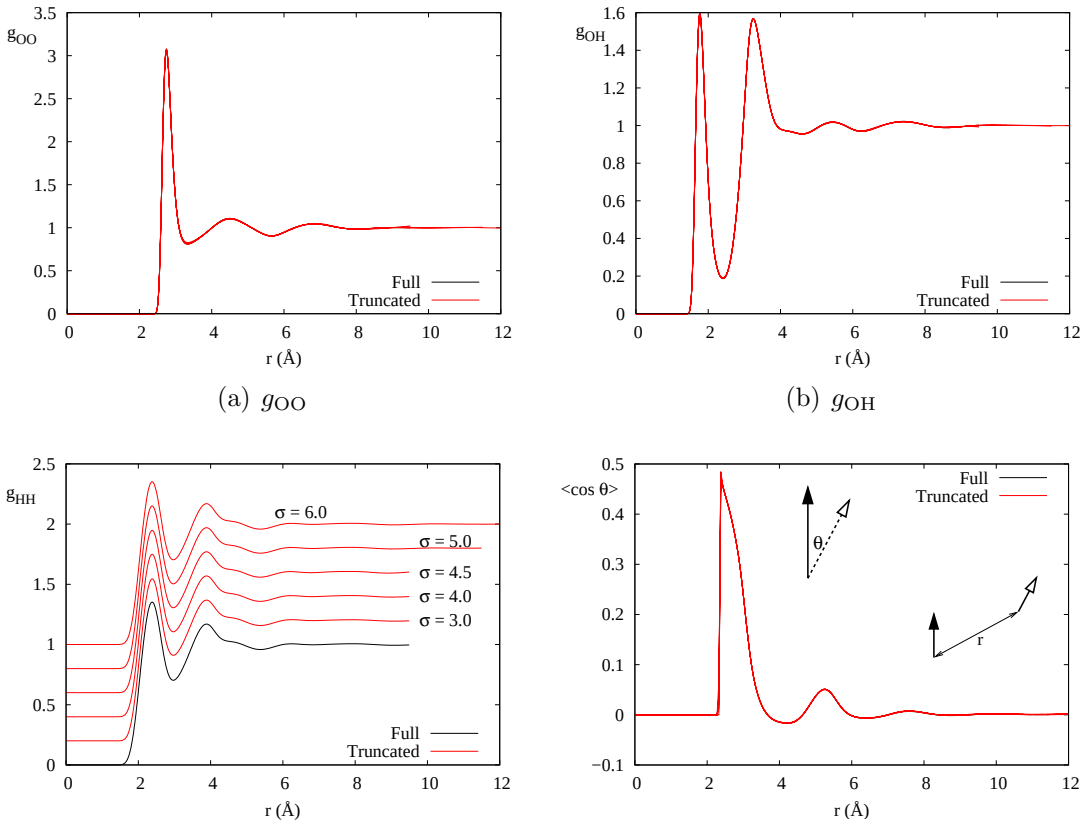

(a) g_{OO} (b) g_{OH}

(c) g_{HH} (d) Dipole-Dipole Correlations

Figure 5.2: Correlation functions for bulk SPC/E water treated with three-dimensional Ewald sums (Full) and with a range of Gaussian-truncated $v_0(r)$ (Truncated). The smoothed truncation length σ varies from 3.0 Å to 6.0 Å. The site-site correlation functions $g_{\mathrm{OO}}(r)$, g_{OH}, and g_{HH} are displayed as well as $\langle \cos\theta \rangle (r)$. The latter function is the average dot product between dipole unit vectors for molecules separated by r, as shown in the inset in (d). In (c), the correlation functions due to various $v_0(r)$ are vertically staggered by 0.2 to emphasize that 6 functions lie directly on top of each other in the other plots.

the bulk.

However, the agreement of the dipole-dipole correlation functions is surprising; this was first observed by Hu [41] for acetonitrile. The correlation function $\langle \cos\theta \rangle (r)$ is defined as the average dot product of two dipole unit vectors separated by a distance r in the fluid. The plot in Fig. 5.2(d) shows that within the nearest shell of water molecules, the dipoles are strongly positively correlated with each other, mostly due to the fact that the preponderance of hydrogen-bonded configurations have dipoles pointing in similar directions. The plot also shows that this correlation decays very quickly into the bulk. Nezbeda [75] found that while a molecule-based cutoff scheme yielded accurate site-site correlation functions, the dipole-dipole correlation function was highly inaccurate. He found a long-ranged anticorrelation of dipoles with his cutoff scheme. It seemed possible that a site-based truncation would be even less accurate for that function since at some intermediate radius, the GT water molecule could be viewed as having "non-zero" charge since the forces due to only some fraction of the sites would be felt. However, our results suggest that the truncation of Nezbeda [75] fails not as a result of issues with spherical truncations in general but rather owing to his insufficiently large cutoff radii. The largest cutoff radii considered was 7 Å, and apparently this led to severe neglect of orientational correlations even while the site-site correlation functions were quite accurate.

5.3.4 Thermodynamic Results

Shown in Table 5.1 are calculations of energy and pressure for the bulk SPC/E system. Simply from the simulation output of DLPOLY, we may obtain values for the energy and pressure of the mimic system in the SCA and also for SPC/E water simulated with Ewald sums. While we expect the latter to yield an accurate energy and pressure for the system, under no circumstances should U_0 and P_0 be accurate, where the 0 subscript is meant to indicate the contributions of $v_0(r)$ and $u_{\mathrm{LJ}}(r)$ to the energy and pressure. The results for U_0 and P_0 bear this out.

However, just as for simple ionic systems studied by previous researchers [14, 22], we expect to be able to accurately approximate the long-ranged contribution to the energy. Naïvely, we might hope to carry out the integration

$$\frac{U_1}{N} = \frac{\rho_B q^2}{2} \int v_1(r) \left\{ h_{\mathrm{OO}}(r) + h_{\mathrm{HH}}(r) - 2h_{\mathrm{OH}}(r) \right\} d\mathbf{r} \tag{5.12}$$

to calculate U_1/N, using the pair correlation functions from SCA simulations with $h(r) \equiv g(r) - 1$ and with $q \equiv q_{\mathrm{O}}$. From now on, we will define

$$h_{\mathrm{tot}}(r) = h_{\mathrm{OO}}(r) + h_{\mathrm{HH}}(r) - 2h_{\mathrm{OH}}(r). \tag{5.13}$$

However, this approach will be highly unreliable since the SCA pair correlation functions will most likely not be accurate for small k components, which are actually the dominant contributor the integral above. Just as in [14], we write U_1 as an integral over $\mathbf{k}$ using Parseval's theorem,

$$\frac{U_1}{N} = \frac{\rho_B q^2}{2} \frac{1}{(2\pi)^3} \int \frac{4\pi}{k^2} e^{-k^2\sigma^2/4} \hat{h}_{\mathrm{tot}}(k) d\mathbf{k}. \tag{5.14}$$

System	U_0/N		U_1/N	U_{tot}/N	
	k_BT	kJ/mol	k_BT	k_BT	kJ/mol
Ewald	N/A	N/A	N/A	-15.704 ± 0.006	-39.172 ± 0.016
SCA: $\sigma = 3.0$ Å	-13.689 ± 0.005	-34.146 ± 0.011	-1.759	-14.448 ± 0.005	-38.534 ± 0.011
SCA: $\sigma = 4.0$ Å	-14.873 ± 0.004	-37.098 ± 0.011	-.7422	-15.615 ± 0.004	-38.949 ± 0.011
SCA: $\sigma = 4.5$ Å	-15.112 ± 0.004	-37.695 ± 0.011	-.5213	-15.633 ± 0.004	-38.995 ± 0.011
SCA: $\sigma = 5.0$ Å	-15.287 ± 0.005	-38.131 ± 0.014	-.3800	-15.667 ± 0.005	-39.079 ± 0.014
SCA: $\sigma = 6.0$ Å	-15.466 ± 0.005	-38.576 ± 0.012	-.2200	-15.686 ± 0.005	-39.125 ± 0.012

System	P_0	P_1	P_{tot}
	katm	katm	katm
Ewald	N/A	N/A	0.044 ± 0.015
SCA: $\sigma = 3.0$ Å	0.263 ± 0.009	-0.134	0.129 ± 0.009
SCA: $\sigma = 4.0$ Å	0.107 ± 0.015	-0.056	0.051 ± .015
SCA: $\sigma = 4.5$ Å	0.072 ± 0.013	-0.039	0.033 ± 0.013
SCA: $\sigma = 5.0$ Å	0.066 ± 0.019	-0.029	0.037 ± 0.019
SCA: $\sigma = 6.0$ Å	0.060 ± 0.010	-0.017	0.043 ± 0.010

Table 5.1: Energies and pressures calculated for SPC/E water using Ewald sums, the strong coupling approximation, and applying corrections U_1 and P_1 due to the simple formulae outlined in the text.

As shown in Appendix D, building on material from [10] and [37], we may write a small k expansion of $\hat{h}_{\text{tot}}$ in a manner analogous to the zeroth and second moment expansion for Coulomb systems. At small k,

$$\hat{h}_{\text{tot}} \simeq 0 + \hat{h}^{(2)}_{\text{tot}} k^2, \tag{5.15}$$

where $\hat{h}^{(2)}_{\text{tot}}$ is a constant. This constant may be related to the dipole moment, density, and dielectric constant of water as

$$q^2 \hat{h}^{(2)}_{\text{tot}} = \frac{k_B T}{4\pi\rho_B^2} \frac{\epsilon - 1}{\epsilon} - \frac{\mu^2}{3\rho_B}. \tag{5.16}$$

Aside from the ratio $(\epsilon - 1)/\epsilon$, the first term is equivalent to the κ_D^2 contribution for ionic solutions determined by Stillinger and Lovett [94]. The second term is a nontrivial contribution from the dipole moment. In fact this constant is *negative* and may be bounded from above by assuming $\epsilon \to \infty$ as

$$q^2 \hat{h}^{(2)}_{\text{tot}} \leq -3.145 \times 10^3 \frac{\text{kJ} \cdot \text{Å}^6}{\text{mol}}. \tag{5.17}$$

Since water has a large dielectric constant and the dipole moment contribution is large in magnitude, this is actually a relatively tight upper bound. Given this expansion, we may analytically approximate U_1/N as

$$\frac{U_1}{N} \simeq q^2 \hat{h}^{(2)}_{\text{tot}} \rho_B \frac{2}{\sqrt{\pi}} \frac{1}{\sigma^3}. \tag{5.18}$$

This correction is shown in Table 5.1, and the inclusion of this correction brings all of the SCA energies much closer to the Ewald energy. Furthermore, all the U_0/N and $(U_0 + U_1)/N$ are plotted as a function of σ in Fig. 5.3. The Ewald energy is shown as a horizontal line, and this approximate correction performs quite well.

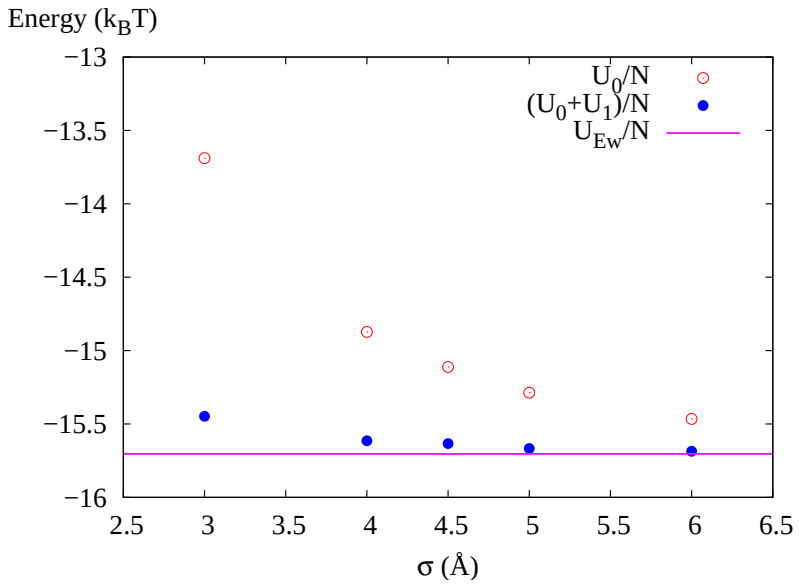

Figure 5.3: Plots of U_0/N and the correction U_1/N as a function of σ compared to Ewald results. Even for a conservative σ such as 4.5 Å, U_0/N is still incorrect by about 0.5 k_BT per molecule. The analytical long-ranged correction U_1/N which varies as σ^{-3} resolves these inaccuracies on a systematic basis. Error bars are the size of the symbols or less.

The SCA pressure data in Table 5.1 also performs inadequately relative to Ewald sums. All SCA systems have a pressure higher than that of the Ewald sums. This meshes with an observation by Izvekov *et al.* [50] that when simulating a system very similar to SCA with $\sigma \simeq 5.0$ Å using the NPT ensemble, the bulk density was slightly too low. The SCA systems are missing some net attractive forces based on the pressure values, and therefore, an SCA system with variable volume would require an additional applied external pressure in lieu of the net aggregate attractive forces.

Initially, given the success of the energy correction above, we hoped to apply a similar approach using the virial equation

$$P_1 = -\frac{\rho_B^2 q^2}{6} \int \frac{\partial v_1}{\partial r} \cdot h_{\text{tot}}(r) d\mathbf{r}. \tag{5.19}$$

Given our choice of $v_1(r)$, this may be exactly reexpressed using an integral over k as

$$P_1 = \frac{\rho_B^2 q^2}{6} \frac{1}{(2\pi)^3} \int \left(\frac{4\pi}{k^2} e^{-k^2\sigma^2/4} - 2\sigma^2 \pi e^{-k^2\sigma^2/4} \right) \hat{h}_{\text{tot}}(k) d\mathbf{k}. \tag{5.20}$$

Plugging in the small k expansion however leads to a pressure correction which is explicitly positive. According to [37, p. 347], this generalization of the virial equation should not suffice – more information than the pair correlation functions alone is needed to calculate the pressure.

Instead, we use a thermodynamic expression for the pressure,

$$P = T \left(\frac{\partial S}{\partial V} \right)_{T,N} - \left(\frac{\partial U}{\partial V} \right)_{T,N}, \tag{5.21}$$

to calculate a correction for pressure in simulations. In general, we do not know the energy or the entropy as a function of V; however we do have an analytical approximation to U_1/N. If we also assume that the entropy of the full system is well captured by the mimic system, *i.e.* $S \simeq S_0$, then we simply need to calculate the partial derivative of U_1 with respect to V in order to determine the pressure correction. Writing U_1 in terms of N, V, and T, we find

$$U_1(N, V, T) = \frac{2}{\sqrt{\pi}\sigma^3} \left(\frac{V k_B T}{4\pi} \frac{\epsilon - 1}{\epsilon} - \frac{N\mu^2}{3} \right). \tag{5.22}$$

Rather logically, the intramolecular contribution to energy due to rigid molecular dipoles does not depend on volume.

Taking the partial derivative of $U_1(N,V,T)$ with respect to V, we find

$$\begin{aligned} P_1 = -\left(\frac{\partial U_1}{\partial V}\right)_{T,N} &= -\frac{k_B T}{2\pi^{3/2}\sigma^3}\frac{\epsilon-1}{\epsilon} \\ &= -\frac{0.2240}{\sigma^3}\frac{\epsilon-1}{\epsilon}\ \frac{\text{kJ}}{\text{mol}\,\text{Å}^3} \\ &= -\frac{3.671}{\sigma^3}\frac{\epsilon-1}{\epsilon}\ \text{katm}, \end{aligned} \tag{5.23}$$

with σ given in Å. This correction term is purely negative, just as we expect. Since, the term involving ϵ is now the only correction term, we use the experimental dielectric constant of water, $\epsilon = 78$. As shown in Table 5.1, including P_1 brings nearly all pressures into agreement with the Ewald result. Neither P_1 nor U_1/N brought the $\sigma = 3.0$ Å data into full agreement with the Ewald results due to the fact that the second order k-space expansion is inappropriate for the smallest σ used.

This data with error bars is also plotted in Fig. 5.4. Since the pressure data is much noiser than the energy data, several of the higher σ were already barely within error bars. However, the correction improves the agreement and is quite notable for $\sigma = 4.0$ Å.

In general, as has been well established [14, 22], despite the highly accurate structures for SCA, the impact of the long-ranged forces on thermodynamics cannot be neglected. A simple analytical energy correction yields much more accurate results for both pressure and energy. The pressure correction could prove useful in carrying out NPT simulations of an SCA fluid.

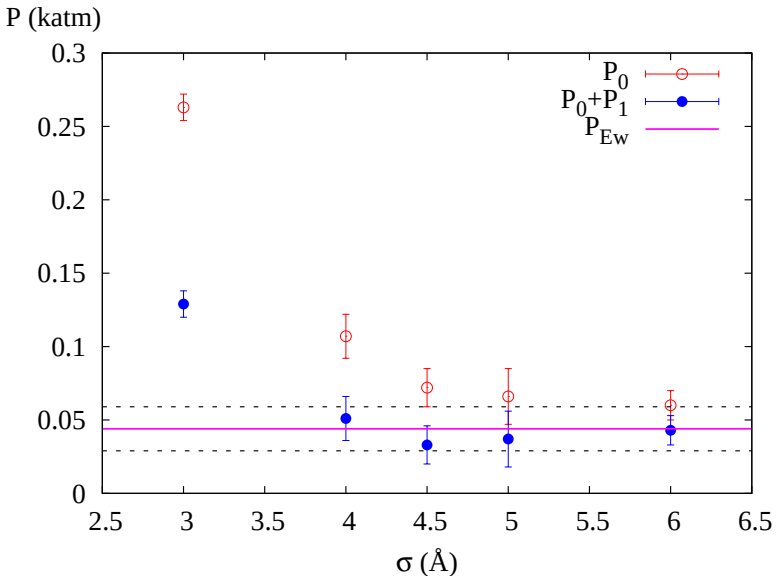

Figure 5.4: Plots of P_0 and the correction P_1 as a function of σ compared to Ewald results. Error bars are given for all data points, and the error bars on the Ewald pressure are indicated by the thin dashed lines above and below the thick horizontal line at 0.044 katm. The P_1 correction brings all pressures into better agreement with the Ewald result.

5.4 Why is SCA So Successful for Dense Bulk Fluids?

In essence, the success of SCA for the structure of bulk SPC/E water means that the forces due to $\mathcal{V}_{R1}$ are negligible. There will be constant corrections to energy and pressure, but simulating in the NVT ensemble means that the incorrect long-ranged pressure does not impact the structure. The success of SCA implies that $\mathcal{V}_{R1}$ should simply be a function of r and that it is quite slowly varying.

One might posit that the $\mathcal{V}_R$ we seek would be obtained by placing each site at the origin (separately) leading to separate $\mathcal{V}_{R,\alpha}$ indexed by the site α placed at the origin. Defining $\mathcal{V}_\alpha(r) = q_\alpha/r$, the LMF site-site equation from Eq. (5.11) can be used. In other words, LMF would lead to a set of $\{\mathcal{V}_{R,\alpha}(\mathbf{r})\}$ spanning each instance of a site fixed at the origin.

However, this formulation ignores the fact that site α is inextricably bound to the other sites in that molecule. The key to incorporating the physical reality is to start with a more specific $\mathcal{V}_R$ and then average that to a spherically symmetric situation. This will not be the explicitly correct $\mathcal{V}_R$ but it will be a solid approximation for a bulk situation. In formulating a more specific molecular $\mathcal{V}_R$, we follow the prescription from Chen and Weeks [15] for fields due to fixed charged species.

We may define a $\mathcal{V}_R$ for a given orientation $\mathbf{R_M}$ of a central molecule M with site α fixed at the origin. In essence $\mathcal{V}(\mathbf{r})$ implicitly depends on that chosen orientation $\mathbf{R}_M$ with $\mathbf{r}_M^{(\alpha)}$ at the origin $\mathbf{0}$. Thus we will write both $\mathcal{V}_R$ and $\mathcal{V}$ to indicate their mutual dependence on $\mathbf{r}$ and $\mathbf{R_M}$ as $\mathcal{V}_{R,\alpha}(\mathbf{r};\mathbf{R_M})$ and $\mathcal{V}_\alpha(\mathbf{r};\mathbf{R_M})$. As suggested previously we may split $\mathcal{V}_\alpha$ with short- and long-ranged parts defined as

$$\mathcal{V}_{0,\alpha}(\mathbf{r};\mathbf{R_M}) = q_{\alpha M} v_0(r) + \sum_{\gamma\neq\alpha}^{n_M} q_{\gamma M} v_0\left(\left|\mathbf{r}-\mathbf{r}_{\mathbf{M}}^{(\gamma)}\right|\right) \tag{5.24}$$

$$\mathcal{V}_{1,\alpha}(\mathbf{r};\mathbf{R_M}) = q_{\alpha M} v_1(r) + \sum_{\gamma\neq\alpha}^{n_M} q_{\gamma M} v_1\left(\left|\mathbf{r}-\mathbf{r}_{\mathbf{M}}^{(\gamma)}\right|\right). \tag{5.25}$$

With this first step, we may also now write $\mathcal{V}_{R,\alpha} = \mathcal{V}_{0,\alpha} + \mathcal{V}_{R1,\alpha}$ with the long-ranged part defined as

$$\mathcal{V}_{R1,\alpha}(\mathbf{r};\mathbf{R_M}) = \mathcal{V}_{1,\alpha}(\mathbf{r};\mathbf{R_M}) + \int d\mathbf{r}' \rho_{R,q|M}(\mathbf{r}'|\mathbf{R_M};[\mathcal{V}_{R,\alpha}])\, v_1\left(|\mathbf{r}-\mathbf{r}'|\right) \tag{5.26}$$

where $\rho_{q|M}(\mathbf{r}|\mathbf{R_M})$ is the conditional *inter*molecular charge density at $\mathbf{r}$ given the molecule orientation $\mathbf{R_M}$ with α at $\mathbf{0}$. Here the LMF equation involves a conditional density simply because the imposed external field in this case may be mapped to placing a molecule at position $\mathbf{R_M}$ with α at the origin.

As stated at the beginning of this section, the success of SCA for treating bulk

water suggests that $\mathcal{V}_{R1,\alpha}(\mathbf{r};\mathbf{R_M}) \simeq 0$. Given the uniformity of the fluid, in some sense the long-ranged forces will not be dominated by any single molecular orientation but rather the averaged effect of the molecular rotating about the fixed site α. Thus, it seems quite plausible to approximate

$$\mathcal{V}_{R1,\alpha}(\mathbf{r};\mathbf{R_M}) \simeq \langle \mathcal{V}_{R1,\alpha}(\mathbf{r};\mathbf{R_M}) \rangle_{M|\alpha} = \mathcal{V}_{R1,\alpha}(r). \tag{5.27}$$

The $\langle A \rangle_{M|\alpha}$ indicates an ensemble average of A over all possible orientations of M given that α is at the origin $\mathbf{0}$. This may be represented via equation as

$$\langle A \rangle_{M|\alpha} = \int \cdots \int A \cdot \varrho_{M|\alpha}(\mathbf{R_M}|\mathbf{0}) \left(\frac{d\mathbf{R_M}}{d\mathbf{r}_{\mathbf{M}}^{(\alpha)}} \right) \tag{5.28}$$

where $\varrho_{M|\alpha}(\mathbf{R_M}|\mathbf{0})$ is the conditional *intra*molecular density that the molecule will be oriented as $\mathbf{R_M}$ given that α is at $\mathbf{0}$. The differential fraction on the right indicates that we integrate over all molecular sites except site α. In essence, this means that all orientation-specific interactions are encompassed wholly by the short-ranged $\mathcal{V}_{0,\alpha}$.

We begin by determining the Boltzmann-weighted average of $\mathcal{V}_{1,\alpha}(\mathbf{r};\mathbf{R_M})$,

$$\langle \mathcal{V}_{1,\alpha}(\mathbf{r};\mathbf{R_M}) \rangle_{M|\alpha} = q_{\alpha M} v_1(r) + \sum_{\gamma \neq \alpha}^{n_M} q_{\gamma M} \left\langle v_1 \left(\left| \mathbf{r} - \mathbf{r}_{\mathbf{M}}^{(\gamma} \right| \right) \right\rangle_{M|\alpha}. \tag{5.29}$$

We first compute

$$\left\langle v_1 \left(\left| \mathbf{r} - \mathbf{r}_{\mathbf{M}}^{(\gamma} \right| \right) \right\rangle_{M|\alpha} = \int \cdots \int \varrho_{M|\alpha}(\mathbf{R_M}|\mathbf{0}) v_1 \left(\left| \mathbf{r} - \mathbf{r}_{\mathbf{M}}^{(\gamma)} \right| \right) \left(\frac{d\mathbf{R_M}}{d\mathbf{r}_{\mathbf{M}}^{\alpha}} \right) \tag{5.30}$$

$$= \int d\mathbf{r}_{\mathbf{M}}^{(\gamma)} \varrho_{\gamma|\alpha} \left(r_M^{(\gamma)} | \mathbf{0} \right) v_1 \left(\left| \mathbf{r} - \mathbf{r}_{\mathbf{M}}^{(\gamma)} \right| \right). \tag{5.31}$$

Since $\varrho_{\gamma|\alpha} \left(r_M^{(\gamma)} | \mathbf{0} \right)$ depends only on $r_M^{(\gamma)}$ and not on $\mathbf{r}_{\mathbf{M}}^{(\gamma)}$, we may integrate v_1 over spherical shells, as done in Sect. B.2, and yield

$$\int d\mathbf{r}_{\mathbf{M}}^{(\gamma)} \varrho_{\gamma|\alpha} \left(r_M^{(\gamma)} | \mathbf{0} \right) v_1 \left(\left| \mathbf{r} - \mathbf{r}_{\mathbf{M}}^{(\gamma)} \right| \right) = \int d\mathbf{r}_{\mathbf{M}}^{(\gamma)} \varrho_{\gamma|\alpha} \left(r_M^{(\gamma)} | \mathbf{0} \right) \mathcal{G} \left(r; r_M^{(\gamma)} \right). \tag{5.32}$$

As derived in Sect. B.2, $\mathcal{G}(r;R)$ is the Gaussian-smoothed Green's function associated with a spherical shell of unit charge located at R. With this writing, we may express $\mathcal{V}_{1,\alpha}$ as

$$\langle \mathcal{V}_{1,\alpha}(\mathbf{r};\mathbf{R_M})\rangle_{M|\alpha} = q_{\alpha M} v_1(r) + \int d\mathbf{r}' \varrho_{q|\alpha}(r'|\mathbf{0})\, \mathcal{G}(r;r')\,. \tag{5.33}$$

Here $\varrho_{q|\alpha}(r|\mathbf{0})$ is meant to represent the intramolecular charge density at radius r given that α is located at the origin $\mathbf{0}$.

To write the spherically averaged $\mathcal{V}_{R1,\alpha}$, the final average we must take is

$$\left\langle \int d\mathbf{r}' \rho_{R,q|M}(\mathbf{r}'|\mathbf{R_M};[\mathcal{V}_{R,\alpha}])\, v_1(|\mathbf{r}-\mathbf{r}'|) \right\rangle_{M|\alpha}. \tag{5.34}$$

This task is most clear when we explicitly write out the average and simplify from there:

$$\begin{aligned}
&\left\langle \int d\mathbf{r}' \rho_{R,q|M}(\mathbf{r}'|\mathbf{R_M};[\mathcal{V}_{R,\alpha}])\, v_1(|\mathbf{r}-\mathbf{r}'|) \right\rangle_{M|\alpha} \\
&\quad = \int \cdots \int \left(\int d\mathbf{r}'\, \rho_{R,q|M}(\mathbf{r}'|\mathbf{R_M};[\mathcal{V}_{R,\alpha}])\, v_1(|\mathbf{r}-\mathbf{r}'|) \right) \cdot \varrho_{R,M|\alpha}(\mathbf{R_M}|\mathbf{0}) \left(\frac{d\mathbf{R_M}}{d\mathbf{r}_{\mathbf{M}}^{(\alpha)}} \right) \\
&\quad = \int d\mathbf{r}'\, v_1(|\mathbf{r}-\mathbf{r}'|\rangle \left\{ \int \cdots \int \rho_{R,q|M}(\mathbf{r}'|\mathbf{R_M};[\mathcal{V}_{R,\alpha}])\, \varrho_{R,M|\alpha}(\mathbf{R_M}|\mathbf{0}) \left(\frac{d\mathbf{R_M}}{d\mathbf{r}_{\mathbf{M}}^{(\alpha)}} \right) \right\} \\
&\quad = \int d\mathbf{r}'\, \rho_{R,q|\alpha}(r'|\mathbf{0};[\mathcal{V}_{R,\alpha}]) \cdot v_1(|\mathbf{r}-\mathbf{r}'|)
\end{aligned} \tag{5.35}$$

As before, since $\rho_{q|\alpha}(r|\mathbf{0})$ depends only on the radial distance, we may average $v_1(r)$ over spherical shells and find

$$\left\langle \int d\mathbf{r}' \rho_{R,q|M}(\mathbf{r}'|\mathbf{R_M};[\mathcal{V}_{R,\alpha}])\, v_1(|\mathbf{r}-\mathbf{r}'|) \right\rangle_{M|\alpha} = \int d\mathbf{r}'\, \rho_{R,q|\alpha}(r'|\mathbf{0};[\mathcal{V}_{R,\alpha}]) \cdot \mathcal{G}(r;r'). \tag{5.36}$$

Thus in the end, we find the following expression for a spherically averaged $\mathcal{V}_{R1,\alpha}$:

$$\langle \mathcal{V}_{R1,\alpha}(\mathbf{r};\mathbf{R_M})\rangle_{M|\alpha} = q_{\alpha M} v_1(r) + \int d\mathbf{r}'\, \left\{ \varrho_{R,q|\alpha}(r'|\mathbf{0}) + \rho_{R,q|\alpha}(r'|\mathbf{0}) \right\} \mathcal{G}(r;r'). \tag{5.37}$$

The sole difference between this and the simple calculation for a charge mixture is that we now include a v_1 for the shells of charge due to atoms constrained to site α by intramolecular bonds. [2]

For neutral, compact molecules like water, the sum of the first two terms will be quite small, much smaller than $q_\alpha v_1(r)$. Also for rigid molecules like SPC/E water, we may express $\varrho_{q|\alpha}(r'|\mathbf{0})$ as solely a sum of δ-functions. For example if the oxygen site is fixed at the origin, then we have

$$\rho_{q|O}(r'|\mathbf{0}) = \frac{2q_H \cdot \delta(r' - r_{OH})}{4\pi r_{OH}^2}. \tag{5.38}$$

As suggested, the resulting $\mathcal{V}_{1,\alpha}$ for each site, as shown in Fig. 5.5, is substantially smaller than the original $q_\alpha v_1(r)$ due to the fixed atomic sites at the origin. We also simultaneously expect that the force corrections due to long-ranged intermolecular interactions will be small in magnitude in a bulk fluid. While the energy corrections are nonzero, as shown in Sect. 5.3.4, the spherically averaged force resulting from $\mathcal{V}_{R1,\alpha}$ will likely be quite small, just as $\mathcal{V}_{1,\alpha}$.

The meaning of $\mathcal{V}_{R,\alpha}$ is subtly different from the original spherical formulation based on mixtures. We may not escape the fact that the short-ranged interactions contained in ϕ_R are very orientation specific. However, this orientational dependence

[2] In essence, this expression could again be expressed as a mixture LMF equation if we treated the particles bound to site α as different mixture components than sites not bound to α [41]. The particles bound to α would have u_0 purely due to bonding energies but their $v_1(r)$ would contribute to the long-ranged interactions.

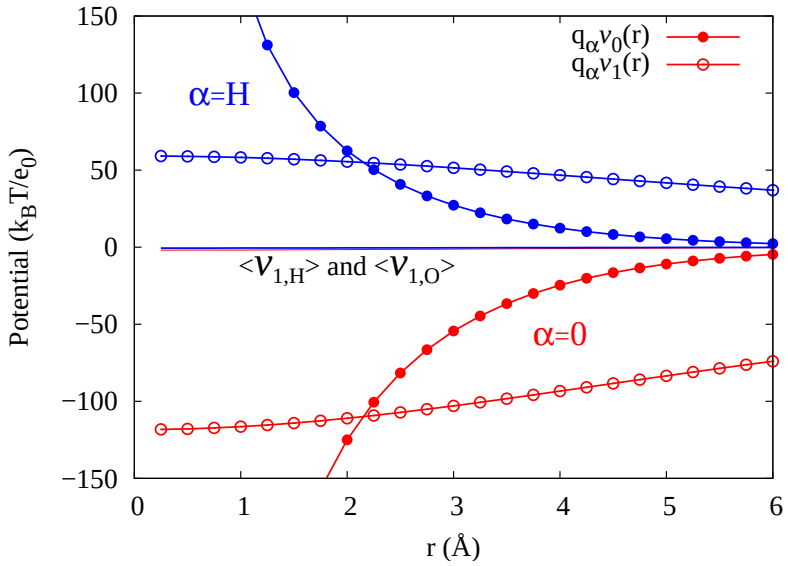

Figure 5.5: Comparison of $\langle \mathcal{V}_{1,\alpha} \rangle (r)$ with the original potentials $q_\alpha v_0(r)$ and $q_\alpha v_1(r)$ for both oxygen and hydrogen fixed at the origin. Here σ is chosen to be 4.5 Å.

need only be contained in the short-ranged interactions, as expressed by

$$\mathcal{V}_{R,\alpha}(\mathbf{r};\mathbf{R}_M) \simeq q_{\alpha M} v_0(r) + \sum_{\gamma \neq \alpha} q_{\gamma M} v_0(|\mathbf{r} - \mathbf{r}_\gamma|) + \langle \mathcal{V}_{R1,\alpha} \rangle_{M|\alpha} (r), \tag{5.39}$$

and for bulk water as we studied $\partial \langle \mathcal{V}_{R1,\alpha} \rangle_{M,\alpha} (r)/\partial r \ll 1$.

This success for bulk ambient SPC/E water should not suggest that the SCA approximation will be sufficient at lower density states, unless the σ were chosen substantially larger. Further, with a smaller σ, LMF theory may succeed, but perhaps the spherical averaging demonstrated in this section will not be valid. Therefore LMF averaging would be relative to a given molecular orientation, and thus much more geometrically complex.

5.5 Deriving an LMF Equation for Larger Site-Site Molecules

Given the derivation of the site-site molecular equation in Sect. 5.2, one might mistakenly assume that for larger molecules like phospholipids or proteins, one must choose σ large enough to produce all relevant intramolecular correlations with the short-ranged potential, given that we assumed in Eq. (5.10) that

$$\rho_M\left(\mathbf{R_M};[\phi]\right) \simeq \rho_{R,M}\left(\mathbf{R_M};[\phi_R]\right).$$

For all-atomistic molecular simulations, such a σ would be so large that it would not be numerically tractable. However, the derivation given in Sect. 5.2 also begins with a statement of the potential energy function $\mathcal{U}$ that does not mesh with the implementation in molecular dynamics programs such as DLPOLY [89], AMBER [25], CHARMM [64], and NAMD [77].

In such programs and associated parameter sets, $\mathcal{U}$ may be more reasonably represented by

$$\begin{aligned}\mathcal{U} = &\sum_{\alpha=1}^{\eta_S}\sum_{i=1}^{N_\alpha}\sum_{\substack{\gamma\\ \text{1-2}}} w_b^*\left(\left|\mathbf{r}_\mathbf{i}^{(\alpha)}-\mathbf{r}^{(\gamma)}\right|\right) + \sum_{\alpha=1}^{\eta_S}\sum_{i=1}^{N_\alpha}\sum_{\substack{\gamma,\delta\\ \text{1-2-3}}} w_a^*\left(\mathbf{r}_\mathbf{i}^{(\alpha)},\mathbf{r}_{\text{1-2}}^{(\gamma)},\mathbf{r}_{\text{1-3}}^{(\delta)}\right)\\ &+\sum_{\alpha=1}^{\eta_S}\sum_{i=1}^{N_\alpha}\sum_{\substack{\gamma,\delta,\zeta\\ \text{1-2-3-4}}} w_d^*\left(\mathbf{r}_\mathbf{i}^{(\alpha)},\mathbf{r}_{\text{1-2}}^{(\gamma)},\mathbf{r}_{\text{1-3}}^{(\delta)},\mathbf{r}_{\text{1-4}}^{(\zeta)}\right)\\ &+\sum_{\alpha=1}^{\eta_S}\sum_{i=1}^{N_\alpha}\phi^{(\alpha)}\left(\mathbf{r}_\mathbf{i}^{(\alpha)}\right) + \frac{1}{2}\underbrace{\sum_{\alpha=1}^{\eta_S}\sum_{\gamma=1}^{\eta_S}\sum_{i=1}^{N_\alpha}\sum_{j=1}^{N_\gamma}}_{\text{1-4 and beyond}}\left(1-\delta_{\alpha\gamma}\delta_{ij}\right)u_{\alpha\gamma}\left(\left|\mathbf{r}_\mathbf{i}^{\alpha}-\mathbf{r}_\mathbf{j}^{\gamma}\right|\right)\end{aligned} \tag{5.40}$$

where there are η_S distinct types of sites and N_α particles of each site type α. The intramolecular bonding is now represented by specific bond vibration terms (w_b^*) of two directly connected atoms, angle bending terms (w_a^*) of three linearly connected

atoms, and dihedral torsion terms (w_d^*) of 4 linearly connected atoms, rather than one full molecular bonding potential energy function like $w^*(\mathbf{R_M})$. The subscripts 1-2, 1-3, and 1-4 on positions are meant to represent relative positions between atoms connected via bonds, angles, and dihedral torsions respectively. It should be understood that care is exercised with the sums to only count each bond, angle and torsion once. Further, there exist long-ranged, non-bonded interactions $u_{\alpha\gamma}(r)$ between all pairs of sites, provided that their closest linkage is a 1-2-3-4 dihedral link. Some parameter sets actually scale down the Coulomb terms by a constant factor if particles are connected via a dihedral link, but we will assume for the purpose of this discussion that no scaling occurs.

For such a $\mathcal{U}$, we find the YBG equation in Sect. A.5 as follows,

$$\begin{aligned}
-k_BT\vec{\nabla}\ln\rho_\alpha^{(1)}(\mathbf{r}) = &\sum_{\substack{\gamma\\ \text{1-2}}}\int d\mathbf{r}'\,\left[\vec{\nabla}w_b^*(\mathbf{r},\mathbf{r}')\right]\varrho_{\gamma|\alpha}(\mathbf{r}'|\mathbf{r})\\
&+\sum_{\substack{\gamma,\delta\\ \text{1-2-3}}}\int d\mathbf{r}'d\mathbf{r}''\,\left[\vec{\nabla}w_a^*(\mathbf{r},\mathbf{r}',\mathbf{r}'')\right]\varrho_{\gamma\delta|\alpha}(\mathbf{r}',\mathbf{r}''|\mathbf{r})\\
&+\sum_{\substack{\gamma,\delta,\zeta\\ \text{1-2-3-4}}}\int d\mathbf{r}'d\mathbf{r}''d\mathbf{r}'''\,\left[\vec{\nabla}w_d^*(\mathbf{r},\mathbf{r}',\mathbf{r}'',\mathbf{r}''')\right]\varrho_{\gamma\delta\zeta|\alpha}(\mathbf{r}',\mathbf{r}'',\mathbf{r}'''|\mathbf{r})\\
&+\sum_{\gamma=1}^{\eta_S}\int d\mathbf{r}'\rho_{\gamma|\alpha}(\mathbf{r}'|\mathbf{r})\vec{\nabla}u_{\alpha\gamma}^{\mathrm{LJ}}(|\mathbf{r}-\mathbf{r}'|)\\
&+\vec{\nabla}\phi_\alpha(\mathbf{r})+\frac{q_\alpha}{\epsilon}\int d\mathbf{r}'\rho_{q|\alpha}(\mathbf{r}'|\mathbf{r})\vec{\nabla}\frac{1}{|\mathbf{r}-\mathbf{r}'|}.
\end{aligned}\tag{5.41}$$

Here $\rho_{q|\alpha}(\mathbf{r}'|\mathbf{r})$ is the conditional *charge* density at $\mathbf{r}'$ given that particle α is located at $\mathbf{r}$ and $\rho_{\gamma|\alpha}(\mathbf{r}';\mathbf{r})$ is the standard site-site conditional density. Both technically exclude those atoms within one or two bonds of site α. Note that ϱ in the first three integrals are explicitly for sites connected via bonds, angles, and dihedrals respectively.

Following yet again the same path for derivation, we find that the *weaker* conditions for accuracy are:

* for sites α and γ connected via bonds,

$$\varrho^{(2)}\left(\mathbf{r}^{(\alpha)},\mathbf{r}^{(\gamma)};[\phi]\right)\simeq\varrho_R^{(2)}\left(\mathbf{r}^{(\alpha)},\mathbf{r}^{(\gamma)};[\phi_R]\right) \tag{5.42}$$

* for three sites α, γ, and δ connected via a bond angle,

$$\varrho^{(3)}\left(\mathbf{r}^{(\alpha)},\mathbf{r}^{(\gamma)},\mathbf{r}^{(\delta)};[\phi]\right)\simeq\varrho_R^{(3)}\left(\mathbf{r}^{(\alpha)},\mathbf{r}^{(\gamma)}\mathbf{r}^{(\delta)};[\phi_R]\right) \tag{5.43}$$

* and for sites α, γ, δ, and ζ involved in dihedral rotations,

$$\varrho^{(4)}\left(\mathbf{r}^{(\alpha)},\mathbf{r}^{(\gamma)},\mathbf{r}^{(\delta)},\mathbf{r}^{(\zeta)};[\phi]\right)\simeq\varrho_R^{(4)}\left(\mathbf{r}^{(\alpha)},\mathbf{r}^{(\gamma)}\mathbf{r}^{(\delta)},\mathbf{r}^{(\zeta)};[\phi_R]\right). \tag{5.44}$$

These approximations are much more easily supported by mimic systems with reasonably small σ. This σ may have to be on the order of 1-4 distances since 1-4 pairs have Coulomb interactions. In general though, we expect that LMF theory can be applied in standard biomolecular all-atomistic simulations with reasonable success as well.

Again, this bears to reason, given the success of SCA-like spherical short-ranged potentials in dealing with Coulomb systems. However it is promising to know that the strong results for nonuniform systems of water described in the next chapter should be equally applicable to biophysically more interesting nonuniform simulation choices.

5.6 Summary and Conclusions

In this chapter, we derived the further approximations needed to make the simple LMF equation for a rescaled electrostatic potential valid for site-site molecular models. For small molecules, the basic requirement is that the density profile, depending on both molecular position and orientation, is well-captured by the mimic system, as given in Eq. (5.10). For this approximation to hold the smoothed truncation length σ should be at least the size of the molecule. However, for larger molecules described by typical CHARMM-like intramolecular potentials, less restrictive approximations hold, as stated in Eqs. (5.42), (5.43), and (5.44). These additional necessary approximations for larger molecules imply that σ, the length-scale defining the range of the short-ranged pair interactions, should be of the order of a few bond lengths so that the mimic system can capture all necessary short-ranged interactions. This greatly extends the usefulness of LMF theory for biomolecular simulations because σ will only need to be about 5 Å rather than the size of lipids or proteins, which can be at least several nm in size.

Furthermore, the success of the strong coupling approximation in predicting structure for uniform bulk fluids was shown in Fig. 5.2. Other similar short-ranged truncations have been shown previously to accurately predict the pair correlations in bulk; so this alone is not a new result. However, in Sect. 5.4, we use the LMF framework to examine why the SCA is so accurate. We show that the long-ranged forces due to sites on a central molecule are small when averaged spherically about any molecular site. The accurated structure predicted by the strong coupling approximation

suggests that this is true for the long-ranged forces represented by $\mathcal{V}_{R1}$ as well.

However, the impact of long-ranged forces on thermodynamics cannot be neglected. As shown in Sect. 5.3.4, understanding the LMF approach from the perspective of perturbation theory allows us to correct the energies and the pressures generated via simulations in a simple and reliable manner. Figures 5.3 and 5.4 compare the results due to the strong coupling approximation alone and the thermodynamic results when the correction is included. Since the long-ranged energies neglected are attenuated in k-space via a Gaussian with a width of $2/\sigma$, we employed the small-k expansion of intermolecular pair correlation functions due to Chandler [10] to develop an analytical energy correction which led to much more accurate energies. In addition, appealing to a simple thermodynamic relation, we correctly included the impact of long-ranged forces on the pressure. The demonstrated value of these analytical thermodynamic corrections is very encouraging, and we hope to build on these developments in the future.

Chapter 6

Water Confined Between Walls

While the results for bulk SPC/E water presented in Sect. 5.3 are impressive, they are well understood from a practical standpoint. LMF theory provides an interesting window into why such spherical truncations of the $1/r$ potential are successful in simulations, but the structure produced using the strong coupling approximation is not unique to our choice of $v_0(r)$.

Given the success of spherical truncations of $1/r$ in the simulations presented, one might reasonably ask why such approaches are not more broadly used in simulations. They are used in large-scale biosimulations where the time scale of the interesting transitions is greater that that reasonably accessible to simulations using series summation techniques [91], and there has recently been a study suggesting that various spherical truncation techniques can yield folding landscapes in good agreement with Ewald summation [83]. Work continues to this day developing good spherical truncation schemes for $1/r$ [29, 50, 75]. However, most of the successes reported with spherical truncation schemes are in relatively uniform situations, where, as argued in the previous chapter, we would expect the SCA to perform well. Even many all-atomistic protein simulations might be considered reasonably uniform in *charge density* though certainly not in molecular identity.

In essence, consideration of only short-ranged forces to the exclusion of long-ranged

dipolar forces has molecular level impact [93]. As previously discussed in Sect. 4.6.2, Spohr [93] observed that the fault of spherical truncations in slab geometries lies in the neglect of net-additive long-ranged forces. Magnets are physical examples of a system where the local ordering competes with long-ranged energetic effects. This leads to the formation of domain walls in magnets, which the short-ranged Ising model fails to predict. In liquid water, the long-ranged forces for water models can similarly have effects that propagate down to a molecular length scale.

None of the current work on spherical truncation schemes aside from LMF theory is formulated so that it can address this long-standing well-known issue with such approaches – the simulation of water in *nonuniform* situations such as in a slab geometry [28].

6.1 Simulation Details

In this chapter, we will examine SPC/E water confined to a finite width in the z-direction by walls at $\pm z_w$. In the first few sections, the confining walls are modeled by the hydrophobic smoothed LJ walls [59], as shown in Fig. 6.1. The functional form of each wall is

$$U_{\mathrm{LJw}}(z; z_w) = \frac{A}{|z - z_w|^9} - \frac{B}{|z - z_w|^3} \tag{6.1}$$

with the constants of proportionality defined to be

$$A = 17447.5 \, \frac{\mathrm{kJ}}{\mathrm{mol}} \mathrm{\AA}^9 \qquad B = 76.1496 \, \frac{\mathrm{kJ}}{\mathrm{mol}} \mathrm{\AA}^3$$

in order to model paraffin [59]. The well depth of this functional form is on the order of $k_B T$, supporting the description of these walls as hydrophobic. We will also

simulate confinement between model Pt(111) walls, but description of this surface and simulation details specifically related to it are delayed until Sect. 6.6 when those results are introduced.

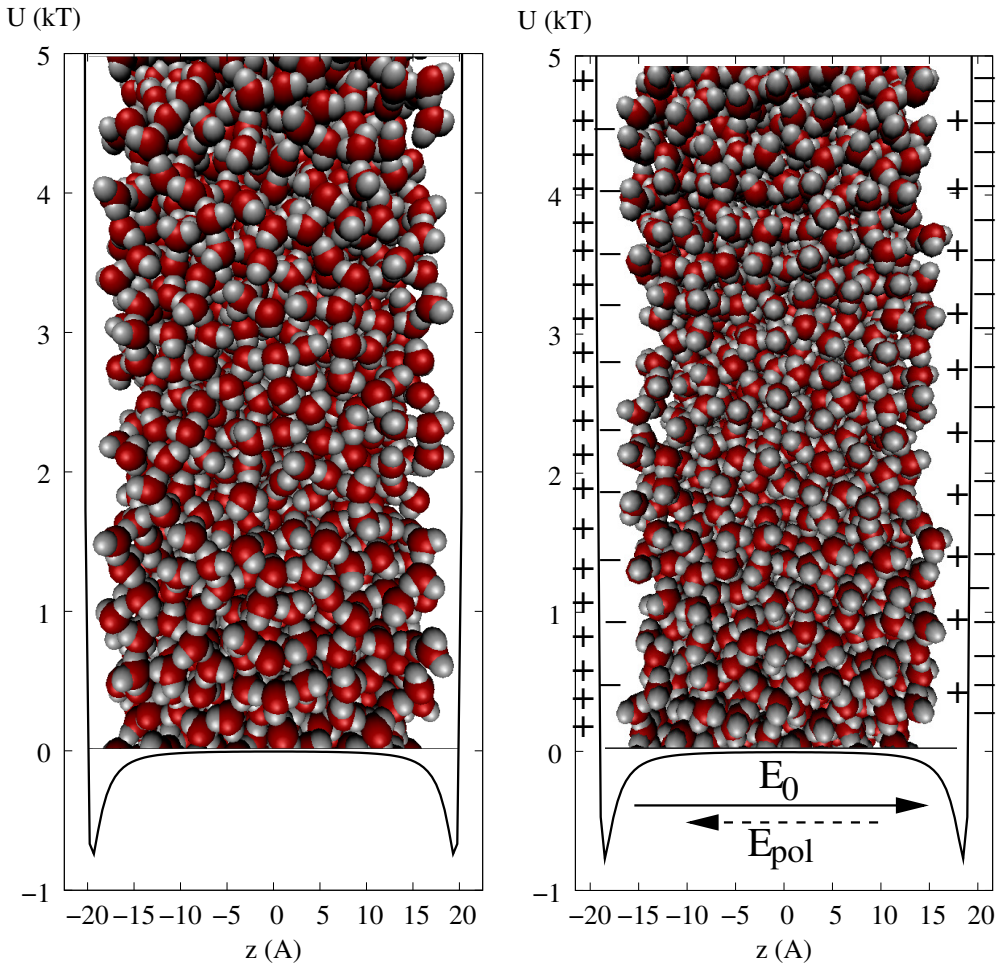

(a) $E_0 = 0.0$ V/Å (b) $E_0 = 1.0$ V/Å

Figure 6.1: Snapshots of SPC/E water confined between hydrophobic LJ walls as defined by Eq. (6.1). Initially we will study systems where no electric field is applied as in (a), but we will later examine systems where electric fields are applied normal to the walls as in (b). In such cases, the spacing between walls is adjusted to maintain bulk density in the center, and the water slab polarizes in response to the applied field.

We again use a modifed version of DLPOLY2.16 [89]. Each simulation has 1024 SPC/E water molecules at 298 K maintained by a Berendsen thermostat [6] with a

time constant of 0.50 ps. A timestep of 1 fs is employed. The lateral area of the simulation box is 27.72 Å × 27.72 Å. The spacing between walls z_w is adjusted to yield bulk water density in the central region. We will examine systems where there is no applied electric field and where there is an applied field E_0. Table 6.1 gives the z_w for each applied field.

E_0 (V/Å)	0.0	1.0	2.0	2.5	2.7	3.0
z_w (Å)	22.5	21.53	21.19	20.72	20.97	21.07

Table 6.1: Hydrophobic wall spacings for varying applied fields E_0.

We will treat electrostatics in the simulations in three ways. Our benchmark will be corrected three-dimensional Ewald sums [114] as described in Sect. 4.6.2, and we will label these results as "Full." For these simulations, L_z is set equal to 140.0 Å, such that L_z is over three times greater than the width of the water slab in the z-direction and is 5 times as large as the lateral spacing of periodic images, making the approximations in corrected three-dimensional Ewald sums reasonable. For these simulations, the Ewald convergence parameter α is set to 0.34 Å^{-1} (equivalent to $\sigma = 2.94$ Å) and the number of k-space vectors are (12,12,60). The real space cutoff radius used for Coulomb and van der Waals interactions is 9.5 Å.

The other two electrostatics techniques used will be Gaussian-truncated water using solely $v_0(r)$ interactions, labelled "Truncated," and full LMF theory using $v_0(r)$ interactions in tandem with a self-consistent $\mathcal{V}_R$, labelled "LMF." Here a conservative σ of 6.0 Å is chosen. We believe that $\sigma = 4.5$ Å should be greater than $\sigma_{\min}$ as well; however a smaller choice of σ leads to greater difficulty in obtaining a self-consistent solution of the LMF equation. Details of the self-consistent solution are delayed until

Sect. 6.5. A cutoff radius of 9.5 Å is maintained for LJ interactions, but the cutoff radius is increased to 13.5 Å for the $v_0(r)$ interactions due to the larger σ.

For all simulations, the system is equilibrated for at least 500 ps, and then data are collected for 1.5 ns. Any error bars shown below are calculated by looking at the standard deviation of data calculated for separate 100 ps sub-windows of the simulation.

6.2 Failure of the Strong Coupling Approximation

As pointed out by Feller, Pastor, Rojnuckarin, Bogusz, and Brooks [28], spherically truncated water fails when confined into a slab geometry, such as a water-vapor interface or a water-membrane junction. Here we first examine nonuniformity created by confining SPC/E water between two hydrophobic walls modeled by smoothed Lennard-Jones walls with no applied field. For this system, the strong coupling approximation consists of $v_0(r)$ interactions and the confining $U_{\mathrm{LJw}}(z)$ since there are no external fixed applied charges.

In this system, water molecules restructure at the hydrophobic wall interface in order to break only one hydrogen bond per molecule on average rather than two [59]. In the process of doing so, the water molecules form a dipole layer near each hydrophobic surface with the dipole pointing toward the walls. The long-ranged forces oppose the further organization of the dipoles near the wall, in a manner similar to Le Chatelier's principle. However, the short-ranged system includes no penalty for the formation of a dipole layer and as such, the wall-proximal layer of water over-orients the dipole

to maximize hydrogen-bonding, and the dipolar orientation propagates into the bulk region and does not relax to an average of zero except in the center as dictated by symmetry. Perturbations in water structure near the wall results in a propagation of the related electrostatic properties into the bulk region of the liquid. In Fig. 6.2, we see the profiles of both the hydrogen bonding and the dipolar orientation. There are a wide variety of geometric hydrogen-bond definitions [58]. We define a hydrogen bond as all water molecules within 3.5 Å of each other with an H$\cdots$O-H hydrogen bond angle θ that is greater than 150°. The number of hydrogen bonds has no discernible difference throughout the bulk region. However the dipole orientation, described by the dot product of the dipole unit vector with the $\hat{z}$ unit vector, shows substantial differences throughout the entire slab region. We do expect the hydrogen-bonding near the surface to be somewhat enhanced in the Gaussian-truncated (GT) system. By the geometric criterion we use, virtually no difference in hydrogen-bonding is evident, but likely the energetic binding due to hydrogen-bonding is stronger. Instead, looking at the probability of various intramolecular O-H bond orientations relative to the wall normal pointing towards the bulk supports the picture that one OH bond points more towards the wall. Figure 6.3 shows the probability density of various OH bond orientations in the 1 Å layer closest to the hydrophobic wall. The increased probability density of orientations with $\cos\theta \simeq -1$ for the GT water models relative to SPC/E water indicate the enhancement of hydrogen bonds.

Shown in Fig. 6.4 are the density profiles of oxygen and hydrogen as well as the charge density for this system. Aside from slight deviations in the peak proximal to the walls, there is good agreement between the density profile determined with

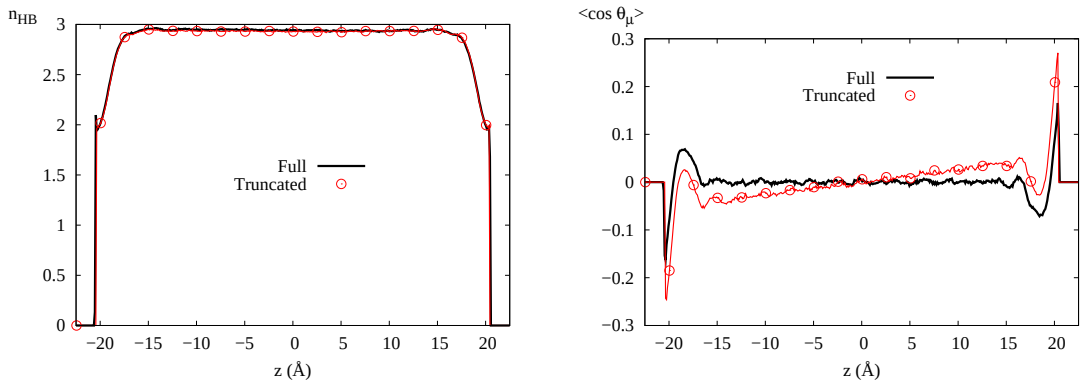

(a) H-bond profile

(b) Dipole profile

Figure 6.2: Plots showing (a) the hydrogen bonding profile and (b) the dipole orientation profile of Gaussian-truncated water compared to that of SPC/E water treated with corrected three-dimensional Ewald sums. Using the geometric criterion described in the text there is no discernible difference in the hydrogen-bonding profile. The dipole orientation profile, defined as the average dot product between the dipole unit vector and the wall normal point toward the bulk, is clearly wrong, with strong overorientation near the surfaces propagating into the bulk region. Only one in every 25 data points is plotted.

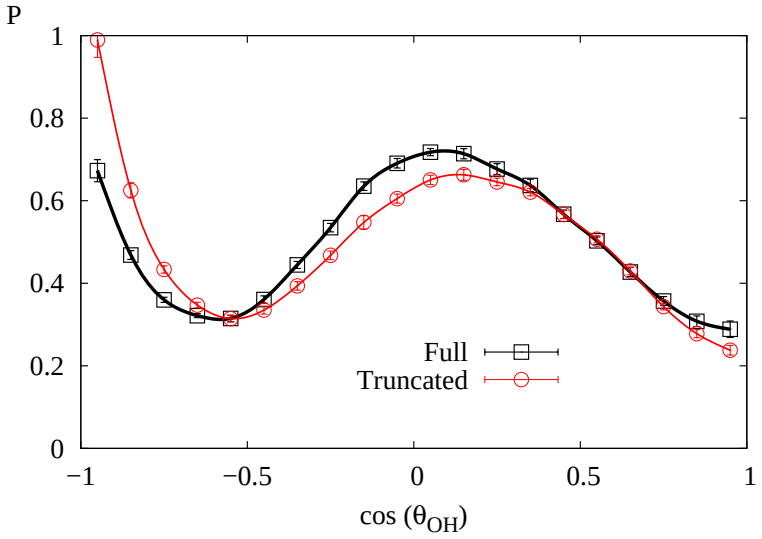

Figure 6.3: Probability distribution for various intramolecular OH bond orientations for water molecules in the 1 Å layer closest to the surface. We define $\cos(\theta_{\mathrm{OH}})$ as the dot product between a bond vector pointing from O to H with the wall normal point toward the bulk. GT water clearly has a greater propensity to orient one of its hydroxyl groups toward the wall than SPC/E water. Smooth lines provided as a guide to the eye.

corrected three-dimensional Ewald sums and that determined by spherical truncation using $v_0(r)$. Even the charge density profile defined as $\rho^q(z) = q_{\mathrm{H}} \cdot \rho_{\mathrm{H}}(z) + q_{\mathrm{O}} \cdot \rho_{\mathrm{O}}(z)$ looks quite reasonable, and the formation of a dipolar charge layering near the walls appears evident.

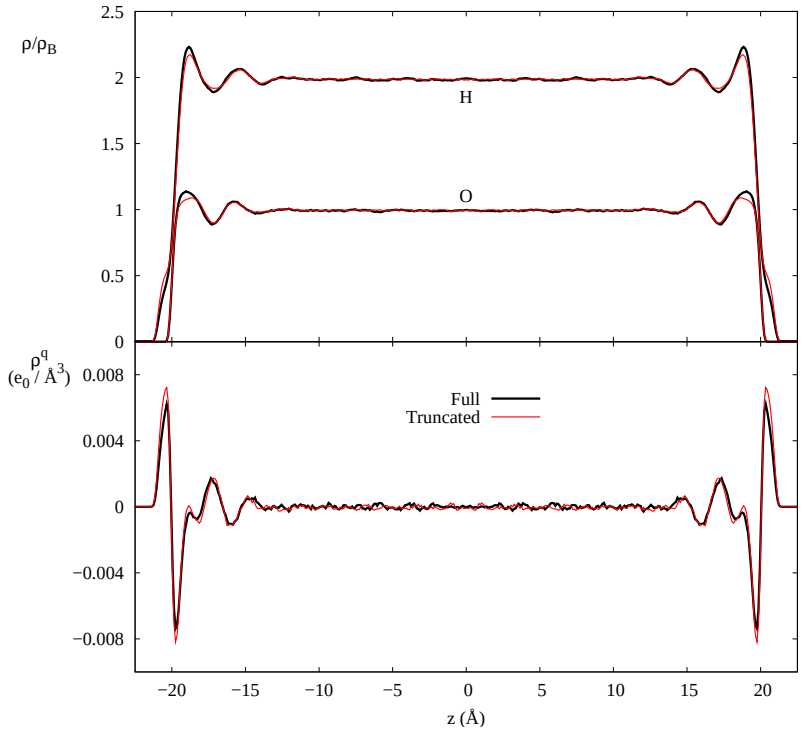

Figure 6.4: In the top panel, $\rho_{\mathrm{O}}(z)$ and $\rho_{\mathrm{H}}(z)$ are plotted relative to the bulk density of water. In the lower panel, the charge density ρ^q is plotted. ρ^q is defined as the linear combination $q_{\mathrm{O}}\rho_{\mathrm{O}}(z) + q_{\mathrm{H}}\rho_{\mathrm{H}}(z)$. For the most part substantial agreement is evident between the density profiles for SPC/E water and for GT water. Very slight deviations in the wall-proximal peaks are present.

In fact, these observations seem to contradict the previous conjecture that local perturbations in molecular structure have long lengthscale effects in electrostatic properties. The charge density profile appears to be quite accurate, aside from slight deviations in the peak near the walls. This contradiction may be understood if we look at the *smoothed* charge density $\rho^{q_\sigma}(z)$ in Fig. 6.5, as initially discussed in Ch. 4.

The smoothed charge density of the system treated with corrected Ewald sums clearly displays the dipole layer near each wall with first a layer of positive charge density and then a layer of negative charge density. In contrast, when the system is simulated with solely $v_0(r)$, a finite width dipole layer clearly does not form. We might interpret this as the smoothed charge density reflecting true electro*static* behavior of the system. The atomic level charge density ρ^q contains hints of the true electrostatic behavior, however the relevant aggregate smoothed charge densities are two orders of magnitude smaller than the peaks in the atomic level charge density. Furthermore, the peaks in ρ^q span only 2 Å and we might reasonably assume that such details should be averaged over an atomic volume, as suggested in introductory electrostatics texts [17]. Smoothing the charge density achieves just that.

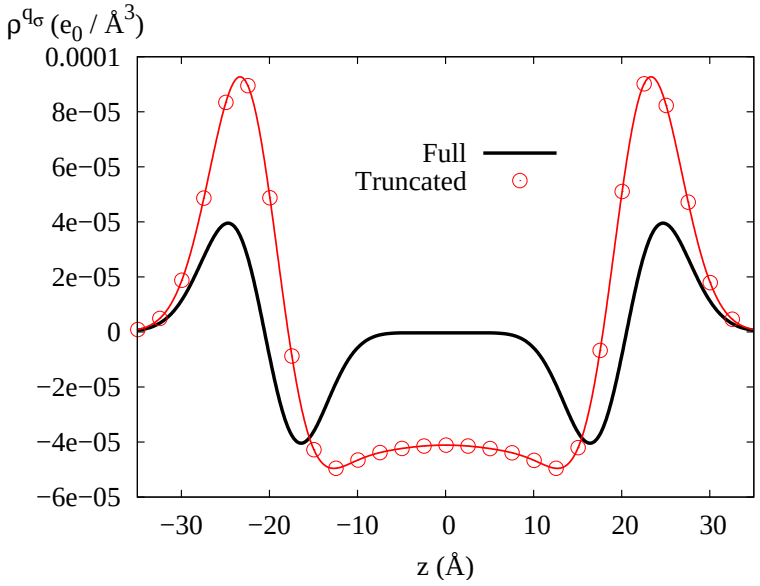

Figure 6.5: Gaussian-smoothed charge density of full SPC/E and GT water confined between hydrophobic walls. The smoothing length σ is 6.0 Å, and one in every 25 points is shown. The failure of GT water to create a well-defined dipole layer localized to the wall region is much more evident in $\rho^{q\sigma}$ and than it was in ρ^q.

One criticism of the observation of the two orders of magnitude separation between

ρ^q and ρ^{q_σ} peak heights is that the peaks now span a much broader range in the z-direction. However, that span is only one order of magnitude different, so there still exists an approximately one order of magnitude difference in the peak areas. Furthermore, the incorrect plateau region for the smoothed charge density of the $v_0(r)$ system is still two orders of magnitude smaller and thus on the scale of the noise in the simulation.

The alternate interpretation of the LMF treatment of electrostatics as the potential due to a Gaussian-smoothed charge density greatly clarifies when short-ranged interactions without a self-consistent $\mathcal{V}_R$ will be successful. If we view the short-ranged cores as altered to reflect both Lennard-Jones cores as well as hydrogen-bonding and polar attractions represented by $v_0(r)$, then the charge density which reflects the long-ranged electrostatics is not ρ^q, but rather the Gaussian-smoothed equilibrium charge density ρ^{q_σ}. The Gaussian-truncated water model then encompasses short-ranged effects like hydrogen-bonding. The longer-ranged electrostatics is represented by a smoothing of the charge density, which is more in-line with the quantum-mechanical reality that molecules have electron clouds, not pseudo-point charges. Given that σ may be chosen as any value greater than some $\sigma_{\min}$ for LMF simulations, too much significance should not be assigned to a chosen σ. But interpreting the electrostatic behavior based on some smoothed charge density rather than the atomic level charge density may better reveal the long-ranged effects. Previous authors [44] have suggested the atomic-level charge density profile as a less-biased representation of electrostatic effects than some molecular-based cutoff scheme; perhaps a smoothed profile is even less biased.

An extreme exhibit of the failure of spherically truncated water more commonly found in the literature [93, 114] is the electrostatic potential profile $\Phi_{\rm pol}(z)$, defined as

$$\Phi_{\rm pol}(z) = -\frac{1}{\epsilon_0}\int_{-L/2}^{z} dz' \int_{-L/2}^{z'} dz'' \rho^q(z'') \tag{6.2}$$

in SI units. This potential profile is wholly due to the polarization of the water molecules as a result of the presence of the surface. It should have a negative shift proceeding from the surfaces into the water since the the water dipoles orient towards the walls, and then a plateau should form representing the subsequently bulk nature of that water. As shown in Fig. 6.6, GT water clearly does not exhibit a plateau while true SPC/E water does. The lack of a plateau in $\Phi_{\rm pol}(z)$ occurs for GT water for exactly the same reason that ρ^{q_σ} does not have clearly formed dipole layers nor a bulk region of zero charge density. GT water models preferentially form as strong a hydrogen-bonding network as possible without energetically penalizing surface conformations with strong dipolar ordering. This effect is shown qualitatively in Fig. 6.7.

6.3 $\mathcal{V}_R$ Enables Gaussian-Truncated Water to Succeed

The inclusion of a self-consistent $\mathcal{V}_R$ corrects the prominent difficulties of using short-ranged water for this system. As shown in Fig. 6.8, using $\mathcal{V}_R(z)$ in tandem with $v_0(r)$ leads to exactly the plateau we expect for the polarization potential profile $\Phi_{\rm pol}(z)$ in the central bulk region, as well as correcting all other previously observed structural and electrostatic deficiencies with GT water simulations:

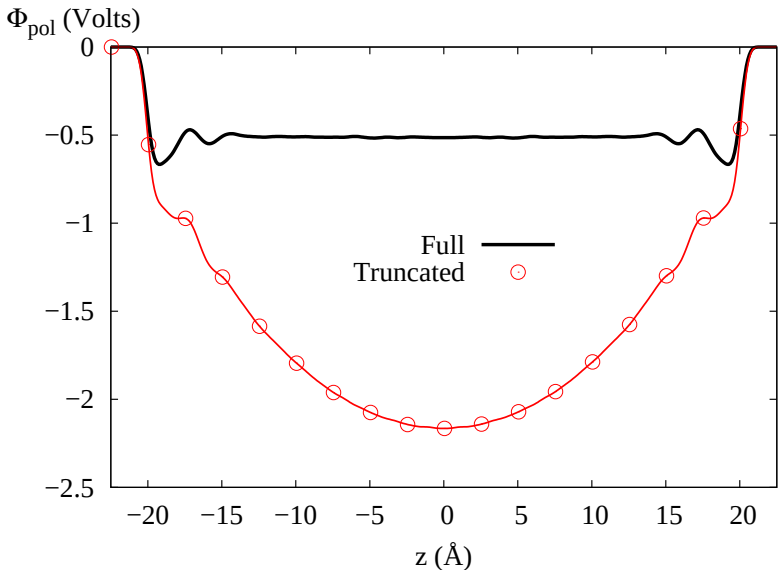

Figure 6.6: The electrostatic potential profile $\Phi_{\rm pol}(z)$ due to water polarization near the surface, as defined in Eq. (6.2), is plotted. SPC/E water exhibits a relatively discrete decrease in potential moving from the wall into the bulk region. GT water never forms a true "electrostatic" bulk region, identified here as a plateau in $\Phi_{\rm pol}$. One in 25 data points is shown.

- the dipole orientation profile throughout the slab,
- intramolecular O-H bond orientation profile,
- the oxygen, hydrogen, and atomic-level charge densities near the wall, and
- the smoothed charge densities throughout the slab.

If we examine the orientations of water molecules near the surfaces in more detail we again find substantial agreement between the full system and the treatment with a self-consistent LMF solution. Shown in Fig. 6.9, are the dipole orientation profiles for four distinct 1.0 Å width slabs of water normal to the walls. Each graph depicts the probability density of a given water molecule orientation relative to the wall defined as $\cos\theta_\mu = \hat{\mu}\cdot\hat{z}$ where $\hat{z}$ points into the bulk. Since $\cos\theta$ spans $[-1,1)$, if

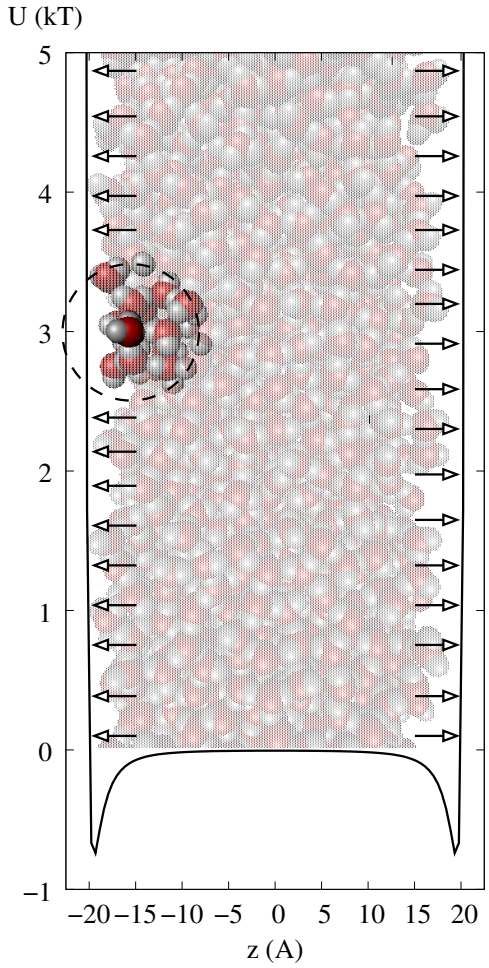

Figure 6.7: Diagram sketching the failure of GT water to account for the long-ranged effects of dipolar aggregation near each wall. As represented pictorially above, GT water simply includes forces within $\sim \sigma$, indicated by the fully shaded water molecules within the dashed circle. There is no energetic penalty to associated with the formation of the dipole layer shown with the arrows because the GT water molecule does not interact with the lightly shaded molecules at all.

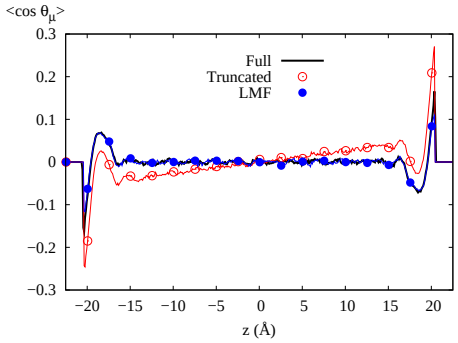

(a) $\langle \cos(\theta_\mu) \rangle (z)$

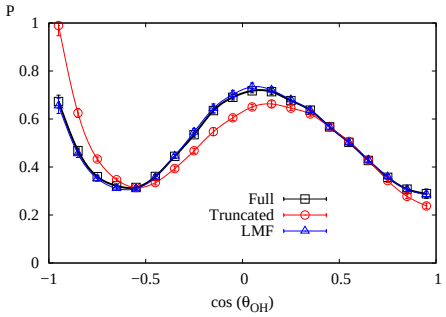

(b) $P(\cos\theta_{\mathrm{OH}})$

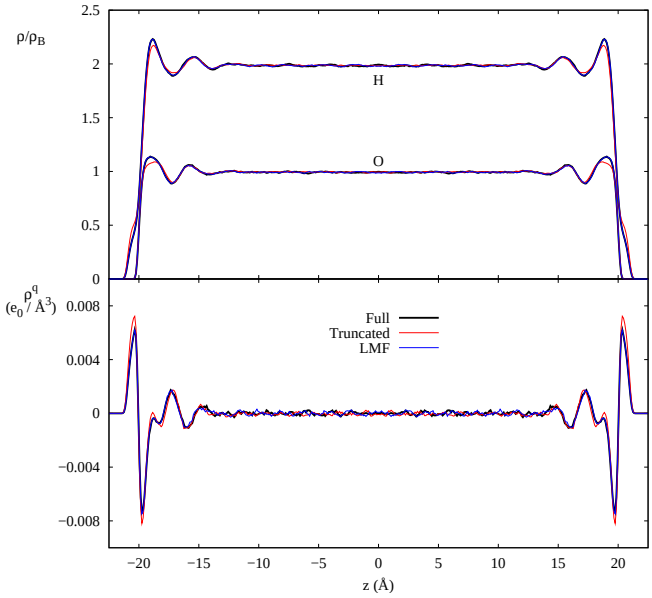

(c) $\rho_{\mathrm{O}}(z)$, $\rho_{\mathrm{H}}(z)$, and $\rho^q(z)$

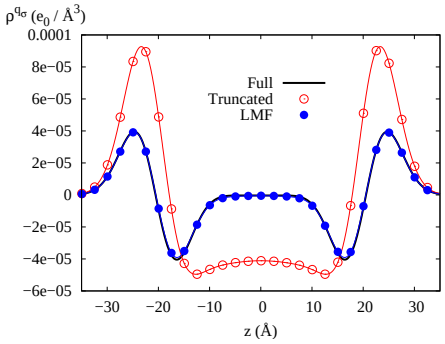

(d) ρ^{q_σ}

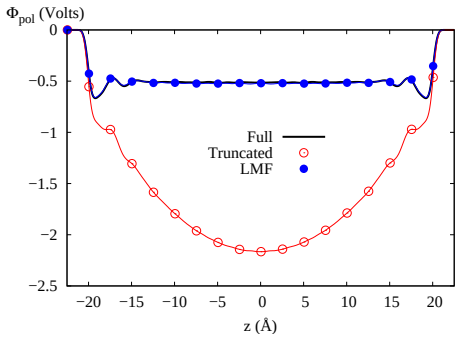

(e) $\Phi_{\mathrm{pol}}(z)$

Figure 6.8: Using the LMF-dictated $\mathcal{V}_R$ corrects all structural and electrostatic properties for GT water. All properties above have excellent agreement between the full LMF treatment and the corrected Ewald approach used for SPC/E. When the thick black line for SPC/E is not visible, this is due to the LMF data overlapping so well.

there is an equal likelihood of each orientation as we expect in the bulk region, then $P(\cos\theta_\mu) \simeq 0.5$. In the layer closest to the wall, a preference for dipoles pointing towards the wall ($\cos\theta_\mu < 0$) is evident, as well as the tendency for GT water to allow *over*orientation of the dipole. While the probability distributions do not look vastly different, it is exactly these slight shifts which lead to the errors in $\langle\cos\theta_\mu\rangle(z)$ and in $\Phi_{\rm pol}(z)$. The poor predictions of GT water and the appropriate corrections due to the LMF equation continue for several layers of water. In the central bulk region, the errors in GT water are not as evident; this is largely due to the zero dictated by symmetry. The trends for intermediate distances from the wall show that GT water does indeed continue to skew orientational distributions well into the bulk region, and at a detailed level, $\mathcal{V}_R$ corrects these skews to within error bars.

The form of $\mathcal{V}_R$ in Fig. 6.10 makes the reason for the success of clear. For the full system there is no applied external potential $\mathcal{V}$; however there are net long-ranged electrostatic effects due to the overall ordering of water molecules. The nonzero $\mathcal{V}_R(z)$ reflects this effect by applying a reorienting torque on surface water molecules. The favorability of maintaining hydrogen bonds drives one intramolecular O-H bond to orient with the hydrogen facing the wall. $\mathcal{V}_R$ exerts a torque opposing this tendency. The self-consistency of $\mathcal{V}_R$ represents a statistical mechanical balance between the favorability of maintaining hydrogen bonds and the penalty for creating an overly severe dipole layer.

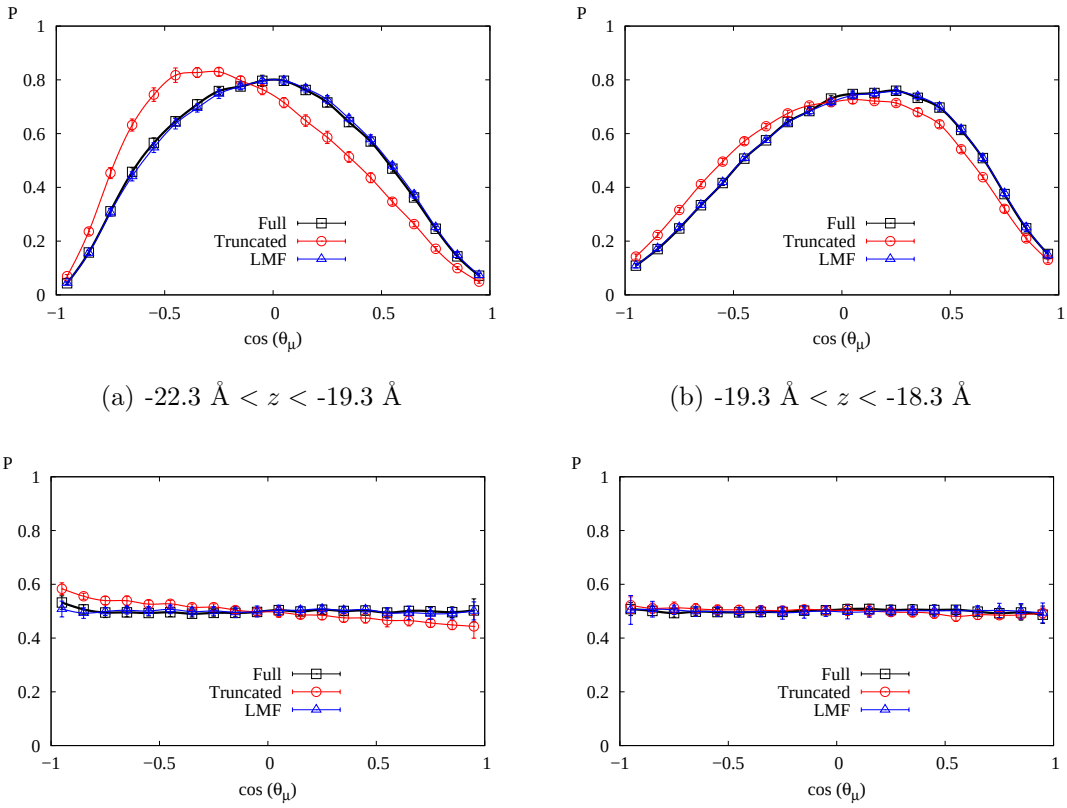

(a) -22.3 Å $< z <$ -19.3 Å

(b) -19.3 Å $< z <$ -18.3 Å

(c) -14.3 Å $< z <$ -13.3 Å

(d) -4.3 Å $< z <$ -3.3 Å

Figure 6.9: Plots of $P(\cos\theta_\mu)$, the probability distribution of dipole orientations, in various 1 Å thick slabs. The layers shown represent wall proximal layers in (a) and (b) and bulk region layers in (c) and (d). Orientation of of the dipole pointing toward the wall is evident in the closest layer to the wall. Detailed short-ranged interactions of the water molecules actually lead the dipole to point on average slightly into the bulk in the next 1 Å layer. The incorrect behavior of GT water, as compared to full SPC/E and the LMF approach, is evident in every layer but the final layer. Such deviations there are within the error bars because of the required symmetry about $z = 0$.

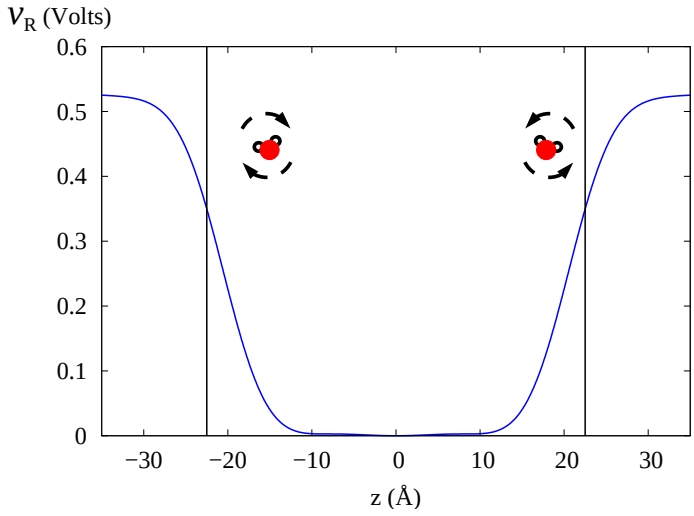

Figure 6.10: Plot of self-consistent $\mathcal{V}_R(z)$ for water between the hydrophobic walls. The main effect of $\mathcal{V}_R$ is to exert a torque on the surface water molecules, opposing the tendency of a hydroxyl group to point toward the wall. Self-consistency leads to a statistical mechanical balance between the maintenance of hydrogen-bonding and the opposition to dipole ordering.

6.4 Application of an Electric Field

Application of an electric field normal to the walls containing the slab of water, as depicted in Fig. 6.1(b), actually results in a more extreme and obvious failure of spherically truncated water. To the best of our knowledge, this failure has not been published, but it is known by some researchers. When an electric field is applied to a slab of water, the confined water should behave as a dielectric slab from introductory electrostatics [17, 80]. Thus the water molecules should polarize in response to the field to attenuate the applied field, and the dielectric constant is the ratio between the applied field and the total field in the central region. This field E_{tot} is defined in

the following formualae as

$$E_{\mathrm{pol}}(z) = \int_{-\infty}^{z} \frac{\rho^q(z')}{\epsilon_0}\, dz' \tag{6.3}$$

$$E_{\mathrm{tot}}(z) = E_0 + E_{\mathrm{pol}}(z) \tag{6.4}$$

$$\epsilon = \frac{E_0}{\langle E_{\mathrm{tot}} \rangle_c}, \tag{6.5}$$

where $\langle \cdots \rangle_c$ indicates an average over the central region of the slab. The naïve use of spherical truncations actually leads to a *negative* dielectric constant with this definition.

The calculation of ϵ is not immediately necessary though since the failure of such spherical truncations is evident in the density profiles of atoms and charge. The profiles shown in Fig. 6.11 are *qualitatively* incorrect for GT water alone. Even for 1.0 V/Å, the weakest field strength we examine, GT water has organized in a near crystalline fashion normal to the wall. Here we also see a milder example of the failure of three-dimensional Ewald sums when they are not corrected, as beautifully explained by Yeh and Berkowitz [114]. The reasons for this failure have been explored to an extent in Sect. 4.6.2. Various examples of this failure will be seen throughout this section on applied fields.

As depicted schematically in Fig. 6.12, using spherical truncations alone neglects the long-ranged ordering of the water molecules in response to the applied field E_0. As in the case with no applied electric field, the long-ranged forces act to attenuate and weaken the applied electric field in the central region as in Le Chatelier's principle. Thus the water molecules over-order with the unattenuated electric field. The failure of GT water is again an overdeference to short-ranged interac-

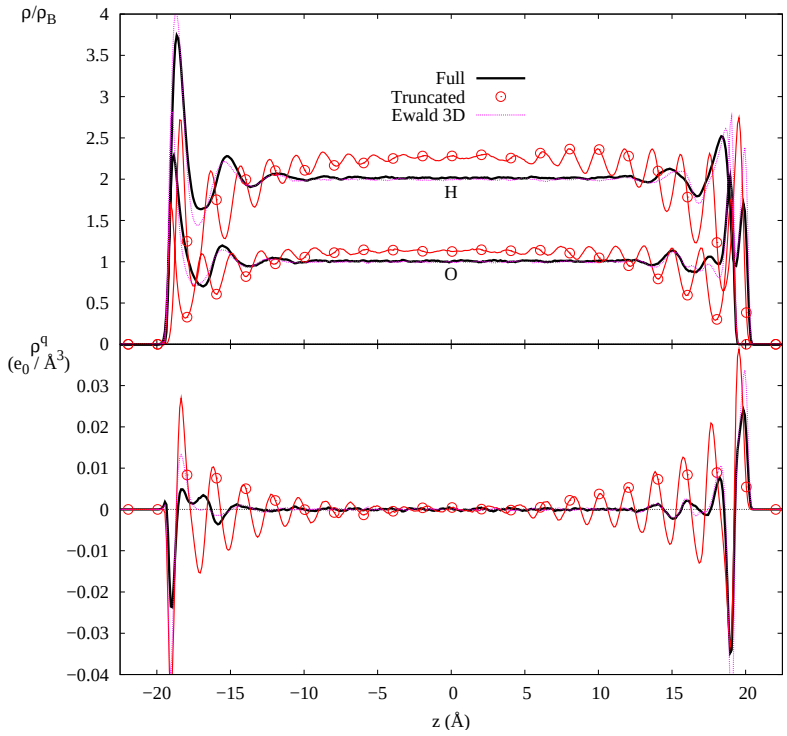

Figure 6.11: Density profiles when a field of 1.0 V/Å is applied. The top panel displays $\rho_{\mathrm{O}}(z)$ and $\rho_{\mathrm{H}}(z)$, and the bottom panel shows $\rho^q(z)$. GT water is distinctly incorrect for any density profile, and even three-dimensional Ewald sums (Ewald 3D) without the appropriate slab correction due to Yeh and Berkowitz [114] are visibly incorrect near the walls. One in 25 data points in plotted.

tions without the consequences of the opposing net long-ranged forces. In contrast to the previous case where the dominant short-ranged force was hydrogen bonding, in this case there is another strong short-ranged force – the externally applied electric field. An energetically-favored arrangement of hydrogen bonding can actually reinforce an incorrect strongly-ordered state favored throughout the liquid for strong applied fields. Comparing the hydrogen-bonding profiles between the full system and Gaussian-truncated system in Fig. 6.13, a greater degree of hydrogen bonding in the GT system is clear throughout the bulk region. This hydrogen-bond stabilization of an incorrect ordered state driven by electrostatics actually leads to very obvious differences in structure.

In this section we will examine the range of electric field strengths studied by Yeh and Berkowitz [112, 114], though these fields would reasonably be considered quite strong [18, 98]. This choice is a somewhat direct, practical result of the impact of fluctuations in the short-ranged systems, to be examined in more detail in Sect. 6.5.

One could attempt a strong coupling approximation where the electric fields are generated by smooth walls of charge located at $\pm z_w$. However such an approximation is nowhere near as successful as the strong coupling approximation used in Ch. 3. This is caused by two different reaons. First the strong coupling approximation in this system essentially assumes full shielding of the electric field in the central region, which is appropriate for ionic systems but not for dipolar systems. Secondly, the electric field generates an asymmetry in the charge density relative to wall positions, and there is no unbiased fashion for shifting the origin of the charged walls to account for this. Since a true SCA is not successful in this system, we mainly focus on the

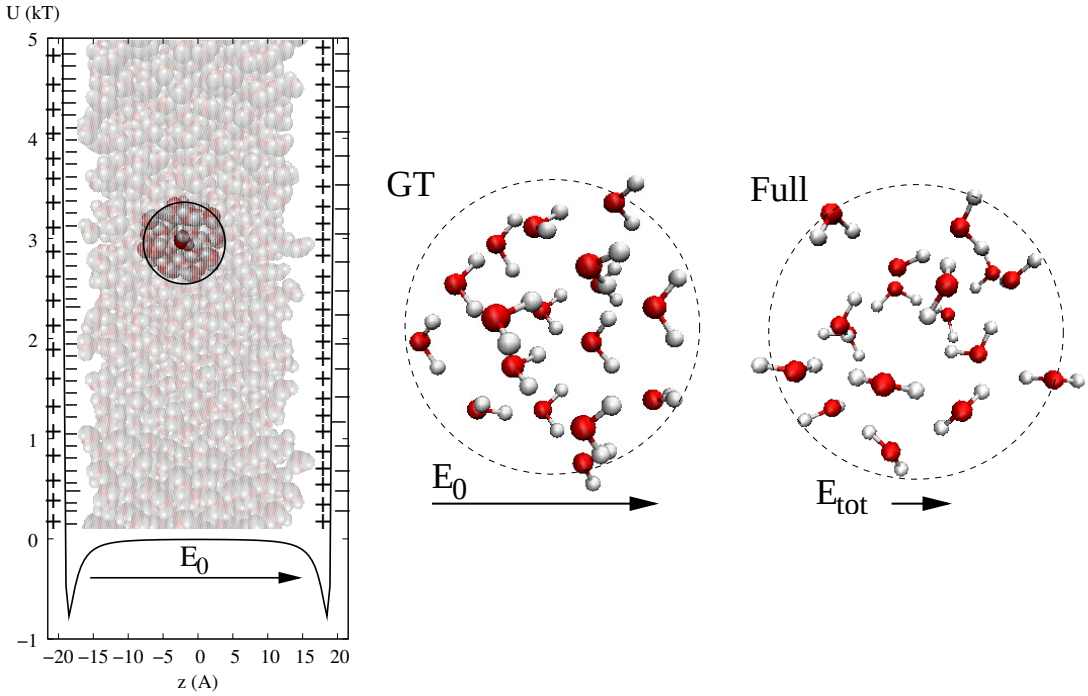

(a) Full Width (b) Central Region

Figure 6.12: Schematics showing the net impact of neglecting the long-ranged forces when a field is applied. In (a), the particles that exert forces on a given water particle are shown in a darker color. Also, the full applied field E_0 acts on that given particle. In (b), a snapshot of particles within 10 Å of the origin in the simulation cell is given for both the GT system and the full SPC/E system. The strong ordering of GT water in the full applied field E_0 is in sharp contrast with the mild orientation of the SPC/E water with the attenuated total field E_{tot}.

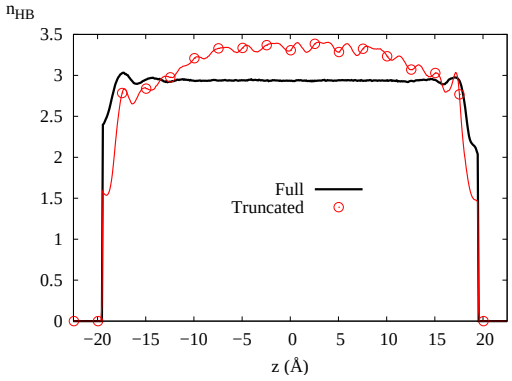

Figure 6.13: Plot of the hydrogen bonding as a function of z for GT water and the full system when $E_0 = 1.0$ V/Å. The enhancement of hydrogen bonding in the applied field is evident.

self-consistent LMF approach.

The inclusion of a self-consistent $\mathcal{V}_R(z)$ to represent the long-ranged net effect of water-molecule polarization makes the density profiles again agree quite nicely with the results for the full system. The form of $\mathcal{V}_R(z)$ as compared to the original applied $\mathcal{V}(z)$ in Fig. 6.14 demonstrates why the LMF approach is successful. In the purely short-ranged system, the water molecules in the central region experience the full force due to the applied field E_0 without any attenuation of the field due to the polarization of the water in response to the field. A self-consistent solution of the LMF equation to yield $\mathcal{V}_R(z)$ includes the effects of those long-ranged forces, such that near the walls, the molecules experience nearly the full effect of the applied field E_0, while in the bulk region, the molecules experience only the net electric field E_{tot} which is substantially lessened.

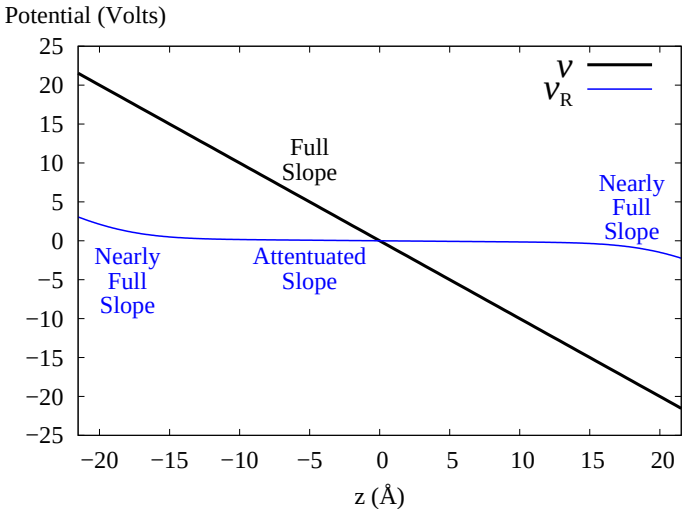

Figure 6.14: Plot of $\mathcal{V}_R(z)$ for $E_0 = 1.0$ V/Å. The full electrostatic potential $\mathcal{V}$ with a constant slope of -1.0 V/Å is rescaled such that nearly the full electric field is applied near the walls but the slope is substantially attenuated in the bulk region applying the much weaker E_{tot} on the GT water molecules in that region.

Given a self-consistent $\mathcal{V}_R(z)$, determined as described later in Sect. 6.5, good

agreement for all density profiles is found. The results for $\rho_{\mathrm{O}}(z)$, $\rho_{\mathrm{H}}(z)$, and $\rho^q(z)$ are shown in Fig. 6.15 for the full range of applied field E_0 studied. [1] The inclusion of $\mathcal{V}_R(z)$ makes a *substantial* improvement over the GT water simulations using solely $v_0(r)$.

Furthermore, for two of the studied fields, 1.0 V/Å and 2.5 V/Å, the more detailed analysis of water molecule orientations shows equally strong agreement, in contrast to simply Gaussian-truncated water. In Fig. 6.16, just as in Fig. 6.9, the probability density of various orientations of water molecules relative to the walls are shown. In $P(\cos\theta_\mu)$, $\cos\theta_\mu$ is defined as $\hat{\mu}\cdot\hat{z}$ with $\hat{z}$ point in the positive z-direction, just as the electric field. When a water molecule orients with the field $\cos\theta_\mu > 0$ and the molecule is anti-aligned when $\cos\theta_\mu < 0$. When an electric field is applied, the symmetry about $z = 0$ is broken and thus orientations at the walls at $\pm z_w$ are not equivalent, just as the densities near each wall in Fig. 6.15 were not equivalent either. Only three 1.0 Å width layers are shown for each field in Fig. 6.16, the closest layer to each wall, each of which exhibits strong orientational ordering, and a central layer which has less net orientation, provided that long-range forces due to the water ordering are accounted for. The asymmetry between the water layers near each wall is evident. Charge density asymmetry might be viewed as simply due to the fact that the LJ walls confining the water hold the oxygen centers relatively symmetrically confined, but the hydrogen atoms preferentially orient towards the $+z$ direction due to the action of the electric field. However, the asymmetric orientations of dipoles is due to

[1] $E_0 = 2.7$ V/Å is omitted for space but data for the corresponding dielectric constant will be presented later.

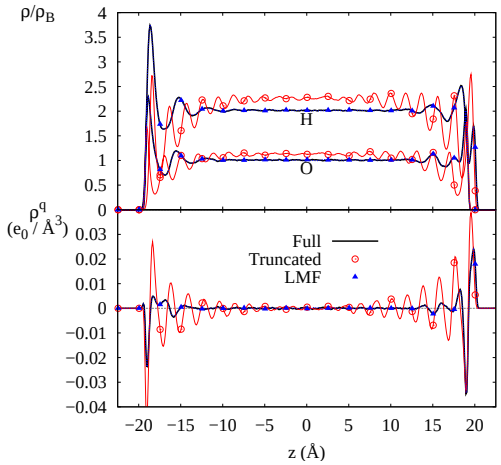

(a) $E_0 = 1.0$ V/Å

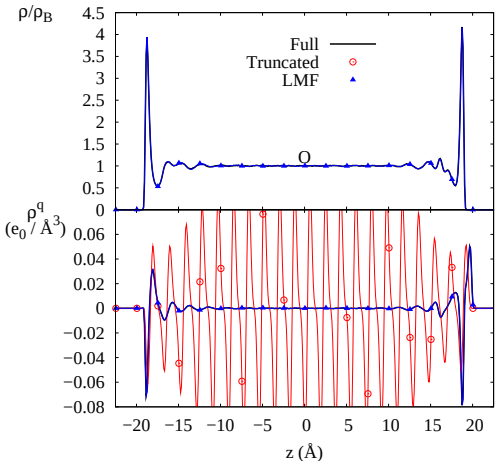

(b) $E_0 = 2.0$ V/Å

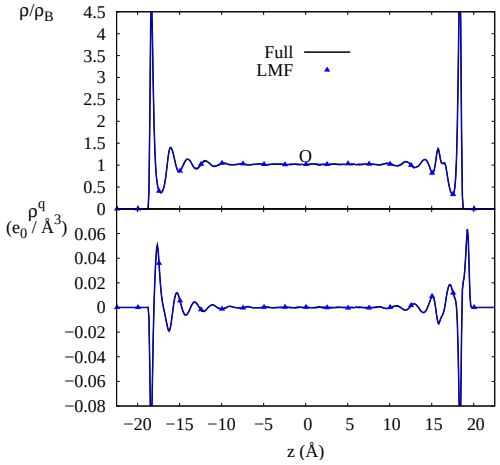

(c) $E_0 = 2.5$ V/Å

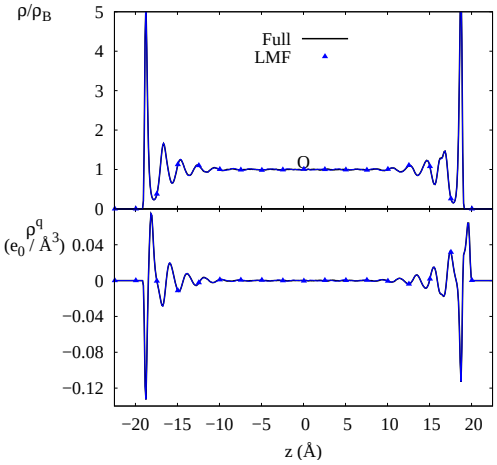

(d) $E_0 = 3.0$ V/Å

Figure 6.15: The density profiles $\rho_{\mathrm{O}}(z)$, $\rho_{\mathrm{H}}(z)$, and $\rho^q(z)$ for the range of applied field strengths. The site density profiles are in the top panels and the charge density profiles are in the lower panels. For clarity, $v_0(r)$ plots are omitted on several of the graphs and $\rho_{\mathrm{H}}(z)$ is only shown for $E_0 = 1.0$ V/Å. The excellent agreement between SPC/E water and the LMF approach is evident. One in 25 data points in plotted

the fact that near the $+z$ wall, the field orients the water dipole towards the wall, just as the minimizing of hydrogen-bond breaking would do. In contrast near the left wall, these two effects are in opposition. Therefore, this asymmetry is not surprising; it is a direct consequence of the fact that the water slab has an atomic structure. In the bulk region, we expect that $\langle \cos\theta_\mu \rangle$ should be greater than 0; in other words the molecules orient on average with the electric field. However the net effect of the water molecule polarization should ensure that this average orientation in the bulk dielectric region should be weaker than near the walls.

In fact, given the degree of structure across the entire slab when an electric field is applied, it is interesting to look at the entire set of $P(\cos\theta_\mu)$ for all slabs of water. This data is shown for the same two applied fields in Fig. 6.17. In Figs. 6.17(a) and 6.17(b), three-dimensional plots show the $P(\cos\theta_\mu)$ of GT water for each z. The vertical axis denotes the probability density, the horizontal axis the the z-value, and the axis projecting into the page is $\cos\theta_\mu$. Since each z-value has a unique probability density function associated with it, any two-dimensional slice for a fixed z-value should have a total area of 1. For each field, there is substantial orientation with the field (high probability density for $\cos\theta_\mu > 0$. In fact, even for $E_0 = 1.0$ V/Å, nearly all dipoles are aligned with the field, regardless of position within the slab when only $v_0(r)$ is used.

Those two orientational surfaces are in sharp contrast with the true surfaces for SPC/E water shown in Figs. 6.17(c) and 6.17(d). These surfaces are shown as a two-dimensional projection of the three-dimensional plot, with the color or grayscale indicating the value of the probability density. Looking at these projections, there

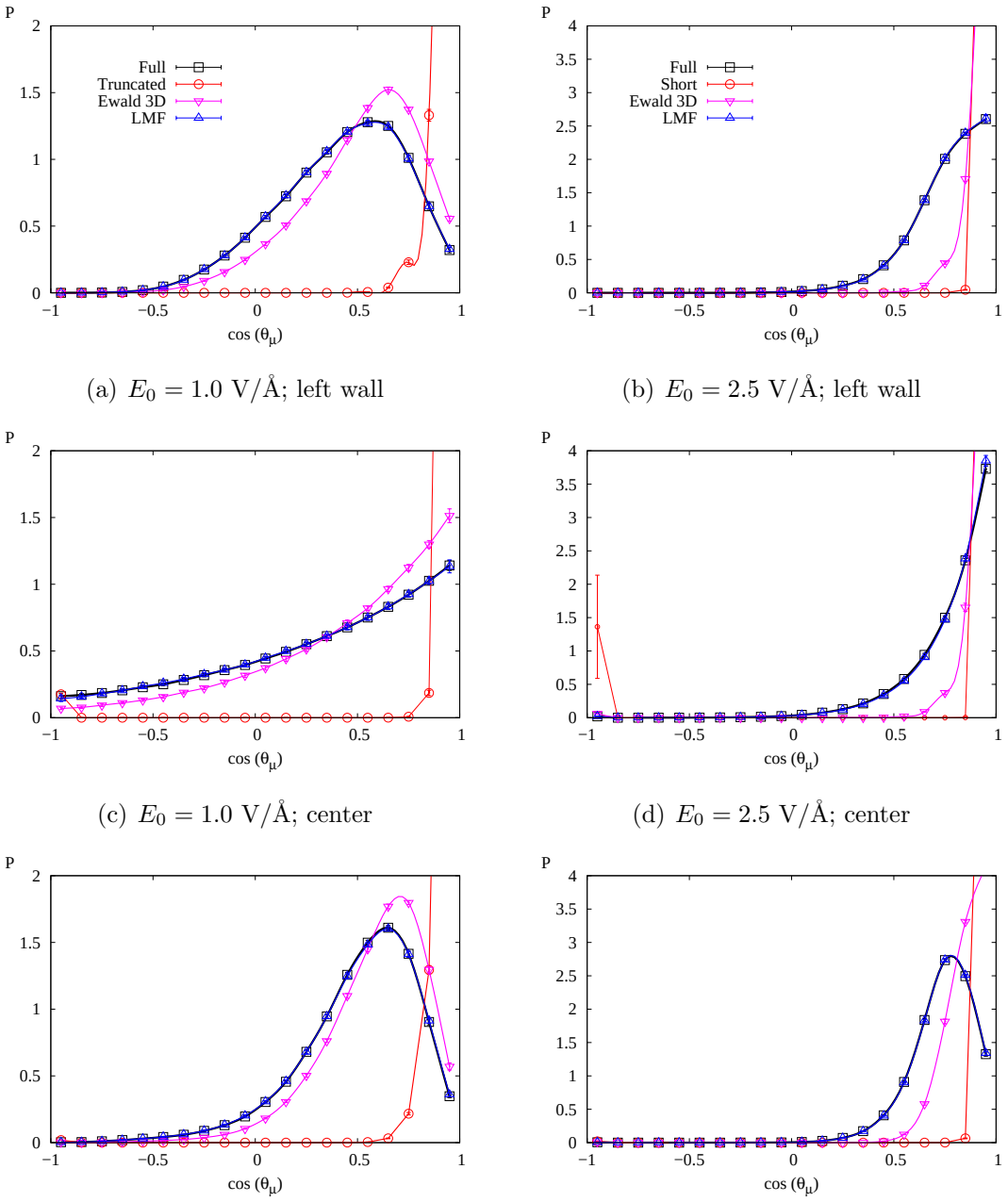

(a) $E_0 = 1.0$ V/Å; left wall

(b) $E_0 = 2.5$ V/Å; left wall

(c) $E_0 = 1.0$ V/Å; center

(d) $E_0 = 2.5$ V/Å; center

(e) $E_0 = 1.0$ V/Å; right wall

(f) $E_0 = 2.5$ V/Å; right wall

Figure 6.16: Plots of $P(\cos\theta_\mu)$ within 1 Å wide layers for $E_0 = 1.0$ V/Å and $E_0 = 2.5$ V/Å. $\cos\theta_\mu$ is determined by the dot product between the dipole unit vector and $\hat{z}$. Layers proximal to the left wall, (a) and (b), proximal to the right wall, (e) and (f), and in the central bulk region, (c) and (d), are shown. There are distinct profiles in the three regions due distinct structuring near each wall and in the bulk region. In all cases, GT water clearly overorients the water molecules with the field. Three-dimensional Ewald sums without the slab correction also overorient the water molecules. The agreement between SPC/E water and GT water combined with $\mathcal{V}_R$ is evident.

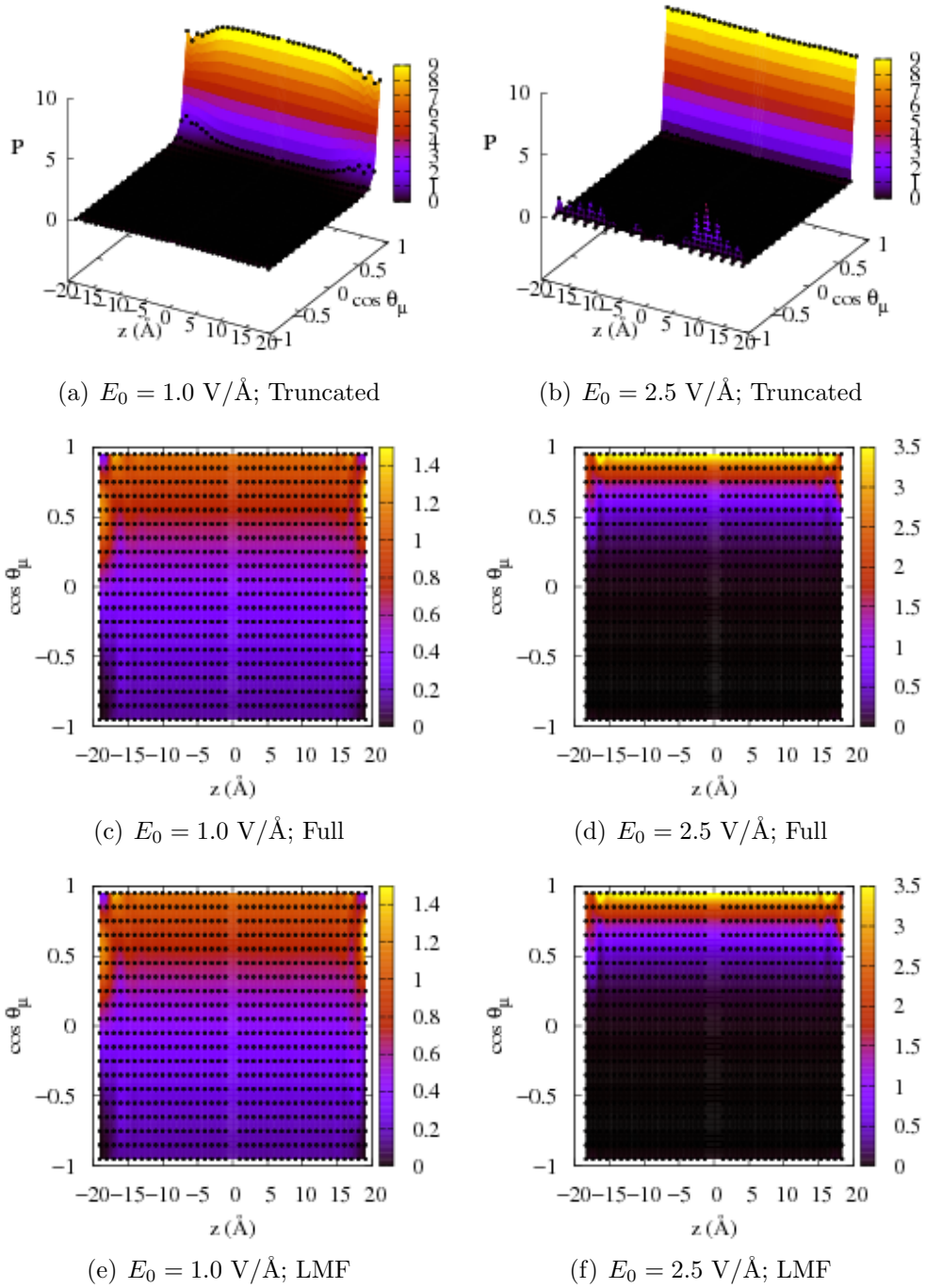

(a) $E_0 = 1.0$ V/Å; Truncated

(b) $E_0 = 2.5$ V/Å; Truncated

(c) $E_0 = 1.0$ V/Å; Full

(d) $E_0 = 2.5$ V/Å; Full

(e) $E_0 = 1.0$ V/Å; LMF

(f) $E_0 = 2.5$ V/Å; LMF

Figure 6.17: Plots of $P(\cos\theta_\mu)$ for each z for E_0 of 1.0 V/Å and 2.5 V/Å. Data for GT water in are presented in three-dimensional plots. Data for SPC/E water and for GT water LMF-corrected with $\mathcal{V}_R$ are presented as two-dimensional projections with the color variation indicating different probability densities as indicated by the scale to the right of each graph. Actual data points are represented by black dots, with interpolation between points carried out by GNUPLOT.

is clearly a strong tendency to align with the field near each wall. However, there is also a significant possibility of dipoles even anti-aligning with the field in the central bulk region. This is more prevalent for the weaker electric field, but, nonetheless, the differences of each from the results using simply $v_0(r)$ are quite severe. Treating the simulations using LMF theory leads to strong agreement throughout the water slab for all water orientations as shown in Figs. 6.17(e) and 6.17(f).

The results with dipole orientation already suggest that the LMF treatment captures not only the atomic density profiles but also the electrostatic behavior, since dipole orientations followed the trend of electrostatics rather than densities for the wate slab without a field. However the atomic level charge densities in Fig. 6.15 (repeated in Fig. 6.18) are not particularly evocative of the electrostatic behavior we expect. Since the water slab should behave as a classical dielectric, we expect positive charge to build up at the $+z$ wall, negative charge to conglomerate at the $-z$ wall, and no net charge in the central region. The atomic level charge densities contain so much detail about the ordering of oxygen and hydrogen atoms that the underlying electrostatic behavior is not as clear. As in the case of no applied field, smoothing the charge density, as shown in Fig. 6.18, displays the appropriate "electrostatic" behavior.

Further, as suggested by the analogy to a dielectric, we may calculate the dielectric constant for various approaches using the formulae in Eq. (6.5). From the charge density profiles, we determine the total electric field as a function of z. This profile is shown for $E_0 = 1.0$ V/Å in Fig. 6.19. The ratio between the applied field and the total electric field in the central bulk region should simply be the dielectric constant, as

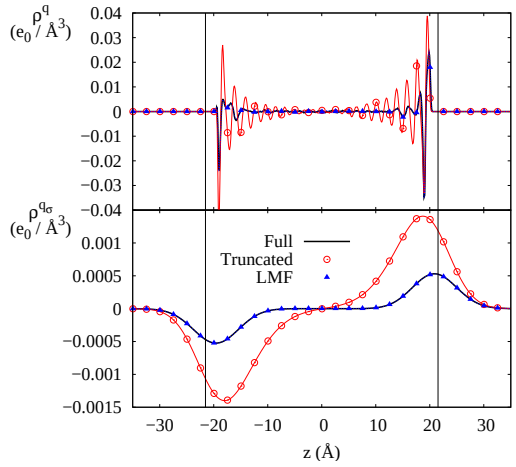

(a) $E_0 = 1.0$ V/Å

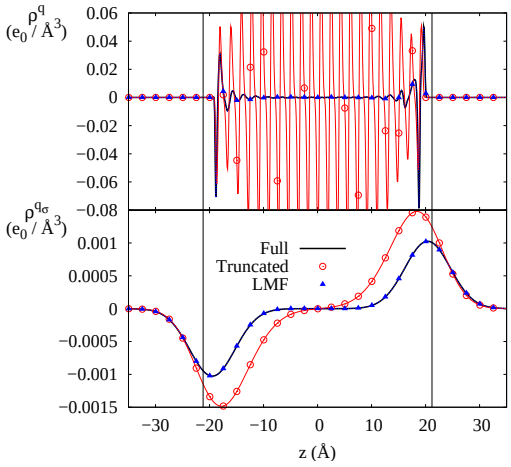

(b) $E_0 = 2.0$ V/Å

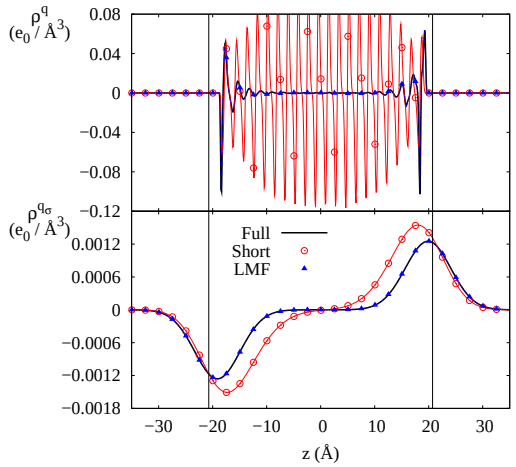

(c) $E_0 = 2.5$ V/Å

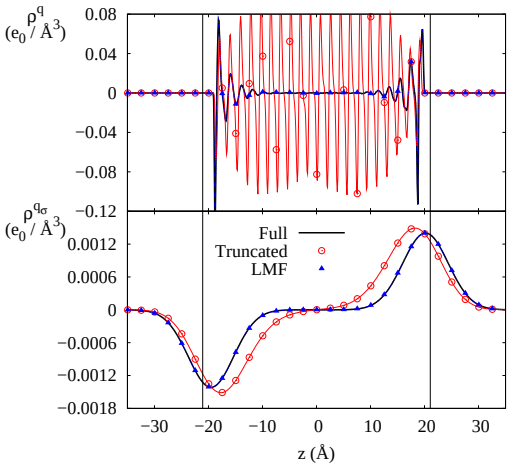

(d) $E_0 = 3.0$ V/Å

Figure 6.18: Site charge densities $\rho^q(z)$ and smoothed charge densities $\rho^{q\sigma}(z)$ for the applied field strengths. The atomic level charge densities are repeated for comparisons sake. While the dielectric slab inherent to the simulations is not immediately clear in ρ^q, $\rho^{q\sigma}$ clearly shows positive charge near the right wall, negative charge near the left wall, and zero charge density in the central region. GT water is obviously incorrect in all cases, and the inclusion of $\mathcal{V}_R$ leads to quite strong agreement. One in 25 data points is plotted.

calculated in [112]. As is evident from the graph, E_{pol} and E_0 are of approximately the same magnitude in the bulk region, thus the dielectric constant is determined through division by a comparatively small number, E_{tot}. In the tables below, we will report both $1/\epsilon$ and ϵ since $1/\epsilon$ varies linear with the quantity calculated through simulation, E_{tot}. In essence, identifying $\langle E_{\text{tot}} \rangle$ should be straightforward. However, there exists variations due to simulation uncertainty and also possibly slight residual atomic level structural details since the width between walls is certainly not a macroscopic or even mesoscopic distance. A previously used approach was to average the polarization field over 5 Å or 10 Å windows in order to best determine $\langle E_{\text{tot}} \rangle$ [112]. In these results, we instead integrate $E_{\text{pol}}(z)$ to determine $\mathcal{V}_{\text{pol}}(z)$. Then the slope of a linear fit to the central region yields the average polarization field response and seems relatively insensitive to the choice of fitting range. Figure 6.19 also shows that incorrect electrostatic approaches such as solely spherical truncations and using three-dimensional Ewald sums without a slab correction lead to overpolarization of the water slab, and consequently a negative dielectric constant as calculated by the charge density response.

The results for dielectric constant ϵ and also $1/\epsilon$ are shown in Table 6.2. For all applied electric fields, both the spherical truncation $v_0(r)$ and uncorrected three-dimensional Ewald sums fail quite spectacularly. The water slabs overpolarize in response to the applied field, leading to negative dielectric constants, though for different reasons. In the case of traditional three-dimensional Ewald sums, the overpolarization is due to interaction between the slab and the *spurious* dipole layer images in the z-direction. For spherical truncations, the overpolarization is due to the lack of

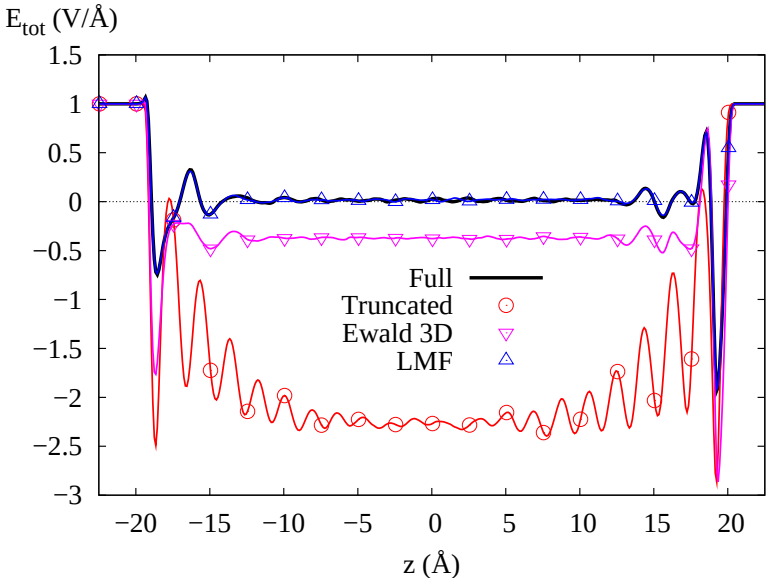

Figure 6.19: Plot of the total electric field as a function of z, defined to be a sum of the applied field and the polarization response of the water, E_{pol}. We expect that E_{tot} should be much smaller in the bulk region but still positive. The GT system and the system treated with three-dimensional Ewald sums clearly do not meet this physical expectation since they overpolarize in response to the field. In contrast GT water treated with self-consistent LMF theory appears accurate. One in 25 data points is plotted.

any long-range forces resulting from the ordering of the water molecules. As before, the data resulting from corrected three-dimensional Ewald sums are our benchmark. Yeh and Berkowitz [114] showed that this approach to electrostatics is accurate compared to two-dimensional Ewald sums that correctly represent the overall slab nature of the system. Including the self-consistent $\mathcal{V}_R(z)$ in combination with $v_0(r)$ leads to substantially more accurate calculations of E_{pol} and ϵ. However, these results are *less* precise than those for corrected three-dimensional Ewald sums. The reasons for this will be discussed further in the following section. This imprecision is tied to the fact that LMF theory is still only a mean-field approach, and this simultaneously has implications for the self-consistent solution of the LMF equation.

6.5 Fluctuations in LMF Electrostatics and Solving the LMF Equation

If we were to solely analyze properties such as ρ^q and the $P(\cos(\theta_\mu), z)$ surface, simple linear mixing of the LMF solution with relatively few iterations would be sufficient. However, very slight variations in these properties coherently add to lead to inaccuracies in the integrated electrostatic properties such as $\Phi_{\text{pol}}(z)$ and ϵ. Since we are interested in these properties as a stringent test of the utility of LMF theory, we must carefully consider why ϵ is more imprecise than corrected Ewald sums and address this in our self-consistent solution of the LMF equation.

The imprecision in ϵ is due to the greater fluctuations about equilibrum charge density profiles in the LMF simulations than in the Ewald simulations. Shown in

E_0 (V/Å)		$\langle E_{\rm pol} \rangle_c$ (V/Å)	$1/\epsilon$	ϵ
1.0	Ewald3DC	-0.9842 ± 0.0015	0.01580 ± 0.0015	63.4 ± 5.4
	Ewald3D	-1.3720 ± 0.0016	-0.3720 ± 0.0016	N/A (-2.7)
	GT	-3.2681 ± 0.0034	-2.2681 ± 0.0034	N/A (-0.44)
	LMF	-0.983 ± 0.010	0.017 ± 0.010	58.0 ± 55
2.0	Ewald3DC	-1.94956 ± 0.0019	0.02522 ± 0.00095	39.7 ± 1.5
	Ewald3D	-2.5310 ± 0.0027	-0.2655 ± 0.0014	N/A (-3.8)
	GT	-3.31285 ± 0.00050	-0.65643 ± 0.00025	N/A (-1.5)
	LMF	-1.945 ± 0.011	0.0275 ± 0.0055	36.1 ± 7.9
2.5	Ewald3DC	-2.3914 ± 0.0015	0.04344 ± 0.00075	23.03 ± 0.32
	Ewald3D	-2.8106 ± 0.0027	-0.1242 ± 0.0011	N/A (-8.0)
	GT	-3.3841 ± 0.0040	-0.3536 ± 0.0016	N/A (-2.8)
	LMF	-2.4031 ± 0.0070	0.03876 ± 0.0028	25.8 ± 1.8
2.7	Ewald3DC	-2.5268 ± 0.0021	0.06415 ± 0.00078	15.59 ± 0.18
	Ewald3D	-2.9189 ± 0.0007	-0.08107 ± 0.00026	N/A (-12.3)
	GT	-3.3487 ± 0.0024	-0.2403 ± 0.0009	N/A (-4.2)
	LMF	-2.5266 ± 0.0032	0.0642 ± 0.0012	15.57 ± 0.29
3.0	Ewald3DC	-2.6799 ± 0.0022	0.1067 ± 0.0007	9.371 ± 0.065
	Ewald3D	-2.9278 ± 0.0024	0.0241 ± 0.0008	N/A (41.5)
	GT	-3.3465 ± 0.0030	-0.1155 ± 0.0010	N/A (-8.7)
	LMF	-2.6875 ± 0.0045	0.1042 ± 0.0015	9.60 ± 0.14

Table 6.2: Comparison of polarization field due to the dielectric water slab and the resulting dielectric constant ϵ for various applied fields E_0. The results due to full LMF theory agree reasonably well with corrected three-dimensional Ewald sums, though not always quite within error bars. Both $1/\epsilon$ and ϵ are given since $1/\epsilon$ is linearly related to the quantity determined via simulation. The overpolarization with uncorrected Ewald sums or spherical truncations is clearly evident.

Fig. 6.20 are the results for both LMF simulations and Ewald simulations, without an applied field. In each case, results for the total 1.5 ns of simulation are shown in solid thick black lines, and results for individual 100 ps blocks of the simulation are shown in thin red lines. The electrostatic property plotted is the polarization potential $\Phi_{\text{pol}}(z)$. As is clearly evident, lattice summation simulations display far smaller fluctuations than spherical truncation techniques, even with a self-consistent $\mathcal{V}_R(z)$. The problem is compounded when seeking the ϵ for a given applied field because ϵ is calculated by taking the inverse of the sum of two numbers with similar magnitude but opposite sign, E_0 and E_{pol}. Very slight differences in a given E_{pol} will lead to substantial differences in ϵ.

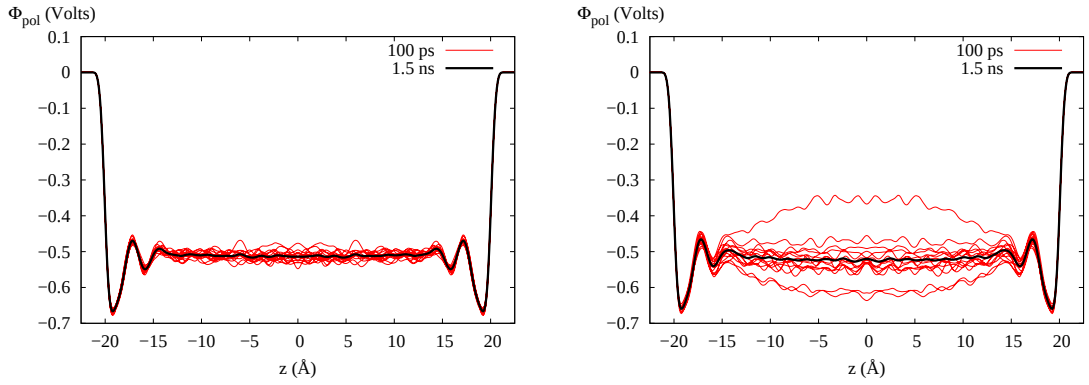

(a) Corrected Ewald 3D Sums

(b) LMF Simulations

Figure 6.20: Fluctuations of $\Phi_{\text{pol}}(z)$ for water between hydrophobic walls with no applied field. The thick black line represents the average over 1.5 ns and the thin red lines are the results for 100 ps blocks within that 1.5 ns time period. GT water corrected by $\mathcal{V}_R$ has substantially more fluctuations about the equilibrium average than corrected three-dimesional Ewald yields.

The reason for this is inherently tied to how the forces due to instantaneous fluctuations of the charge density away from the equilibrium charge density are dealt with. In general, the long-ranged forces resulting from any fluctuation of the charge

density profile away from the average profile will have a damping effect, driving the instantaneous configuration back towards the equilibrium profile. For lattice summation techniques, any fluctuation away from equilibrium is replicated across all periodic images in the x- and y-directions, thus leading to an overestimation of the system's instantaneous reponse. For the LMF approach, since the only representation of long-ranged forces is through the $\mathcal{V}_R$, which represents the mean-field *equilibrium* effect of the long-ranged forces, there is no penalty for instantaneous fluctuations away from equilibrium. This is not a surprise since in Coulomb systems, it has been shown that fluctuations should go as the surface area [68], and in short-ranged systems, fluctuations vary as the volume. Relative to the true disordered fluid system, we hypothesize that lattice summation techniques represent an *over*damping of fluctuations and the LMF technique represents an *under*damping.

Such concerns about fluctations were not present in the uniformly-charged-wall system in Ch. 3 because the charged sites were not connected to each other via bonds and each particle had a net charge. For that system, the main effect of $\mathcal{V}_R$ was to exert a force on the center-of-mass of the single-site charged species. For the water systems examined here, each water molecule is overall neutral, thus the main effect of $\mathcal{V}_R$ is not a net force on each molecule but rather a reorienting torque on each molecule. Typical orientations of individual molecules are a result of both the detailed local environment, and therefore hydrogen-bonding options, as well as the $\mathcal{V}_R$; thus one would expect much more substantial fluctuations in any electrostatic property resulting from the charge density of the species.

Another reality of these fluctuations is that they grow greater as more interactions

are included in $v_1(r)$ and thus treated by $\mathcal{V}_R$. Figure 6.21 shows the fluctuations about $\Phi_{\text{pol}}(z)$ for σ chosen to be 4.5 Å and 6.0 Å. While either of these σ might reasonably be considered larger than σ_{min} for water as shown in the bulk results, solution of the LMF equation was more straightforward with the large σ because there were weaker inherent fluctuations. For the walls with specific binding considered in the next section, $\sigma = 4.5$ Å was more feasible; likely the specific binding of water orientations at the wall driven by localized interactions rendered the fluctuations less extreme. Given that LMF theory is an equilibrium theory and not a dynamical one, we will not be overly concerned with this other than its impact on solving the LMF equation; however perhaps further theoretical development would allow some connection between the short-ranged LMF system and the true disordered fluid.

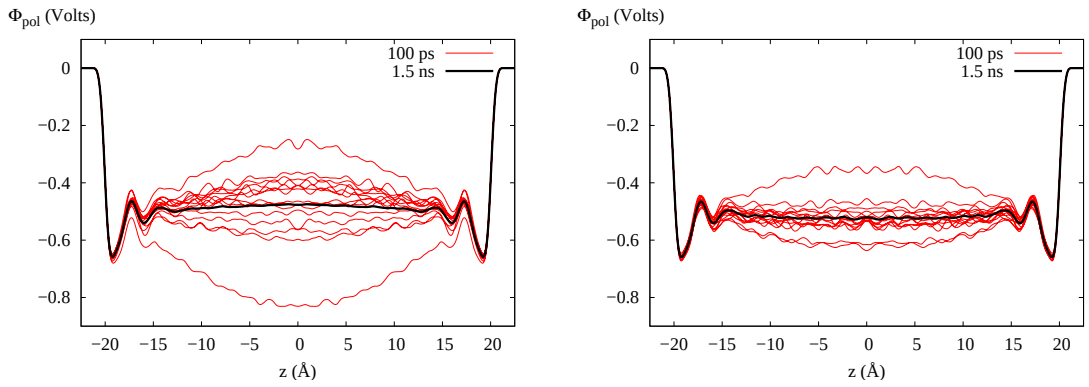

(a) $\sigma = 4.5$ Å (b) $\sigma = 6.0$ Å

Figure 6.21: Comparison of fluctuations about $\Phi_{\text{pol}}(z)$ for water between hydrophobic walls for two different choices of σ greater than σ_{min}.

As mentioned, these fluctuations do complicate the LMF self-consistent solution for these systems. In essence the reason for this is that with each iteration step, we must be able to distinguish between

- the inherent charge fluctuations in the system, and

- changes in response to the variation of $\mathcal{V}_R$ from iteration to iteration.

Various methods have been explored to make this distinction including iterative techniques used for self-consistent equations [81] in quantum chemistry and integral equations for fluids [49, 56, 56, 78, 79] and a modified LMF equation developed to tame the $k = 0$ term in LMF iteration as described in Appendix E. However, we found that a simple ensemble-like approach best addressed the variations mainly due to uncertainty in simulations. The requisite modification in the self-consistent LMF solution is shown in Fig. 6.22. In essence, the idea is to run N parallel simulations using a given $\mathcal{V}_R^{(i)}$ with distinct initial configurations. This modification proved to be necessary for only three $\mathcal{V}(z)$ – those due to no applied field, $E_0 = 1.0$ V/Å, and $E_0 = 2.0$ V/Å. In these cases, using 10 parallel simulations proved to be sufficient. Details of the timestep, simulation length, and steps to solution are given in Table 6.3 for all applied field values. Note that for the larger fields, simple linear mixing as done for the previous MC simulations was successful, but for the weaker fields, aside from running N parallel simulations per iteration timestep, linear mixing was employed as well. [2]

This approach to self-consistently solving the LMF equation is certainly not an optimized approach. We expect that an approach more appropriate to adaptive solu-

[2]The one exception was generating reasonable independent initial configurations for no applied field. In order to keep fluctuations bounded about the approximate plateau of $\Phi_{\text{pol}}(z)$, the real-space iteration scheme described in Appendix E that tames the $k = 0$ component of $\mathcal{V}_R$ was employed with λ chosen to be σ. Once these initial configurations were generated for the first solution pass, linear mixing was employed.

Hydrophobic Walls:							
E_0 (V/Å)	σ (Å)	N_{ensemble}	Δt (fs)	N_{eq}	N_{ave}	λ	N_{iter}
0.0	4.5	10	2.5	10^4	2×10^4	0.05	9*
0.0	6.0	10	2.5	10^4	2×10^4	0.1	3
1.0	6.0	10	2.5	10^4	2×10^4	0.05	15
2.0	6.0	10	1.0	5×10^3	10^4	0.1	7
2.5	6.0	N/A	1.0	5×10^3	10^4	0.1	20**
2.7	6.0	N/A	1.0	5×10^3	10^4	0.1	20**
3.0	6.0	N/A	1.0	5×10^3	10^4	0.1	20**
Corrugated Walls:							
E_0 (V/Å)	σ (Å)	N_{ensemble}	Δt (fs)	N_{eq}	N_{ave}	λ	N_{iter}
0.0	4.5	10	2.5	10^4	2×10^4	0.1	10
0.0	6.0	10	2.5	10^4	2×10^4	0.5	3

Table 6.3: Details for solution of LMF equation for water systems. Details for the corrugated wall simulations discussed in the next section are also given. N_{iter} is the iteration number needed for sufficient self-consistency to attain reasonable electrostatic properties such as $\Phi_{\text{pol}}(z)$ profiles and ϵ calculations. Far fewer N_{iter} would be necessary for ρ^{q_σ} and and dipole distributions that are quite accurate. Slight variations in these properties coherently add to lead to inaccuracies in the integrated electrostatic properties. * This solution was not as well converged as others, so this is an underestimate. ** $\mathcal{V}_R$ used for simulation was determined from the average of the charge densities obtained from the final 10 linear mixing iterations.

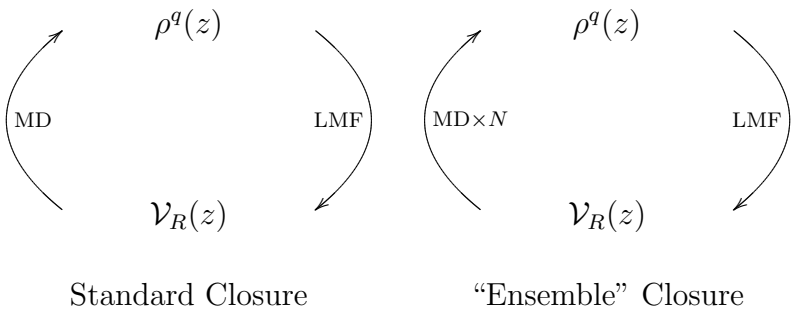

Figure 6.22: Modification of the LMF solution iteration scheme to address inherent fluctuations in water slab simulations.

tion of the equation during the simulation would look quite different than this. One potentially fruitful path based on a Car-Parrinello-like approaches, as reviewed by Frenkel and Smit [31], is discussed as future work in Ch. 8.

6.6 Atomically Corrugated Walls and Significance of ρ^{q_σ}

By replacing the hydrophobic walls with empirical Pt(111) surfaces [82], we may extend the LMF approach to moderately more realistic molecular surfaces. These empirical surfaces order the water molecules near the surfaces, attracting the oxygen atoms to localized binding sites. This surface is meant to represent specific interactions and detailed ordering of water molecules at an atomically corrugated surface. Figure 6.23(a) contains a schematic of a (111)-surface rectangular unit cell displaying the spacing of the topmost layers of atoms. The potential we use does not have explicit atoms or charges, but rather simply encompasses the presence of binding sites through exponential functions and various cosine functions to represent the periodicity of the surface. Due to these localized binding sites, we expect that $\rho^q(\mathbf{r})$ will be expressly a function of $\mathbf{r}$ and not simply z.

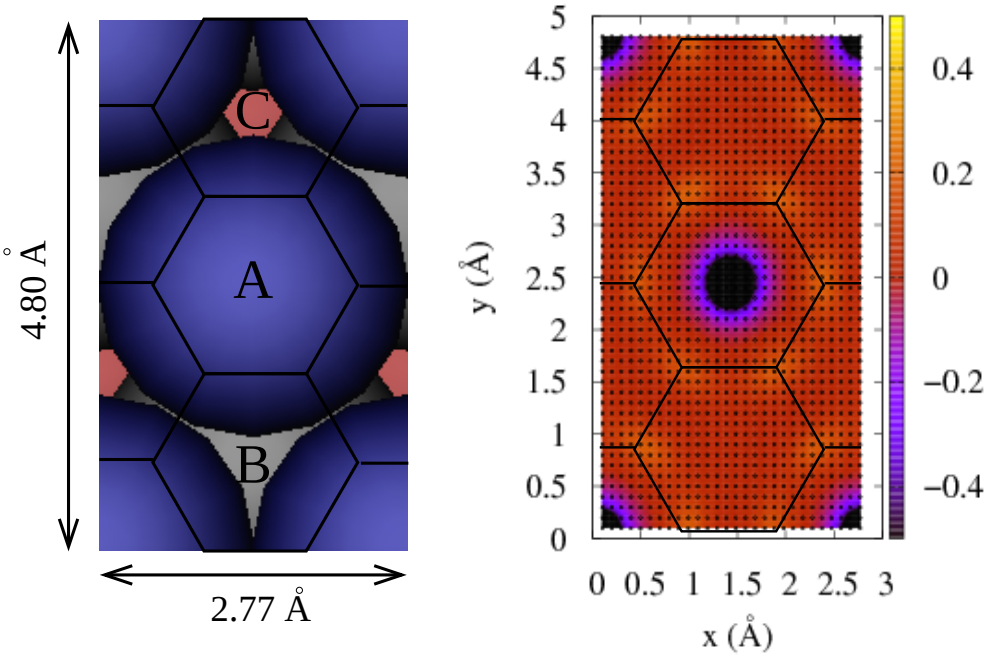

(a) Schematic of (111) unit-cell

(b) $\rho^q(\mathbf{r})$ Near Wall

Figure 6.23: Display of (111) unit cell and associated nearby charge density. In (a), three distinct subhexagons are also labeled that will be used to analyze nonuniform density above the surface. However, despite this schematic, the surface modeled in simulations is an approximate combination of exponentials and cosines to empirically represent the effect of a (111)-surface In (b), the charge density of the 1.5 Å layer closest to the wall is displayed in a two-dimensional projection. Actual data points are shown as black dots, and GNUPLOT interpolated between those points.

This corrugated surface is treated quite similarly to the hydrophobic surfaces in simulation as described in Sects. 6.1 and 6.5. The simulation cell instead has a volume of 30.49 Å × 28.806 Å × 140.0 Å to match the symmetry of the (111)-surface of a solid with lattice constant 3.92 Å. The wall position parameter z_m defined in [82] is set to ± 15.4 Å to achieve bulk density in the central region. The simulation cell now contains 1054 molecules. The corrected Ewald sum now has a k-vector set of (13,12,60). The substantial difference is that we use a σ of 4.5 Å and correspondingly decrease R_c to 9.5 Å. The smaller σ is qualitatively easier to iterate to self-consistency in the corrugated system, suggesting that perhaps charge fluctuations are dampened by the presence of specific binding at the surface.

In Fig. 6.23(b), the two-dimensional projection of the charge density in the 1.5 Å layer nearest the (111)-wall onto the same unit cell shows that the expectation that $\rho^q(\mathbf{r}) \neq \rho^q(z)$ is maintained. The surface induces a charge density very nonuniform in the x- and y-directions. The apparent periodicity is due to the fact that the 2.77 Å between binding sites is commensurate with the first peak in the bulk water $g_{\mathrm{OO}}(r)$ at 2.8 Å. However, as shown in Fig. 6.24, approximating $\mathcal{V}_R(\mathbf{r})$ as $\mathcal{V}_R(z)$ leads to accurate results for the electrostatic potential profile between the (111)-walls. While the electrostatic potential jump is of an opposite sign than for the hydrophobic walls due to the different ordering of water molecules near the (111)-walls, the general LMF framework remains identical to that for the hydrophobic walls with no applied electric field. None of the other properties such as orientational distributions will be presented. They are quantitatively different from the results for hydrophobic wall confinement, but they all lead to exactly the same picture of the success of the LMF

approach. The specific ordering of molecules near the walls is distinctly different but the underlying reasons for the failure of $v_0(r)$ alone and for the success of $\mathcal{V}_R(z)$ remain the same.

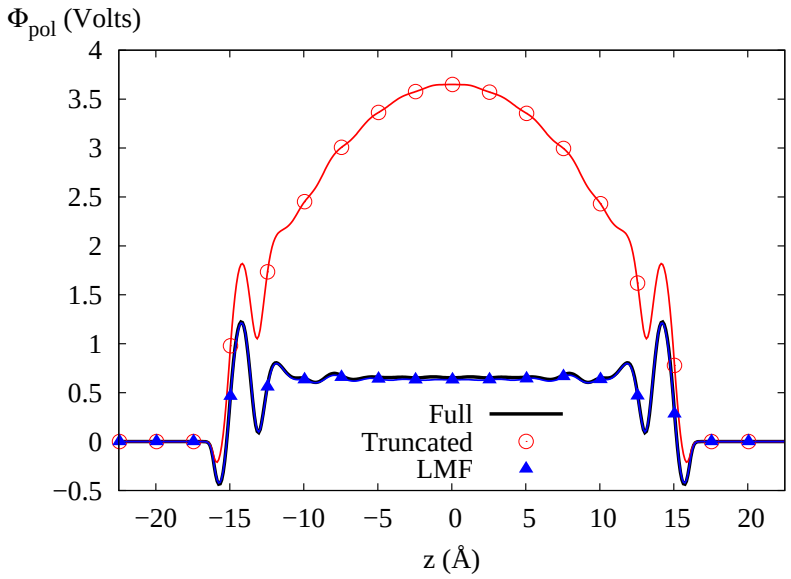

Figure 6.24: The polarization potential profile $\Phi_{\rm pol}(z)$ between corrugated walls. While the details of this potential profile are different than that for the hydrophobic walls due to the specific binding of water molecules of the surface, the basic conclusion remains the same. Inclusion of $\mathcal{V}_R$ leads to substantial agreement while GT water alone fails. For this simulation we have approximation $\mathcal{V}_R(\mathbf{r})$ as $\mathcal{V}_R(z)$. One in every 25 data points is shown.

The apparent contradiction of having $\mathcal{V}_R$ depend on only z while ρ^q depends on $\mathbf{r}$ can be resolved by understanding the smoothing effect included in calculating $\mathcal{V}_R$. As can be seen in Fig. 6.25, if the (111)-surface is divided into three distinct hexagonal binding regions – A, B, and C as labeled in Fig. 6.23(a) – the $\rho^q(z)$ measured along each hexagonal prism looks quite unique. However the negative charge density enhancement over the topmost platinum location, site A, is only evident within about 6.0 Å of the wall. Further the σ used (4.5 Å) is somewhat larger than the spacing of sites on the (111)-surface. Thus we expect the local effect of the binding sites

to be reasonably encompassed by $v_0(r)$. Examining the Gaussian-smoothed charge density leading to $\mathcal{V}_R$ highlights which variations are important. Convoluting $\rho^q(\mathbf{r})$ with Gaussians in the x- and y-directions and subsequently analyzing sites A, B, and C, we see that this density $\rho_{2D}^{q_\sigma}$ is indistinguishable from $\rho^q(z)$ calculated initially as only a function of z. The full three-dimensional smoothed charge density profiles ρ^{q_σ} again match exactly, indicating the same dipole layer formation regardless of position laterally along the wall. This final convolution step is crucial in assessing the validity of our conclusions. For the hydrophobic surface, $\rho^q(z)$ for GT water and for full system simulations looked indistinguishable until examined with complete Gaussian smoothing. As before, the long-ranged interactions for the corrugated surfaces in essence remain dominated by the slab-like geometry of the system, not by the atomic-level detail of the slab in the lateral directions.

The success of the approximation $\mathcal{V}_R(\mathbf{r}) \simeq \mathcal{V}_R(z)$ seems quite promising for the application of LMF to other slab geometries such as model biological membranes or liquid-liquid interfaces. In general the charge density smoothing inherent in the definition of the LMF equation also suggests that greater symmetries in solutions of $\mathcal{V}_R(\mathbf{r})$ may exist than intially suggested by the detailed symmetries of the problem. [3] Also, when studying the molecular simulations of atomically corrugated surfaces, the smoothed charge densities reveal the underlying electrostatic asymmetries rather than the detailed local structure.

We suggest that this smoothed charge density allows for a more direct analogy between molecular simulations and classical electrostatics. The LMF approach naturally

[3] This observation has also been made in work using LMF theory for a nonequilibrium system [21].

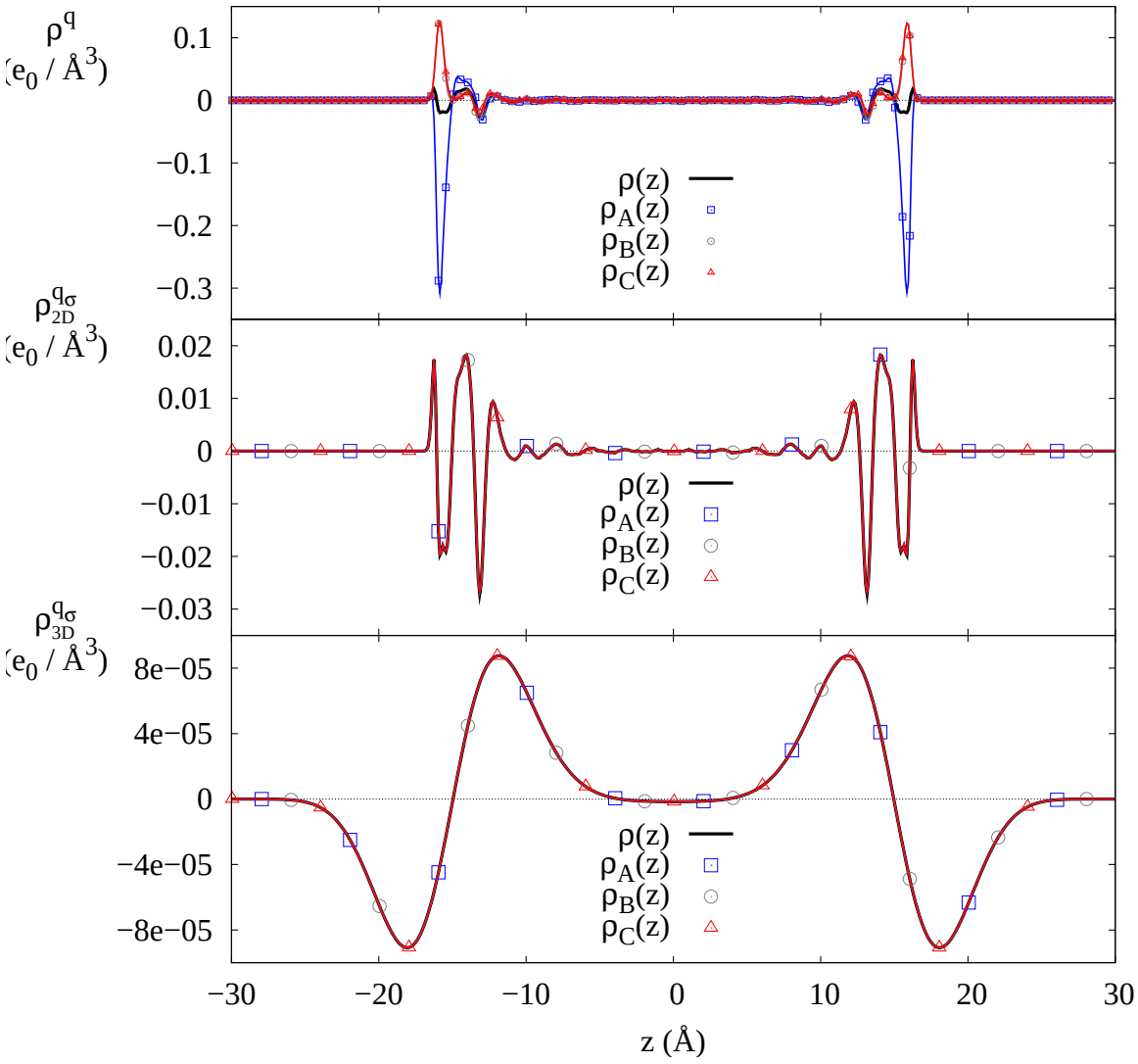

Figure 6.25: Plot of various charges densities for water between corrugated (111)-surfaces, both as purely a function of z and separated into the separate charge densities based on position above the surface. A, B, and C are indicated in Fig. 6.23(a). The top panel shows ρ^q, and there are clear distinctions in the various charge densities. The middle panel displays the effect of convoluting the charge density with a Gaussian of width σ in the x- and y-directions. With this smoothing, no distinction amongst positions above the surface can be made. The full $\rho^{q\sigma}$ is displayed in the bottom panel and all profiles fully agree and display the expected dipole layer near each wall. σ is 4.5 Å, and only a subset of data points is displayed for clarity.

distinguishes the long-ranged charge-charge interactions representing overall dipolar ordering from the short-ranged charge-charge interactions in simulations which capture hydrogen-bonding and short-ranged polar attraction. As previously discussed in Sect. 2.6, any σ large enough to capture the relevant short-ranged interactions like hydrogen-bonding should be correct for simulations. For physical interpretation of ρ^{q_σ}, we suggest use of a σ close to the minimum value that will work for simulations. However we do no suggest that the smoothed charge density alone contains all relevant charge-charge interaction information, since hydrogen bonding can be crucial in determining the overall liquid structure. We instead propose that it encompasses the net long-ranged effects best described by classical electrostatics and charge density. The results presented in this chapter at least demonstrate the utility of including the smoothed potential $\mathcal{V}_R(z)$ due to this smoothed charge density in simulating short-ranged interactions in nonuniform situations.

6.7 Applicability to More Realistic Corrugated Surfaces

The surface used in the previous section does have molecular-scale corrugation; however, it is not implemented like most detailed molecular models. The model was originally developed to model metallic Pt(111) surfaces [82]. More realistic metallic surfaces would require a treatment of image charges, which we will not address here. However molecular surfaces modeled with standard force fields would at least have charges at atomic sites near the surface. If the charges are free to move throughout the simulation as would generally be the case for biological membranes or liquid-liquid

interfaces, absolutely no change in tactic would be necessary. The charges associated would those molecules would also be included in ρ^{q_σ}.

However, if the charges are held fixed as is more likely for solid surfaces in classical simulations of solid-liquid interfaces, then we must be a bit more careful. It will no longer be true that $\mathcal{V}_R(\mathbf{r}) \simeq \mathcal{V}_R(z)$, however a closely related approximation will be true. A potential for silica surfaces modeled by atoms [33] is currently being extended by Hu [41] for work in the group. This potential includes point charges assigned to Si, O, and H atoms that are predominantly held fixed. These surfaces have a $\mathcal{V}_R$ that will explicitly depend on $\mathbf{r}$; however we will argue that the long-ranged portions of $\mathcal{V}_R$ encompassed by $\mathcal{V}_{R1}$ will to a good approximation depend on only z.

For these fixed surfaces, the external "field" would now consist of both nonelectrostatic components and electrostatic components. The imposed external electrostatic potential $\mathcal{V}(\mathbf{r})$ would be

$$\mathcal{V}(\mathbf{r}) = \sum_{\text{sites } i} \frac{q_i}{\epsilon \left|\mathbf{r} - \mathbf{r_i}\right|}, \tag{6.6}$$

where the sum is understood to include sites outside of the simulation cell. This external potential may be split into short-ranged component $\mathcal{V}_0$ and long-ranged component $\mathcal{V}_1$ as

$$\mathcal{V}_0(\mathbf{r}) = \sum_{\text{sites } i} \frac{q_i}{\epsilon} v_0(|\mathbf{r} - \mathbf{r_i}|), \tag{6.7}$$

$$\mathcal{V}_1(\mathbf{r}) = \sum_{\text{sites } i} \frac{q_i}{\epsilon} v_1(|\mathbf{r} - \mathbf{r_i}|). \tag{6.8}$$

The sum for $\mathcal{V}_0$ is strictly over the minimum image, but the second sum implicitly includes all sites in the surface. This suggests that a lattice sum technique will be required, but for exactly the same reasons as why $\mathcal{V}_R$ was simply a function of z for

the corrugated (uncharged) walls, we expect that to a very good approximation

$$\mathcal{V}_1(\mathbf{r}) \simeq \mathcal{V}_1(z). \tag{6.9}$$

The sole requirement should be that σ be larger than relevant lateral spacing of sites on the surface, such that the lateral charge density is sufficiently smoothed. In these cases, $\mathcal{V}_R$ is a function of $\mathbf{r}$, but all dependence on x and y is contained in $\mathcal{V}_0(\mathbf{r})$.

As a quick demonstration of the validity of this approximation, we construct a (111)-surface with lattice constant $a = 3.92$ Å as for the previous surface. However we arbitrarily assign charges of $+1e_0$ for the first layer of atoms, $-2e_0$ for the second layer of atoms, and $+1e_0$ for the third layer of atoms, as shown schematically in Fig. 6.26. Then we calculate the difference between $\mathcal{V}_1(\mathbf{r})$ and $\mathcal{V}_1(z)$ over a variety of sites at two distances Δh above the (111)-surface unit cell.

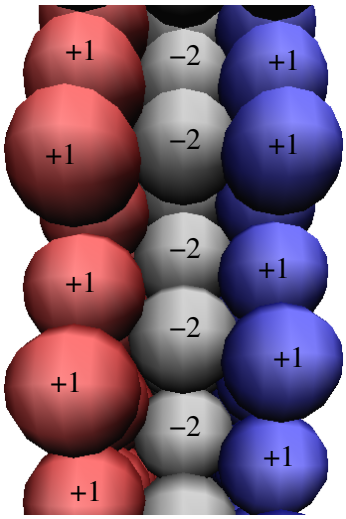

Figure 6.26: Model (111)-surface with charges assigned to each layer.

The corresponding $\mathcal{V}_1(z)$ would be determined by smoothing out the charges in each layer laterally, such that the charged (111)-surface is now approximated by three uniformly charged planes. With this representation we may exactly express $\mathcal{V}_1(z)$ as

the sum of three exact analytical functions,

$$\mathcal{V}_1(z) = \sum_{i \in \text{layers}} \frac{2\pi\lambda_i}{\epsilon} G(z, z_i), \tag{6.10}$$

where λ_i is the surface charge density of each layer. $\mathcal{V}_1(z)$ is plotted in Fig. 6.27 and has a nontrivial contribution to the forces near the surface. However, since the surface is net neutral, it decays to zero within a distance of approximately 2σ from the surface.

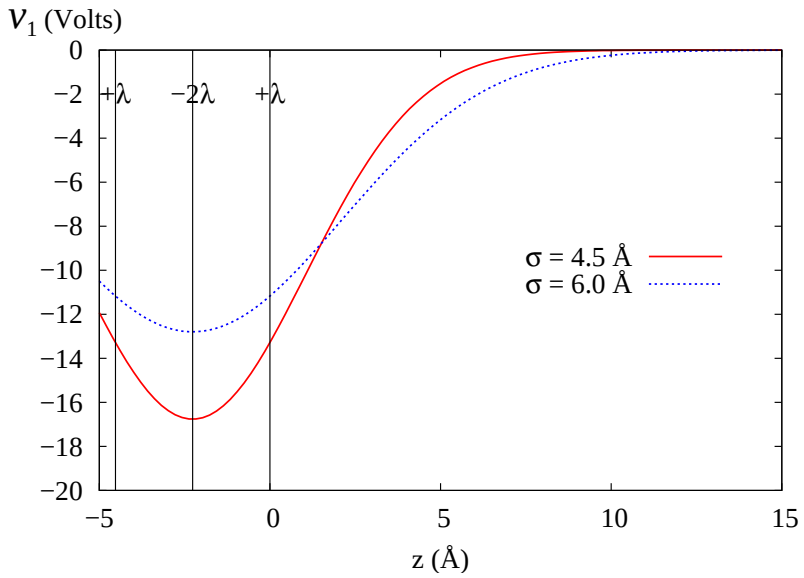

Figure 6.27: The one-dimensional $\mathcal{V}_1(z)$ for charged (111)-surface for two different σ. This approximation to $\mathcal{V}_1(\mathbf{r})$ is nonnegligible within σ of the surface.

We approximate $\mathcal{V}(\mathbf{r})$ by employing corrected three dimensional Ewald sums, but this requires some care since we can only employ Ewald sums in simulations that are net neutral. Shown in Fig. 6.28 is a sketch of the simulation cell we used. The basic idea is to construct the surface we are interested in with a +1 test charge above it and then to construct a second mirror surface with opposite charges with a −1 test charge above it. Specifically we constructed two (111)-surfaces of the same lateral size as

that simulated in the previous section with $L_z = 280$ Å and the two surfaces equally spaced from each other in the simulation cell, in order to decouple the discreteness of the charge on the two surfaces as much as possible.

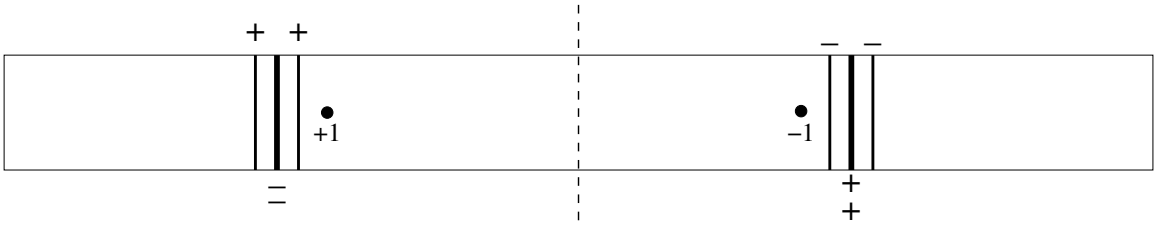

Figure 6.28: Sketch of Ewald simulation cell used to estimate $\mathcal{V}(\mathbf{r})$. The (111)-surface we are interested in (on the left) is mirrored across the dashed plane and the signs of charges are reversed. Then there is a positive test charge on the left and a miror negative test charge on the right. This combination allows us to approximate the electrostatic potential above the left surface. The simulation cell is chosen to be quite long in the z-direction in order to decouple the two surfaces as well as possible.

By carrying out single point energy calculations for the two test charges above the appropriate (x, y) location on each surface, we may approximate $\mathcal{V}(\mathbf{r})$ because the total energy of that system is a combination of $\mathcal{V}$ and the interaction between the positive and negative test charges ($U_{+-}(z)$) and the interaction amongst the two net neutral walls (U_{walls}),

$$\mathcal{V}(\mathbf{r}) \simeq \mathcal{V}_{\text{Ewald}}(\mathbf{r}) = 0.5 \left\{ U_{\text{Ewald}}(\mathbf{r}) - U_{+-} - U_{\text{walls}} \right\}. \tag{6.11}$$

We may exactly calculate $\mathcal{V}_0(\mathbf{r})$ for the configuration of one wall with a test charge, to within the simulation energy precision, by carrying out single point energy calculations for the positive test charge interacting with the surface via $v_0(r)$. Thus we determine $\mathcal{V}_1(\mathbf{r})$ as

$$\mathcal{V}_1(\mathbf{r}) \simeq \mathcal{V}_{\text{Ewald}}(\mathbf{r}) - \mathcal{V}_0(\mathbf{r}). \tag{6.12}$$

This is approximate since the Ewald sums will propagate the test charges into all the periodic image cells, but given that the lateral area spans 11×6 repeats of the minimum rectangular (111)-surface unit cell of 2.77 Å $\times$ 4.80 Å, this should be a more than adequate approximation.

Figure 6.29 shows the difference

$$\Delta\mathcal{V}_1(\mathbf{r}) \equiv \mathcal{V}_1(\mathbf{r}) - \mathcal{V}_1(z) \tag{6.13}$$

for a test charge placed two distances about the surface – a distance equivalent to the spacing between (111)-surface layers (2.26 Å) and a distance of 4.5 Å. Each of these distances leads to a substantial $\mathcal{V}_1(z)$. However as shown in the projection plots in Fig. 6.29, $\Delta\mathcal{V}_1(\mathbf{r})$ is an incredibly small perturbation for a σ of either 4.5 Å or 6.0 Å. Again, the importance of the charge smoothing inherent in the LMF equation is evident.

For exactly the same reasons as for the corrugated surface explored in the previous section, we fully expect that $\rho^{q_\sigma}(\mathbf{r}) \simeq \rho^{q_\sigma}(z)$. Thus, even for fixed charged slab confinements,

$$\mathcal{V}_{R1}(\mathbf{r}) \simeq \mathcal{V}_{R1}(z) \tag{6.14}$$

should hold to a very good approximation. In fact, we expect this to be an even better approximation for $\mathcal{V}_{R1}$ since the mobile charge density is included and will act to neutralize the fixed charged sites to an extent. Thus, these systems would be treatable by exactly the same techniques as used throughout this chapter with the sole difference that we must now include an applied electrostatic potential $\mathcal{V}(\mathbf{r})$ representing the charged surface. This $\mathcal{V}$ may be approximated as the sum of $\mathcal{V}_0(\mathbf{r})$

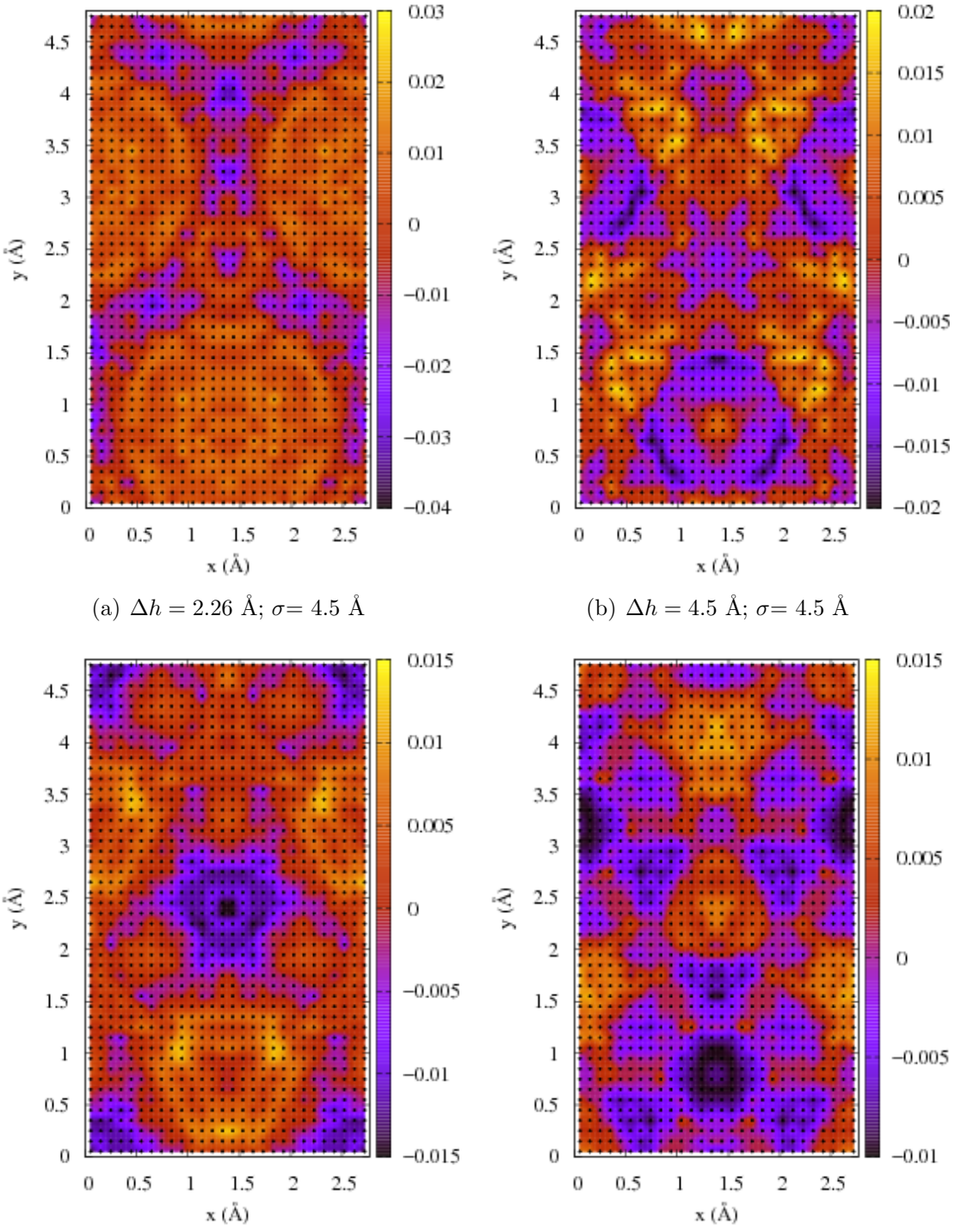

(a) $\Delta h = 2.26$ Å; $\sigma = 4.5$ Å

(b) $\Delta h = 4.5$ Å; $\sigma = 4.5$ Å

(c) $\Delta h = 2.26$ Å; $\sigma = 6.0$ Å

(d) $\Delta h = 4.5$ Å; $\sigma = 6.0$ Å

Figure 6.29: The residual $\Delta\mathcal{V}_1(\mathbf{r})$ in Volts projected onto the xy-plane for two heights above the surface with two different σ. In each case the value of $\mathcal{V}_1(z)$ several volts, but the correction $\Delta\mathcal{V}_1(\mathbf{r})$ is substantially smaller.

determined from $v_0(r)$ for all fixed point charges and a single analytical $\mathcal{V}_1(z)$.

6.8 Summary and Conclusions

In the first half of this chapter, we examined the ability of LMF theory to address the failings of spherical truncations of water when in a slab geometry. We studied SPC/E water confined between hydrophobic walls, both with and without an applied electric field normal to the walls. The case of no applied field has long been used as an example of why the success of spherical truncations of water in bulk is "misleading." While the density profiles of spherical truncations of water in Fig. 6.4 appear accurate, the semi-discrete jump in polarization potential at the surfaces is not reproduced at all. Indeed, as shown in Fig. 6.6, spherical truncations never yield a plateau in the potential in the bulk region as physically demanded. When an electric field is applied, even the density profiles determined with spherical truncations alone are highly inaccurate as dramtically illustrated in Fig. 6.11, and the predicted dielectric constants in Table 6.2 are negative.

LMF theory provides a way to include the long-ranged forces neglected by spherical truncations of charge interactions in a self-consistent manner via the LMF rescaled potential $\mathcal{V}_R(z)$. The subtle structural and electrostatic failings seen in previous calculations for truncated water confined between walls with no field are corrected by the LMF treatment in Fig. 6.8. Furthermore, all structural and electrostatic properties of water under an applied electric field in Sect. 6.4 are much more accurate with the inclusion of a self-consistent $\mathcal{V}_R$. The LMF approach even yields the correct dielec-

tric constants in Table 6.2 in contrast to the negative values for Gaussian-truncated water alone. In addition, the interpretation of $\mathcal{V}_R$ as the electrostatic potential due to a Gaussian-smoothed charge density discussed previously in Sect. 4.1 suggested examination of just that charge density. The form of ρ^{q_σ} proved to be illustrative of the underlying electrostatic effects, demonstrating the formation of a dipole layer at each wall without a field in Fig. 6.8(d) and the accumulation of positive (negative) charge density at the right (left) plate when an electric field was applied in Fig. 6.18. The smoothed charge density also clearly showed the failure of spherical truncations alone; this failure was not obvious from the atomic-level charge density profile with no applied field.

While LMF theory is very successful in correcting equilibrium properties in this system, we found in Sect. 6.5 that the fluctuations about the equilibrium polarization potential profiles in molecular dynamics simulations of the LMF-corrected system are much stronger than we found using the corrected three-dimensional Ewald procedure. We hypothesize that the dynamical fluctuations of the true disordered fluid might lie between the two extremes, but more theoretical development of LMF theoyr is required since it is only valid for equilibrium properties at the moment. But regardless, the fluctuations during molecular dynamics simulations have consequences for the iterative self-consistent solution of the LMF equation in weak applied fields. In this thesis, we have dealt with these fluctuations by simulating a small "ensemble" of systems at each step of the iteration to self-consistency. However, the difficulty posed by these fluctuations in the self-consistent solution of the LMF equation merits further research so that LMF theory may be more broadly available as a technique for sim-

ulating electrostatic interactions. In the concluding chapter, one possible approach to self-consistent solution which might be reasonably integrated into simulation programs is proposed.

In Sects. 6.6 and 6.7, we demonstrated that the simple one-dimensional solution of the LMF equation we used for smooth confining surfaces should have much broader applicability for slab simulations. We simulated water confined between a corrugated surface. This surface induces density profiles which are a function of x, y, and z, as shown by Yeh and Berkowitz [113] and plotted in Fig. 6.23(b). Despite the three-dimensional variation of the charge density profile, we successfully used the one-dimensional LMF equation to correct for the neglected long-ranged forces. The only important long-ranged *electrostatic* effect was the formation of dipole layers at each corrugated surface, and, as shown in Fig. 6.25, the Gaussian-smoothing of the charge density inherent to the LMF equation accurately isolated that effect as a function of z alone. We further demonstrated in Sect. 6.7 that very similar approximations should hold even for corrugated surfaces which also carry fixed charges. This indicates not only that LMF theory should be broadly applicable to more detailed molecular models, as shown in the previous chapter, but also that such an application might prove much simpler than the atomically-detailed symmetries of the systems might suggest.

Chapter 7

Hydrophobic interactions

This chapter presents preliminary thoughts on hydrophobicity via analysis by LMF theory. It is by no means meant to be a comprehensive study of this topic, but may rather be viewed as a series of interesting and useful observations that we hope to use as groundwork for future theoretical work.

An often-cited theory for hydrophobic interactions developed by Lum, Chandler, and Weeks [62] (LCW) is motivated by ideas from local molecular field theory. In this chapter, we shall attempt to highlight the connections between two different derivations of LCW theory for hydrophobicity [62, 102] and the approach to LMF theory we have taken thus far in this thesis. Furthermore by quantitative analysis of simulation data using the standard LMF equation, we seek to understand the impact of a criticized approximation in LCW theory – the treatment of water without reference to tetrahedral structure or hydrogen bonding. In particular, since the previous chapter dealt with water between hydrophobic walls, we will attempt to draw connections between an LMF treatment of simulated confined SPC/E water and the LCW theoretical approach.

7.1 LCW theory

The original derivation of LCW theory [62] proceeded by stating in essence the standard van der Waals surface excess free energy functional [88] though for three dimensions rather than one dimension,

$$F_0[\rho(\mathbf{r})] = \int d\mathbf{r} \left[w(\rho(\mathbf{r})) + \frac{1}{2} \left| \vec{\nabla} \rho(\mathbf{r}) \right|^2 \right]. \tag{7.1}$$

In this equation $w(\rho(\mathbf{r}))$ is a local free energy density. By taking a functional derivative of Eq. (7.1) with respect to $\rho(\mathbf{r})$, placing appropriate boundary conditions on $\rho(\mathbf{r})$, and making a series of approximations, one finds

$$\frac{\partial w(\mathbf{r})}{\partial \rho(\mathbf{r})} = m \vec{\nabla}^2 \rho_s(\mathbf{r}) + 2a \left[\bar{\rho}(\mathbf{r}) - \bar{\rho}_s(\mathbf{r}) \right]. \tag{7.2}$$

In this equation ρ_s is a seemingly heuristic slowly-varying component of the interfacial density profile and a bar over either ρ_s or ρ indicates a smoothing of that density profile over a length λ that is typical of the range of interparticle attractions in the fluid. In the context of LCW theory, this smoothing is defined as a Gaussian convolution. This convolution might suggest our smoothing of the charge density with a Gaussian of width σ, but the density in this equation refers to the center-of-mass density profile, or alternately the atomic oxygen density profile. This equation is closed by a van der Waals definition of $w(\rho(\mathbf{r}))$ and a linear response treatment of the water density changes to the excluded volume of hydrophobic species. However, the connection of LMF theory to the presentation of the LCW derivation in the original paper is unclear; thus, in lieu of the original derivation, we will discuss a derivation based on a review by Weeks [102].

In several papers on LMF theory and on hydrophobicity, authors refer to a "two-step process" in using the LMF approach [54, 62, 67, 102]. During the course of this thesis, we have often appealed to a different two-step process demonstrated in Fig. 7.1. Simulation to determine $\rho(\mathbf{r})$ alternated with insertion of $\rho(\mathbf{r})$ into the LMF equation to determine $\phi_R(\mathbf{r})$ leads to a self-consistent solution of the LMF equation. The LMF equation for LJ fluids may be written as

$$\phi_R(\mathbf{r}) = \phi_0(\mathbf{r}) + \phi_1(\mathbf{r}) \tag{7.3}$$

$$\phi_{R1}(\mathbf{r}) = \phi_1(\mathbf{r}) + \int \rho_R(\mathbf{r}'; [\phi_R])\, u_1(|\mathbf{r} - \mathbf{r}'|)\, d\mathbf{r}' + 2a\rho_B. \tag{7.4}$$

The parameter a is essentially the typical a for a van der Waals fluid representing the "strength" of interparticle attractions and may be defined as

$$a = -\frac{1}{2} \int u_1(\mathbf{r})\, d\mathbf{r}. \tag{7.5}$$

In connecting with previous authors' work on hydrophobicity and drying, it seems clearer to view their process as a three-step process instead, as shown in Fig. 7.2. The abbreviations in the figure will be explained shortly.

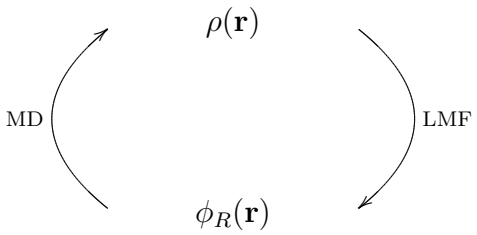

Figure 7.1: Simulation closure of the LMF equation.

In the three-step process, the single step of using simulation to find the density response of the reference fluid to the current form of $\phi_R(\mathbf{r})$ has been replaced by two

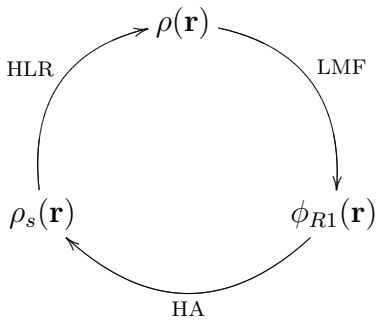

Figure 7.2: The "three-step" process employed by other authors in closing the LMF equation without using simulation for the density response.

approximate numerical steps indicated by HA and HLR. [1] In the typical LCW theory, HLR is not the closure used; an alternate linear response approach is used instead. However, since we mostly will be following the derivation in [102], this closure path seems the more natural to follow. We will make connections with typical LCW later.

HA refers to the hydrostatic approximation. This approximation is appropriate for slowly-varying fields, thus it is only applied to the slowly-varying ϕ_{R1}. In the hydrostatic approximation, the slowly-varying density $\rho_s(\mathbf{r})$ at each position $\mathbf{r}$ is assumed to depend solely on the value of $\phi_{R1}(\mathbf{r})$ at $\mathbf{r}$. The density of the reference system is exactly that which would exist in a bulk reference system with chemical potential

$$\mu_{s,0}(\mathbf{r}) = \mu_0 - \phi_{R1}(\mathbf{r}). \tag{7.6}$$

Thus ρ_s may be written as the function

$$\rho_s(\mathbf{r}) = \rho_s(\mu_0 - \phi_{R1}(\mathbf{r})). \tag{7.7}$$

Weeks [102] combines this HA approximation with the LMF equation using Eq. (7.6)

[1] The two-step process referred to by other authors actually is achieved by combining the LMF and HA steps into a single step.

and inserting the LMF definition of ϕ_{R1} into that equation. We will cover this after discussing HLR since understanding approximations and identifications following from this substitution is crucial in connecting to the original LCW formula.

HLR stands for hydrostatic linear response and the crucial assumption is that excluded volume effects resulting from ϕ_0 and also from the reference fluid cores may be represented reasonably by linear response about the smoothly varying hydrostatic density. The HLR equation is

$$\rho_0(\mathbf{r}) = \rho_s(\mathbf{r}) \left\{ 1 + \int c_0(|\mathbf{r} - \mathbf{r}'|\,; \rho_s(\mathbf{r}))\, [\rho_0(\mathbf{r}') - \rho_s(\mathbf{r})]\; d\mathbf{r}' \right\}. \tag{7.8}$$

In this equation, $c_0(r;\rho)$ is the direct correlation function of the uniform reference fluid at uniform density ρ. Since c_0 is the *direct* correlation function and tends to be a shorter-ranged indicator of particle correlations, each iteration of the equation stresses correlations in the near vicinity of the hydrostatic density at $\mathbf{r}$ where the field ϕ_{R1} should not vary substantially, and thus seems reaonable for density response for the hydrostatic approximation. Self-consistency of $\rho_0(\mathbf{r})$ in the equation above allows for a more "non-local" representation of the correlations.

7.1.1 Standard LCW Equation

The usual differential form of the LCW equation as stated in Eq. (7.2), with a modification to allow for slowly-varying attractions in the external field $\phi(\mathbf{r})$, may be found through the following steps, again as described in [102]. The hydrostatic approximation and LMF equation are combined to yield

$$\mu_{s,0}(\mathbf{r}) = \mu_0 - \phi_1(\mathbf{r}) - \int \rho_0(\mathbf{r}')\, u_1(|\mathbf{r} - \mathbf{r}'|)\, d\mathbf{r}' - 2a\rho_B. \tag{7.9}$$

The connection with LCW relies on computing a series of differences. First we define $\Delta\rho_0(\mathbf{r}) = \rho_0(\mathbf{r}) - \rho_s(\mathbf{r})$, the difference between the full density distribution of the reference system and the slowly varying density. With this definition, we may write

$$\mu_{s,0}(\mathbf{r}) = \mu_0 - \phi_1(\mathbf{r}) - \int \Delta\rho_0(\mathbf{r}')\, u_1(|\mathbf{r}-\mathbf{r}'|)\, d\mathbf{r}' - \int \rho_s(\mathbf{r}')\, u_1(|\mathbf{r}-\mathbf{r}'|)\, d\mathbf{r}'. \quad (7.10)$$

Using the mean-field theory statement that $\mu(\rho) = \mu_0(\rho) - 2a\rho$ and also generalizing the identity between a and the integral of u_1 given in Eq. (7.5) to define a smoothing of density profiles over the range of attractions as

$$2a\bar{\rho}(\mathbf{r}) = -\int \rho(\mathbf{r}')\, u_1(|\mathbf{r}-\mathbf{r}'|)\, d\mathbf{r}', \quad (7.11)$$

we find

$$\begin{aligned}\mu_{s,0}(\mathbf{r}) - 2a\rho_s(\mathbf{r}) = \mu_0 - 2a\rho_B - \phi_1(\mathbf{r}) \\ - \int \Delta\rho_0(\mathbf{r}')\, u_1(|\mathbf{r}-\mathbf{r}'|)\, d\mathbf{r}' \\ - \int [\rho_s(\mathbf{r}') - \rho_s(\mathbf{r})]\, u_1(|\mathbf{r}-\mathbf{r}'|)\, d\mathbf{r}' \quad (7.12)\end{aligned}$$

$$\begin{aligned}\mu_s(\mathbf{r}) = \mu - \phi_1(\mathbf{r}) + 2a\,[\bar{\rho}_0(\mathbf{r}') - \bar{\rho}_s(\mathbf{r}')] \\ - \int [\rho_s(\mathbf{r}') - \rho_s(\mathbf{r})]\, u_1(|\mathbf{r}-\mathbf{r}'|)\, d\mathbf{r}'. \quad (7.13)\end{aligned}$$

We may Taylor expand $\rho_s(\mathbf{r}')$ about $\rho_s(\mathbf{r})$ to second order. Since $u_1(r)$ is a spherically-symmetric, even function, the only terms surviving in the final integral will be those due to $(x'-x)^2$, $(y'-y)^2$, and $(z'-z)^2$. Furthermore, those three terms will be identical. Thus we can write

$$-\int [\rho_s(\mathbf{r}') - \rho_s(\mathbf{r})]\, u_1(|\mathbf{r}-\mathbf{r}'|)\, d\mathbf{r}' = m\vec{\nabla}^2\rho_s(\mathbf{r}) \quad (7.14)$$

with the constant m defined as

$$m \equiv -\frac{1}{6}\int r^2 u_1(r) d\mathbf{r}. \tag{7.15}$$

Finally making the identification as in Rowlinson and Widom [88, p. 54] that

$$\mu_s(\mathbf{r}) - \mu = \frac{\partial w}{\partial \rho} \tag{7.16}$$

where $w(\rho)$ is the local surface-excess free energy density, we have the standard LCW equation

$$\frac{\partial w(\rho_s(\mathbf{r}))}{\partial \rho_s(\mathbf{r})} = -\phi_1(\mathbf{r}) + m\vec{\nabla}^2\rho_s(\mathbf{r}) + 2a\left[\bar{\rho}_0(\mathbf{r}) - \bar{\rho}_s(\mathbf{r})\right]. \tag{7.17}$$

Therefore, as explained in [102], the slowly-varying density characterizing the interface used in LCW theory is the hydrostatic density. The hydrostatic density is considered a *local* response to the value of ϕ_{R1}. However, ϕ_{R1} is due to the convolution of the attractive forces and the density, so it is not a purely local function, though it is an equilibrium-averaged function. In standard LCW theory $\bar{\rho}$ is defined as a convolution with a Gaussian of width λ, where $\lambda^2 \equiv m/a$, to approximately average over the range of slowly-varying attractions. The LMF approach would argue that $\bar{\rho}$ is better defined by convoluting the density by the long-ranged attractions as in Eq. (7.11), but Gaussian smoothing is not a terrible choice provided a reasonable λ.

LCW theory also uses an alternate linear response closure in lieu of the HLR approximation. And $w(\rho)$ is defined using a simple van der Waals functional form rather than dealing with chemical potentials. Details of the properties of water are obtained by choosing the van der Waals a and b parameters such that the liquid density and compressibility of the van der Waals fluid at 298 K match those of water.

7.2 Criticisms of LCW Theory

At a qualitative level, LCW theory seems to suggest that a vapor layer exists between a hydrophobic surface and the surrounding water, since the equation for the density profile is determined from liquid-vapor coexistence equations. Analysis of simulations often leads researchers to conclude that such a vapor layer does not exist since density profiles do not have a smooth liquid-vapor-like interface (see *e.g.* [3]). Also detailed questions related to the strength of interactions between solutes and water molecules have been raised as a counterpoint to LCW theory (see, *e.g.*, [16]. However, the development of density profiles is a numerically complicated phenomena. Even in the case of an intrinsically vapor-like interface, it can depend on a delicate balance of attractions between the solutes and liquids. LMF analysis of such simulation data is a way of quantitatively understanding this balance of attractions.

Other approximations in the theory have been questioned as well. Given that local density fluctuations in water are Gaussian [42], the linear response closures used in the theory above should be fine in the liquid phase, and a linear response closure is exact in an ideal gas. However, the linear response closure used by LCW chooses a simple interpolation between the two, and it is not at all clear that this is correct at intermediate densities through interfaces. Furthermore, the linear response closure used by Weeks [102] assumes that the reference fluid may exist at all intermediate densities between the coexistence phases of the full liquid. For LJ interactions, the reference system WCA may exist at all densities, and as such this is reasonable. However, for liquid water, it is not at all clear that we may choose a reference fluid

that fulfills this criterion; we will explore this point a bit further below.

One might also question the overall representation of water as essentially a LJ fluid. Since the van der Waals parameters are chosen to match liquid water's density and compressibility and surface tension, one obvious fault is that the energetic binding likely is qualitatively greater than the $\varepsilon_{\mathrm{LJ}}$ used for SPC/E water for example since that energetic binding must account not just for long-ranged dispersive forces but also for hydrogen bonding. Water's surface tension is unusually large due to the broken hydrogen bonds near the surface, and inclusion of this data allows the simple LCW model to have a critical distance for drying between plates that is on the order of nm rather than Å.

In contrast to the LCW approach, a given *molecular* model has $\varepsilon_{\mathrm{LJ}}$ and σ_{LJ} chosen in tandem with point charges assigned to various sites in order to lead to a careful balance of hydrogen-bonding, packing, and long-ranged dipolar behavior. Results presented in the previous chapter suggest that at a minimum the long-ranged dipolar behavior does not affect the density distribution when no electric field is applied. We will quantify this observation shortly. Subsequent analysis of simulation data with LMF theory will allow us to further dissect certain quantitative contributions to surface behavior. We will then conjecture how one might synthesize understanding from simulations and LMF theory to perhaps expand on the LCW/LMF theoretical approach.

7.3 LMF theory for van der Waals attractions

In the analysis of slab simulations of water molecules, it will at times be informative to understand the relative magnitudes of the contributions of Lennard-Jones attractions and of the long-ranged electrostatic interactions on the centers-of-mass of the water molecules. Since the Lennard-Jones site is centered on the oxygen atoms, we may consider the application of LMF theory to Gaussian-truncated (GT) repulsive-core (RC) water where the interparticle interactions are composed of $v_0(r)$ between point charge sites and additionally $u_{\rm WCA}(r)$ between oxygen sites rather than $u_{\rm LJ}(r)$. Use of the strong coupling approximation for GT RC water in the bulk works just as well as that for GT water as shown in Fig. 7.3. The reason for this is that relative to the LJ core, water molecules are quite densely packed ($\rho\sigma_{\rm LJ}^3 = 1.06$), and thus the attractive portion of the LJ interaction cancels to a *very* good approximation.

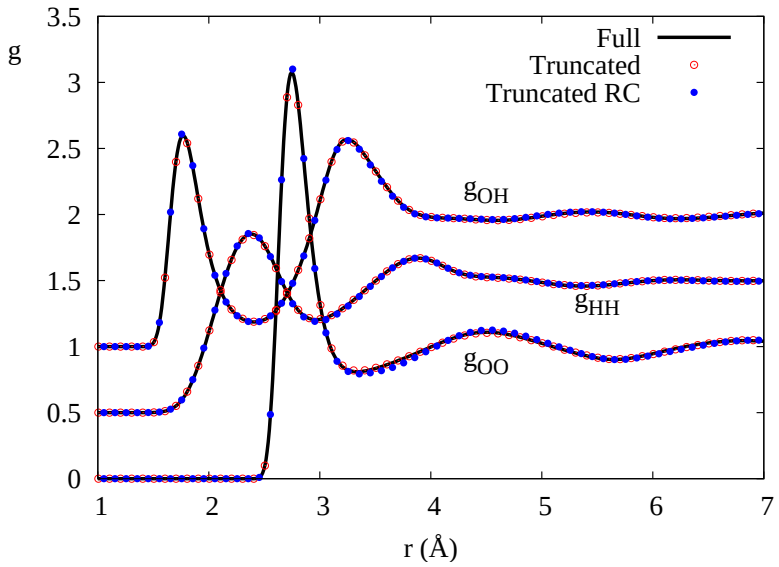

Figure 7.3: Site-site pair correlation functions compared for bulk full SPC/E water, Gaussian-truncated water, and Gaussian-truncated repulsive-core (RC) water. All three functions agree quite well. For GT and GT RC water, one in every 10 data points is plotted for clarity.

Use of GT RC water for the mimic system in a slab simulation leads to an effective external potential energy surface for oxygen sites that may be decomposed as

$$\phi_R^{\mathrm{O}}(z) = q_{\mathrm{O}}\mathcal{V}_R(z) + \phi_R^{\mathrm{LJ}}(z) \tag{7.18}$$

$$= q_{\mathrm{O}}\mathcal{V}_R(z) + U_{\mathrm{LJw}}(z) + \int d\mathbf{r}'\rho_R^{\mathrm{O}}(z')u_{\mathrm{attr}}(|\mathbf{r}-\mathbf{r}'|) + C. \tag{7.19}$$

No alteration for the hydrogen sites is necessary since they do not have LJ interactions associated with them. The general LMF equation for LJ interactions above is reexpressed for the slab symmetry in Appendix F.

As suggested in Sect. 2.4, we may also split $U_{\mathrm{LJw}}(z)$, the smoothed LJ wall potential used in the previous chapter, in a WCA-like manner into a short-ranged, purely repulsive component $U_{0,\mathrm{LJw}}(z)$ and the remaining attractive interactions are represented by $U_{1,\mathrm{LJw}}(z)$. In this case, the repulsive-core contributions to the structure will result from $U_{0,\mathrm{LJw}}(z)$ and the pair interactions $u_{\mathrm{WCA}}(r)$. The LJ attractions from both the wall and the bulk fluid will lead to a slowly-varying modulation $\phi_{R1}^{\mathrm{O}}(z)$.

7.4 Balance between forces

As a first exercise in understanding the various contributions of forces, we examine the equilibrium between a liquid slab and vapor slab for

- full SPC/E water,
- GT water defined as $v_0(r) + u_{\mathrm{LJ}}(r)$, and
- GT RC water defined as $v_0(r) + u_{\mathrm{WCA}}(r)$.

We simulate each of these systems with 100 ps of equilibration and 400 ps of data collection. Aside from the length of data collection and the lack of confining walls, the simulations are identical to those described in Sect. 6.1.

Examining $\rho^{\mathrm{O}}(z)$ in Fig. 7.4, the density profile is only different for GT RC water. This may be understood as suggesting that the impact of $\phi_R^{\mathrm{LJ}}(z)$ defined in this case as

$$\phi_R^{\mathrm{LJ}}(z) = \int d\mathbf{r}' \rho_R^{\mathrm{O}}(z') u_{\mathrm{attr}}(|\mathbf{r} - \mathbf{r}'|) + C \tag{7.20}$$

is much more substantial than the effect of $\mathcal{V}_R(z)$.

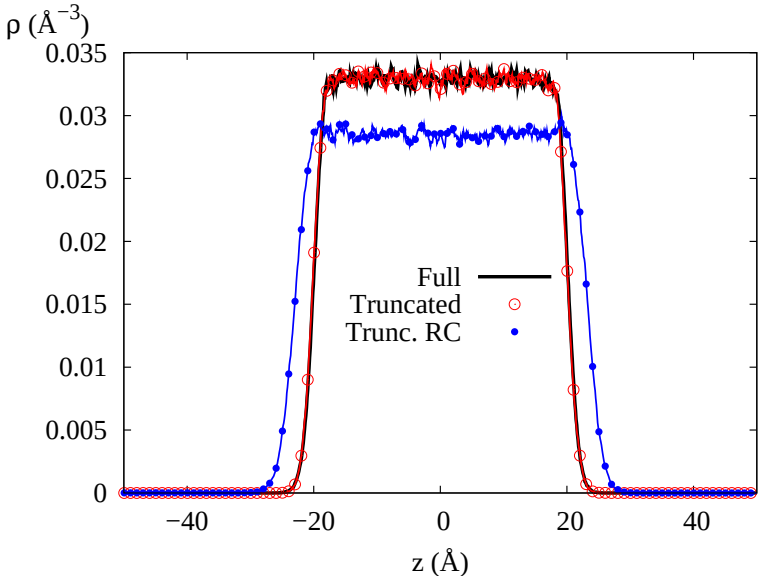

Figure 7.4: $\rho_{\mathrm{O}}(z)$ profiles for slabs of full SPC/E water, GT water, and GT RC water with vapor at the interfaces. GT water agrees well with SPC/E water, but GT RC water develops a lower bulk density phase in equilibrium with a vapor phase. For GT water and GT RC water, one in every 10 data points is shown.

The two potential energies, $q_{\mathrm{O}}\mathcal{V}_R$ and ϕ_R^{LJ}, acting on the oxygen atoms are shown in Fig. 7.5(a). [2] The conclusion that ϕ_R^{LJ} is more consequential than $\mathcal{V}_R$ seems

[2]For this section we will not be self-consistently solving the LMF equation; rather we simply use the LMF equation as a way to analyze the net contribution of long-ranged forces to the full SPC/E

impossible based on their relative magnitudes.

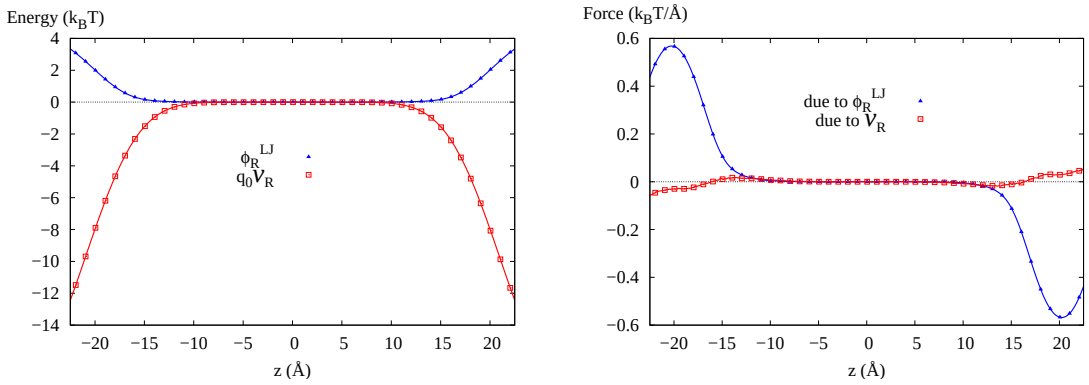

(a) $q_O \cdot \mathcal{V}_R$ and ϕ_R^{LJ} (b) Net force on *molecules*

Figure 7.5: Impact of $\mathcal{V}_R$ and ϕ_R^{LJ} compared. The magnitude of $q_O \cdot \mathcal{V}_R$, plotted relative to k_BT in (a), is much larger than ϕ_R^{LJ}. However average net forces due to $\mathcal{V}_R$ on water *molecules* are much less than those due to ϕ_R^{LJ}, as shown in (b). One in every 10 data points in shown.

However, the key is that the net effect of $\mathcal{V}_R$ is to exert a torque on the water molecules. The relevant comparison is between the force due to $\phi_R^{LJ}(z)$ and the *net* force that $\mathcal{V}_R(z)$ exerts on each water molecule. As shown in Fig. 7.5(b), this comparison meshes solidly with our expectations based on the vapor slab results. This seems to suggest that at surfaces ϕ_R^{LJ} will matter much more for density profiles than $\mathcal{V}_R(z)$. This should not suggest that the effect of the charges on the water molecules leading to hydrogen-bonding are not important to the formation of the liquid interface. They are quite crucial, and are included in all three of our water models examined. Further discussion of this reality will be delayed until later.

Since GT water accurately predicts the overall density profile for the vapor slab and also for the confinement between hydrophobic walls, we will now mainly consider Gaussian-truncated water and GT repulsive-core water in order to conserve simulation

water simulations.

time. The dipole orientations will not be accurate, but we will not be examining those for the moment. We will next simulate the following four wall-water combinations:

- GT water confined by U_{LJw} (as in Ch. 6),
- GT water confined by $U_{0,\mathrm{LJw}}$ (the repulsive portion of the LJ walls),
- GT RC water confined by U_{LJw}, and
- GT RC water confined by $U_{0,\mathrm{LJw}}$.

As for the simulations in the previous chapter, we consider a total of 1.5 ns of simulation after 500 ps of equilibration. The density profile for each system is shown in Fig. 7.6. The fact that all density profiles look distinct is a clear sign that both the attractions due to the LJ walls and the attractions due to $\phi_R^{\mathrm{LJ}}(z)$ contribute meaningfully to the balance. Note that the SCA approximation for the walls (GT RC water + U_{WCAw}) does not perform nearly as well for density profiles as the SCA for Coulomb interactions did. We would only expect this to be the case if there were an *exact* balance between the wall attractions and bulk attractions.

These density profiles reflect our general expectations. Removing the LJ attractions on the water cores lead to greater particle accumulation near the surface, and thus high $\rho(z)$ peaks near the walls. Removing the LJ attractions from the walls led to less particle accumulation near the walls compared to corresponding water model simulated with LJ attractions on the walls. Interestingly the shift in particle density is much more substantial for the removal of LJ cores from the fluid particles than for the removal of attractions from the walls. Shown in Fig. 7.7 are the full ϕ_R^{LJ}

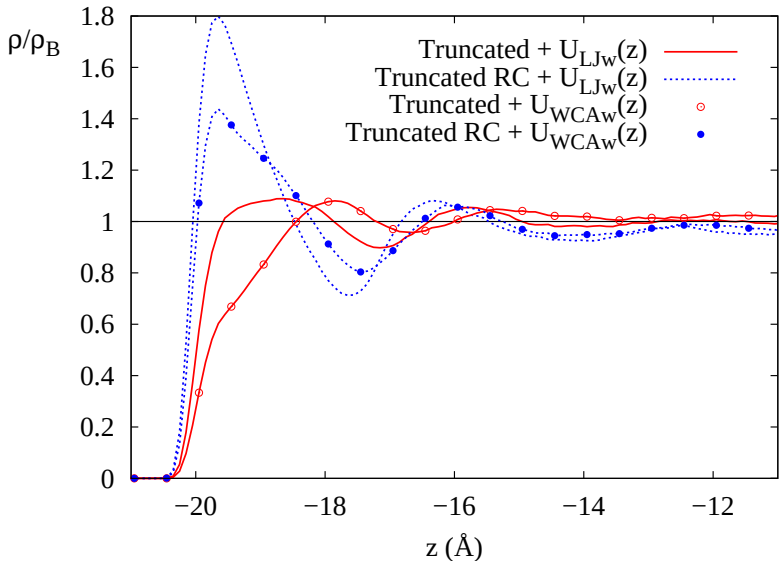

Figure 7.6: The density profile $\rho^{\mathrm{O}}(z)$ for the various permutations of GT or GT RC water paired with LJ walls or WCA walls. The region near the left wall is displayed, but symmetry holds about $z = 0$. GT water is shown in solid red lines and GT RC water is shown with dotted blue lines. LJ walls are shown with simply lines, and WCA walls also have points associated with them. Only one in 5 data points are displayed.

for the GT water particles and the contributions from $U_{0,\mathrm{LJw}}(z)$, $U_{1,\mathrm{LJw}}(z)$, and from the interparticle attractions. [3] Using the LMF analysis, we may quantitatively say that all water molecules at the surface experience a *much* greater effect from the bulk attractions than from the LJ wall attraction.

We may also again do a calculation of the full force on water molecules due to the LJ attractions and the long-ranged Coulomb forces, and compare those results to the vapor interface examined in the previous section. Here we use the density determined by corrected three-dimensional Ewald sums. Looking at the relative force effects in

[3] Again this is not a self-consistent solution of the LMF equation but rather an analysis based on using the density profile due to GT water + $U_{\mathrm{LJw}}(z)$ in the LMF equation in order to dissect the contributions.

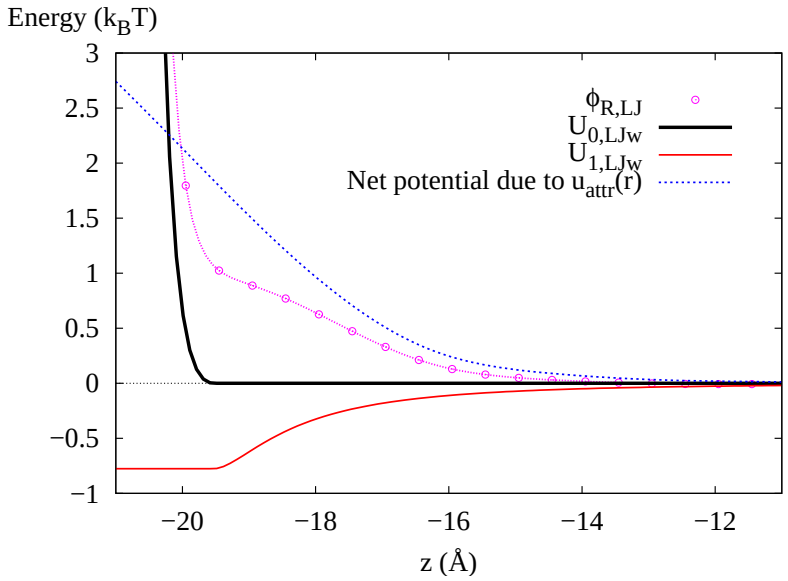

Figure 7.7: Breakdown of various contributions to ϕ_R^{LJ} for the system simulated using $v_0(r) + u_{\mathrm{LJ}}(r) + U_{\mathrm{LJw}}(z)$. Again, we simply use the LMF equation as an analysis tool rather than a simulation tool. The net attraction due to the bulk LJ fluid easily dominates the attraction due to the LJ wall, and a net repulsion from the wall is therefore exerted by ϕ_R^{LJ}.

Fig. 7.8, we can see that the net force due to long-ranged Coulomb forces remains the same except for an abrupt termination of the force when the wall confinement renders the presence of any molecule highly unlikely. In that sense, the effects of dipolar forces may be slightly greater for liquid-vapor interfaces, but this is predominantly due to a somewhat more diffuse interface. The slight differences due to the shape of the water interface in confinement have a greater difference on the profile of net forces due to the interparticle LJ attraction.

The results above suggest that the surface density profile is a question of a quantitative balance between solute (hydrophobic walls) and solvent (water) LJ attractions, *provided* that hydrogen-bonding and packing are already well-represented. LCW hoped that this would be captured by using the experimental $g(r)$ and surface ten-

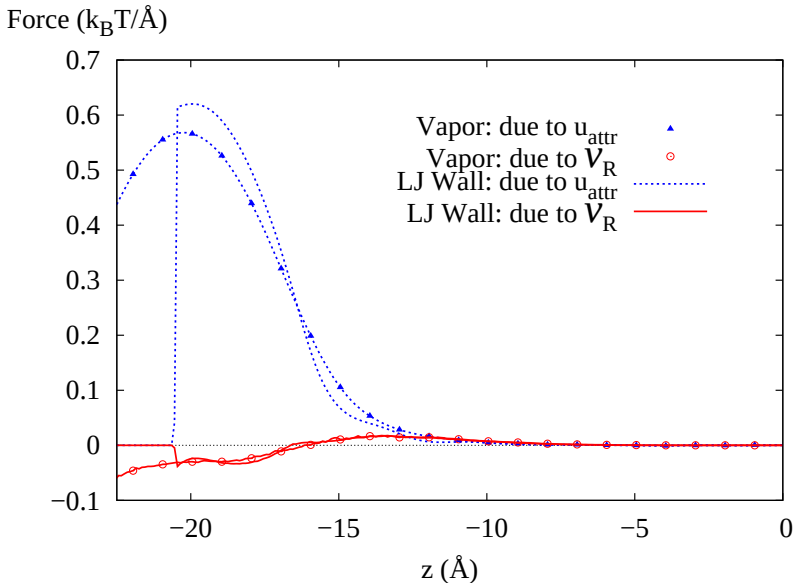

Figure 7.8: Net force on SPC/E water molecules due to interparticle LJ attractions and due to $\mathcal{V}_R$ for the confinement between hydrophobic walls and repeated for the vapor slab. One in 10 data points are shown for the LJ wall force profiles.

sions. This general point about quantitative balance has also been made in relation to simulations by Maibaum and Chandler [67] in an examination of the solvation of hydrophobic clusters, but the LMF construct gives a more complete manner of quantifying the contribution of solvent attractions. The data presented here is the first step toward using the full LMF equation in a quantitative examination of hydrophobicity. Interestingly, the impact of dipolar interactions is only slight on molecules at the liquid vapor interface and it retains a similar impact for the liquid-hydrophobic interface profile.

The provision that hydrogen-bonding and packing must be well-represented is clearly a stringent criterion for theory. However it is worth noting that England *et al.* [26] recently developed a mean-field theory for the behavior of liquid water near hydrophobic surfaces with the application of an electric field. The crux of the model

was positing three distinct lattice sites: liquid, field-aligned, and empty sites and the asserting a functional form for the transition between vapor and liquid between walls. This density profile ansatz is certainly a reasonable starting point, but the LMF approach could quite easily yield self-consistent equations for the density profile and the alignment profile within a similar model. This, however, is speculation and requires much further work.

Alternately, if we were to try to build on the work using the hydrostatic approximation and linear response as described in Sect. 7.1 to develop a theory, it is not at all clear what the appropriate reference system would be. One of the major assumptions in the hydrostatic approximation is that the reference system can exist at all densities between the vapor and bulk density. As shown in Fig. 7.4, both Gaussian-truncated water and GT repulsive-core water clearly have a liquid-vapor equilibrium, though GT RC water does have a smaller bulk density. As a check to make certain that this was not simply an artifact of an unequilibrated system, we also simulated GT RC at a lower density with the initial configuration distributing water molecules evenly across the cell. In a relatively short time, a clear vapor bubble had developed with a higher density bulk region. Overall this should not be a surprise, but rather a result of the important contribution of hydrogen bonding to water's properties. GT RC water still contains the short-ranged contributions to hydrogen bonding even as it excludes the LJ attractions. This does not resolve the question of what a good reference system is but rather opens the way for more questions. As stated at the start of this chapter, this was not meant to be a complete exploration of hydrophobicity via LMF theory, but rather a collection of useful observations that we can glean from

simple simulations. There is much more to be explored on this topic.

7.5 Summary and Future Work

In this chapter, we first reviewed the LCW theory for hydrophobicity [62] and tried to draw connections with LMF theory as presented in this thesis. In that discussion we closely followed the treatment of Weeks [102] closely. We then presented a more detailed application of LMF theory in Sect. 7.3 for treatment of the LJ attractions in water models. We introduced a second truncated version of water, which we called Gaussian-truncated (GT) repulsive-core (RC) water, which not only replaces $1/r$ interactions with $v_0(r)$, but also replaces the LJ core with a purely repulsive WCA core. Even GT RC water maintains a liquid-vapor interface in the vapor-liquid slab geometry owing to the ability of $v_0(r)$ to capture hydrogen-bonding; however, the bulk density is lower because the LJ attractions are also an important contributor to surface tension.

In Sect. 7.3, we used LMF theory as a tool to analyze the relative contributions of forces to the interfacial structure of water molecules. Via such analysis, we showed that the net contribution of LJ attractions to the surface forces are much more substantial than the net forces on molecules due to the long-ranged electrostatic forces encompased by the LMF rescaled electrostatic potential $\mathcal{V}_R$. We also explained the variation in water density profiles near surfaces for various combinations of inclusion and neglect of LJ attractions for water molecules and for the hydrophobic walls. Analysis inspired by the LMF equation shows that the dominant long-ranged force on

molecules at interfaces is the net LJ attraction pulling surface molecules back towards the bulk.

The analysis of simulation data we presented proved enlightening, but much further work will be necessary to gain a new theoretical perspective on hydrophobicity. Further examination of the mean-field approach of England *et al.* [26] to water, which addressed both electrostatic ordering and hydrophobic effects using a simple lattice model, might prove fruitful when connected with LMF theory. One might also hope to further develop the LCW approach to hydrophobicity since it represents a simplification of the LMF approach. However, one must better understand what the most appropriate reference system may be since Gaussian-truncated repulsive-core water cannot exist at all densities, and such a property is useful in harnessing previous analytical closures to the LMF equation such as the hydrostatic approximation and also hydrostatic linear response.

Chapter 8

Conclusions and Future Work

In most of this thesis, we have explored local molecular field theory as it applies to electrostatics. Derivations of LMF for both simple fluids and for various molecular models were presented in order to justify the use of what appears to be only a mean-field equation. We also made contact with many other electrostatic techniques, highlighting their connections to LMF theory.

Overall, we have found the LMF approach to electrostatics to work remarkably well in determining the equilibrium structure of charged fluids both in uniform and nonuniform environments. LMF theory succeeds where spherical truncations alone fail purely owing to the rescaled electrostatic potential $\mathcal{V}_R$.

One should be encouraged by the results presented herein, but there are certainly many more questions to address. The previous chapter dealt with the first steps in expanding this research to connect with hydrophobicity. Several other extensions have been touched on briefly in the text, but here we will examine them a little further.

Improvements can be made in calculating the thermodynamics of bulk fluids using the strong coupling approximation. Simulations of the Gaussian-truncated water model in tandem with simple analytical corrections yielded accurate values for the internal energy and the pressure. However, ultimately, free energies are the most important thermodynamic quantity. First order perturbation theory states [69, p. 303]

that

$$\frac{A}{N} = \frac{A_0}{N} + \frac{\left\langle U_N^{(1)} \right\rangle_0}{N}. \tag{8.1}$$

In this equation the energy in brackets may be identified as the U_1 determined for molecular fluids in Sect. 5.3.4. In essence, this equation means that the mimic system reasonably captures all entropic contributions, an assumption which we already employed for our pressure correction. If this approximation generally holds, then we may apply the analytical expression for U_1 to correct the free energy for the mimic system calculated through simulation. More work will be required to test this hypothesis.

The LMF approach has worked remarkably well in slab geometries, both for ionic liquids and for site-site molecular models. Since the derivation of LMF for CHARMM-like models in Sect. 5.5 led to the same LMF equation we have used throughout this thesis, expansion to more physically relevant slab geometries seems quite feasible. Biological membranes and liquid-liquid interfaces should be treatable within an identical framework. Furthermore, for fixed surfaces, such as the silica surface studied by Hu [41], we have shown in Sect. 6.7 that the LMF equation should collapse into the one-dimensional form used for all the slab simulations herein to a very good approximation.

Another interesting future direction would be to study the phenomena of electrostriction between surfaces. Classical electrostriction theory states that densities should increase with the application of a field, but Vaitheeswaran, Yin, and Rasaiah have found a decrease in density for certain fields. Since then, simulations by Daub, Bratko, Leung, and Luzar have contradicted these findings and theoretical

development by England, Park, and Pande supports both results [8, 18, 26]. LMF simulations offer an interesting opportunity. In all the simulations thus far, the treatment of electrostatics with a field applied between walls has been troublesome. In the original simulations [98], the researchers applied an electric field only between two finite plates and had surrounding bulk water. Electrostatics overall were treated with traditional three-dimensional Ewald sums, and edge effects for the plates were ignored. In the simulations by Daub *et al.* [18], a grand canonical simulation of water between two semi-infinite plates was conducted, using spherical truncations to treat electrostatics. Intuition informed by work in this thesis suggests that the spherical truncations should be quite problematic, but the use of three-dimensional Ewald sums may have issues as well. Also, in the simulations with finite plates, the plates were only one atom wide, and thus there was electrostatic coupling between the "bulk" reservoir of water molecules. LMF techniques would allow us to study the original system with short-ranged electrostatics, such that we can remove coupling between the "bulk" and the interstitial water, while still incorporating the long-ranged effects of polarization.

One issue that we have barely explored in this dissertation is the computational time needed to perform self-consistent LMF simulations. We have viewed our solutions of the LMF equation as a demonstration of the principle, not as a detailed exploration of how to best implement LMF. We have therefore focused more on the theoretical development of LMF theory and on gleaning useful intuition from the LMF approach. However, given a self-consistent solution, we found approximately a factor of four speed-up in water slab simulations using the LMF approach with

$\sigma = 6$ Å as opposed to corrected Ewald sums. This speed-up is not great, so timing may never be a compelling reason to employ LMFtheory unless one could develop an optimized and easily conducted path to the solution of the LMF equation.

A particularly interesting option for adaptive solution of the LMF equation during simulation is developing a Car-Parinello-like approach. Following a discussion in Frenkel and Smit [31], the essence of such approaches relies on writing a potential energy function whose minimum yields the desired equation that typically is solved for iteratively whether it be the Schrödinger equation for electron clouds about moving nuclei or the dipoles of moving polarizable molecules as discussed in [31]. By then assigning psuedo-dynamics to the associated degrees of freedom, such as the dipole polarization, the extended Lagrangian can yield equations of motion to propagate those degrees of freedom. A lower temperature is assigned to the pseudo-dynamics so that the degrees of freedom remain close to their minimum energy state, the solution to the equation of interest. This is because typical Car-Parinello methods seek to evolve the solution adiabatically such that at any given instant in the molecular dynamics simulation, degrees of freedom are quite close to their instantaneous minimum energy state, so small masses are usually assigned to the degrees of freedom. In the case of an LMF solution, we do not want the instantaneously appropriate energy; rather we would like the $\mathcal{V}_R$ appropriate to the equilibrium-averaged charge density. Perhaps we can use the same framework and simply assign a large mass to the degrees of freedom associated with the $\mathcal{V}_R$ solution.

Based on a treatment in Arfken and Weber [2] and Jackson [51] for electrostatics, one sees that Poisson's equation for the electrostatic potential ϕ results from the

minimization of the following energy-like functional $U[\phi]$ with respect to ϕ,

$$U[\phi] = \frac{\epsilon}{2} \int d\mathbf{r} \left(\vec{\nabla}\phi \cdot \vec{\nabla}\phi \right) - \int d\mathbf{r} \rho(\mathbf{r}) \phi(\mathbf{r}). \tag{8.2}$$

Provided that $\delta\phi$ vanishes on the surface, the functional derivative is

$$\frac{\delta U}{\delta \phi} = -\epsilon \vec{\nabla}^2 \phi - \rho(\mathbf{r}). \tag{8.3}$$

In other words, functional minimization of $U[\phi]$ leads naturally to Poisson's equation. Previous researchers [65] have rejected this functional on the basis that the functional actually yields the *negative* of the true electrostatic energy for the minimum. However those workers were explicitly interested in using the formulation as an alternative to evaluation of electrostatic energy at each time step. We would rather be interested in using the functional as a tool to solve the self-consistent LMF equation adaptively.

Since $\mathcal{V}_R$ may be expressed as the solution of a modified Poisson's equation, we posit that $U[\mathcal{V}_R]$ may be expressed as

$$U[\mathcal{V}_R] = \frac{\epsilon}{2} \int \left(\vec{\nabla}\mathcal{V}_R \cdot \vec{\nabla}\mathcal{V}_R \right) d\mathbf{r} - \int \left\{ \rho^q_{\text{ext}}(\mathbf{r}) + \rho^{q\sigma}(\mathbf{r}) \right\} \mathcal{V}_R(\mathbf{r}) d\mathbf{r}. \tag{8.4}$$

Both the charge density of fixed objects, ρ^q_{ext}, and the smoothed charge density of mobile charges $\rho^{q\sigma}$ must be included. We may take the functional derivative as before and find

$$\frac{\delta U[\mathcal{V}_R]}{\delta \mathcal{V}_R} = -\epsilon \vec{\nabla}^2 \mathcal{V}_R - \rho^q_{\text{ext}}(\mathbf{r}) - \rho^{q\sigma}(\mathbf{r}). \tag{8.5}$$

Just as U is now a functional of $\mathcal{V}_R$, the kinetic energy T is now a functional of $\mathcal{V}_R$, namely,

$$T[\mathcal{V}_R] = \frac{1}{2} M_{\mathcal{V}_R} \int \left(\frac{\partial \mathcal{V}_R}{\partial t} \right)^2 d\mathbf{r}. \tag{8.6}$$

Therefore, the Lagrangian associated with the LMF equation is

$$\mathcal{L} = T[\mathcal{V}_R] - U[\mathcal{V}_R], \tag{8.7}$$

and, for the LMF solution, the equation of motion reads

$$\frac{\partial}{\partial t} p_{\mathcal{V}_R} = M_{\mathcal{V}_R} \ddot{\mathcal{V}}_R \equiv \frac{\delta \mathcal{L}}{\delta \mathcal{V}_R} = \epsilon \vec{\nabla}^2 \mathcal{V}_R + \rho^q_{\text{ext}}(\mathbf{r}) + \rho^{q_\sigma}(\mathbf{r}). \tag{8.8}$$

Note also here, that the charge density due to the fixed charges will cancel out exactly with the $\mathcal{V}$ portion of $\mathcal{V}_R$, leaving only the portion due to the Gaussian-smoothed charge density. In many senses, this approach has great similarities to standard numerical solutions of Poisson's equation and to Car-Parinello approaches used classically; however, the problem posed by the self-consistent solution of the LMF equation ties these two problems together in a unique way potentially treated by the evolution equation above.

In summary, LMF theory has been shown to be useful in the treatment of electrostatics in simulations, but there is much more work that could be done in its implementation and in using it for even more physically-relevant and interesting systems.

Appendix A

Derivation of Various YBG Equations

In this appendix, we review the derivation of several YBG equations, specifically for

- a single component monatomic system,
- a mixture of monatomic components,
- a molecular fluid characterized by positions and Euler angles,
- a mixture of site-site molecules with intermolecular interactions expressed as a sum over pair interactions between various atomic sites and the intramolecular bonding interaction as a function for the whole molecule, and
- a mixture of site-site molecules with interactions described via a CHARMM-like potential energy function.

These are well-established formulae with a well-known path to derivation; however, the latter three equations are not easily found in textbooks. We appeal to these equations in our derivations of an LMF equation for molecular fluids; thus they are established here. Further, derivation of the former two provides the tools and notation we will use in the later derivations.

Most of this discussion will be carried out specifically for intermolecular pair interactions. The YBG formula for simple fluids and mixtures is generalizable to multi-

body forces; however, LMF theory applies only for pairwise summable forces so focus is applied to that situation.

Also, for notation, we will mainly follow the conventions of Chandler and Pratt [10, 11] developed for site-site models of molecular fluids in building towards a YBG equation for a site-site molecular mixture; any substantial deviations will be noted.

A.1 YBG Equation for Simple Fluid

The derivation of the first equation in the Yvon-Born-Green hierarchy for a simple fluids begins with the definition of single-particle and two-particle densities, $\rho^{(1)}(\mathbf{r})$ and $\rho^{(2)}(\mathbf{r}, \mathbf{r}')$ respectively. Here, we will define these densities in the canonical ensemble (NVT) as

$$\rho^{(1)}(\mathbf{r}) = \left\langle \sum_{i=1}^{N} \delta(\mathbf{r} - \mathbf{r_i}) \right\rangle \tag{A.1}$$

$$= \frac{N}{Z} \int \cdots \int d\mathbf{r_2} ... d\mathbf{r_N}\, e^{-\beta \mathcal{U}(\mathbf{r}, \mathbf{r_2}, ..., \mathbf{r_N})}, \tag{A.2}$$

$$\text{with} \qquad \mathcal{U}(\mathbf{r_1}, ..., \mathbf{r_N}) = \sum_{i=1}^{N} \phi(\mathbf{r_i}) + \frac{1}{2} \sum_{i,j=1}^{N} (1 - \delta_{ij}) \cdot u(r_{ij}), \tag{A.3}$$

$$\text{and} \qquad Z = \int \cdots \int d\mathbf{r_1} ... d\mathbf{r_N}\, e^{-\beta \mathcal{U}(\mathbf{r_1}, \mathbf{r_2}, ..., \mathbf{r_N})}. \tag{A.4}$$

The function $\phi(\mathbf{r})$ specifies the external potential energy surface in which the fluid exists. For the sum over pair interactions, the factor of $1/2$ ensures that the interaction of each pair of particles is counted only once and the factor of $1 - \delta_{ij}$ ensures that we exclude the interaction of each particle with itself. When $\phi = 0$, $\rho^{(1)}(\mathbf{r})$ is simply the

bulk density, ρ_B. We may similarly define $\rho^{(2)}(\mathbf{r},\mathbf{r}')$ as

$$\rho^{(2)}(\mathbf{r},\mathbf{r}') = \left\langle \sum_{i,j=1}^{N} (1-\delta_{ij}) \cdot \delta(\mathbf{r}-\mathbf{r_i})\delta(\mathbf{r}'-\mathbf{r_j}) \right\rangle \tag{A.5}$$

$$= \frac{N(N-1)}{Z} \int \cdots \int d\mathbf{r_3}...d\mathbf{r_N} e^{-\beta \mathcal{U}(\mathbf{r},\mathbf{r}',\mathbf{r_3},...,\mathbf{r_N})}. \tag{A.6}$$

The two-particle density may be related to the standard pair correlation function as

$$\rho^{(2)}(\mathbf{r},\mathbf{r}') = \rho^{(1)}(\mathbf{r})\,\rho^{(1)}(\mathbf{r}')\,g(\mathbf{r},\mathbf{r}'). \tag{A.7}$$

The first equation in the YBG hierarchy follows quite quickly when the gradient of $\rho^{(1)}(\mathbf{r})$ is taken, as follows,

$$\vec{\nabla}\rho^{(1)}(\mathbf{r}) = -\beta\frac{N}{Z} \int \cdots \int d\mathbf{r_2}...d\mathbf{r_N} \vec{\nabla}\mathcal{U}(\mathbf{r},\mathbf{r_2},...,\mathbf{r_N}) e^{-\beta \mathcal{U}(\mathbf{r},\mathbf{r_2},...,\mathbf{r_N})} \tag{A.8}$$

$$-k_B T\vec{\nabla}\rho^{(1)}(\mathbf{r}) = \frac{N}{Z}\vec{\nabla}\phi(\mathbf{r}) \int \cdots \int d\mathbf{r_2}...d\mathbf{r_N} e^{-\beta \mathcal{U}(\mathbf{r},\mathbf{r_2},...,\mathbf{r_N})}$$

$$+ \frac{N}{Z}\sum_{j=2}^{N} \int \cdots \int d\mathbf{r_2}...d\mathbf{r_N} \vec{\nabla} u(r_{1j}) e^{-\beta \mathcal{U}(\mathbf{r},\mathbf{r_2},...,\mathbf{r_N})} \tag{A.9}$$

$$= \vec{\nabla}\phi(\mathbf{r})\,\rho^{(1)}(\mathbf{r}) + \int d\mathbf{r}'\vec{\nabla}u(|\mathbf{r}-\mathbf{r}'|)\,\rho^{(2)}(\mathbf{r},\mathbf{r}')\,. \tag{A.10}$$

If we now further define the conditional singlet density $\rho(\mathbf{r}'|\mathbf{r})$ as the density at point $\mathbf{r}'$ given that another particle is located at $\mathbf{r}$,

$$\rho(\mathbf{r}'|\mathbf{r}) \equiv \frac{\rho^{(2)}(\mathbf{r},\mathbf{r}')}{\rho^{(1)}(\mathbf{r})}, \tag{A.11}$$

we obtain the representation of the YBG equation used as a starting point for the derivation of the LMF equation in Ch. 2, namely,

$$-k_B T\vec{\nabla}\ln\rho^{(1)}(\mathbf{r}) = \vec{\nabla}\phi(\mathbf{r}) + \int d\mathbf{r}'\vec{\nabla}u(|\mathbf{r}-\mathbf{r}'|)\,\rho(\mathbf{r}'|\mathbf{r})\,. \tag{A.12}$$

For connection with the mixture definitions that follow, we finally note that a general n-point density distribution function may be written as

$$\rho^{(n)}(\mathbf{r_1},...,\mathbf{r_n}) = \frac{N!}{(N-n)!}\frac{1}{Z}\int\cdots\int e^{-\beta\mathcal{U}} d\mathbf{r_{n+1}}...d\mathbf{r_N}. \tag{A.13}$$

A.2 YBG Equation for Mixtures of Simple Fluids

As we move to more complex systems, the dominant difficulty will be one of counting and keeping the indices straight. To begin with, we defined a multi-point distribution function for a mixture composed of η_S simple particle species labeled by α in a canonical ensemble defined by $\{N_\alpha\}VT$ where $\{N_\alpha\}$ represents the set of particle numbers for each of η_S species. This multi-point distribution function shall be denoted $\rho^{(\mathfrak{N})}_{\{\alpha\}}(\mathfrak{r})$ where $\mathfrak{N} = \sum_{\alpha=1}^{\eta_S} n_\alpha$ indicates the total number of positions held constant and n_α specifies the number of points for each species α held constant with α spanning all possible species that have particles fixed. Thus $\mathfrak{r} = \left\{\mathbf{r_i^{(\alpha)}}\right\}$ indicates the set of $\mathbf{r}_i^{(\alpha)}$ where $1 < i < n_\alpha$ and α again spans all species that have fixed points.

$$\rho^{(\mathfrak{N})}_{\{\alpha\}}(\mathfrak{r}) = \left(\prod_{\gamma=1}^{\eta_S}\frac{N_\gamma!}{(N_\gamma - n_\gamma)!}\right)\frac{1}{Z}\times\int\cdots\int e^{-\beta\mathcal{U}}\left(\prod_{\gamma=1}^{\eta_S}\prod_{i=n_\gamma+1}^{N_\gamma} d\mathbf{r_i^{(\gamma)}}\right) \tag{A.14}$$

where $\mathcal{U}$ is defined as

$$\mathcal{U} = \sum_{\alpha=1}^{\eta_S}\sum_{i=1}^{N_\alpha}\phi^{(\alpha)}\left(\mathbf{r_i^{(\alpha)}}\right) + \frac{1}{2}\sum_{\alpha=1}^{\eta_S}\sum_{\gamma=1}^{\eta_S}\sum_{i=1}^{N_\alpha}\sum_{j=1}^{N_\gamma}(1-\delta_{\alpha\gamma}\delta_{ij})\cdot u_{\alpha\gamma}\left(\left|\mathbf{r_i^{(\alpha)}} - \mathbf{r_j^{(\gamma)}}\right|\right) \tag{A.15}$$

This expression for $\mathcal{U}$ is quite similar to that for the simple fluid. The most notable difference other than more summations is the factor $1-\delta_{\alpha\gamma}\delta_{ij}$, which has been modified from simply $1-\delta_{ij}$ in order to achieve the same goal, to exclude self-interactions of particles.

We now may proceed quite similarly to the simple fluid to write the YBG equation for simple mixtures. We define the shorthand

$$d\mathfrak{R} \equiv \prod_{\gamma=1}^{\eta_S} \prod_{i=1}^{N_\gamma} d\mathbf{r_i}^{(\gamma)}. \tag{A.16}$$

Additional division of $d\mathfrak{R}$ by $d\mathbf{r_1}^{(\alpha)}$ indicates exclusion of integration over the coordinates of the 1^{st} particle of type α. Below we write the single site distribution function for species α, substituting position $\mathbf{r}$ for the position $\mathbf{r_1}^{(\alpha)}$ in $\mathcal{U}$.

$$\rho_\alpha^{(1)}(\mathbf{r}) = \frac{N_\alpha}{Z} \int \cdots \int e^{-\beta \mathcal{U}} \left(\frac{d\mathfrak{R}}{d\mathbf{r_1}^{(\alpha)}} \right) \tag{A.17}$$

$$-k_B T \vec{\nabla} \rho_\alpha^{(1)}(\mathbf{r}) = \frac{N_\alpha}{Z} \int \cdots \int \left(\vec{\nabla} \mathcal{U} \right) e^{-\beta \mathcal{U}} \left(\frac{d\mathfrak{R}}{d\mathbf{r_1}^{(\alpha)}} \right) \tag{A.18}$$

Viewing the expression for $\mathcal{U}$, we may write

$$\vec{\nabla} \mathcal{U} = \vec{\nabla} \phi^{(\alpha)}(\mathbf{r}) + \sum_{j=2}^{N_\alpha} \vec{\nabla} u_{\alpha\alpha} \left(\left| \mathbf{r} - \mathbf{r_j}^{(\alpha)} \right| \right) + \sum_{\gamma \neq \alpha} \sum_{j=1}^{N_\gamma} u_{\alpha\gamma} \left(\left| \mathbf{r} - \mathbf{r_j}^{(\gamma)} \right| \right). \tag{A.19}$$

Substituting this in the equation for the gradient of the singlet density profile of site α, we find

$$\begin{aligned} -k_B T \vec{\nabla} \rho_\alpha^{(1)}(\mathbf{r}) = {} & \vec{\nabla} \phi_\alpha(\mathbf{r}) \frac{N_\alpha}{Z} \int \cdots \int e^{-\beta \mathcal{U}} \left(\frac{d\mathfrak{R}}{d\mathbf{r_1}^{(\alpha)}} \right) \\ & + \frac{N_\alpha (N_\alpha - 1)}{Z} \int d\mathbf{r_2}^{(\alpha)} \vec{\nabla} u_{\alpha\alpha} \left(\left| \mathbf{r} - \mathbf{r_2}^{(\alpha)} \right| \right) \int \cdots \int e^{-\beta \mathcal{U}} \left(\frac{d\mathfrak{R}}{d\mathbf{r_1}^{(\alpha)} d\mathbf{r_2}^{(\alpha)}} \right) \\ & + \sum_{\gamma \neq \alpha}^{\eta_S} \frac{N_\alpha N_\gamma}{Z} \int d\mathbf{r_2}^{(\gamma)} \vec{\nabla} u_{\alpha\gamma} \left(\left| \mathbf{r} - \mathbf{r_2}^{(\gamma)} \right| \right) \int \cdots \int e^{-\beta \mathcal{U}} \left(\frac{d\mathfrak{R}}{d\mathbf{r_1}^{(\alpha)} d\mathbf{r_2}^{(\gamma)}} \right) \end{aligned} \tag{A.20}$$

Within this expression, we may identify the two-point distribution from Eq. (A.14), written as

$$\rho_{\alpha\gamma}^{(2)}(\mathbf{r}, \mathbf{r}') = \frac{N_\alpha (N_\gamma - \delta_{\alpha\gamma})}{Z} \int \cdots \int \left(\frac{d\mathfrak{R}}{d\mathbf{r_1}^{(\alpha)} d\mathbf{r_2}^{(\gamma)}} \right) e^{-\beta \mathcal{U}}. \tag{A.21}$$

Now substituting $\mathbf{r}'$ for $\mathbf{r}_2^\gamma$ in the integral and writing this in terms of one- and two-point distribution functions leads to

$$-k_BT\vec{\nabla}\rho_\alpha^{(1)}(\mathbf{r}) = \vec{\nabla}\phi^{(\alpha)}(\mathbf{r})\rho_\alpha^{(1)}(\mathbf{r}) + \sum_{\gamma=1}^{\eta_S}\int d\mathbf{r}'\rho_{\alpha\gamma}^{(2)}(\mathbf{r},\mathbf{r}')\vec{\nabla}u_{\alpha\gamma}(|\mathbf{r}-\mathbf{r}'|). \tag{A.22}$$

Writing this in the form which leads naturally to the LMF equation, we find

$$-k_BT\vec{\nabla}\ln\rho_\alpha^{(1)}(\mathbf{r}) = \vec{\nabla}\phi^{(\alpha)}(\mathbf{r}) + \sum_{\gamma=1}^{\eta_S}\int d\mathbf{r}'\rho_{\gamma|\alpha}(\mathbf{r}'|\mathbf{r})\vec{\nabla}u_{\alpha\gamma}(|\mathbf{r}-\mathbf{r}'|), \tag{A.23}$$

where $\rho_{\gamma|\alpha}(\mathbf{r}'|\mathbf{r})$ is the conditional density of a particle of type γ being at $\mathbf{r}'$ given that a particle of type α is located at $\mathbf{r}$.

A.3 YBG Equation for Molecular Fluids

When treating molecular correlations, one of the most natural starting points is generalizing the density distribution functions to depend not only on positions of molecules but also orientations of molecules. In this way, as stated in Gray and Gubbins [34, pp. 202-203], a YBG equation for intermolecular correlations may be written as

$$-k_BT\vec{\nabla}\rho^{(1)}(\mathbf{r}\boldsymbol{\Omega}) = \vec{\nabla}\phi(\mathbf{r}\boldsymbol{\Omega})\rho^{(1)}(\mathbf{r}\boldsymbol{\Omega}) + \iint d\mathbf{r}'d\boldsymbol{\Omega}'\vec{\nabla}u(|\mathbf{r}-\mathbf{r}'|\Omega\Omega')\rho^{(2)}(\mathbf{r}\boldsymbol{\Omega},\mathbf{r}'\boldsymbol{\Omega}'), \tag{A.24}$$

with Ω meant to represent molecular orientation.

The LMF equation formulated by Chen [13] for generalized charged distributions by starting from the LMF equation for charged fluid mixtures and generalizing to other lowest-order multipole moments may also be understood as being derived from this equation, with u_1 resulting from the lowest order multipole moment of the molecule as suggested in [13, 15].

For reasons discussed in Ch. 5, we find it more convenient to formulate an LMF equation based on a YBG equation for site-site molecular models.

A.4 YBG Equation for General Mixtures of Smaller Site-Site Molecular Fluids

Previous work [95] for site-site YBG equations begins the derivation by writing the singlet density for a molecular site in terms of the singlet density for the entire molecule, taking appropriate gradients on either side, and then reducing to a site-site representation. Since that work was designed for use in uniform fluids of hard sphere dimers and subsequently extended to chains and square well monomer units, writing a general formulation of the first equation in the YBG hierarchy based on their approach is not so clearly done.

However, using the general formalism developed by Chandler and Pratt [11] for the partition functions and density distribution functions of mixtures of site-site molecular models, we may follow a similar path to the derivation of a general YBG equation. The formalism originally was developed to also account for the possibility of chemical reactions, and since this is not a concern in the inherently classical systems we study, a few alterations will be made to simplify notation, with no impact on the meaning of the equations.

The partition function for a mixture of molecular species M with total sites n_M on each molecule labeled by Greek characters such as α is given below with the position of the α site on the i^{th} molecule of type M given as $\mathbf{r}_{iM}^{(\alpha)}$ and the positions of all n_M

sites on the i^{th} molecule of type M given as $\mathbf{R_{iM}}$.

$$Q(\{M\}) = \left(\prod_M N_M! \nu_M^{N_M} \prod_{\alpha=1}^{n_M} \left(\Lambda_M^{(\alpha)} \right)^{3N_M} \right)^{-1} \int \cdots \int e^{-\beta \mathcal{U}} \left(\prod_{M,i} d\mathbf{R_{iM}} \right) \tag{A.25}$$

where $\mathcal{U}$ is defined as

$$\begin{aligned} \mathcal{U} = & \sum_M \sum_{i=1}^{N_M} w_M^*(\mathbf{R_{iM}}) + \sum_M \sum_{i=1}^{N_M} \sum_{\alpha=1}^{n_M} \phi^{(\alpha M)}(\mathbf{r_{iM}^{(\alpha)}}) \\ & + \frac{1}{2} \sum_M \sum_{M'} \sum_{i=1}^{N_M} \sum_{j=1}^{N_{M'}} (1 - \delta_{MM'} \delta_{ij}) \sum_{\alpha=1}^{n_M} \sum_{\gamma=1}^{n_{M'}} u_{\alpha M \gamma M'} \left(\left| \mathbf{r_{iM}^{(\alpha)}} - \mathbf{r_{jM'}^{(\gamma)}} \right| \right). \end{aligned} \tag{A.26}$$

In this, ν_M is the symmetry number of the molecule. For example, for H_2O, $\nu = 2$ for 2 equivalent orientations, and for CH_4, $\nu = 12$ for 12 different equivalent orientations – 3 equivalent rotations for each of 4 different C-H bonds fixed in position. With symmetry numbers included, each "equivalent" atom may be correctly viewed as a *unique* site. Thus H_2O has 3 sites and CH_4 would have 5 sites. $\Lambda_M^{(\alpha)}$ is the thermal de Broglie wavelength for the atom α on molecule M.

Beyond the symmetry number, the expression for the partition function does not look drastically different from the partition function for mixtures aside from having summations both over the types of molecules and over the sites on each molecule. The crucial difference comes in the definition of w_M^* to represent bonding terms within each molecule. This also represents our greatest divergence from the notation of Pratt and Chandler. In their paper, rather than defining energies, they defined bonding factors as

$$b_M^*(\mathbf{r_{1M}^{(1)}}, \mathbf{r_{1M}^{(2)}}, ..., \mathbf{r_{1M}^{(n_M)}}) = H_M(\mathbf{R_{1M}}) e^{-\beta w_M^*(\mathbf{R_{1M}})}, \tag{A.27}$$

which were meant to represent the Boltzmann factor of the intramolecular energies when none of the bonds in that molecule were broken. In this formula, $\mathbf{R_{1M}}$ rep-

resents all of the position coordinates of the 1st molecule of type M and w_M^* is the intramolecular energy due to bonds. $H_M(\mathbf{R_{1M}})$ is 1 if all bonds are formed, and 0 otherwise. We instead do no worry about bond-breaking events and pull w_M^* into the expression for $\mathcal{U}$.

Now following the same path as done for simple fluids and mixtures, we write the single-site density distribution function. Following the simplified notation used for mixtures $\prod_{M,i} d\mathbf{R_{iM}}$ will be written as $d\mathfrak{R}$, and division by $d\mathbf{r}_{1M}^{(\alpha)}$ indicates integration over all particle positions except the α site on the 1^{st} molecule of type M. Thus, we have

$$\rho_{\alpha M}^{(1)}(\mathbf{r}) = \frac{N_M}{Z} \int \cdots \int e^{-\beta \mathcal{U}} \left(\frac{d\mathfrak{R}}{d\mathbf{r}_{\mathbf{1M}}^{(\alpha)}} \right). \tag{A.28}$$

Here again, $\mathbf{r}$ has replaced $\mathbf{r}_{\mathbf{1M}}^{(\alpha)}$ in $\mathcal{U}$. Now taking the gradient with respect to $\mathbf{r}$,

$$\begin{aligned}
-k_B T \vec{\nabla} \rho_{\alpha M}^{(1)}(\mathbf{r}) = & \frac{N_M}{Z} \int \cdots \int \left[\vec{\nabla} w_M^*(\mathbf{1_M}) \right] e^{-\beta \mathcal{U}} \left(\frac{d\mathfrak{R}}{d\mathbf{r}_{\mathbf{1M}}^{(\alpha)}} \right) \\
& + \left[\vec{\nabla} \phi^{(\alpha M)}(\mathbf{r}) \right] \frac{N_M}{Z} \int \cdots \int e^{-\beta \mathcal{U}} \left(\frac{d\mathfrak{R}}{d\mathbf{r}_{\mathbf{1M}}^{(\alpha)}} \right) \\
& + \frac{N_M (N_M - 1)}{Z} \int \cdots \int \left[\sum_{\gamma=1}^{n_M} \vec{\nabla} u_{\alpha M \gamma M} \left(\left| \mathbf{r} - \mathbf{r}_{\mathbf{2M}}^{(\gamma)} \right| \right) \right] e^{-\beta \mathcal{U}} \left(\frac{d\mathfrak{R}}{d\mathbf{r}_{1M}^{(\alpha)}} \right) \\
& + \frac{N_M N_{M'}}{Z} \int \cdots \int \left[\sum_{M' \neq M} \sum_{\gamma=1}^{n_{M'}} \vec{\nabla} u_{\alpha M \gamma M'} \left(\left| \mathbf{r} - \mathbf{r}_{\mathbf{1M'}}^{(\gamma)} \right| \right) \right] e^{-\beta \mathcal{U}} \left(\frac{d\mathfrak{R}}{d\mathbf{r}_{1M}^{(\alpha)}} \right).
\end{aligned} \tag{A.29}$$

Following definitions made by Chandler and Pratt [11] and subsequently Chandler [10] as written below, we may simplify the site-site molecular YBG equation in terms of an intramolecular density distribution function, $\rho_M^{(1)}(\mathbf{R_M})$, and a two-point intermolecular site-site density distribution function, $\rho_{\alpha M \gamma M'}^{(2)}(\mathbf{r}, \mathbf{r}')$, specifically defined to exclude intramolecular site-site correlations. Here we set $\mathbf{R_{1M}} = \mathbf{R_M}$, $\mathbf{r}_{\mathbf{1M}}^{(\alpha)} = \mathbf{r}$, and $\mathbf{r}_{\mathbf{2M'}}^{(\gamma)} = \mathbf{r}'$

in $\mathcal{U}$:

$$\rho_M^{(1)}(\mathbf{R}_M) = \frac{N_M}{Z} \int \cdots \int e^{-\beta \mathcal{U}} \left(\frac{d\mathfrak{R}}{d\mathbf{R}_{1M}} \right) \tag{A.30}$$

$$\rho_{\alpha M \gamma M'}^{(2)}(\mathbf{r}, \mathbf{r}') = \frac{N_M (N_{M'} - \delta_{MM'})}{Z} \int \cdots \int e^{-\beta \mathcal{U}} \left(\frac{d\mathfrak{R}}{d\mathbf{r}_{\mathbf{1M}}^{(\alpha)} d\mathbf{r}_{\mathbf{2M'}}^{(\gamma)}} \right). \tag{A.31}$$

Substituting these definitions into the expression for the gradient of $\rho_{\alpha M}^{(1)}(\mathbf{r})$, we find

$$\begin{aligned} -k_B T \vec{\nabla} \rho_{\alpha M}^{(1)}(\mathbf{r}) = & \int \cdots \int \left[\vec{\nabla} w_M^*(\mathbf{R_M}) \right] \rho_M^{(1)}(\mathbf{R_M}) \left(\frac{d\mathbf{R_M}}{d\mathbf{r}_{\mathbf{M}}^{(\alpha)}} \right) \\ & + \left[\vec{\nabla} \phi_{\alpha M}(\mathbf{r}) \right] \rho_{\alpha M}^{(1)}(\mathbf{r}) + \sum_{M'} \sum_{\gamma=1}^{n_{M'}} \int d\mathbf{r}' \rho_{\alpha M \gamma M'}^{(2)}(\mathbf{r}, \mathbf{r}') \vec{\nabla} u_{\alpha M \gamma M'}(|\mathbf{r} - \mathbf{r}'|). \end{aligned} \tag{A.32}$$

This final equation is quite similar to the YBG equation for mixtures. Indeed, the only difference is the term including the gradient of the bonding energy and the intramolecular density distribution function. Thus we must focus on this term to determine what approximations are reasonable.

In order to put the YBG equation in the form with which the LMF equation is derived, we must divide each side by the singlet density of site α on molecule M.

$$\begin{aligned} -k_B T \vec{\nabla} \left(\ln \rho_{\alpha M}(\mathbf{r}) \right) = & \int \cdots \int \left[\vec{\nabla} w_M^*(\mathbf{R_M}) \right] \varrho_{M|\alpha}(\mathbf{R_M}|\mathbf{r}) \left(\frac{d\mathbf{R_M}}{d\mathbf{r}_{\mathbf{M}}^{(\alpha)}} \right) \\ & + \vec{\nabla} \phi_{\alpha M}(\mathbf{r}) + \sum_{M'} \sum_{\gamma=1}^{n_{M'}} \int d\mathbf{r}' \rho_{\gamma M'|\alpha M}(\mathbf{r}'|\mathbf{r}) \vec{\nabla} u_{\alpha M \gamma M'}(|\mathbf{r} - \mathbf{r}'|) \end{aligned} \tag{A.33}$$

Here we introduce conditional densities again. $\rho_{\gamma M'|\alpha M}(\mathbf{r}'|\mathbf{r})$ is the equivalent of the standard conditional density, an intermolecular conditional density of finding site γ on molecule M' at position $\mathbf{r}'$ given that a site α on molecule M is located at position $\mathbf{r}$. $\varrho_{M|\alpha}(\mathbf{R_M}|\mathbf{r})$ is the intramolecular conditional density of a molecular orientation $\mathbf{R_M}$ given that site α is located at position $\mathbf{r}$. This notation for intramolecular density

does diverge from Chandler and Pratt [11]; it is the equivalent of their two point contraction function $s^{(2)}$.

A.5 YBG Equation for General Mixtures of Larger Site-Site Molecular Fluids

Here, we derive a separate YBG expression for larger site-site molecules because in most simulation potentials, such as those defined by the CHARMM [64] and AMBER [25] parameter sets, the potential energy due to "intermolecular" interactions (LJ interactions and point charge interactions) is not written as distinct summations over molecules and their intramolecular sites. Rather the LJ and charge interaction contribution to $\mathcal{U}$ is a sum over all sites separated by at least three bonds (*i.e.* excluding atoms bonded or connected via angle bending).

The expression for the partition function Q does not change, but $\mathcal{U}$ does. Here α is summed over the total distinct sites in the system, $\eta_S = \sum_M n_M$. w_b^* is a bond energy function, w_a^* is the angle energy function for three sites, and w_d^* is an energy function depending on the torsion angle between two bonds around a connecting bond

axis. With this notation, we find

$$\begin{aligned}\mathcal{U} = &\sum_{\alpha=1}^{\eta_S}\sum_{i=1}^{N_\alpha}\sum_{\substack{\gamma \\ \text{1-2}}} w_b^*\left(\left|\mathbf{r}_\mathbf{i}^{(\alpha)} - \mathbf{r}^{(\gamma)}\right|\right) + \sum_{\alpha=1}^{\eta_S}\sum_{i=1}^{N_\alpha}\sum_{\substack{\gamma,\delta \\ \text{1-2-3}}} w_a^*\left(\mathbf{r}_\mathbf{i}^{(\alpha)}, \mathbf{r}_{\text{1-2}}^{(\gamma)}, \mathbf{r}_{\text{1-3}}^{(\delta)}\right) \\ &+ \sum_{\alpha=1}^{\eta_S}\sum_{i=1}^{N_\alpha}\sum_{\substack{\gamma,\delta,\zeta \\ \text{1-2-3-4}}} w_d^*\left(\mathbf{r}_\mathbf{i}^{(\alpha)}, \mathbf{r}_{\text{1-2}}^{(\gamma)}, \mathbf{r}_{\text{1-3}}^{(\delta)}, \mathbf{r}_{\text{1-4}}^{(\zeta)}\right) \\ &+ \sum_{\alpha=1}^{\eta_S}\sum_{i=1}^{N_\alpha}\phi^{(\alpha)}\left(\mathbf{r}_\mathbf{i}^{(\alpha)}\right) + \frac{1}{2}\underbrace{\sum_{\alpha=1}^{\eta_S}\sum_{\gamma=1}^{\eta_S}\sum_{i=1}^{N_\alpha}\sum_{j=1}^{N_\gamma}}_{\text{1-4 and beyond}}\left(1-\delta_{\alpha\gamma}\delta_{ij}\right)u_{\alpha\gamma}\left(\left|\mathbf{r}_\mathbf{i}^{\alpha} - \mathbf{r}_\mathbf{j}^{\gamma}\right|\right). \end{aligned} \quad \text{(A.34)}$$

Note that $\mathcal{U}$ written in this way is identical to the mixture $\mathcal{U}$ other than the first three terms related to bonding interactions. Following the same rules for unique sites within molecules, the $N_\alpha = N_M$ for site α on molecule of type M. The first three terms are for bond vibrations, angle vibrations, and dihedral rotations of two bonds around a connecting bond. Technically, these usually depend on only r, θ, and ϕ respectively, but we include positions for generality and application later. These sums are understood to count sets of atoms connected via bond, angular, or torsional potentials only once. Also, the brace beneath the four sums indicates that interactions are only included here if sites are at most connected by a dihedral bonding term (and no other bonds). One complication for the AMBER force field is that non-bonded interactions are scaled down for 1-4 (dihedral) pairs. LJ interactions for 1-4 pairs are divided by 2.0 and Coulomb interactions are divided by 1.2. We will not address this complication, but it conceivably could be included in this formalism as well. The new all-atom force field for CHARMM does not scale the Coulomb interactions for 1-4 pairs.

Just as before, we write the singlet density distribution function as

$$\rho_{\alpha}^{(1)}(\mathbf{r}) = \frac{N_{\alpha}}{Z} \int \cdots \int e^{-\beta \mathcal{U}} \left(\frac{d\mathfrak{R}}{d\mathbf{r}_{\mathbf{1}}^{(\alpha)}} \right). \tag{A.35}$$

Taking the gradient of the $\mathcal{U}$ defined in Eq. (A.34), we find

$$\begin{aligned}
-k_B T \vec{\nabla} \rho_{\alpha}^{(1)}(\mathbf{r}) = {} & \frac{N_{\alpha}}{Z} \sum_{\substack{\gamma \\ 1-2}} \int \cdots \int \left[\vec{\nabla} w_b^* \left(\mathbf{r}, \mathbf{r}_{1\text{-}2}^{(\gamma)} \right) \right] e^{-\beta \mathcal{U}} \left(\frac{d\mathfrak{R}}{d\mathbf{r}_{\mathbf{1}}^{(\alpha)}} \right) \\
& + \frac{N_{\alpha}}{Z} \sum_{\substack{\gamma,\delta \\ 1-2-3}} \int \cdots \int \left[\vec{\nabla} w_a^* \left(\mathbf{r}, \mathbf{r}_{1\text{-}2}^{(\gamma)}, \mathbf{r}_{1\text{-}3}^{(\delta)} \right) \right] e^{-\beta \mathcal{U}} \left(\frac{d\mathfrak{R}}{d\mathbf{r}_{\mathbf{1}}^{(\alpha)}} \right) \\
& + \frac{N_{\alpha}}{Z} \sum_{\substack{\gamma,\delta,\zeta \\ 1-2-3-4}} \int \cdots \int \left[\vec{\nabla} w_d^* \left(\mathbf{r}, \mathbf{r}_{1\text{-}2}^{(\gamma)}, \mathbf{r}_{1\text{-}3}^{(\delta)}, \mathbf{r}_{1\text{-}4}^{(\zeta)} \right) \right] e^{-\beta \mathcal{U}} \left(\frac{d\mathfrak{R}}{d\mathbf{r}_{\mathbf{1}}^{(\alpha)}} \right) \\
& + \left[\vec{\nabla} \phi^{(\alpha)}(\mathbf{r}) \right] \frac{N_{\alpha}}{Z} \int \cdots \int e^{-\beta \mathcal{U}} \left(\frac{d\mathfrak{R}}{d\mathbf{r}_{\mathbf{1}}^{(\alpha)}} \right) \\
& + \frac{N_{\alpha}(N_{\alpha}-1)}{Z} \int \cdots \int \left[\sum_{\gamma=1}^{\eta_S} \vec{\nabla} u_{\alpha\alpha} \left(\left| \mathbf{r} - \mathbf{r}_{\mathbf{2}}^{(\alpha)} \right| \right) \right] e^{-\beta \mathcal{U}} \left(\frac{d\mathfrak{R}}{d\mathbf{r}_{\mathbf{1}}^{(\alpha)}} \right) \\
& + \frac{N_{\alpha} N_{\gamma}}{Z} \int \cdots \int \left[\sum_{\gamma \neq \alpha}^{\eta_S} \vec{\nabla} u_{\alpha\gamma} \left(\left| \mathbf{r} - \mathbf{r}_{\mathbf{2}}^{(\gamma)} \right| \right) \right] e^{-\beta \mathcal{U}} \left(\frac{d\mathfrak{R}}{d\mathbf{r}_{\mathbf{1}}^{(\alpha)}} \right).
\end{aligned} \tag{A.36}$$

Making appropriate substitutions and dividing through by the singlet density of site α as usual, we find

$$\begin{aligned}
-k_B T \vec{\nabla} \ln \rho_{\alpha}^{(1)}(\mathbf{r}) = {} & \sum_{\substack{\gamma \\ 1-2}} \int d\mathbf{r}' \left[\vec{\nabla} w_b^*(\mathbf{r}, \mathbf{r}') \right] \varrho_{\gamma|\alpha}(\mathbf{r}'|\mathbf{r}) \\
& + \sum_{\substack{\gamma,\delta \\ 1-2-3}} \int d\mathbf{r}' d\mathbf{r}'' \left[\vec{\nabla} w_a^*(\mathbf{r}, \mathbf{r}', \mathbf{r}'') \right] \varrho_{\gamma\delta|\alpha}(\mathbf{r}', \mathbf{r}''|\mathbf{r}) \\
& + \sum_{\substack{\gamma,\delta,\zeta \\ 1-2-3-4}} \int d\mathbf{r}' d\mathbf{r}'' d\mathbf{r}''' \left[\vec{\nabla} w_d^*(\mathbf{r}, \mathbf{r}', \mathbf{r}'', \mathbf{r}''') \right] \varrho_{\gamma\delta\zeta|\alpha}(\mathbf{r}', \mathbf{r}'', \mathbf{r}'''|\mathbf{r}) \\
& + \vec{\nabla} \phi_{\alpha}(\mathbf{r}) + \sum_{\gamma=1}^{\eta_S} \int d\mathbf{r}' \rho_{\gamma|\alpha}(\mathbf{r}'|\mathbf{r}) \vec{\nabla} u_{\alpha\gamma}(|\mathbf{r} - \mathbf{r}'|).
\end{aligned} \tag{A.37}$$

Here again, ϱ indicates some sort of *intra*molecular conditional density, but because we specifically know how many points each force term refers to, we do not have to give those conditional densities in terms of the whole molecule's orientation, but rather just the density of the local relative orientations. And now the standard conditional density $\rho_{\gamma|\alpha}(\mathbf{r}'|\mathbf{r})$ will explicitly exclude atoms which are bonded to site α or within 2 bonds of site α.

If we separate $u_{\alpha\gamma}$ as

$$u_{\alpha\gamma}(r) = u^{\mathrm{LJ}}_{\alpha\gamma} + \frac{q_\alpha q_\gamma}{\epsilon r}, \tag{A.38}$$

then we may write a simpler formulation with which to do the LMF derivation (at least for keeping track of indices),

$$\begin{aligned}
-k_B T\vec{\nabla}\ln\rho^{(1)}_\alpha(\mathbf{r}) = &\sum_{\substack{\gamma\\1-2}}\int d\mathbf{r}'\,\left[\vec{\nabla}w^*_b(\mathbf{r},\mathbf{r}')\right]\varrho_{\gamma|\alpha}(\mathbf{r}'|\mathbf{r})\\
&+\sum_{\substack{\gamma,\delta\\1-2-3}}\int d\mathbf{r}'d\mathbf{r}''\,\left[\vec{\nabla}w^*_a(\mathbf{r},\mathbf{r}',\mathbf{r}'')\right]\varrho_{\gamma\delta|\alpha}(\mathbf{r}',\mathbf{r}''|\mathbf{r})\\
&+\sum_{\substack{\gamma,\delta\\1-2-3-4}}\int d\mathbf{r}'d\mathbf{r}''d\mathbf{r}'''\,\left[\vec{\nabla}w^*_d(\mathbf{r},\mathbf{r}',\mathbf{r}'',\mathbf{r}''')\right]\varrho_{\gamma\delta\zeta|\alpha}(\mathbf{r}',\mathbf{r}'',\mathbf{r}'''|\mathbf{r})\\
&+\sum_{\gamma=1}^{\eta_S}\int d\mathbf{r}'\rho_{\gamma|\alpha}(\mathbf{r}'|\mathbf{r})\vec{\nabla}u^{\mathrm{LJ}}_{\alpha\gamma}(|\mathbf{r}-\mathbf{r}'|)\\
&+\vec{\nabla}\phi_\alpha(\mathbf{r})+\frac{q_\alpha}{\epsilon}\int d\mathbf{r}'\rho_{q|\alpha}(\mathbf{r}'|\mathbf{r})\vec{\nabla}\frac{1}{|\mathbf{r}-\mathbf{r}'|}.
\end{aligned}\tag{A.39}$$

Here $\rho_{q|\alpha}(\mathbf{r}'|\mathbf{r})$ is the conditional *charge* density at $\mathbf{r}'$ given that particle α is located at $\mathbf{r}$.

Appendix B

Smoothed Green's functions for Various Geometries

The LMF equation is derived in Ch. 2 for very general geometries and boundary conditions. Therefore, Eq. (2.13) and Eq. (4.9) involve three-dimensional integrals. However, for two geometries considered in this thesis – slab confinement in the z-direction and radial symmetry about the origin – the integrals may be simplified to dependence on only one variable. In the course of this simplification, Green's functions smoothed by a Gaussian of width σ occur naturally. In this appendix, we derive out these smoothed Green's function which prove useful in solving the LMF equation in Chs. 3 and 6 and in analyzing certain bulk water results in Sect. 5.4.

In essence, for each geometry, we seek to write equivalents of the standard LMF Green's function for long-ranged electrostatics,

$$v_1(|\mathbf{r}-\mathbf{r}'|) = \frac{\mathrm{erf}\left(\frac{|\mathbf{r}-\mathbf{r}'|}{\sigma}\right)}{|\mathbf{r}-\mathbf{r}'|}, \tag{B.1}$$

that depend only on a single variable. This leads to simpler solutions of the LMF equation in real-space using simulation data.

In general, these simplifications are exact when the singlet density profile $\rho_R(\mathbf{r};[\phi_R])$ depends not on $\mathbf{r}$ but rather on a single variable like z or r. As shown in Sect. 6.6, since the original Green's function arises from a Gaussian-smoothed charge density, these simplifications to the LMF equation will be approximately true even for density profiles which contain greater local variation.

Since the LMF equation may be expressed in terms of electrostatic potentials, as explained in Sect. 4.1, we will base the analysis on the following writing of the LMF equation as

$$\mathcal{V}_R(\mathbf{r}) = \mathcal{V}(\mathbf{r}) + \frac{1}{\epsilon}\int d\mathbf{r}'\,\rho^q(\mathbf{r}';[\mathcal{V}_R])\cdot v_1\left(|\mathbf{r}-\mathbf{r}'|\right) + C, \tag{B.2}$$

where $\mathcal{V}_R$ is the LMF rescaled external electrostatic potential, and $\mathcal{V}$ is the originally imposed external electrostatic potential.

B.1 Planar 1-D $G(z, z')$

For slab simulations where there is complete uniformity in the the external field $\mathcal{V}$ in the x and y directions such that $\mathcal{V}$ is only a function of z, we may simplify the LMF equation to a one-dimensional equation as shown in [13, 15]. This can be done by direct manipulation of Eq. (B.2), written for this symmetry as

$$\mathcal{V}_R(z) = \mathcal{V}(z) + \frac{1}{\epsilon}\int d\mathbf{r}'\,\rho^q(z';[\mathcal{V}_R])\cdot v_1\left(|\mathbf{r}-\mathbf{r}'|\right) + C. \tag{B.3}$$

In essence what we seek is a Green's function $G(z;z')$ such that

$$\mathcal{V}_R(z) = \mathcal{V}(z) + \frac{2\pi}{\epsilon}\int dz'\,\rho^q(z';[\mathcal{V}_R])\cdot G\left(z;z'\right) + C. \tag{B.4}$$

In other words, using the rewriting of Eq. (B.2) as

$$\mathcal{V}_R(z) = \mathcal{V}(z) + \frac{1}{\epsilon}\int dz'\rho^q(z';[\mathcal{V}_R])\int d\mathbf{r}''\delta(z'-z'')v_1(|\mathbf{r}-\mathbf{r}''|) + C, \tag{B.5}$$

we may define $G(z;z')$ as

$$\begin{aligned} G(z;z') &= \frac{1}{2\pi}\int d\mathbf{r}''\delta(z'-z'')v_1(|\mathbf{r}-\mathbf{r}''|) \\ &= \int s''ds''v_1\left(\sqrt{s''^2+(z-z')^2}\right). \end{aligned} \tag{B.6}$$

Defining $\zeta \equiv z - z'$, we find

$$G(\zeta) = \int s\,ds\,\frac{\operatorname{erf}\left(\frac{\sqrt{s^2+\zeta^2}}{\sigma}\right)}{\sqrt{s^2+\zeta^2}}. \tag{B.7}$$

If we were to integrate this equation explicitly, an infinite constant would result, thus the simpler path is to take the derivative of this equation with respect to ζ, solve the s-integral, and then integrate back to obtain G. Since the original LMF equation was only defined up to a constant, the constant of integration will be swept into the existing integration constant C and used to set the zero point of energy:

$$\begin{aligned}\frac{\partial}{\partial\zeta}G(\zeta) = -\zeta\int_0^\infty \operatorname{erf}\left(\frac{\sqrt{s^2+\zeta^2}}{\sigma}\right)\frac{s\,ds}{(s^2+\zeta^2)^{3/2}} \\ + \zeta\int_0^\infty \frac{1}{\sqrt{s^2+\zeta^2}}\cdot\frac{2}{\sigma\sqrt{\pi}}\frac{e^{-(s^2+\zeta^2)/\sigma^2}}{\sqrt{s^2+\zeta^2}}\,sds.\end{aligned} \tag{B.8}$$

These integrals over s may be solved quickly by identifying

$$\begin{aligned} v &= \frac{1}{\sqrt{s^2+\zeta^2}}, & dv &= -\frac{s\,ds}{(s^2+\zeta^2)^{3/2}}, \\ u &= \operatorname{erf}\left(\frac{\sqrt{s^2+\zeta^2}}{\sigma}\right), & du &= \frac{2}{\sigma\sqrt{pi}}\frac{e^{-(s^2+\zeta^2)/\sigma^2}}{\sqrt{s^2+\zeta^2}}\,sds. \end{aligned} \tag{B.9}$$

Now using integration by parts, we find

$$\begin{aligned}\frac{\partial}{\partial\zeta}G(\zeta) &= \zeta\operatorname{erf}\left(\frac{\sqrt{s^2+\zeta^2}}{\sigma}\right)\frac{1}{\sqrt{s^2+\zeta^2}}\Bigg|_0^\infty \\ &= -\frac{\zeta}{|\zeta|}\operatorname{erf}\left(\frac{|\zeta|}{\sigma}\right) = -\operatorname{erf}\left(\frac{\zeta}{\sigma}\right).\end{aligned} \tag{B.10}$$

So now we may find $G(z;z')$ by integrating over ζ from $\zeta = z_0 - z'$ to $\zeta = z - z'$ where

z_0 is the chosen zero point of the potential,

$$G(z;z') = \int_{z_0-z'}^{z-z'} d\zeta\, \frac{\partial G(\zeta)}{\partial \zeta} = -\int_{z_0-z'}^{z-z'} d\zeta\, \mathrm{erf}\left(\frac{\zeta}{\sigma}\right) \tag{B.11}$$

$$= -\zeta\, \mathrm{erf}\left(\frac{\zeta}{\sigma}\right) - \frac{\sigma}{\sqrt{\pi}} e^{-\zeta^2/\sigma^2}\Bigg|_{z_0-z'}^{z-z'} \tag{B.12}$$

$$= -|z-z'|\, \mathrm{erf}\left(\frac{|z-z'|}{\sigma}\right) - \frac{\sigma}{\sqrt{\pi}} \exp\left(-\left(\frac{z-z'}{\sigma}\right)^2\right)$$
$$+ |z_0-z'|\, \mathrm{erf}\left(\frac{|z_0-z'|}{\sigma}\right) + \frac{\sigma}{\sqrt{\pi}} \exp\left(-\left(\frac{z_0-z'}{\sigma}\right)^2\right). \tag{B.13}$$

This $G(z;z')$ represents the potential at position z due to a Gaussian-smoothed sheet of charge placed at z'.

B.2 Spherically Symmetric 1-D $G(r,r')$

For simulations of bulk substances where the external field $\mathcal{V}$ is simply a function of r, we may again simplify the LMF equation into an equation depending on only one variable. As done in the previous section we proceed by directly manipulating

$$\mathcal{V}_R(r) = \mathcal{V}(r) + \frac{1}{\epsilon}\int d\mathbf{r}'\rho^q(r';[\mathcal{V}_R])\cdot v_1(|\mathbf{r}-\mathbf{r}'|) + C. \tag{B.14}$$

Again we seek a Green's function, this time denoted $\mathcal{G}(r;r')$ such that

$$\mathcal{V}_R(r) = \mathcal{V}(r) + \frac{1}{\epsilon}\int d\mathbf{r}'\rho^q(r';[\mathcal{V}_R])\cdot \mathcal{G}(r;r') + C. \tag{B.15}$$

The function $\mathcal{G}(r;r')$ is the potential at r due to a unit charge smoothed into a spherical shell at r' and then Gaussian-smoothed. Again writing

$$\mathcal{V}_R(r) = \mathcal{V} + \frac{1}{\epsilon}\int d\mathbf{r}'\rho^q(r';[\mathcal{V}_R])\int d\mathbf{r}''\frac{\delta(r'-r'')}{4\pi r'^2}\, v_1(|\mathbf{r}-\mathbf{r}''|) + C, \tag{B.16}$$

we may identify $\mathcal{G}$ as

$$\mathcal{G}(r;r') = \int_0^{2\pi} d\phi \int_{-1}^{1} d(\cos\theta) \int_0^{\infty} r''^2 dr' \frac{\delta(r'-r'')}{4\pi r'^2} \frac{\operatorname{erf}\left(\frac{|\mathbf{r}-\mathbf{r}''|}{\sigma}\right)}{|\mathbf{r}-\mathbf{r}''|}. \tag{B.17}$$

Carrying out the integration we find

$$\begin{aligned}
\mathcal{G}(r;r') &= \frac{1}{2}\int_{-1}^{1} d(\cos\theta) \frac{\operatorname{erf}\left(\frac{\sqrt{r^2-2rr'+r'^2}}{\sigma}\right)}{\sqrt{r^2-2rr'+r'^2}} \\
&= \frac{1}{2rr'}\left[|r+r'|\operatorname{erf}\left(\frac{|r+r'|}{\sigma}\right) + \frac{\sigma}{\sqrt{\pi}} e^{-\left(\frac{r+r'}{\sigma}\right)^2}\right. \\
&\qquad \left. - |r-r'|\operatorname{erf}\left(\frac{|r-r'|}{\sigma}\right) - \frac{\sigma}{\sqrt{\pi}} e^{-\left(\frac{r-r'}{\sigma}\right)^2}\right].
\end{aligned} \tag{B.18}$$

One point to keep in mind for this expression for $\mathcal{G}$ is that for large r [1], *i.e.* the potential at large distances ($r - r'$ large) due to a source charge shell r',

$$\lim_{r\to\infty} \mathcal{G}(r;r') \cdot r = 1. \tag{B.19}$$

In other words, this expression yields correct behavior at large distances because a shell of charge at r' centered about the origin should appear no different than a point charge at the origin. As always, we expect our correct pair distribution functions to decay sufficiently fast at large r, such that

$$\mathcal{V}_R(r) = \mathcal{V}(r) + \frac{1}{\epsilon}\int d\mathbf{r}' \rho^q(r';[\mathcal{V}_R]) \cdot \mathcal{G}(r;r') + C$$

will not diverge. However, if this equation is closed to obtain self-consistency one must take care with the k-space components. As shown by Chen *et al.* [14] for the MPB closure, if the closure is analytical, it is almost certain that solving the LMF equation in k-space is more appropriate, using the mixing shown in Appendix E. If the closure is achieved with simulations, the r-space version of the k-space mixing

[1] We use the large x expansion of $\operatorname{erf}(x) \simeq 1 - \exp(-x^2)/(x\sqrt{\pi})$.

scheme shown in Appendix E should be employed to take care of the $k = 0$ divergence of $\mathcal{G}$.

Appendix C

Determining Pressure for the Charged Two Wall System

This appendix is intended to be a companion to Ch. 3; therefore many of the symbols briefly defined in this appendix are expained in more depth in that chapter. The essential goal of this appendix is to explain the formulae used to calculate the pressure of a system composed of point counterions contained between two uniformly charged walls. These relations are given briefly in Sects. 3.1 and 3.4.5. At times, the pressure in this system is called osmotic pressure in analogy with systems in equilibrium with a bulk salt solution.

Osmotic pressure is the external pressure needed to apply to a solution in order to counterbalance the osmotic flow of solvent into the solution through a semi-permeable membrane. In the case of the uniformly-charged-wall model with point counterions, the osmotic pressure and pressure might be considered interchangeable because the solvent only occurs as the uniform dielectric constant. The solution is defined as the space between the two walls including the counterions. If osmotic pressure between walls is positive, then a positive pressure would have to be applied to the walls to oppose the flow of solvent into the system. Since space is essentially the solvent then this can be interpreted as the force per unit area needed to be applied to the walls in order to keep the walls separated at that distance d, *i.e.*, not allow open space to flow into or out of the system.

For this simple system, one may describe the osmotic pressure by focusing on a single plane in the system and making a few physically motivated arguments. Since osmotic pressure may be readily compared with a more traditional description of pressure in this system, there will always be a positive contribution to pressure due to the particle density at that chosen plane. Recall that osmotic pressure is the *external* pressure needed to oppose the osmotic flow of solvent into the system. Therefore we must also take into account the internal attractive forces between the charged wall and the oppositely charged particles *across* the plane. So regardless of what position z_{plane} between the walls we choose to examine, we would expect the osmotic pressure to take the form

$$P_{\text{osm}} = k_B T \, \rho(z_{\text{plane}}) + \frac{\langle F_{LR} \rangle}{A} \tag{C.1}$$

where $\langle F_{LR} \rangle$ is the average force felt on objects to the right of a dividing plane at z_{plane} due to the objects on the left of the plane and A is the cross-sectional area of that dividing plane in the actual simulation cell.

This simple argument is not sufficient proof of the formula. However this formula has been obtained approximately by imposing the requirement of a hard plane at the center of the simulation cell [36], and much more generally through use of the local pressure tensor and continuity equations [38, 97].

C.1 Contact Theorem

Perhaps the most obvious choice for dividing plane is directly adjacent to one of the confining walls. This plane gives rise to what is commonly called the "contact

theorem,"

$$P_{\text{osm}} = k_B T\, \rho(z_{\text{wall}}) - \frac{2\pi\, q_w^2}{\epsilon}. \tag{C.2}$$

Here, $\rho(z_{\text{wall}})$ is particle density *contacting* a wall, q_w is the charge density on the uniformly charge wall. This equation has been derived by Wennerström *et al.* [108] via a statistical mechanical analysis of the configurational partition function for several geometries of the cell model for polyelectrolytes. Since the position of the hard wall is the lower limit for integration in the z-direction, the "ideal" gas term $k_B T\, \rho(z_{wall})$ is part of the pressure. The wall position is part of a constant associated with the potential energy; therefore, the second term results as well.

Alternatively, the second term may be easily motivated through the idea of the net force between the objects to the left and right of the dividing plane. Since there is only a static uniformly charged wall on one side of the plane, averaging the force is not necessary; the force between the wall on one side of the plane and every other object on the other side of the plane is a constant. Assuming that the dividing plane is immediately next to the left wall, the total force on the left wall may be written as a sum of the force on the left wall due to all $2N$ ions and the force on the left wall due to the right wall. Thus we have

$$\frac{F_{LR}}{A} = \frac{1}{A}\left(F_{\text{Ions-on-LW}} + F_{\text{RW-on-LW}}\right). \tag{C.3}$$

The electric field E_{wall} due to a uniformly charged wall is a constant $2\pi q_w/\epsilon$ pointing out from the wall. Thus, we may expand the force on each ion ion as the charge on that ion multiplied by the field, Ze_0E_{wall}. We do the same for the total force

between walls using the total charge on the other wall within the simulation box, $q_w A$. Therefore,

$$\frac{F_{LR}}{A} = \frac{1}{A}\left(\sum_{i=1}^{2N} Ze_0 \frac{2\pi q_w}{\epsilon} + q_w A \frac{2\pi q_w}{\epsilon}\right). \tag{C.4}$$

The sum above runs over $2N$ particles since we assume that N particles the area A of *one* wall. The summand is a constant, so we simply multiply the summand by the total of $2N$ particles, yielding

$$\frac{F_{LR}}{A} = \frac{2\pi q_w}{\epsilon}\left(\lambda + \frac{2NZe_0}{A}\right). \tag{C.5}$$

Finally, we may use an identity required by neutrality,

$$\frac{NZe_0}{A} = -q_w, \tag{C.6}$$

to simplify the expression for F_{LR} further. Thus, we find

$$\frac{F_{LR}}{A} = \frac{2\pi q_w Ze_0}{\epsilon}\left(q_w - 2q_w\right) = -\frac{2\pi q_w^2}{\epsilon}. \tag{C.7}$$

With the appropriate definition of reduced pressure as discussed in Sect. 3.1, the osmotic pressure at contact may be written very simply as

$$\tilde{P}_{\text{osm}} = \frac{L_w^2 L_G}{k_B T} P_{\text{osm}} = n(\tilde{z}_{wall}) - 1. \tag{C.8}$$

The length L_w is associated with the area of wall required to neutralize a single counterion, and L_G is the distance away from the wall at which a single wall potential is equal to $k_B T$.

As has been noted by several authors, this equation poses numerical difficulties in regions where the pressure crosses over between attractive and repulsive. The contact theorem requires one to take the difference between two nearly equal quantities. Often

this is emphasized as the reason for wanting to determine the osmotic pressure using the midplane as dividing plane [36, 71]. However, as shown later, finding the pressure at the midplane also involves taking the difference of nearly equal quantities. A more careful statement of why the midplane is preferable involves the difficulties in accurately extrapolating the particle density at the wall from a simulation [99]. Since either the contact theorem or the midplane "theorem" involve the difference of similar values, the crucial difference is that the density at midplane may be determined to much greater accuracy than the density at contact even with finite-sized histogram bin widths because the density is so much more slowly-varying at the center of the simulation cell.

C.2 P_{osm} at Midplane With a Hard Wall

Guldbrand *et al.* [36] derive an alternate formula for the pressure based on particle density at the midplane, again by analysis of the configurational integral. In their analysis, the presence of a hard wall at midplane ($z = 0$) is required in order to derive the expression. This wall keeps an exactly neutralizing N counterions in each half of the simulation but allows interactions between particles to penetrate from one side to another. This expresion is

$$P_{\text{osm}} = k_B T \, \rho(z = 0) + \frac{\langle F_{LR} \rangle}{A}, \tag{C.9}$$

where F_{LR} is the average force between walls and particles to the left of the plane and walls and particles to the right. The hard wall is used in both the derivation of the formula and in simulations in that paper and in Moreira and Netz's simulations [36,

71].

Guldbrand *et al.* [36] assert that the presence of the hard wall does not alter the results in the thermodynamic limit. In fact they find a convergence in their results as the lateral dimension of the simulation cell is increased. In addition, Moreira and Netz [71] use this technique for simulations with larger distances between walls where the pressure is numerically small and state they find no difference with values obtained by the contact theorem. We use these latter simulations as benchmarks in Ch. 3.

However in the case of the uniformly-charged-wall and point-counterion system, the polarized states, e.g. $N+1$ ions on the left and $N-1$ ions on the right, could potentially make $\langle F_{LR} \rangle$ more attractive, for then there is a net attractive charge pair to the left and right of the plane. The results in [71] seem to suggest that for larger distances where the particles are already predominantly in two layers, these polarized states do not contribute to the configuration integral significantly. However, at intermediate distances when particles are transitioning from single layer ordering to double layer arrangement, these fluctuations could be significant, and the use of a hard wall completely cuts out those contributions. However, without a hard wall, one should use electrostatice techniques relying on the periodicity of the simulation cell with care, for these would result in a far more macroscopic fluctuation in net charge and overestimate the resulting attraction between sides.

C.3 P_{osm} at Any Plane via the Local Pressure Tensor

A more rigorous way of deriving the general formula can be found via the local pressure tensor $\underline{\underline{P}}(\underline{r})$. Writing $\underline{\underline{P}}$ in index notation as $P_{\alpha\gamma}$, the local pressure tensor may be defined as the infinitesimal force in the α direction across a planar infinitesimal area with its normal in the γ direction [38, 97], in other words,

$$d\underline{F} = d\underline{A} \cdot \underline{\underline{P}} \qquad \text{thus} \qquad dF_\alpha = dA_\gamma \, P_{\alpha\gamma}. \tag{C.10}$$

The local pressure tensor has two contributions, kinetic and potential. The kinetic term may be best understood as the rate of momentum transfer per unit area from one side to the other as a particle traverses the dividing surface dA_γ. The potential contribution may be seen as the forces that cross the dividing surface, a point we will return to.

The kinetic contribution to $P_{\alpha\gamma}$ due to particle i crossing the surface dA_γ is a combination of its momentum in the α direction and the rate at which it crosses the surface in the γ direction so that

$$P^K_{\alpha\gamma}(\underline{r}) = \sum_{i=1}^{N} p_{i\alpha} v_{i\gamma} \delta\left(\underline{r}_i - \underline{r}\right). \tag{C.11}$$

To find the equilibrium $\underline{\underline{P}}(\underline{r})$ one must average over phase space. Assuming equal masses for all particles, this equation can be written as

$$P^K_{\alpha\gamma}(\underline{r}) = \frac{N \int d\underline{r}^N \int d\underline{p}^N \frac{p_{1\alpha} p_{1\gamma}}{m} \delta(\underline{r}_1 - \underline{r}) e^{-\beta U(\underline{r}^N)} e^{-\beta K(\underline{p}^N)}}{\int d\underline{r}^N \int d\underline{p}^N e^{-\beta U(\underline{r}^N)} e^{-\beta K(\underline{p}^N)}}. \tag{C.12}$$

Using appropriate rearrangements and simplifications, such as $\left\langle \underline{p}_i \right\rangle = 0$ and $\langle p^2_{i\alpha}/m \rangle = \frac{1}{\beta}$, this simplifies to

$$P^K_{\alpha\gamma}(\underline{r}) = k_B T \rho(\underline{r}) \delta_{\alpha\gamma} \qquad \text{or} \qquad \underline{\underline{P}}^K(\underline{r}) = k_B T \rho(\underline{r}) \underline{\underline{I}}.f \tag{C.13}$$

The kinetic term has been identified with an ideal gas contribution [100]. The potential term, however, has ambiguity for this very general form of the local pressure tensor; the identification of a force between two distal particles as being "present" at point $\underline{r}$ is ambiguous. The symmetry of this situation instead makes the identification of particle contributions clearer. Before fully addressing this point, some basic results for equilibrated systems in the planar geometry will be described [88, 100].

For a system in equilibrium, mechanical stability implies $\vec{\nabla} \cdot \underline{\underline{P}} = \underline{0}$. Additional requirements are that off-diagonal components of $\underline{\underline{P}}$ are zero and that the two transverse components of the pressure tensor, P_{xx} and P_{yy}, are equal to one another. This all combines to show that $\underline{\underline{P}}$ is a function of z only and furthermore P_{zz} is constant and equal to the external pressure applied to the surfaces.

Given these simplifications, the choice of the "method of planes" (MOP) to explicitly integrate over the x- and y-directions makes sense. Starting from continuity equations, Todd *et al.* [97] derive the following components of the pressure tensor across a macroscopic dividing plane with its normal in the z-direction. There is no constraint on the z-position of this plane, because any choice should yield the same pressure. All information about the transverse terms is lost, but the crucial P_{zz} remains, so that

$$P_{\alpha z}^{U}(z) = \frac{1}{2A} \sum_{i} F_{i\alpha} \operatorname{sgn}(z_i - z), \tag{C.14}$$

$$P_{\alpha z}^{K}(z) = \frac{1}{A} \sum_{i} \frac{p_{i\alpha} p_{iz}}{m} \delta(z_i - z). \tag{C.15}$$

The kinetic term yields the expected ideal gas term $\rho(z) k_B T \, \delta_{\alpha z}$. The potential term is a sum over the net force on each particle i in the α direction, $F_{i\alpha}$, with the sign

changing depending on whether the particle is on the left or the right of the plane. This can easily be shown to be equivalent to $\frac{\langle F_{LR}\rangle}{A}$ when pair interactions are used. Since we know from symmetry that only P_{zz} of all three $P_{\alpha z}$ is nonzero, we now only examine P_{zz},

$$P_{zz}^{U}(z) = \frac{1}{2A}\sum_{i}\sum_{j\neq i}\mathrm{sgn}(z_i - z)F_{z,ij}, \tag{C.16}$$

where $F_{z,ij}$ is the force on particle i due to particle j in the z-direction. This leads to

$$\begin{aligned} P_{zz}^{U}(z) &= \frac{1}{2A}\sum_{i\in R}\sum_{j\neq i}F_{z,ij} - \frac{1}{2A}\sum_{i\in L}\sum_{j\neq i}F_{z,ij} \\ &= \frac{1}{2A}\sum_{i\in R}\sum_{j\in L}F_{z,ij} + \frac{1}{2A}\sum_{i\in R}\sum_{j\in R}^{j\neq i}F_{z,ij} - \frac{1}{2A}\sum_{i\in L}\sum_{j\in R}F_{z,ij} - \frac{1}{2A}\sum_{i\in L}\sum_{j\in L}^{j\neq i}F_{z,ij}. \end{aligned} \tag{C.17}$$

In the second line, the second and fourth terms vanish because the expansion of each summation yields pairs like $F_{z,12} + F_{z,21}$ which cancel identically. On using the symmetry $F_{z,ij} = -F_{z,ji}$, the remaining two sums may be combined to obtain

$$P_{zz}^{U}(z) = \frac{1}{2A}\sum_{i\in R}\sum_{j\in L}F_{z,ij} - \frac{1}{2A}\sum_{i\in L}\sum_{j\in R}F_{z,ij} = \frac{1}{A}\sum_{i\in R}\sum_{j\in L}F_{z,ij}. \tag{C.18}$$

Therefore, the osmotic pressure, which may be identified as the external applied pressure needed to maintain mechanical stability, will be given by

$$P_{\mathrm{osm}} = \rho(z)k_BT + \frac{\langle F_{LR}\rangle}{A} \qquad \text{with} \qquad F_{LR} = \sum_{i\in R}\sum_{j\in L}F_{z,ij}. \tag{C.19}$$

The inclusion of wall-particle and wall-wall interactions in this scheme is relatively simple to accomplish. The walls will not contribute to the kinetic term because they are held immobile. However the walls will be two more objects to include in the sum over forces between the left and right sides. In the paper by Varnik *et al.* [100], only

the wall-ion forces are included in this sum, perhaps because this wall-wall force is negligible in a Lennard-Jones system, however the wall-wall force contribution should certainly be included in this Coulombic system [100].

As opposed to using continuity equations, Heinz *et al.* [38] have also derived this MOP from the local pressure tensor by understanding it as extending the dividing plane with a normal in the z-direction such that it occupies the entire simulation cell area in the x- and y-directions [38].

C.3.1 Summary

Via the method of planes, a very general equilibrium expression for osmotic pressure at any chosen dividing plane ($z = z_p$) becomes

$$P_{\text{osm}} = \rho(z_p)\, k_B T + \frac{1}{A} \left\langle \sum_{z_i > z_p} \sum_{z_j < z_p} F_{z,ij} \right\rangle . \tag{C.20}$$

In the reduced units of Ch. 3, this equation is

$$\tilde{P}_{\text{osm}} = n(z_p) + \frac{2\pi\xi}{\tilde{A}} \left\langle \sum_{\tilde{z}_i > \tilde{z}_p} \sum_{\tilde{z}_j < \tilde{z}_p} \tilde{F}_{\tilde{z},ij} \right\rangle , \tag{C.21}$$

where ξ is the coupling strength of the system as defined in Sect. 3.1, and a tilde indicates division of lengths by L_G and division of energies by $k_B T$.

C.4 Method of Planes for the Two Wall System

We must take careful account of the fact that the two walls should be regarded as "particles" in the summation above. By explicitly separating contributions due to

ions and due to walls, we may write

$$\tilde{P}_{\text{osm}} = n(z_p) + \frac{2\pi\xi}{\tilde{A}} \left(F_{\text{LI-on-RW}} + F_{\text{RI-on-LW}} + F_{\text{LW-on-RW}} + \sum_{i\in L} \sum_{j\in R} \tilde{f}^z(r_{ij}) \right). \quad \text{(C.22)}$$

The abbreviation LI indicates ions with $z < z_p$ and RI represents ions with $z > z_p$. Similarly, LW and RW indicate the left wall and the right wall, respectively. The terms $F_{\text{LI-on-RW}} + F_{\text{RI-on-LW}} + F_{\text{LW-on-RW}}$ add up to -1 for similar reasons as for our determination of the contact theorem at the beginning of this appendix. The final term in the first line is essentially $F_{\text{LI-on-RI}}$ expanded in terms of forces between individual ions. The summand $\tilde{f}^{(z)}(r_{ij})$ is equivalent to $\tilde{F}_{z,ij}$, but we now have used the fact that these pair interactions are spherically symmetric.

Following the LMF approach, we split each $\tilde{f}^{(z)}(r_{ij})$ into short-ranged and long-ranged contributions – $\tilde{f}_0^{(z)}(r_{ij})$ and $\tilde{f}_0^{(z)}(r_{ij})$ – as

$$\tilde{P}_{\text{osm}} = n(z_p) - 1 + \frac{2\pi\xi}{\tilde{A}} \left\langle \sum_{i\in L} \sum_{j\in R} \tilde{f}_0^{(z)}(r_{ij}) \right\rangle + \frac{2\pi\xi}{\tilde{A}} \left\langle \sum_{i\in L} \sum_{j\in R} \tilde{f}_1^{(z)}(r_{ij}) \right\rangle. \quad \text{(C.23)}$$

We may explicitly calculate the average of $\tilde{f}_0^{(z)}$ during the simulations, but $\tilde{f}_1^{(z)}$ is long-ranged. For us to exactly calculate that contribution we would require a lattice sum. However, as explained in Sect. 3.4.5, we may quite reasonably approximate this as

$$\left\langle \sum_{i\in L} \sum_{j\in R} \tilde{f}_1^{(z)}(r_{ij}) \right\rangle \simeq \left\langle \sum_{j\in R} \int_0^{z_p} dz' n(z') \operatorname{erf}\left(\frac{z_j - z'}{\sigma} \right) \right\rangle. \quad \text{(C.24)}$$

The midplane theorem employed involves choosing $z_p = d/2$. Furthermore, with the LMF electrostatic approach, we are equipped to handle polarized states with $N+1$ ions on the left and $N-1$ ions on the right without violating macroscopic neutrality because such instantaneous polarization does not propagate out to infinity.

Appendix D

Molecular Moment Conditions and Energy Corrections

In this appendix, we derive the small k-expansion of bulk pair correlation functions for site-site molecular models, as originally done by Chandler [10]. This expansion is the molecular analog of the standard Stillinger-Lovett moment conditions [94], and we will use it to correct the thermodynamics of bulk water simulated using the strong coupling approximation (SCA).

In Sect. 5.3.4, we study the thermodynamics of bulk SPC/E water simulated with SCA by using only the Gaussian-smoothed truncation of $1/r$,

$$v_0(r) = \frac{\operatorname{erfc}(r/\sigma)}{r}. \tag{D.1}$$

As with thermodynamic perturbation theory, we expect that the total nergy of the system will be composed of two contributions,

$$U_{\text{tot}} = U_0 + U_1, \tag{D.2}$$

where the Gaussian-truncated (GT) water will yield U_0 and the neglected interactions due to

$$v_1(r) = \frac{\operatorname{erf}(r/\sigma)}{r} \tag{D.3}$$

are contained in U_1.

In general, the total energy of bulk water in simulation may be written as

$$\frac{U_{tot}}{N} = \frac{U_{LJ}}{N} + \frac{\rho_B}{2} q^2 \int \frac{1}{r} \left\{ g_{\text{OO}}(r) + g_{\text{HH}}(r) - 2 g_{\text{OH}}(r) \right\} d\mathbf{r} \tag{D.4}$$

where $q \equiv |q_{\mathrm{O}}|$. When we simulate truncated water, we obtain both U_{LJ} and the electrostatic energy due to $v_0(r)$ exactly; we identify that sum as U_0. As is evident from the data presented in Sect. 5.3.4, the remaining U_1 is an important contribution to the total energy.

Thus we need to find the neglected U_1 which we cannot calculate during the simulation:

$$\frac{U_1}{N} = \frac{\rho_B}{2} q^2 \int v_1(r) \left[g_{\mathrm{OO}}(r) + g_{\mathrm{HH}}(r) - 2 g_{\mathrm{OH}}(r) \right] d\mathbf{r} = \frac{\rho_B}{2} q^2 \int v_1(r) h_{\mathrm{tot}}(r) d\mathbf{r}. \quad \text{(D.5)}$$

One might consider using the simulation-calculated g in the equation above to obtain U_1; however this would be a poor approximation. Instead, we follow a path very similar to that used for the strongly-coupled ionic solution, relying on the first and second moments of the molecular solution in k-space [14, 22]. The Fourier transform of $v_1(r)$ is

$$\hat{v}_1(k) = \frac{4\pi \exp\left(-k^2\sigma^2/4\right)}{k^2}. \quad \text{(D.6)}$$

Therefore, by Parseval's theorem, the energy correction in Fourier space is

$$\frac{U_1}{N} = \frac{\rho_B}{2} q^2 \frac{1}{(2\pi)^3} \int \frac{4\pi}{k^2} \exp\left(-k^2\sigma^2/4\right) \hat{h}_{\mathrm{tot}}(k) d\mathbf{k}. \quad \text{(D.7)}$$

The bulk of this appendix is devoted to determining an accurate small-k expansion for $\hat{h}_{\mathrm{tot}}(k)$, in the vein of those derived by Stillinger and Lovett [94] for ionic solutions. Only a small-k expansion is required because the exponential in the integral above is only non-zero for small-k values.

D.1 Exact Moment Conditions

Both Høye and Stell [40] and Chandler [10] derived an equation for the dielectric constant in terms of the site-site correlation functions. In reviewing various molecular results, Hansen and McDonald [37] refer to Martin [68] in stating that such equations may be derived based on sum rules. However, a point that may not be fully appreciated in the context of *molecular* fluids is that these sum rules may quite easily be used to approximate the correction U_1 discussed above.

We proceed by essentially following steps in [10] with slight alterations since there appears to be differences in the definition of $\chi_{\alpha M \gamma M'}$ between Chandler [10] and Hansen and McDonald [37]. In essence, these moment conditions are not new results. However, since we will be using the formula for numerical applications in Sect. 5.3, stepping through the derivation allows us to fully understand the formula and to take care with units.

Given a test charge Q immersed in a dielectric fluid, we expect that for large r

$$\lim_{r\to\infty} V(\mathbf{r}) \cdot r = \frac{Q}{\epsilon}, \tag{D.8}$$

and alternately in k-space,

$$\lim_{k\to 0} \hat{V}(\mathbf{k}) \cdot k^2 = \frac{4\pi Q}{\epsilon}. \tag{D.9}$$

If, instead, we look at the microscopic response of the site-site molecular fluid, we expect

$$V_{micro}(\mathbf{r}) = \frac{Q}{r} + \langle V_{pol}(\mathbf{r}) \rangle_Q \,, \tag{D.10}$$

which in k-space is

$$\hat{V}_{micro}(\mathbf{k}) = \frac{4\pi Q}{k^2} + \sum_{M,\alpha} z_{\alpha M} \hat{\rho}_{\alpha M|Q}(\mathbf{k}) \frac{4\pi}{k^2}. \tag{D.11}$$

The final term is basically a statement of Poisson's equation for the charge density profile of the molecular sites given that a charge Q is fixed at the origin.

Taking Q to be small, we appeal to linear response in order to calculate the charge density response of the molecular sites. By definition, we have

$$\frac{\delta \hat{\rho}_{\alpha M}(\mathbf{k})}{\delta \hat{\psi}_{\gamma M'}(\mathbf{k})} = \chi_{\alpha M \gamma M'}(\mathbf{k}), \tag{D.12}$$

where $\hat{\psi}_{\gamma M'}$ is a weak external potential energy field that couples to the density of site $\gamma M'$ [37, p. 64]. For a charge Q at the origin, this energy would be $4\pi Q z_{\gamma M'}/k^2$. Therefore, to linear order,

$$\begin{aligned} \hat{\rho}_{\alpha M|Q}(\mathbf{k}) &= \hat{\rho}_{\alpha M|0}(\mathbf{k}) + \sum_{\gamma M'} \chi_{\alpha M \gamma M'}(\mathbf{k}) \frac{4\pi Q z_{\gamma M'}}{k^2} \\ &= (2\pi)^3 \cdot \rho_M \cdot \delta(\mathbf{k}) + \sum_{\gamma M'} \chi_{\alpha M \gamma M'}(\mathbf{k}) \frac{4\pi Q z_{\gamma M'}}{k^2}. \end{aligned} \tag{D.13}$$

Applying this statement to the equation for $\hat{V}_{micro}(\mathbf{k})$ and appealing to net intramolecular neutrality, we find

$$\begin{aligned} \hat{V}_{micro}(\mathbf{k}) &= \frac{4\pi Q}{k^2} + (2\pi)^3 \frac{4\pi}{k^2} \sum_{M,\alpha} z_{\alpha M} \cdot \rho_M \cdot \delta(\mathbf{k}) + \frac{4\pi}{k^2} \sum_{\alpha M} \sum_{\gamma M'} \frac{4\pi Q}{k^2} z_{\alpha M} \cdot z_{\gamma M'} \cdot \chi_{\alpha M \gamma M'}(\mathbf{k}) \\ &= \frac{4\pi Q}{k^2} \left\{ 1 + \frac{4\pi}{k^2} \sum_{\alpha M} \sum_{\gamma M'} z_{\alpha M} \cdot z_{\gamma M'} \cdot \chi_{\alpha M \gamma M'}(\mathbf{k}) \right\}. \end{aligned} \tag{D.14}$$

Matching this linear response formula with the macroscopic expectation, we have

$$\frac{1}{\epsilon} = 1 + \frac{4\pi}{k^2} \sum_{\alpha M} \sum_{\gamma M'} z_{\alpha M} \cdot z_{\gamma M'} \cdot \chi_{\alpha M \gamma M'}(\mathbf{k}) \tag{D.15}$$

For a typical conducting fluid with $\epsilon \to \infty$, this would lead immediately to

$$1 = \lim_{k\to 0} \left\{ \frac{4\pi\beta e_0^2}{k^2} \rho\, S_{ZZ}(k) \right\} \tag{D.16}$$

where ρ is the total number density of all particles. This means that up to second order in k, we have

$$S_{ZZ}(k) = 0 + \frac{k_B T}{4\pi\rho e_0^2} k^2, \tag{D.17}$$

the typical zeroth and second moment conditions for ionic fluids [37].

However, for molecular fluids we must be more careful. The response functions $\chi_{\alpha M \gamma M'}$ depend on both intramolecular and intermolecular behavior. First, we restate the equation we will build from:

$$\left(\frac{1}{\epsilon} - 1\right) = \lim_{k\to 0} \left\{ \frac{4\pi}{k^2} \sum_{\alpha M} \sum_{\gamma M'} z_{\alpha M} \cdot z_{\gamma M'} \cdot \chi_{\alpha M \gamma M'}(\mathbf{k}) \right\}.$$

As Chandler [10] noted, from the compressibility theorem, we know that

$$\lim_{k\to 0} \hat{\chi}_{\alpha M \gamma M'}(k) = -\frac{\partial \rho_{M'}}{\partial \mu_M} = \hat{\chi}^{(0)}_{M\,M'}, \tag{D.18}$$

where μ_M indicates the chemical potential of molecule M, and the dependence on site identity is lost. Expanding $\hat{\chi}_{\alpha M \gamma M'}$ up to second order in k as

$$\hat{\chi}_{\alpha M \gamma M'}(k) = \hat{\chi}^{(0)}_{M\,M'} + k^2 \hat{\chi}^{(2)}_{\alpha M \gamma M'} + O(k^4) \tag{D.19}$$

leads to

$$\left(\frac{1}{\epsilon} - 1\right) = \frac{4\pi}{k^2} \sum_{M} \sum_{M'} \left(\sum_{\alpha} z_{\alpha M} \right) \left(\sum_{\gamma} z_{\gamma M} \right) \hat{\chi}^{(0)}_{M\,M'} + 4\pi \sum_{\alpha M} \sum_{\gamma M'} z_{\alpha M} z_{\gamma M'} \hat{\chi}^{(2)}_{\alpha M \gamma M'}. \tag{D.20}$$

The first term vanishes owing to the neutrality of each molecule; thus we know exactly

$$\left(\frac{1}{\epsilon} - 1\right) = 4\pi \sum_{\alpha M} \sum_{\gamma M'} z_{\alpha M} z_{\gamma M'} \hat{\chi}^{(2)}_{\alpha M \gamma M'}. \tag{D.21}$$

We may also write $\hat{\chi}_{\alpha M\gamma M'}(\mathbf{k})$ in terms of intramolecular and intermolecular distribution functions as

$$\hat{\chi}_{\alpha M\gamma M'}(\mathbf{k}) = -\beta\rho_M\delta_{MM'}\hat{\omega}_{\alpha\gamma M}(\mathbf{k}) - \beta\rho_M\rho_{M'}\hat{h}_{\alpha M\gamma M'}(\mathbf{k}), \tag{D.22}$$

where we define the intramolecular correlation function as

$$\hat{\omega}_{\alpha\gamma M}(\mathbf{k}) = \delta_{\alpha\gamma} + \hat{\varrho}_{\alpha|\gamma}(\mathbf{k}), \tag{D.23}$$

with $\varrho_{\alpha|\gamma}(\mathbf{r})$ again representing the conditional intramolecular density of site α being at $\mathbf{r}$ given that site γ is at the origin. Before proceeding, note the similarity to the response function for a simple mixture:

$$\hat{\chi}_{\alpha\gamma}(\mathbf{k}) = -\beta\rho_\alpha\delta_{\alpha\gamma} - \beta\rho_\alpha\rho_\gamma\hat{h}_{\alpha\gamma}(\mathbf{k}). \tag{D.24}$$

The sole differences lie in the self term requiring a Kronecker delta for both the site and the molecule and in a requisite contribution from intramolecular correlations.

Using the alternate definition of $\hat{\chi}$ in terms of $\hat{\omega}$ and $\hat{h}$, we may expand those definitions in terms of k alternatively. The k^0 term of $\hat{\omega}_{\alpha\gamma M}$ is

$$\hat{\omega}^{(0)}_{\alpha\gamma M} = \delta_{\alpha\gamma} + \int \varrho_{\alpha|\gamma}(\mathbf{r})d\mathbf{r} = \delta_{\alpha\gamma} + (1 - \delta_{\alpha\gamma}) = 1. \tag{D.25}$$

Therefore the charge-weighted sum of the k^0 terms due to $\hat{\omega}_{\alpha\gamma M}$ for a given molecule M is exactly zero due to the neutrality of the molecule:

$$\sum_{\alpha,\gamma} z_{\alpha M} z_{\gamma M}\hat{\omega}^{(0)}_{\alpha\gamma M} = \sum_{\alpha} z_{\alpha M}\left(\sum_{\gamma} z_{\gamma M}\right) = 0. \tag{D.26}$$

The charge weighted sum of all k^2 terms due to $\hat{\omega}_{\alpha\gamma M}$ for a given molecule M may be found to be

$$\sum_{\alpha,\gamma} z_{\alpha M} z_{\gamma M}\hat{\omega}^{(2)}_{\alpha\gamma M} = -\frac{1}{6}\int \sum_{\alpha,\gamma} z_{\alpha M} z_{\gamma M}\varrho_{\alpha\gamma}(\mathbf{r})r^2 d\mathbf{r} = \frac{\mu_M^2}{3} + \frac{\alpha_M}{\beta}, \tag{D.27}$$

where μ_M now refers to the permanent dipole moment of the molecule in the fluid and α_M is the polarizability of the molecule.

Thus, to second order in k, we may write

$$\sum_M \sum_{\alpha,\gamma} z_{\alpha M} z_{\gamma M} \hat{\omega}_{\alpha\gamma M} \simeq k^2 \sum_M \left(\frac{\mu_M^2}{3} + \frac{\alpha_M}{\beta} \right). \tag{D.28}$$

Now, for the intermolecular correlations, we expand

$$\hat{h}_{\alpha M \gamma M'}(k) = \hat{h}^{(0)}_{MM'} + k^2 \hat{h}^{(2)}_{\alpha M \gamma M'}, \tag{D.29}$$

where $k = 0$ behavior is independent of sites again by the compressibility theorem. Therefore, just as before, summing over all molecules and sites will lead to the k^0 term being zero due to molecular neutrality.

$$\sum_{\alpha M} \sum_{\gamma M'} z_{\alpha M} z_{\gamma M'} \hat{h}_{\alpha M \gamma M'}(k) = 0 + k^2 \sum_{\alpha M} \sum_{\gamma M'} z_{\alpha M} z_{\gamma M'} \hat{h}^{(2)}_{\alpha M \gamma M'}, \tag{D.30}$$

Arguments have been made for why we should expect the second term in the expansion to exist [10]; the easiest argument is that for the dielectric constant to exist, this term must exist. More detailed arguments involve diagrammatic expansions. Given the expansion of $\hat{h}$ to second order in k, we may exactly write

$$\left(\frac{1}{\epsilon} - 1 \right) = -\frac{4\pi\beta}{k^2} \left(k^2 \sum_M \rho_M \left(\frac{\mu_M^2}{3} + \frac{\alpha_M}{\beta} \right) + k^2 \sum_{\alpha M} \sum_{\gamma M'} z_{\alpha M} z_{\gamma M'} \rho_M \rho_{M'} \hat{h}^{(2)}_{\alpha M \gamma M'} \right). \tag{D.31}$$

D.2 Specialization to SPC/E Water

While the previous formula may seem complicated, we can use it to exactly express the small k behavior of $h_{\mathrm{OO}} + h_{\mathrm{HH}} - 2h_{\mathrm{OH}}$. We begin by simplifying all the sums

as appropriate for a single component molecular fluid of density ρ_B and permanent dipole μ without any polarizability α.

$$\frac{\epsilon - 1}{\epsilon} = 4\pi\beta \left(\rho_B \frac{\mu^2}{3} + \rho_B^2 \sum_\alpha \sum_\gamma z_\alpha z_\gamma \hat{h}^{(2)}_{\alpha\gamma} \right) \tag{D.32}$$

Now, carrying out the summations over α and γ, recalling that in the notation of [10] each individual atom is given its own index, [1] we find that

$$\sum_\alpha \sum_\gamma z_\alpha z_\gamma \hat{h}^{(2)}_{\alpha\gamma} = q^2 \left(\hat{h}^{(2)}_{\mathrm{OO}} + \hat{h}^{(2)}_{\mathrm{HH}} - 2\hat{h}^{(2)}_{\mathrm{OH}} \right) = q^2 \hat{h}^{(2)}_{tot}. \tag{D.33}$$

By using this result in the previous equation, we find the exact expression

$$q^2 \hat{h}^{(2)}_{tot} = \frac{k_B T}{4\pi\rho_B^2} \frac{\epsilon - 1}{\epsilon} - \frac{\mu^2}{3\rho_B}. \tag{D.34}$$

Thus at small k, we may approximate $\hat{h}_{tot}$ as

$$q^2 \hat{h}_{tot} \simeq 0 + k^2 \left(\frac{k_B T}{4\pi\rho_B^2} \frac{\epsilon - 1}{\epsilon} - \frac{\mu^2}{3\rho_B} \right). \tag{D.35}$$

D.3 Units

Care must be exercised in numerically applying this formula due to units. The process above used CGS units.

We have

$$k_B T = 4.141 \times 10^{-14}\,\mathrm{erg} \tag{D.36}$$

$$\mu = 0.8476\, e_0\, l_{\mathrm{OH}} \cos\left(\frac{\theta_{\mathrm{HOH}}}{2} \right) = 2.35 \times 10^{-18}\,\mathrm{esu \cdot cm} \tag{D.37}$$

$$\rho_B = 3.335 \times 10^{22} \mathrm{cm}^{-3}. \tag{D.38}$$

[1] In order for this to be correct, the partition function must include corresponding symmetry numbers as mentioned in Appendix A.

Therefore, we may write

$$\frac{k_B T}{4\pi\rho_B^2} = 2.963 \times 10^{-60}\,\mathrm{erg}\cdot\mathrm{cm}^6 \tag{D.39}$$

$$\frac{\mu_B^2}{3\rho_B} = 5.520 \times 10^{-59}\,\mathrm{esu}^2\cdot\mathrm{cm}^5 = 5.520 \times 10^{-59}\,\mathrm{erg}\cdot\mathrm{cm}^6. \tag{D.40}$$

Based off of these values, we find that $q^2\hat{h}_{tot}^{(2)} < 0$ regardless of the ϵ chosen.

An upper bound on $q^2\hat{h}_{tot}$ is found by assigning $\epsilon \to \infty$,

$$q^2\hat{h}_{tot} \leq -\left(5.224 \times 10^{-59}\,\frac{\mathrm{g}\cdot\mathrm{cm}^8}{\mathrm{s}^2}\right)k^2. \tag{D.41}$$

Since the dielectric constant of water is rather large, this upper bound is actually rather tight, within the approximation of a second order expansion in k-space.

Finally, we convert the constant into units of kJ·Å^6/mol in order to simplify our calculations in the text,

$$\begin{aligned}
&5.224 \times 10^{-59}\,\frac{\mathrm{g}\cdot\mathrm{cm}^8}{\mathrm{s}^2}\cdot\left(\frac{1\,\mathrm{kg}}{1000\,\mathrm{g}}\right)\cdot\left(\frac{1\,\mathrm{m}}{100\,\mathrm{cm}}\right)^2 \\
&\quad = 5.224 \times 10^{-66}\left(\frac{1\,\mathrm{J}}{1\,\mathrm{kg}\cdot\mathrm{m}^2/\mathrm{s}^2}\right)\cdot\left(\frac{1\,\mathrm{kJ}}{1000\,\mathrm{J}}\right) \\
&\quad = 5.224 \times 10^{-69}\,\mathrm{kJ}\cdot\mathrm{cm}^6\cdot\left(\frac{6.022\times10^{23}}{1\,\mathrm{mol}}\right)\cdot\left(\frac{10^8\,\text{Å}}{1\,\mathrm{cm}}\right)^6 \\
&\quad = 3.145 \times 10^3\,\frac{\mathrm{kJ}\cdot\text{Å}^6}{\mathrm{mol}}.
\end{aligned} \tag{D.42}$$

D.4 Energy Correction Formula

As stated at the beginning, we may write the energy correction as

$$\frac{U_1}{N} = \frac{\rho_B}{2}q^2\frac{1}{(2\pi)^3}\int\frac{4\pi}{k^2}\exp\left(-k^2\sigma^2/4\right)\hat{h}_{tot}(k)d\mathbf{k}. \tag{D.43}$$

Using our expansion for $\hat{h}_{tot}(k)$ at small k, we have

$$\frac{U_1}{N} \simeq \frac{\rho_B}{2}q^2\hat{h}_{tot}^{(2)}\frac{1}{(2\pi)^3}\int 4\pi\exp\left(-k^2\sigma^2/4\right)d\mathbf{k} \leq 0. \tag{D.44}$$

This integral is exactly solvable and thus we have an analytical approximation for U_1:

$$\frac{U_1}{N} \simeq q^2 \hat{h}_{tot}^{(2)} \frac{4\pi\rho_B}{16\pi^3} \frac{8}{\sigma^3} \pi^{3/2} = q^2 \hat{h}_{tot}^{(2)} \rho_B \frac{2}{\sqrt{\pi}} \frac{1}{\sigma^3}. \tag{D.45}$$

Appendix E

Stable k-space Solution of the LMF Equation

This appendix is based on a technique originally proposed by a former Weeks group member Kirill Katsov and explained in [13] and [14]. The originial scheme has modified to a form more easily transformed to r-space by Weeks [103]. We first explain why the LMF solution would not be stable in k-space. Then the techniques for addressing this problem are discussed.

As discussed in Sect. 4.1, we may write the LMF equation for the rescaled electrostatic potential (not potential energy) as

$$\mathcal{V}_{R1}(\mathbf{r}) = \frac{1}{\epsilon}\int d\mathbf{r}'\rho^q_{\mathrm{R,tot}}(\mathbf{r}';[\phi_R])v_1(|\mathbf{r}-\mathbf{r}'|), \tag{E.1}$$

where $v_1(r) \equiv \mathrm{erf}(r/\sigma)/r$. The charge density in the integral includes both the mobile and stationary charge densities since this is an equation for the slowly-varying part, $\mathcal{V}_{R1}$. The short-ranged contributions of the stationary contributions will be represented separately by $\mathcal{V}_0$.

In k-space, where $\hat{f}(\mathbf{k})$ indicates the Fourier transform of $f(\mathbf{r})$ and our convention is to have $1/(2\pi)^3$ in the k-space to r-space transform, we may write the LMF equation as

$$\hat{\mathcal{V}}_{R1}(\mathbf{k}) = \frac{1}{\epsilon}\hat{\rho}^q_{\mathrm{R,tot}}(\mathbf{k})\exp\left(-\frac{k^2\sigma^2}{4}\right)\frac{4\pi}{k^2} \tag{E.2}$$

For bulk fluid the underlying difficulty of this equation is that when we have the

correct $\mathcal{V}_R$ we expect

$$\hat{\rho}^q_{\mathrm{R,tot}}(k) \simeq 0 + \alpha k^2 + \mathcal{O}(k^4). \tag{E.3}$$

However, unless we have the correct ϕ_R, we instead may find

$$\hat{\rho}^q_{\mathrm{R,tot}}(k) \simeq C + \alpha k^2 + \mathcal{O}(k^4). \tag{E.4}$$

A non-zero C causes iteration of the LMF equation in k-space to diverge. Even if one tries to integrate in r-space this long-ranged difficulty will likely show up.

The technique used in [14] is to exactly rewrite the LMF equation in two ways and then take a linear combination of the two:

$$k^2\hat{\mathcal{V}}_{R1}(\mathbf{k}) = \frac{1}{\epsilon}\hat{\rho}^q_{\mathrm{R,tot}}(\mathbf{k}) \exp\left(-\frac{k^2\sigma^2}{4}\right) 4\pi, \tag{E.5}$$

$$\kappa^2\hat{\mathcal{V}}_{R1}(\mathbf{k}) = \kappa^2\hat{\mathcal{V}}_{R1}(\mathbf{k}). \tag{E.6}$$

Summing these two exact forms, we obtain

$$\hat{\mathcal{V}}_{R1}(\mathbf{k}) = \frac{1}{\epsilon}\hat{\rho}^q_{\mathrm{R,tot}}(\mathbf{k}) \exp\left(-\frac{k^2\sigma^2}{4}\right) \frac{4\pi}{k^2+\kappa^2} + \frac{\kappa^2}{k^2+\kappa^2}\hat{\mathcal{V}}_{R1}(\mathbf{k}). \tag{E.7}$$

Now with a simple (and exact rewriting) this looks like a linear combination of two solutions (with some k-space dependence):

$$\hat{\mathcal{V}}_{R1}(\mathbf{k}) = \frac{k^2}{k^2+\kappa^2}\frac{1}{\epsilon}\hat{\rho}^q_{\mathrm{R,tot}}(\mathbf{k}) \exp\left(-\frac{k^2\sigma^2}{4}\right) \frac{4\pi}{k^2} + \frac{\kappa^2}{k^2+\kappa^2}\hat{\mathcal{V}}_{R1}(\mathbf{k}). \tag{E.8}$$

However, the underlying "trick" is more evident in the writing of the first term given in Eq. (E.7). Even if the k^0 term in Eq. (E.4) in non-zero, this term will no longer diverge. Neither will the second term. Furthermore, self-consistent iteration will drive the k^0 term of $\hat{\rho}^q$ to zero since that is the only way to attain self-consistency. This may be seen for the bulk by expressing both $\hat{\rho}^q_{\mathrm{R,tot}}$ and $\hat{\mathcal{V}}_{R1}(\mathbf{k})$ as even series in k.

In the iteration for the MPB solution, Chen *et al.* [14] found that a choice of κ close to the Debye length led to a stable solution.

The newer observation by Weeks [103] is that any $f(k)$ with a small k-expansion

$$f(k) \simeq k^2 + O(k^4) \tag{E.9}$$

will work as well as $k^2/(k^2+\kappa^2)$. Thus we may generally write

$$\hat{\mathcal{V}}_{R1}(\mathbf{k}) = f(k) \cdot \frac{1}{\epsilon}\hat{\rho}^q_{\mathrm{R,tot}}(\mathbf{k}) \exp\left(-\frac{k^2\sigma^2}{4}\right)\frac{4\pi}{k^2} + [1-f(k)]\cdot\hat{\mathcal{V}}_{R1}(\mathbf{k}). \tag{E.10}$$

Further, if we use

$$f(k) = 1 - e^{-\frac{k^2 l^2}{4}}, \tag{E.11}$$

then these equations are easily integrable.

Thus we obtain

$$\hat{\mathcal{V}}_{R1}(\mathbf{k}) = \cdot\frac{1}{\epsilon}\hat{\rho}^q_{\mathrm{R,tot}}(\mathbf{k}) \exp\left(-\frac{k^2\sigma^2}{4}\right)\left[1-\exp\left(-\frac{k^2 l^2}{4}\right)\right]\frac{4\pi}{k^2} + \hat{\mathcal{V}}_{R1}(\mathbf{k})\exp\left(-\frac{k^2 l^2}{4}\right). \tag{E.12}$$

Converting to real space yields

$$\begin{aligned}\mathcal{V}_{R1}(\mathbf{r}) = \frac{1}{\epsilon}\int d\mathbf{r}'\rho^q_{\mathrm{R,tot}}(\mathbf{r}')\left\{\frac{\mathrm{erf}\left(\frac{|\mathbf{r}-\mathbf{r}'|}{\sigma}\right)}{|\mathbf{r}-\mathbf{r}'|} - \frac{\mathrm{erf}\left(\frac{|\mathbf{r}-\mathbf{r}'|}{\sqrt{\sigma^2+l^2}}\right)}{|\mathbf{r}-\mathbf{r}'|}\right\} \\ + \frac{1}{l^3\pi^{3/2}}\int d\mathbf{r}'\mathcal{V}_{R1}(\mathbf{r}')\exp\left(-\frac{|\mathbf{r}-\mathbf{r}'|^2}{l^2}\right).\end{aligned} \tag{E.13}$$

One may alternately obtain

$$\begin{aligned}\mathcal{V}_{R1}(\mathbf{r}) = \frac{1}{\epsilon}\int d\mathbf{r}'\rho^q_{\mathrm{R,tot}}(\mathbf{r}')\left(\frac{\mathrm{erfc}\left(\frac{|\mathbf{r}-\mathbf{r}'|}{\sqrt{\sigma^2+l^2}}\right)}{|\mathbf{r}-\mathbf{r}'|} - \frac{\mathrm{erfc}\left(\frac{|\mathbf{r}-\mathbf{r}'|}{\sigma}\right)}{|\mathbf{r}-\mathbf{r}'|}\right) \\ + \frac{1}{l^3\pi^{3/2}}\int d\mathbf{r}'\mathcal{V}_{R1}(\mathbf{r}')\exp\left(-\frac{|\mathbf{r}-\mathbf{r}'|^2}{l^2}\right),\end{aligned} \tag{E.14}$$

emphasizing the short-ranged nature of the difference.

Either of these equations may now be converted to use the smoothed Green's functions derived in Appendix B for either a slab geometry or spherical symmetry. In simulations, the r-space version of this k-space iteration scheme is useful for making initial guesses at structure, as in Sect. 6.5.

Appendix F

One-Dimensional LMF Equation for LJ Fluid Between Walls

In Ch. 7, we apply LMF theory to the Lennard-Jones (LJ) attractions between water molecules confined between hydrophobic walls. Just as done for charge interactions in Sect. B.1, we may simplify the LMF equation to an integral over one dimension. In this appendix, we document this transformation.

We specify our functional forms as

$$u_{\mathrm{LJ}}(r) = 4\varepsilon_{\mathrm{LJ}}\left[\left(\frac{\sigma_{\mathrm{LJ}}}{r}\right)^{12} - \left(\frac{\sigma_{\mathrm{LJ}}}{r}\right)^{6}\right] \tag{F.1}$$

$$u_0(r) = u_{\mathrm{WCA}}(r) = \begin{cases} u_{\mathrm{LJ}}(r) + \varepsilon_{\mathrm{LJ}} & \text{if } r \le r_0, \\ 0 & \text{if } r > r_0, \end{cases} \tag{F.2}$$

$$u_1(r) = u_{\mathrm{attr}}(r) = \begin{cases} -\varepsilon_{\mathrm{LJ}} & \text{if } r \le r_0, \\ u_{\mathrm{LJ}}(r) & \text{if } r > r_0, \end{cases} \tag{F.3}$$

where r_0 is the position of the minimum in $u_{\mathrm{LJ}}(r)$, $2^{1/6}\sigma_{\mathrm{LJ}}$.

Starting from the full three-dimensional LMF equation for the Lennard-Jones contribution, namely,

$$\phi_R^{\mathrm{LJ}}(\mathbf{r}) = \int d\mathbf{r}'\rho_R(\mathbf{r}')u_1(|\mathbf{r}-\mathbf{r}'|) + C, \tag{F.4}$$

we may assume that $\mathbf{r} = (x, y, z) = (0, 0, z)$, define $s' = \sqrt{x'^2 + y'^2}$, and recall that

both ρ_R as well as ϕ_R are functions of only z. Then we may write

$$\phi_R^{\mathrm{LJ}}(z) = \int_{-\infty}^{\infty} dz' \int_0^{2\pi} d\theta \int_0^{\infty} s'\, ds'\, \rho_R(z') u_1\left(\sqrt{s'^2 + (z-z')^2}\right) + C, \tag{F.5}$$

where for this appendix we assume that $\phi^{\mathrm{LJ}}(z) = 0$.

We then define $\zeta = z' - z$ and substitute in this definition along with $d\zeta = dz'$ and $z' = z + \zeta$,

$$\phi_R^{\mathrm{LJ}}(z) = 2\pi \int_{-\infty}^{\infty} d\zeta \int_0^{\infty} s'\, ds'\, \rho_R(z+\zeta) u_1\left(\sqrt{s'^2 + \zeta^2}\right) + C. \tag{F.6}$$

The definition of $u_1(\sqrt{s'^2+\zeta^2})$ depends on whether its argument is less than or greater than r_0, and we will obtain terms from the integration for each case.

For all s and ζ such that $\sqrt{s'^2+\zeta^2} \le r_0$, we have

$$u_1(r) = -\varepsilon_{\mathrm{LJ}}, \qquad \zeta \in [-r_0, r_0], \qquad \text{and} \qquad s'^2 \le r_0^2 - \zeta^2. \tag{F.7}$$

Thus $\forall (s', \zeta) : \sqrt{s'^2+\zeta^2} \le r_0$,

$$\phi_R^{\mathrm{LJ}}(z) = -2\pi\varepsilon_{\mathrm{LJ}} \int_{-r_0}^{r_0} d\zeta \int_0^{\sqrt{r_0^2-\zeta^2}} \rho_R(z+\zeta) s' ds' \tag{F.8}$$

$$= -\pi\epsilon_{lj} \int_{-r_0}^{r_0} d\zeta\, \rho_R(z+\zeta) \left[r_0^2 - \zeta^2\right] \tag{F.9}$$

$$\phi_R^{\mathrm{LJ}}(z) = -\pi\varepsilon_{\mathrm{LJ}} \int_0^{r_0} d\zeta \left(\rho_R(z+\zeta) + \rho_R(z-\zeta)\right) \cdot \left[r_0^2 - \zeta^2\right]. \tag{F.10}$$

For all s and ζ such that $\sqrt{s'^2+\zeta^2} > r_0$, we have

$$u_1(r) = u_{\mathrm{LJ}}(r) \qquad \text{and} \qquad \zeta \in (-\infty, \infty). \tag{F.11}$$

The magnitude of ζ also has implications for the range of s', namely,

$$s' \in \begin{cases} [0, \infty) & \text{if } |\zeta| \ge r_0, \\ \left[\sqrt{r_0^2 - \zeta^2}, \infty\right) & \text{if } |\zeta| < r_0. \end{cases} \tag{F.12}$$

Thus $\forall(s',\zeta):\sqrt{s'^2+\zeta^2}>r_0$,

$$\begin{aligned}\phi_R^{\mathrm{LJ}}(z) &= 2\pi\int_{-\infty}^{-r_0} d\zeta\,\rho_R(z+\zeta)\int_0^{\infty} u_{\mathrm{LJ}}\left(\sqrt{s'^2+\zeta^2}\right)s'ds' \\ &\quad + 2\pi\int_{r_0}^{\infty} d\zeta\,\rho_R(z+\zeta)\int_0^{\infty} u_{\mathrm{LJ}}\left(\sqrt{s'^2+\zeta^2}\right)s'ds' \\ &\quad + 2\pi\int_{-r_0}^{r_0} d\zeta\,\rho_R(z+\zeta)\int_{\sqrt{r_0^2-\zeta^2}}^{\infty} u_{\mathrm{LJ}}\left(\sqrt{s'^2+\zeta^2}\right)s'ds' \qquad \text{(F.13)} \\ &= 2\pi\int_{r_0}^{\infty} d\zeta\,\left(\rho_R(z+\zeta)+\rho_R(z-\zeta)\right)\int_0^{\infty} u_{\mathrm{LJ}}\left(\sqrt{s'^2+\zeta^2}\right)s'ds' \\ &\quad + 2\pi\int_{0}^{r_0} d\zeta\,\left(\rho_R(z+\zeta)+\rho_R(z-\zeta)\right)\int_{\sqrt{r_0^2-\zeta^2}}^{\infty} u_{\mathrm{LJ}}\left(\sqrt{s'^2+\zeta^2}\right)s'ds'. \qquad \text{(F.14)}\end{aligned}$$

In order to simplify this formula for ϕ_R^{LJ} we may analytically evaluate

$$\int_a^{\infty} u_{\mathrm{LJ}}\left(\sqrt{s^2+\zeta^2}\right)s\,ds = 4\varepsilon_{\mathrm{LJ}}\int_a^{\infty}\left(\frac{\sigma_{\mathrm{LJ}}^{12}}{(s^2+\zeta^2)^6}-\frac{\sigma_{\mathrm{LJ}}^{6}}{(s^2+\zeta^2)^3}\right)s\,ds. \qquad \text{(F.15)}$$

By defining $\mathcal{R}=s^2+\zeta^2$ and therefore $d\mathcal{R}=2s\,ds$, we may reexpress this as

$$\begin{aligned}\int_a^{\infty} u_{\mathrm{LJ}}\left(\sqrt{s^2+\zeta^2}\right)s\,ds &= 2\varepsilon_{\mathrm{LJ}}\int_{a^2+\zeta^2}^{\infty}\left(\frac{\sigma_{\mathrm{LJ}}^{12}}{\mathcal{R}^6}-\frac{\sigma_{\mathrm{LJ}}^{6}}{\mathcal{R}^3}\right)d\mathcal{R} \qquad \text{(F.16)} \\ &= 2\varepsilon_{\mathrm{LJ}}\left[-\frac{1}{5}\frac{\sigma_{\mathrm{LJ}}^{12}}{\mathcal{R}^5}+\frac{1}{2}\frac{\sigma_{\mathrm{LJ}}^{6}}{\mathcal{R}^2}\right]_{a^2+\zeta^2}^{\infty} \qquad \text{(F.17)} \\ &= 2\varepsilon_{\mathrm{LJ}}\left(\frac{1}{5}\frac{\sigma_{\mathrm{LJ}}^{12}}{(a^2+\zeta^2)^5}-\frac{1}{2}\frac{\sigma_{\mathrm{LJ}}^{6}}{(a^2+\zeta^2)^2}\right). \qquad \text{(F.18)}\end{aligned}$$

Thus $\forall(s',\zeta):\sqrt{s'^2+\zeta^2}>r_0$, we may simplify

$$\begin{aligned}\phi_R^{\mathrm{LJ}}(z) &= 4\pi\varepsilon_{\mathrm{LJ}}\sigma_{\mathrm{LJ}}^2\int_{r_0}^{\infty} d\zeta\,\left(\rho_R(z+\zeta)+\rho_R(z-\zeta)\right)\left(\frac{1}{5}\left(\frac{\sigma_{\mathrm{LJ}}}{\zeta}\right)^{10}-\frac{1}{2}\left(\frac{\sigma_{\mathrm{LJ}}}{\zeta}\right)^{4}\right) \\ &\quad + 4\pi\varepsilon_{\mathrm{LJ}}\sigma_{\mathrm{LJ}}^2\left(\frac{1}{5}\left(\frac{\sigma_{\mathrm{LJ}}}{r_0}\right)^{10}-\frac{1}{2}\left(\frac{\sigma_{\mathrm{LJ}}}{r_0}\right)^{4}\right)\int_0^{\infty} d\zeta\,\left(\rho_R(z+\zeta)+\rho_R(z-\zeta)\right).\end{aligned} \qquad \text{(F.19)}$$

Finally combining the terms for all s' and ζ up to a constant, we find

$$\begin{aligned}\phi_R^{\mathrm{LJ}}(z) = C &- \pi\varepsilon_{\mathrm{LJ}} \int_0^{r_0} d\zeta \left(\rho_R(z+\zeta) + \rho_R(z-\zeta)\right) \cdot \left[r_0^2 - \zeta^2\right] \\ &+ 4\pi\varepsilon_{\mathrm{LJ}}\sigma_{\mathrm{LJ}}^2 \int_{r_0}^{\infty} d\zeta \ \left(\rho_R(z+\zeta) + \rho_R(z-\zeta)\right) \left(\frac{1}{5}\left(\frac{\sigma_{\mathrm{LJ}}}{\zeta}\right)^{10} - \frac{1}{2}\left(\frac{\sigma_{\mathrm{LJ}}}{\zeta}\right)^{4}\right) \\ &+ 4\pi\varepsilon_{\mathrm{LJ}}\sigma_{\mathrm{LJ}}^2 \left(\frac{1}{5}\left(\frac{\sigma_{\mathrm{LJ}}}{r_0}\right)^{10} - \frac{1}{2}\left(\frac{\sigma_{\mathrm{LJ}}}{r_0}\right)^{4}\right) \int_0^{\infty} d\zeta \ \left(\rho_R(z+\zeta) + \rho_R(z-\zeta)\right).\end{aligned} \tag{F.20}$$

Resubstituting $z' - z$ for ζ, we have

$$\begin{aligned}\phi_R^{\mathrm{LJ}}(z) = -\pi\varepsilon_{\mathrm{LJ}} &\int_z^{r_0+z} dz' \left(\rho_R(z') + \rho_R(2z - z')\right) \cdot \left[z'^2 - (z'-z)^2\right] \\ &+ 4\pi\varepsilon_{\mathrm{LJ}}\sigma_{\mathrm{LJ}}^2 \int_{r_0+z}^{\infty} dz' \ \left(\rho_R(z') + \rho_R(2z - z')\right) \left(\frac{1}{5}\left(\frac{\sigma_{\mathrm{LJ}}}{z'-z}\right)^{10} - \frac{1}{2}\left(\frac{\sigma_{\mathrm{LJ}}}{z'-z}\right)^{4}\right) \\ &+ 4\pi\varepsilon_{\mathrm{LJ}}\sigma_{\mathrm{LJ}}^2 \left(\frac{1}{5}\left(\frac{\sigma_{\mathrm{LJ}}}{r_0}\right)^{10} - \frac{1}{2}\left(\frac{\sigma_{\mathrm{LJ}}}{r_0}\right)^{4}\right) \int_z^{\infty} dz' \ \left(\rho_R(z') + \rho_R(2z - z')\right).\end{aligned} \tag{F.21}$$

The constant may be defined from the requirement that $\phi_R^{\mathrm{LJ}}(z=0) = 0$. Numerically, we implement this by choosing C so that $\phi_R^{\mathrm{LJ}}(z=0) = 0$.

Bibliography

[1] M. Allen and D. Tildesley. *Computer Simulation of Liquids*. Oxford: Clarendon Press, 1989.

[2] G. B. Arfken and H. J. Weber. *Mathematical Methods for Physicists*. New York: Harcourt Academic Press, 5th edition, 2001.

[3] H. S. Ashbaugh and M. E. Paulaitis. Effect of solute size and solute-water attractive interactions on hydration water structure around hydrophobic solutes. *J. Am. Chem. Soc.*, 123:10721–10728, 2001.

[4] J. A. Barker and D. Henderson. Perturbation theory and equation of state for fluids. 2. A succesful theory of liquids. *J. Chem. Phys.*, 47:4714–4721, 1967.

[5] H. Berendsen, J. Grigera, and T. Straatsma. The missing term in effective pair potentials. *J. Phys. Chem.*, 91:6269–6271, 1987.

[6] H. J. C. Berendsen, J. P. M. Postma, W. F. van Gunsteren, A. Dinola, and J. R. Haak. Molecular-dynamics with coupling to an external bath. *J. Chem. Phys.*, 81:3684–3690, 1984.

[7] H. J. C. Berendsen, J. P. M. Postma, W. F. van Gunsteren, and J. Hermans. *Intermolecular forces*, pages 331–342. Boston: Reidel, 1981.

[8] D. Bratko, C. D. Daub, K. Leung, and A. Luzar. Effect of field direction on electrowetting in a nanopore. *J. Am. Chem. Soc.*, 129:2504–2510, 2007.

[9] A. Brodka. Errors in the Ewald summation method with electrostatic layer correction for Coulomb interactions in slab geometry. *Chem. Phys. Lett.*, 410:446–451, 2005.

[10] D. Chandler. Dielectric-constant and related equilibrium properties of molecular fluids – Interaction site cluster theory analysis. *J. Chem. Phys.*, 67:1113–1124, 1977.

[11] D. Chandler and L. R. Pratt. Statistical mechanics of chemical equilibria and intramolecular structures of nonrigid molecules in condensed phases. *J. Chem. Phys.*, 65:2925–2940, 1976.

[12] D. Chandler, J. D. Weeks, and H. C. Andersen. van der Waals picture of liquids, solids, and phase-transformations. *Science*, 220:787–794, 1983.

[13] Y.-G. Chen. *General Theory of Nonuniform Fluids: From Hard Spheres to Ionic Fluids*. Ph.D. thesis, University of Maryland, College Park, 2004.

[14] Y. G. Chen, C. Kaur, and J. D. Weeks. Connecting systems with short and long ranged interactions: Local molecular field theory for ionic fluids. *J. Phys. Chem. B*, 108:19874–19884, 2004.

[15] Y. G. Chen and J. D. Weeks. Local molecular field theory for effective attractions between like charged objects in systems with strong Coulomb interactions. *Proc. Nat. Acad. Sci. USA*, 103:7560–7565, 2006.

[16] N. Choudhury and B. Pettitt. On the mechanism of hydrophobic association of nanoscopic solutes. *J. Am. Chem. Soc.*, 127:3556–3567, 2005.

[17] D. Corson and P. Lorrain. *Introduction to Electromagnetic Fields and Waves.* San Francisco: W. H. Freeman and Co., 1962.

[18] C. D. Daub, D. Bratko, K. Leung, and A. Luzar. Electrowetting at the nanoscale. *J. Phys. Chem. C*, 111:505–509, 2007.

[19] J. de Joannis, A. Arnold, and C. Holm. Electrostatics in periodic slab geometries. II. *J. Chem. Phys.*, 117:2503–2512, 2002.

[20] P. Demontis, S. Spanu, and G. Suffritti. Application of the Wolf method for the evaluation of Coulombic interactions to complex condensed matter systems: Aluminosilicates and water. *J. Chem. Phys.*, 114:7980–7988, 2001.

[21] N. A. Denesyuk. Private communication, 2008.

[22] N. A. Denesyuk and J. D. Weeks. A new approach for efficient simulation of Coulomb interactions in ionic fluids. *J. Chem. Phys.*, 128:124109, 2008.

[23] M. Deserno and C. Holm. How to mesh up Ewald sums. I. A theoretical and numerical comparison of various particle mesh routines. *J. Chem. Phys.*, 109:7678–7693, 1998.

[24] M. Deserno and C. Holm. How to mesh up Ewald sums. II. An accurate error estimate for the particle-particle-particle-mesh algorithm. *J. Chem. Phys.*, 109:7694–7701, 1998.

[25] Y. Duan, *et al.* A point-charge force field for molecular mechanics simulations of proteins based on condensed-phase quantum mechanical calculations. *J. Comp. Chem.*, 24:1999–2012, 2003.

[26] J. L. England, S. Park, and V. S. Pande. Theory for an order-driven disruption of the liquid state in water. *J. Chem. Phys.*, 128:044503, 2008.

[27] D. F. Evans and H. Wennerström. *The Colloidal Domain: Where Physics, Chemistry, and Biology Meet.* New York: Wiley-VCH, 2nd edition, 1999.

[28] S. E. Feller, R. W. Pastor, A. Rojnuckarin, S. Bogusz, and B. R. Brooks. Effect of electrostatic force truncation on interfacial and transport properties of water. *J. Phys. Chem.*, 100:17011–17020, 1996.

[29] C. Fennell and J. Gezelter. Is the Ewald summation still necessary? Pairwise alternatives to the accepted standard for long-range electrostatics. *J. Chem. Phys.*, 124:234104, 2006.

[30] J. Forsman. A simple correlation-corrected Poisson-Boltzmann theory. *J. Phys. Chem. B*, 108:9236–9245, 2004.

[31] D. Frenkel and B. Smit. *Understanding Molecular Simulation: From Algorithms to Applications*. New York: Academic Press, 2nd edition, 2002.

[32] W. M. Gelbart, R. F. Bruinsma, P. A. Pincus, and V. A. Parsegian. DNA-inspired electrostatics. *Phys. Today*, 53, 2000.

[33] N. Giovambattista, P. Rossky, and P. Debenedetti. Effect of pressure on the phase behavior and structure of water confined between nanoscale hydrophobic and hydrophilic plates. *Phys. Rev. E*, 73:041604, 2006.

[34] C. G. Gray and K. E. Gubbins. *Theory of Molecular Fluids Volume 1: Fundamentals*. Oxford: Clarendon Press, 1984.

[35] B. Guillot. A reappraisal of what we have learnt during three decades of computer simulations on water. *J. Mol. Liq.*, 101:219–260, 2002.

[36] L. Guldbrand, B. Jönsson, H. Wennerström, and P. Linse. Electrical double layer forces: A Monte Carlo study. *J. Chem. Phys.*, 80:2221–2228, 1984.

[37] J.-P. Hansen and I. R. McDonald. *Theory of Simple Liquids*. New York: Academic Press, 3rd edition, 2006.

[38] H. Heinz, W. Paul, and K. Binder. Calculation of local pressure tensors in systems with many-body interactions. *Phys. Rev. E*, 72:066704, 2005.

[39] B. Honig and A. Nicholls. Classical electrostatics in biology and chemistry. *Science*, 268:1144–1149, 1995.

[40] J. Høye and G. Stell. Dielectric-constant in terms of atom-atom correlation-functions. *J. Chem. Phys.*, 65:18–22, 1976.

[41] Z. Hu. Private communication, 2008.

[42] G. Hummer, S. Garde, A. Garcia, A. Pohorille, and L. Pratt. An information theory model of hydrophobic interactions. *Proc. Nat. Acad. Sci. USA*, 93:8951–8955, 1996.

[43] G. Hummer, L. Pratt, and A. Garcia. Free energy of ionic hydration. *J. Phys. Chem.*, 100:1206–1215, 1996.

[44] G. Hummer, L. Pratt, A. Garcia, B. Berne, and S. Rick. Electrostatic potentials and free energies of solvation of polar and charged molecules. *J. Phys. Chem. B*, 101:3017–3020, 1997.

[45] G. Hummer, D. Soumpasis, and M. Neumann. Pair correlations in an NaCl-SPC water model – Simulations versus extended RISM computations. *Mol. Phys.*, 77:769–785, 1992.

[46] G. Hummer, D. Soumpasis, and M. Neumann. Computer-simulation of aqueous Na-Cl electrolytes. *J. Phys.: Condens. Matt.*, 6:A141–A144, 1994.

[47] G. Hummer and D. M. Soumpasis. Computation of the water density distribution at the ice-water interface using the potentials-of-mean-force expansion. *Phys. Rev. E*, 49:591–596, 1994.

[48] P. H. Hünenberger and J. A. McCammon. Ewald artifacts in computer simulations of ionic solvation and ion-ion interaction: A continuum electrostatics study. *J. Chem. Phys.*, 110:1856–1872, 1999.

[49] I. Ionova and E. Carter. Error vector choice in direct inversion in the iterative subspace method. *J. Comp. Chem.*, 17:1836–1847, 1996.

[50] S. Izvekov, J. M. J. Swanson, and G. A. Voth. Coarse-graining in interaction space: A systematic approach for replacing long-range electrostatics with short-range potentials. *J. Phys. Chem. B*, 112:4711–4724, 2008.

[51] J. D. Jackson. *Classical Electrodynamics*. Hoboken, New Jersey: John Wiley and Sons, Inc., 3rd edition, 1999.

[52] B. Jönsson, H. Wennerström, and B. Halle. Ion distributions in lamellar liquid crystals: A comparison between results from Monte Carlo simulations and solutions of the Poisson-Boltzmann equation. *J. Phys. Chem.*, 84:2179–2185, 1980.

[53] K. Katsov and J. D. Weeks. On the mean field treatment of attractive interactions in nonuniform simple fluids. *J. Phys. Chem. B*, 105:6738–6744, 2001.

[54] K. Katsov and J. D. Weeks. Incorporating molecular scale structure into the van der Waals theory of the liquid-vapor interface. *J. Phys. Chem. B*, 106:8429–8436, 2002.

[55] J. B. Klauda, X. Wu, R. W. Pastor, and B. R. Brooks. Long-range Lennard-Jones and electrostatic interactions in interfaces: Application of the isotropic periodic sum method. *J. Phys. Chem. B*, 111:4393–4400, 2007.

[56] A. Kovalenko, S. Ten-No, and F. Hirata. Solution of three-dimensional reference interaction site model and hypernetted chain equations for simple point charge water by modified method of direct inversion in iterative subspace. *J. Comp. Chem.*, 20:928–936, 1999.

[57] J. Krumhansl and S. Wang. Superposition assumption. I. Low-density fluid argon. *Journal of Chemical Physics*, 56:2179–2189, 1972.

[58] R. Kumar, J. R. Schmidt, and J. L. Skinner. Hydrogen bonding definitions and dynamics in liquid water. *J. Chem. Phys.*, 126:204107, 2007.

[59] C. Y. Lee, J. A. McCammon, and P. J. Rossky. The structure of liquid water at an extended hydrophobic surface. *J. Chem. Phys.*, 80:4448–4455, 1984.

[60] J. Lekner. Summation of Coulomb fields in computer-simulated disordered-systems. *Physica A*, 176:485–498, 1991.

[61] Y. Levin. Electrostatic correlations: From plasma to biology. *Rep. Prog. Phys.*, 65:1577–1632, 2002.

[62] K. Lum, D. Chandler, and J. D. Weeks. Hydrophobicity at small and large length scales. *J. Phys. Chem. B*, 103:4570–4577, 1999.

[63] Y. Ma and S. Garofalini. Application of the Wolf damped Coulomb method to simulations of SiC. *J. Chem. Phys.*, 122:094508, 2005.

[64] J. A. D. MacKerell, *et al.* All-atom empirical potential for molecular modeling and dynamics studies of proteins. *J. Phys. Chem. B*, 102:3586–3616, 1998.

[65] A. Maggs. Auxiliary field Monte Carlo for charged particles. *J. Chem. Phys.*, 120:3108–3118, 2004.

[66] T. S. Mahadevan and S. H. Garofalini. Dissociative water potential for molecular dynamics simulations. *J. Phys. Chem. B*, 111:8919–8927, 2007.

[67] L. Maibaum and D. Chandler. Segue between favorable and unfavorable solvation. *J. Phys. Chem. B*, 111:9025–9030, 2007.

[68] P. Martin. Sum-rules in charged fluids. *Rev. Mod. Phys.*, 60:1075–1127, 1988.

[69] D. A. McQuarrie. *Statistical Mechanics*. Sausalito, California: University Science Books, 2000.

[70] A. Moreira and R. Netz. Strong-coupling theory for counter-ion distributions. *Europhys. Lett.*, 52:705–711, 2000.

[71] A. G. Moreira and R. R. Netz. Simulations of counterions at charged plates. *Eur. Phys. J. E*, 8:33–58, 2002.

[72] P. Nelson. *Biological Physics: Energy, Information, Life*. New York: WH Freeman, 2003.

[73] R. R. Netz. Electrostatics of counter-ions at and between planar charged walls: From Poisson-Boltzmann to the strong-coupling theory. *Eur. Phys. J. E*, 5:557–574, 2001.

[74] M. Neumann. Dipole moment fluctation formulas in computer simulations of polar systems. *Mol. Phys.*, 50:841–858, 1983.

[75] I. Nezbeda. Towards a unified view of fluids. *Mol. Phys.*, 103:59–76, 2005.

[76] L. Onsager. Electric moments of molecules in liquids. *J. Am. Chem. Soc.*, 58:1486–1493, 1936.

[77] J. C. Phillips, *et al.* Scalable molecular dynamics with NAMD. *J. Comp. Chem.*, 26:1781–1802, 2005.

[78] P. Pulay. Convergence acceleration of iterative sequences – the case of SCF iteration. *Chem. Phys. Lett.*, 73:393–398, 1980.

[79] P. Pulay. Improved SCF convergence acceleration. *J. Comp. Chem.*, 3:556–560, 1982.

[80] E. M. Purcell. *Electricity and Magnetism*, volume 2 of *Berkeley Physics Course*. New York: McGraw-Hill, 2nd edition, 1985.

[81] E. Rabani. Private communication, 2007.

[82] K. Raghavan, K. Foster, K. Motakabbir, and M. Berkowitz. Structure and dynamics of water at the Pt(111) interface: Molecular dynamics study. *J. Chem. Phys.*, 94:2110–2117, 1991.

[83] A. Robertson, E. Luttmann, and V. S. Pande. Effects of long-range electrostatic forces on simulated protein folding kinetics. *J. Comp. Chem.*, 29:694–700, 2008.

[84] W. Rocchia, E. Alexov, and B. Honig. Extending the applicability of the nonlinear Poisson-Boltzmann equation: Multiple dielectric constants and multivalent ions. *J. Phys. Chem. B*, 105:6507–6514, 2001.

[85] J. M. Rodgers. Local molecular field theory: An application to non-uniform Coulomb systems. Scholarly paper at University of Maryland, College Park, 2006.

[86] J. M. Rodgers, C. Kaur, Y.-G. Chen, and J. D. Weeks. Attraction between like-charged walls: Short-ranged simulations using local molecular field theory. *Phys. Rev. Lett.*, 97:097801, 2006.

[87] I. Rouzina and V. A. Bloomfield. Macroion attraction due to electrostatic correlation between screening counterions. 1. Mobile surface-adsorbed ions and diffuse ion cloud. *J. Phys. Chem.*, 100:9977–9989, 1996.

[88] J. Rowlinson and B. Widom. *Molecular Theory of Capillarity*. Mineola, New York: Dover, 2002.

[89] W. Smith. DL_POLY-applications to molecular simulation II. *Molec. Sim.*, 32:933–933, 2006.

[90] W. Smith, C. Yong, and P. Rodger. DL_POLY: Application to molecular simulation. *Molec. Sim.*, 28:385–471, 2002.

[91] E. Sorin and V. Pande. Exploring the helix-coil transition via all-atom equilibrium ensemble simulations. *Biophys. J.*, 88:2472–2493, 2005.

[92] R. Sperb. An alternative to Ewald sums – Part I: Identities for sums. *Molec. Sim.*, 20:179–200, 1998.

[93] E. Spohr. Effect of electrostatic boundary conditions and system size on the interfacial properties of water and aqueous solutions. *J. Chem. Phys.*, 107:6342–6348, 1997.

[94] F. H. Stillinger and R. Lovett. General restriction on distribution of ions in electrolytes. *J. Chem. Phys.*, 49:1991–1994, 1968.

[95] M. P. Taylor and J. E. G. Lipson. A site-site Born-Green-Yvon equation for hard sphere dimers. *J. Chem. Phys.*, 100:518–527, 1994.

[96] I. G. Tironi, R. Sperb, P. E. Smith, and W. F. van Gunsteren. A generalized reaction field method for molecular-dynamics simulations. *J. Chem. Phys.*, 102:5451–5459, 1995.

[97] B. Todd, D. J. Evans, and P. J. Daivis. Pressure tensor for inhomogeneous fluids. *Phys. Rev. E*, 52:1627–1638, 1995.

[98] S. Vaitheeswaran, H. Yin, and J. Rasaiah. Water between plates in the presence of an electric field in an open system. *J. Phys. Chem. B*, 109:6629–6635, 2005.

[99] J. Valleau, R. Ivkov, and G. Torrie. Colloid stability: The forces between charged surfaces in an electrolyte. *J. Chem. Phys.*, 95:520–532, 1991.

[100] F. Varnik, J. Baschnagel, and K. Binder. Molecular dynamics results on the pressure tensor of polymer films. *J. Chem. Phys.*, 113:4444–4453, 2000.

[101] S. Wang and J. Krumhansl. Superposition assumption. 2. High-density fluid argon. *Journal of Chemical Physics*, 56:4287–4290, 1972.

[102] J. D. Weeks. Connecting local structure to interface formation: A molecular scale van der Waals theory of nonuniform liquids. *Annu. Rev. Phys. Chem.*, 53:533–562, 2002.

[103] J. D. Weeks. Private communication, 2007.

[104] J. D. Weeks, D. Chandler, and H. C. Andersen. Role of repulsive forces in determining equilibrium structure of simple liquids. *J. Chem. Phys.*, 54:5237–5247, 1971.

[105] J. D. Weeks, K. Katsov, and K. Vollmayr. Roles of repulsive and attractive forces in determining the structure of nonuniform liquids: Generalized mean field theory. *Phys. Rev. Lett.*, 81:4400–4403, 1998.

[106] J. D. Weeks, R. L. B. Selinger, and J. Q. Broughton. Self-consistent treatment of repulsive and attractive forces in nonuniform liquids. *Phys. Rev. Lett.*, 75:2694–2697, 1995.

[107] J. D. Weeks, K. Vollmayr, and K. Katsov. Intermolecular forces and the structure of uniform and nonuniform fluids. *Physica A*, 244:461–475, 1997.

[108] H. Wennerström, B. Jönsson, and P. Linse. The cell model for polyelectrolyte systems: Exact statistical mechanical relations, Monte Carlo simulations, and the Poisson-Boltzmann approximation. *J. Chem. Phys.*, 76:4665–4670, 1982.

[109] D. Wolf. Structure of ionic interfaces from an absolutely convergent solution of the Madelung problem. *Solid State Ionics*, 75:3–11, 1995.

[110] D. Wolf, P. Keblinski, S. Phillpot, and J. Eggebrecht. Exact method for the simulation of Coulombic systems by spherically truncated, pairwise r^{-1} summation. *J. Chem. Phys.*, 110:8254–8282, 1999.

[111] X. Wu and B. R. Brooks. Isotropic periodic sum: A method for the calculation of long-range interactions. *J. Chem. Phys.*, 122:044107, 2005.

[112] I. Yeh and M. Berkowitz. Dielectric constant of water at high electric fields: Molecular dynamics study. *J. Chem. Phys.*, 110:7935–7942, 1999.

[113] I. Yeh and M. Berkowitz. Dielectric constants of water at high electric fields: Molecular dynamics study. In *Abstracts of Papers of the American Chemical Society*, volume 217, pages U377–U377, 1999.

[114] I. Yeh and M. Berkowitz. Ewald summation for systems with slab geometry. *J. Chem. Phys.*, 111:3155–3162, 1999.

[115] D. Zahn, B. Schilling, and S. Kast. Enhancement of the Wolf damped Coulomb potential: Static, dynamic, and dielectric properties of liquid water from molecular simulation. *J. Phys. Chem. B*, 106:10725–10732, 2002.